THE UNIVERSITY OF CHICAGO

CRYSTALLOGRAPHY AND PHASE RELATIONS OF IRON SULFIDES AT EARTH AND PLANETARY CORE CONDITIONS

A DISSERTATION SUBMITTED TO

THE FACULTY OF THE DIVISION OF THE PHYSICAL SCIENCES

IN CANDIDACY FOR THE DEGREE OF

DOCTOR OF PHILOSOPHY

DEPARTMENT OF THE GEOPHYSICAL SCIENCES

BY

CLAIRE CHRISTINE ZURKOWSKI

CHICAGO, ILLINOIS

AUGUST 2021

Table of contents

List of figures

List of tables

List of supplementary files

Supplementary files are available in ProQuest Dissertations & Theses and may also be downloaded at this link:
https://drive.google.com/drive/folders/1j-83sepYJkD-2nyZ-RbBLUJZCzmtuJAk?usp=sharing

SF2a. Quick manual for single-crystal analysis
SF2b. Example .exp file for Absorb in CrysAlisPro
SF3a. C23 Fe_2S CIF file
SF3b. Calculated X-ray diffraction pattern for C23 Fe_2S
SF5a. $Co_{12}P_7$ CIF file
SF6a. C22 Fe_2S CIF file
SF6b. Cr_2P-type Fe_2S CIF file
SF6c. $Fe_{12}S_7$ CIF file
SF7a. Fe-P trigonal phase CIF file

Abstract

Sulfur is a primary alloying element in Earth and planetary cores. Investigating iron-sulfide phase relations at high pressures and temperatures is integral to constraining core chemistry and dynamics. At ambient conditions, numerous iron sulfides adopt complex structures, but little work has been done to examine the crystallography of high *P-T* iron-rich sulfides that may influence the thermodynamics of Earth's complex core. Over the course of this work, I combined single-crystal X-ray diffraction with powder X-ray diffraction techniques on multigrain iron-sulfur samples synthesized in a laser heated diamond anvil cell to 200 GPa and 3500 K. The results unveil novel complexities of the Fe-S system under extreme conditions, and several iron-rich sulfides are characterized and discussed: *C*23 Fe_2S*, Cr_2P-type Fe_2S*, *C*22 Fe_2S, *C*37 Fe_2S, Fe_3S, $Fe_{12}S_7$*, and $Fe_{11}S_4$* (* novel phase discovered in this work). As tetragonal Fe_3S was previously reported to remain stable in iron-rich systems across the *P-T* range of this study, the stability of these additional iron sulfides are placed into the context of iron-rich systems to develop an updated iron-sulfide phase diagram relevant to Earth's core. The complexity of the results highlight the analytical power of combining powder-diffraction techniques for examining phase synthesis *in-situ* with high pressure single-crystal diffraction techniques for analyzing crystal structures at high pressures, and provides critical insight on the material properties of iron-rich sulfides relevant to Earth and terrestrial planetary cores.

Acknowledgment

Portions of this work were performed at GeoSoilEnviroCARS (The University of Chicago, Sector 13), Advanced Photon Source (APS), Argonne National Laboratory. GeoSoilEnviroCARS is supported by the National Science Foundation - Earth Sciences (EAR - 1634415). This research used resources of the Advanced Photon Source, a U.S. Department of Energy (DOE) Office of Science User Facility operated for the DOE Office of Science by Argonne National Laboratory under Contract No. DE-AC02-06CH11357. Use of the COMPRES-GSECARS gas loading system was supported by COMPRES under NSF Cooperative Agreement EAR-1606856 and by GSECARS through NSF grant EAR-1634415 and DOE grant DE-FG02-94ER14466. This research used resources of the Advanced Photon Source, a U.S. Department of Energy (DOE) Office of Science User Facility operated for the DOE Office of Science by Argonne National Laboratory under Contract No. DE-AC02-06CH11357.This material is based upon work supported by a National Science Foundation Graduate Research Fellowship to C.C.Z. This work was also supported by the National Science Foundation by grant EAR-1651017 to A.J.C.

I would like to thank my supervisor, Andrew Campbell for introducing me to mineral physics, allowing me to attempt high pressures soon into my graduate career and recognizing my interest in crystallography. I would also like to thank my advisor in crystallography and multigrain diffraction, Barbara Lavina. Thank you, Barbara, for the time spent helping conduct my experiments and the effort put into teaching me about our experiments and scientific writing on crystallography.

I would also like to acknowledge Stella Chariton for her many helpful insights into single crystal experiments and analyzing single crystal data.

This work would not be possible without the beamline staff at APS Sector's 13 ID-D and 13 BM-D: Vitali Prakapenka, Stella Chariton, Sergey Tkachev, and Eran Greenberg. I appreciate your devotion to maintaining the beamline and designing new tools for better experiments. In particular, the recent single crystal data collection programs have been extremely helpful. Special thanks to Sergey Tkachev, as well, for gas loading samples on short notice at all times and data and night.

This work would also not be possible without the support of my past and current labmates: Nigel Brauser, Anne Davis, Kellie Swadba, Cara Vennari, Bethany Chidester, and Elizabeth Thompson. Thank you to Abigail Case, as well, for allowing me the opportunity to mentor in single crystal X-ray diffraction techniques.

Most importantly, thank you to my family for supporting me on this knowledge journey.

1. Constitution of the Earth, mysteries of its deep interior, and the role of sulfur in Earth and planetary cores

1.1. Earth and its interior

Within the 6,371 km radius of Earth's interior lies incredible chemical and dynamic complexity that sustains life on its surface. Earth and the terrestrial planets are layered structures; composed of silicate mantles and dense metallic cores (Figure 1.1). The Earth's crust, that we inhabit, extends to only 5-10 km depth (~0.2% of the Earth's radius) and is composed of moving plates of continental and oceanic rocks that spread and collide to shape Earth's surface. Movement of the tectonic plates is driven by the convection of a 2,800 km thick viscous silicate mantle. Material from various depths of the chemically heterogeneous upper mantle can be sampled at plate boundaries and volcanoes. The mantle, however, overlies the most mysterious layer of our planet: the ~3,500 km thick metallic core. No processes, natural or manmade, currently exist to exhume material from Earth's core. At the ~3000–6300 km depths of the core, pressures reach 136–360 GPa [~(1.3–3.6)x10^6 atm) and temperatures span ~4000–6500 K (Figure 1.1): conditions that are far too extreme for current excavation methods. We can, however, appreciate that the core plays a critical role in our planet's habitability; namely, the convecting metallic liquid in Earth's core generates the magnetic field that shields life on Earth's surface from destructive cosmic rays. As Earth's core accounts for ~1/2 of the planet's radius and ~1/3 of the planet's mass, investigation into the formation, chemistry and dynamics of planetary cores is imperative to interpreting the origin and evolution of planetary bodies more generally.

Experimental synthesis of core-relevant chemistries at high pressures and temperatures (*P*-*T*) is imperative to achieving an in-depth understanding of Earth and planetary cores. While no physical samples exist that originated directly from Earth's core, constraints that may be combined with experimental approaches to studying planetary cores can be derived from several sources: solar elemental abundances, primitive meteorites thought to originate from various locations in planetary bodies and the solar system, consistent outcomes from models of planet formation, density profiles inverted from seismic wave signals from Earth's deep interior, moment of inertia and chemical measurements from missions to the terrestrial planets, and geomagnetic field observations on Earth and terrestrial planets (e.g., McDonough and Sun, 1995; Treiman et al. 2000; Yang et al. 2010; Scott and Wasson 1975; Birch et al. 1952; Solomon 1976; Anderson 1972; Buffett 2000).

Our knowledge of the origin, formation, chemistry, structure and dynamics of Earth's complex and mysterious core will be introduced here based on the constraints developed in these many previous studies. Using Earth as a model, the interior structures of the terrestrial planets will also be discussed. A compelling thread that is sewn through the many processes inherent to Earth's current state is the presence and role of sulfur. Despite being classified as a volatile element, sulfur is characterized as being significantly more siderophile (iron-loving) than it is lithophile (silicate-loving). To the degree that sulfur is in an asteroid- to Earth-sized planetary body, it is likely to be sequestered into the core. Sulfur alloyed with iron also significantly changes the physical properties of a material compared to pure iron; including its melting

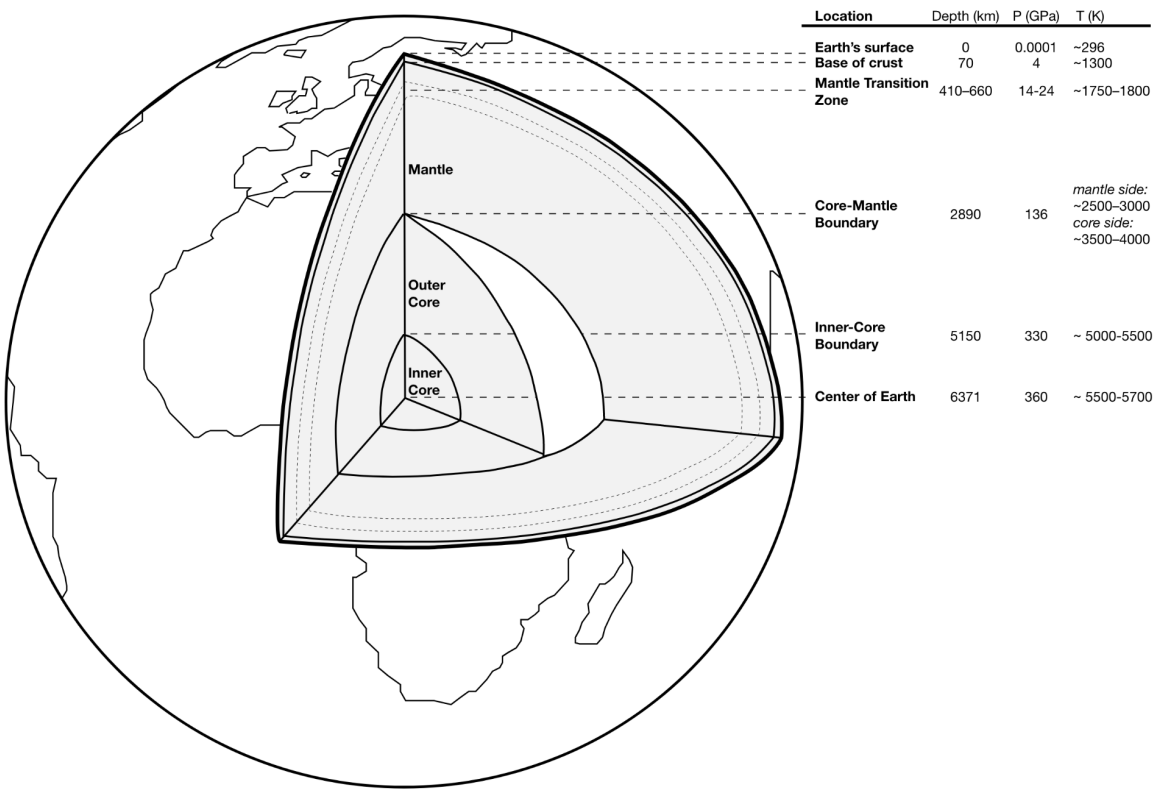

Figure 1.1. Depiction of Earth's layered interior including the depth, pressure and approximate temperature of the boundaries between these layers. The Earth's crust extends to only 70 km depth (~1% of the Earth's radius) and overlies the silicate mantle. The mantle extends to 2890 km, and can be viewed as an upper mantle above 410 km and lower mantle below 660 km. At 2890 km, the silicate mantle is in contact with the liquid metallic outer core. The liquid outer core is convecting as it crystallizes out Fe-rich material into the inner core. The Fe-rich inner core currently has a ~1,200 km radius.

temperature, density and crystallography. As Earth's core is partially liquid and partially crystalline (Figure 1.1), the crystal structure of iron sulfides at Earth's core conditions are an integral component for modeling of core thermodynamics. While the developments in high pressure and temperature experimental methods, namely synchrotron powder X-ray diffraction techniques, have greatly aided in the assessment of core-relevant iron-sulfide melting behavior and density profiles; only recently has the opportunity to investigate the high pressure-

temperature (*P-T*) crystallography of these phases become available. This thesis work exemplifies the novel power of combining powder and single crystal X-ray diffraction techniques on multigrain samples to unravel the story of iron sulfide crystallization and thermodynamics in Earth's complex core.

1.2. Planet formation, origin and composition of Earth's core, and the role of sulfur-rich melts

Through a series of accretionary, collisional, and gravitational processes, the first condensates from the solar nebula evolved into the planetary bodies of our solar system (e.g., Chambers, 2004, Nagasawa et al. 2007, Raymond et al. 2009). For terrestrial planets like Earth, the late stages of formation are marked by high-energy collisions of planetary embryos into the growing planets (e.g., Wetherill 1985; Kokuba and Ida 2002; Raymond et al. 2009). Embryos are characterized as roughly Moon-sized bodies that have reached a size where they accumulate material rather than disperse on collision (e.g., Wetherill and Stewart 1993). These bodies form within approximately 1 million years of solar system formation and are the building blocks for the terrestrial planets (Weidenschilling et al. 1997). When the inner solar system reaches a stage at which the density of planetesimals and embryos are approximately equal, giant collisions result and the largest bodies accumulate material and eventually evolve, on a 10^8-year timescale, into the terrestrial planets of our solar system (e.g., Chambers and Wetherill 1998; Agnor et al. 1999; Kominami and Ida 2002; Raymond et al. 2009).

In the planetesimal-embryo, embryo-embryo, and embryo-protoplanet collisional processes, heat produced from high energy giant impacts, radioactive decay of ^{26}Al, and release of gravitational potential energy results in global melting and core formation (Figure 1.2) (e.g., Benz and Cameron, 1990; Abe 1993; Rubie et al. 2003; Labrosse et al. 2007; Rubie et al. 2011; Ricard et al. 2009; Walter and Tronnes 2003; Yin et al. 2002). Solar abundances of iron and the presence of Fe-rich meteorites thought to originate in the cores of the planetesimals indicate that the elements segregating into the cores of embryos and the proto-Earth were dominated by iron and elements that easily alloy with iron under differentiation conditions (McDonough and Sun 1995; Scott and Wasson 1975). In particular, a key chemical component of metal segregation in Earth, embryo, and planetesimal core formation is the presence of sulfur (Murthy and Hall 1970; Stevenson 1988; Shannon and Agee 1996; Yoshino et al. 2003). Sulfur easily alloys with iron at pressures related to small body and protoplanetary differentiation and sulfur significantly lowers the melting point of pure iron (e.g., Boehler 1992; Fei et al. 1997; Morard et al. 2008). Iron-sulfide melting during planetary accretion promotes metal-melt rainout in a silicate liquid and aids in forming metal-melt percolation networks through a solid silicate matrix (Stevenson 1988; Rubie et al. 2003; Labrosse 2007; Terasaki 2008).

In models of the proto-Earth's differentiation, the formation of a global magma ocean is the most efficient form of differentiation, given the immense heat produced during planetary accretion (e.g., Rubie et al. 2003). In the magma ocean scenario, dense Fe-sulfide melts initially coalesce into droplets that sink through silicate magma towards the center of the planet (Figure 1.2) (Rubie et al. 2003; Labrosse et al. 2007). Simultaneously, as the planet is cooling, the shallow silicate magma begins to crystallize down onto a growing solid mantle. The Fe-sulfide

melt droplets accumulate and pool together on the crystalline silicate layer and become gravitationally unstable. In the form of large diapirs, the liquid metal is thought to rapidly sink to the center of the planet and onto the growing core. The basal magma ocean in contact with the liquid core becomes enriched in Fe, and sustains a liquid state as iron lowers the melting temperature of the silicate (Labrosse et al. 2007). Over time, the basal magma ocean crystallizes upwards onto the solid mantle, while the metallic core remains insulated by the silicate mantle and cools more slowly. Eventually the crystallization of a dense Fe-rich inner core commences and contributes to the compositional and thermally driven convection of the more light-element rich outer core (e.g., Nimmo 2015).

Hf-W isotope chronology suggests that magma ocean formation and segregation of Earth's core occurred early in accretion; within ~30 million years of the 100 Ma accretion timescale (Yin et al. 2002). Models of Earth's core formation also suggest that core formation was multistage and heterogenous, and large concentrations of metal may have been delivered to Earth's growing core via late colliding differentiated embryos (Rubie et al. 2003; 2011). While most of the embryos and planetesimals that aggregated to Earth equilibrated fully (70–100% equilibration) with the mantle and joined the magma ocean core segregation process, the final large and differentiated embryos (~Mars-sized) may have penetrated too deep into the planet to fully equilibrate with mantle before entering directly into the core during impact (Rubie et al. 2011; Rubie et al. 2015; Fischer et al. 2017). The chemistry, structure, size and penetration depth of these late colliding embryos relative to the *P-T* conditions of the evolving core-mantle boundary of the proto-Earth, would have directly and distinctly shaped the chemistry of Earth's

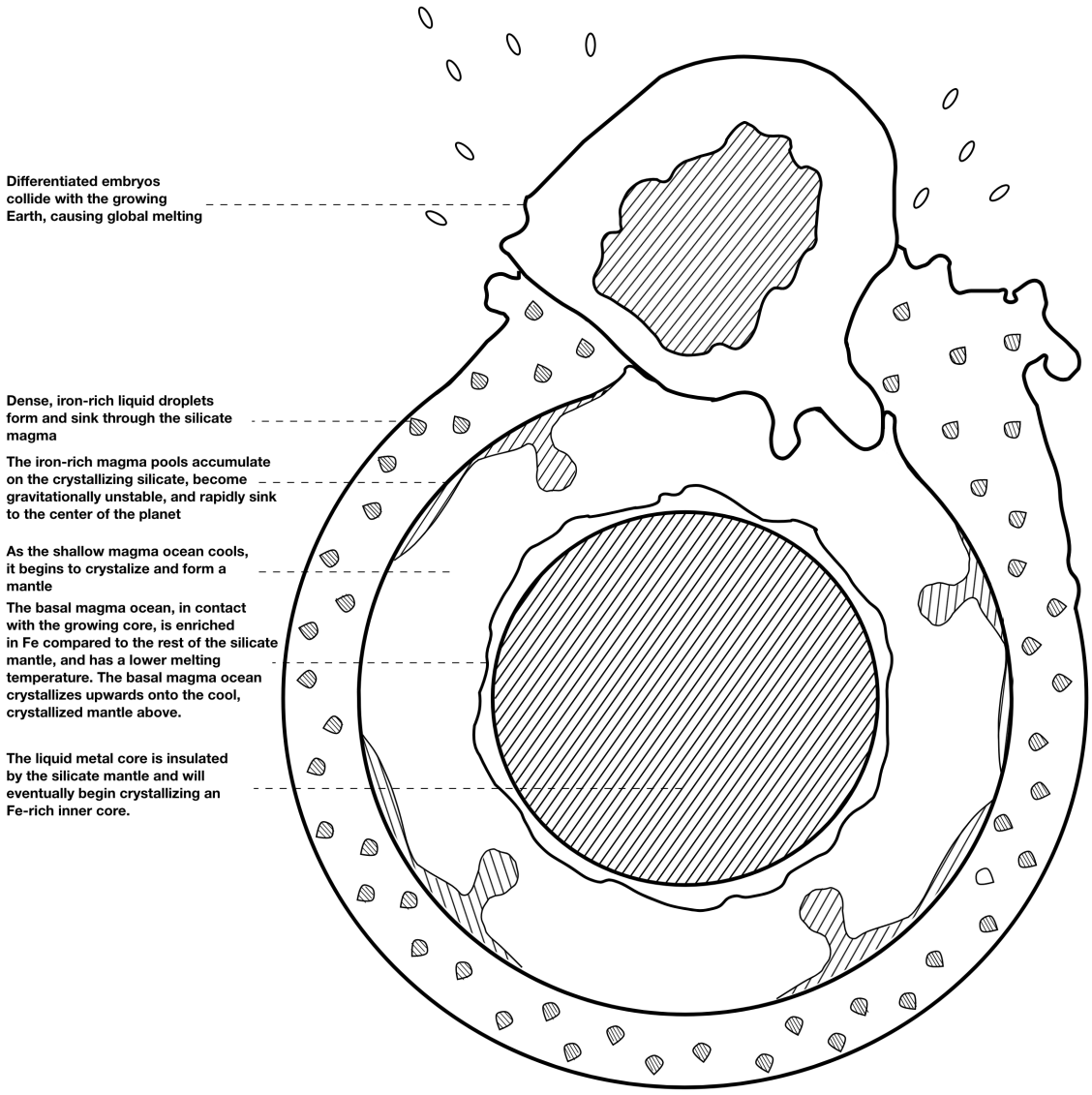

Figure 1.2. An artist's rendition of the proto-Earth's global magma ocean with labels explaining the various processes involved in planetary differentiation (rendered after Labrosse et al. 2007).

mantle and core (e.g., Taylor and Norman, 1990; Greenwood et al. 2005; Rubie et al. 2003; Rubie et al. 2011; Rubie et al. 2015; Fischer et al. 2017; Fischer et al. 2018).

Accretion models that best satisfy Earth's mantle compositions indicate that Earth's core has a significant Si and O component and formed from initially reducing material with late delivery of oxidized material (Rubie et al. 2011; Fischer et al. 2017). Recent metal-silicate partitioning studies of sulfur reveal that sulfur becomes less siderophile with pressure and a significant amount of the core's sulfur content may have been incorporated via the final embryos that integrated directly into the proto-Earth's core (Suer et al. 2017). Rubie et al. 2011 reports a core composition with iron alloyed with ~ 5 wt% Ni, ~ 8 wt% Si, ~ 2 wt% S and ~ 0.5 wt% O. By comparison, geochemical models comparing solar abundances with estimates of the bulk silicate Earth, indicate that Earth's core likely consists of iron alloyed with 5.2wt% Ni + 1.9 wt% S, 6.0 wt% Si, 0.2 wt% C and 600 ppm H (McDonough 2003).

1.3. Sulfur in iron meteorites and the proximity of differentiation to solar system formation

Iron meteorites are thought to be relics of planetesimals cores formed during differentiation of chondritic (primitive solar system material) parent bodies, and the timing of iron meteorite formation marks the period in solar system history when planetary bodies began to form metallic cores. Iron meteorites are composed of Fe, Ni, S, P, C and smaller amounts of the siderophile trace elements (e.g., Lovering 1957; Wasson 1967; Scott and Wasson, 1975; Malvin 1984; Wasson 1989; Jarosewich 1990; Haack and McCoy 2005; Goldstein et al. 2009; Benedix et al. 2014). Iron meteorites are commonly classified into groups, such as IIAB, IID, IIIAB, IVA, and IVB, based on their trace element to Ni ratios (Malvin et al. 1984). Sulfur is most commonly

observed in the form of troilite (FeS) and daubreelite ($FeCr_2S_4$) in iron meteorites (Scott and Wasson 1975). Iron meteorites are expected to form from chondritic material, but $\varepsilon^{182}W$ values determined for the IIAB, IID, IIIAB, IVA, and IVB meteorites reveal that core formation occurred very early in the history of our solar system: ~ 0.7 to ~2.9 My after the formation of CAI's. (Kruijer et al. 2014b; Burkhardt et al. 2012) (Figure 1.3). These results indicate that planetary body melting and differentiation was an early event in solar system formation and that chondrite meteorites formed later and escaped differentiation.

The difference in timing of core formation among the groups of iron meteorites is likely a direct consequence of the abundance of heat from ^{26}Al decay in the early solar system and the sulfur content of the parent body. If a parent body accreted at 1–2 Myr after CAI formation, the abundance of heat from ^{26}Al decay would rapidly heat and differentiate the planet, leaving the accretion and core formation ages indistinguishable (Kruijer et al. 2014a). Parent bodies that formed later were likely more sensitive to bulk sulfur content. Figure 1.3a visualizes the trend in timing of core formation in the iron meteorite parent bodies with bulk sulfur content in their cores (Kruijer et al. 2014a). The general trend suggests parent bodies with high sulfur content differentiated sooner after CAI formation.

Figure 1.3b shows the 1-bar Fe-FeS phase relations from Fei et al. 1997 with dotted lines connecting the bulk sulfur content and approximate superliquidus (above the liquidus) temperatures for the iron-meteorite parent bodies at these conditions (Kruijer et al. 2014a). Differentiation occurred at higher-than-ambient pressures, but within error, these temperature

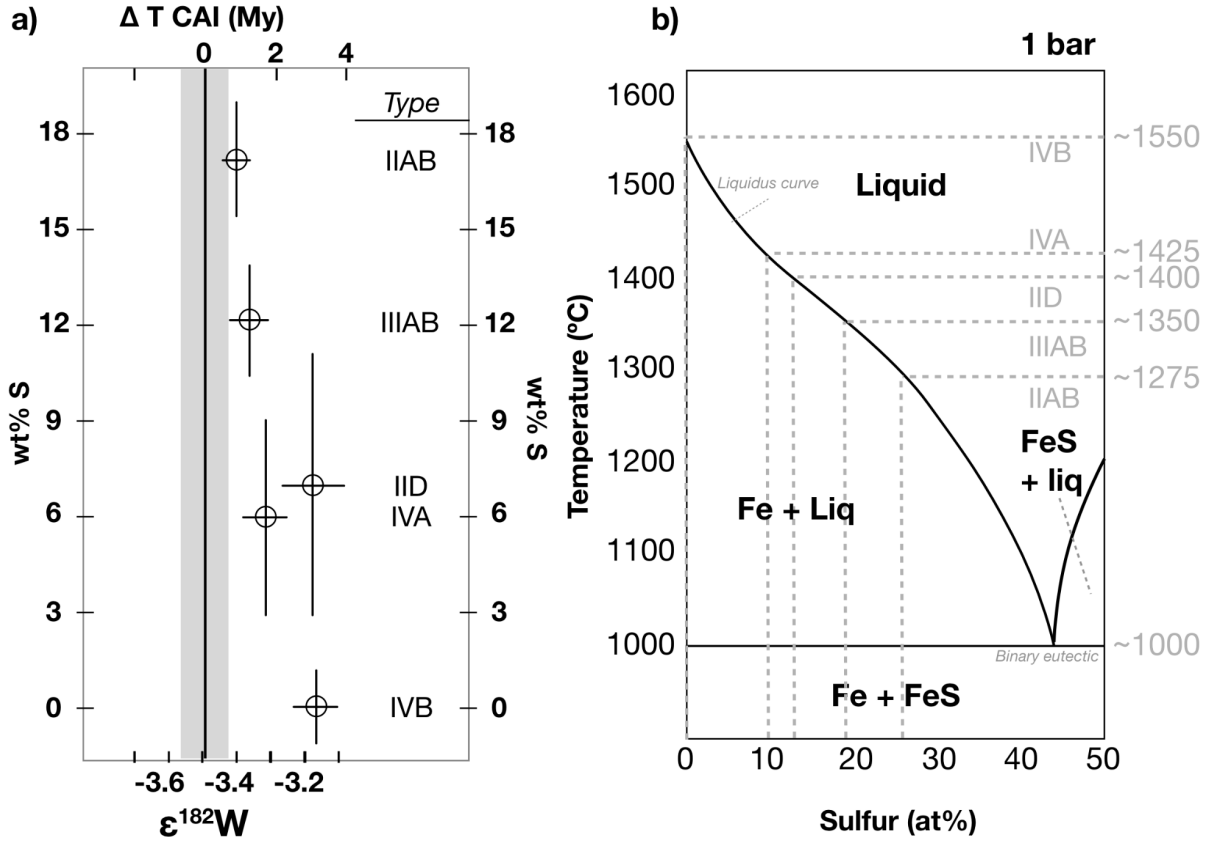

Figure 1.3. a) Iron meteorite sulfur contents (wt%) plotted with formation ages (after CAI) (Kruijer et al. 2014a). b) 1 bar Fe-FeS phase relations (Fei et al. 1997) with temperatures and sulfur compositions of the iron meteorites in (a) joined by the grey dashed lines. The difference in eutectic temperature and liquidus temperature can be compared for the differing iron meteorite groups. Differentiation occurred at higher than ambient pressures, but within error, these temperature values give an example of the effect of sulfur on the evolution of planetesimal cores.

values give an example of the effect of sulfur on the evolution of planetesimal cores. A discussion of reading and interpreting binary temperature-composition phase diagrams is provided in Appendix 1. When the iron meteorite parent bodies reached the Fe-FeS eutectic temperature (~1000 ºC at 1 bar), the first Fe-S melts would form. For S-rich parent bodies, such as the IIAB parent bodies, the planetesimals would only need to increase in temperature by ~275º to melt all of the metal in the planetary body, while the S-poor parent bodies, such as the

IVB parent bodies, would have to increase in temperature by a factor of 2 compared to the IIAB planetesimals in order to completely melt the metal component. For an accretion age of 0.25 Myr after CAI, core formation of iron meteorite parent bodies could have occurred over a 1 My period; therefore, accretion of the iron meteorite groups probably occurred between 0.1 and 0.3 Myr after CAI while the liquidus temperature of iron was not reached in the iron meteorite parent bodies until 0.7-1.3 Myr after CAI (Kruijer et al. 2014a).

Sulfur is not only an important chemical ingredient in iron meteorites and the building blocks of planets like Earth; but its melting behavior is attributable to the timing of core formation and evolution of our early solar system.

1.4. A Model of Earth's interior based on geophysical, thermal and experimental constraints

1.4.1. Geophysical constraints

The previous discussion has established that sulfur was present in the metal component and requisite to the differentiation of protoplanetary bodies. This section aims to develop an interior model of Earth and terrestrial planets to frame our investigations of sulfide crystallography and its effects on the structure and dynamics of Fe-alloy rocky planetary cores.

Reports on the individual light element content in Earth's core differ among studies and remain unknown, but the bulk light element component of Earth's core is well constrained by the density profiles established by inversion models of the seismic waves detected from Earth's deep interior (Figure 1.4) (Birch 1952; Dziewonski and Anderson 1981; Irving et al. 2018; Masters

and Gubbins 1993). The resulting seismological model of Earth's core may then be compared and matched to the experimentally determined equations of state (EoS), or pressure-volume-temperature relationships, of core-relevant Fe-alloy phases.

Early estimations of seismic densities compared with available experimentally determined EoS for relevant minerals supported that Earth's core was predominantly made of iron with a solid Fe inner core and a liquid outer core that is ~10–20% less dense than pure Fe (Birch 1952). In 1979, The Preliminary Reference Earth Model (PREM) was developed to best fit the moment of inertia, body wave travel times, and normal mode data of Earth's interior (Dziewonski and Anderson 1981). The results of PREM are drawn as the solid black lines in Figure 1.4, with lines referring to the density, compressional velocity and sound velocity profiles of Earth's interior.

Overall, the density and compressional wave velocities increase with depth in the Earth's interior. Discontinuities in density and velocity through the mantle are attributable to densification phase transitions and reactions of abundant silicate minerals at depth (e.g., Murakami et al. 2004). Most notably, a ~25% density increase is observed at ~2890 km depth, corresponding to the boundary between the silicate mantle and metallic core. A drop in compressional wave velocity and a loss of shear wave velocity are also observed. As shear waves do not travel through liquids and liquids are more compressible than solids, this observation confirms that the outer core is a liquid. A ~5% density increase is observed at 5150 km depth along with transmitted shear waves, marking the onset of the solid inner core, composed of a denser metal compared to the outer core (Figure 1.4).

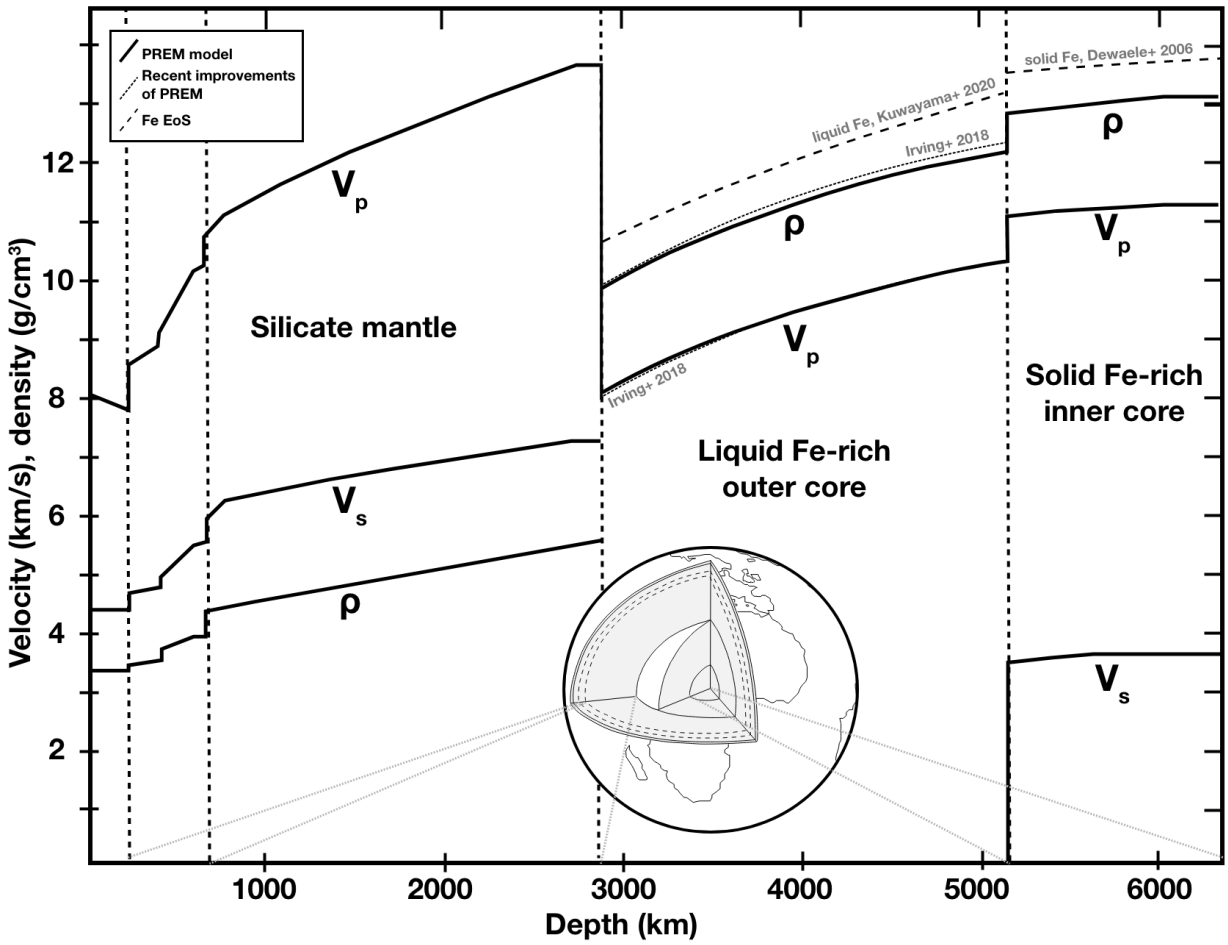

Figure 1.4. Density and velocity profiles for Earth's interior based on the Preliminary Reference Earth Model (PREM) (Dziewonski and Anderson 1981) (black solid lines). Recent seismic models of Earth's outer core and the density jump at Earth's inner core are also included (Irving et al. 2018) (dotted line). The density curve for liquid iron and solid iron extrapolated to Earth's outer and inner core conditions, respectively are also plotted for comparison (Kuwayama et al. 2020; Dewaele et al. 2006). Dashed vertical lines indicate the mantle transition zone, outer core and inner core boundaries.

Recent seismic studies have sought to improve upon the *Preliminary* Reference Earth Model that has reigned true for mineral physicists and geophysicists for decades. The Masters and Gubbins (2003) study examined datasets of Earth's free oscillations or normal mode frequencies that had expanded since the origin of PREM. Portions of this study focused on the

density change at the inner core boundary and revealed a greater density jump compared to PREM (0.82 g/cm^3) as a consequence of a slight increase in inner core density and decrease in outer core density (Masters and Gubbins 2003).

The more recent work by Irving et al. 2018 aimed to improve on the discrepancies in the seismic models of Earth's outer core derived from the body wave signals versus models inverted based on the normal mode frequencies (Irving et al. 2018). In this work, an EoS was developed to directly model the liquid outer core and best match normal mode observations. The resultant model is also consistent with body wave models and markedly improves our understanding of the seismic properties of Earth's outer core. The updated density and velocity profiles of the outer core from this work are shown as the labeled dotted line in Figure 1.4. The compressional velocity of the outer core is lower than that proposed by PREM at the top of the outer core, but overlaps with PREM throughout the rest of the outer core (Figure 1.4). The updated density profile of the outer core reveals a denser outer core than previously thought, and the outer core is about 1.5% more dense at the ICB than previously reported. Irving et al. 2018 concludes that matching the velocity and density profile of the outer core requires a compressible light element component.

1.4.2. Thermal constraints

The thermal profile of Earth's interior is less well constrained compared to the pressure, density and velocity profiles (Figure 1.4), as it is directly dependent on the composition of Earth's interior. Some general thermal constraints of Earth's core can be discussed and are

important for experimental approaches to constraining Earth's core composition. Namely, the physics of Earth's convecting outer core can be modeled as approximately adiabatic (Equation 1.1) (e.g., Loper 1978; Anderson 1998). In an adiabatic system, the thermodynamic parameter called the Grüneisen parameter (ɣ) can be described as the variation in temperature with density at constant entropy (Equation 1). Theoretical evaluation of the Grüneisen parameter compared with experimental geodynamic data, indicates that the Grüneisen parameter for Earth's liquid outer core is around 1.3 (Anderson 1998).

$$\gamma = (d\ln T/d\ln \rho)_s \quad (1.1)$$

The smaller, insulated, and solid inner core can be modeled as approximately isothermal (e.g., Strixrude et al. 1997). The boundary between the solid inner core and liquid outer core marks the equilibrium temperature where the cooling outer core reaches the liquidus temperature and crystallizes out the first solid phase or the *liquidus* phase. In the case of Earth's inner core, the density profile restricts that the liquidus phase at the ICB is denser than the outer core liquid. Furthermore, the temperature at which the liquidus phase begins to crystallize (ICB temperature) must extrapolate along the outer core adiabat (Equation 1) to give a reasonable temperature at the CMB such that the temperatures on the mantle side of the CMB remain subsolidus.

In the simplest case where the core is a unary system composed completely of iron, melting studies of iron have indicated that at ICB pressures, iron melts at around 6200 K (Anzellini et al. 2013). Extrapolating along the adiabat, the temperature on the core side of the purely liquid iron outer core would be around ~4700 K. This temperature is high enough that it would likely result in extensive melting on the mantle side of the CMB (Fiquet et al. 2010), and the velocity profile of the lower mantle affirms that this is not the case (Dziewonski and

Anderson 1981). The incorporation of light elements into the core, therefore, must lower the liquidus temperature compared to the melting temperature of pure iron and the temperature at the inner core boundary must be less than 6200 K (Anzellini et al. 2013).

1.4.3. Experimental constraints

1.4.3.1. Equations of state of pure iron

Equations of state studies of iron extrapolated to core conditions (Figure 1.4, dashed lines) indicate that liquid iron is about 7.5–7.6% more dense than the liquid outer core with the compressional velocities in excess of ~3.7–4.4% (Kuwayama et al. 2020). The density of solid iron at the inner core boundary is about 4% more dense than that of the inner core (Dewaele et al. 2006; Dziewonski and Anderson 1981) (Figure 1.4). The density difference between solid and liquid Fe at ICB conditions is ~2%; not large enough to match the ~4% density discontinuity observed at the ICB (Dziewonski and Anderson 1981; Irving et al. 2018; Dewaele et al. 2006; Kuwayama et al. 2020), and the incorporation of light elements is therefore required to match for the density profile of Earth's core.

1.4.3.2. Experimental investigations of iron alloys

Combining these geophysical and thermal constraints, Earth's Fe-alloy core composition must simultaneously 1) match the density and velocity profiles of the core, 2) crystallize denser material at ICB conditions compared to the remaining liquid, 3) match the density discontinuity at ICB conditions, and 4) lower the melting temperature compared to pure iron for a reasonable thermal profile through the outer core. Figure 1.5 shows the density profiles, melting curves and

phase diagrams of relevant Fe+(S, Si, C, O and H) compared to pure iron (Dewaele et al. 2006; Hu et al. 2019; Thompson et al. 2020; Fischer et al. 2012; Fischer et al. 2011; Anzellini et al. 2013; Morard et al. 2017; Mori et al. 2017; Sakamaki et al. 2009). At present, EoS, melting, and liquidus phase studies of binary Fe-alloys (Fe + Si, S, O, C or H) binary systems have not found a two-component system that can account for these constraints.

All of the Fe-alloy systems have lower melting temperatures than pure iron (Figure 1.5a) (Sakamaki et al. 2009; Anzellini et al. 2013; Fischer et al. 2012; Morard et al. 2017; Mori et al. 2017). For the Fe-Si system, Si dissolves significantly into iron, and does not effectively lower the melting temperature of pure iron compared to the other light elements (Figure 1.5a, c) (Fischer et al. 2012). Si also partitions almost equally between iron liquid and solid, resulting in too small of a density difference to match the solid-liquid density change at inner core boundary (Fischer et al. 2012) (Figure 1.5c). Oxygen forms FeO at core conditions and equations of state studies indicate that ~8 wt% O is required to match the outer core density deficit (Figure 1.5a). While this does fall within the Fe liquidus field of the Fe-FeO phase diagram at outer core conditions (Morard et al. 2017), Fischer et al. 2011 argues that the slopes of the adiabatic density profiles of hcp-Fe and FeO do not combine to match the seismic profile of Earth's core. Therefore, oxygen cannot simultaneously describe the density and velocity profile of the outer core. Accretion models of Earth also consistently indicate that Earth formed predominantly from reducing material (Rubie et al. 2007; Rubie et al. 2011; Fischer et al. 2017). For the Fe-S alloys, EoS studies of Fe_3S and FeS_2 indicate that 11–16 wt% S would match the outer core density profile, but these values are sulfur-rich relative to the eutectic composition at outer core conditions (~ < 6wt%, < 10 atm% S) (Seagle et al. 2006; Mori et al. 2017; Thompson et al. 2016;

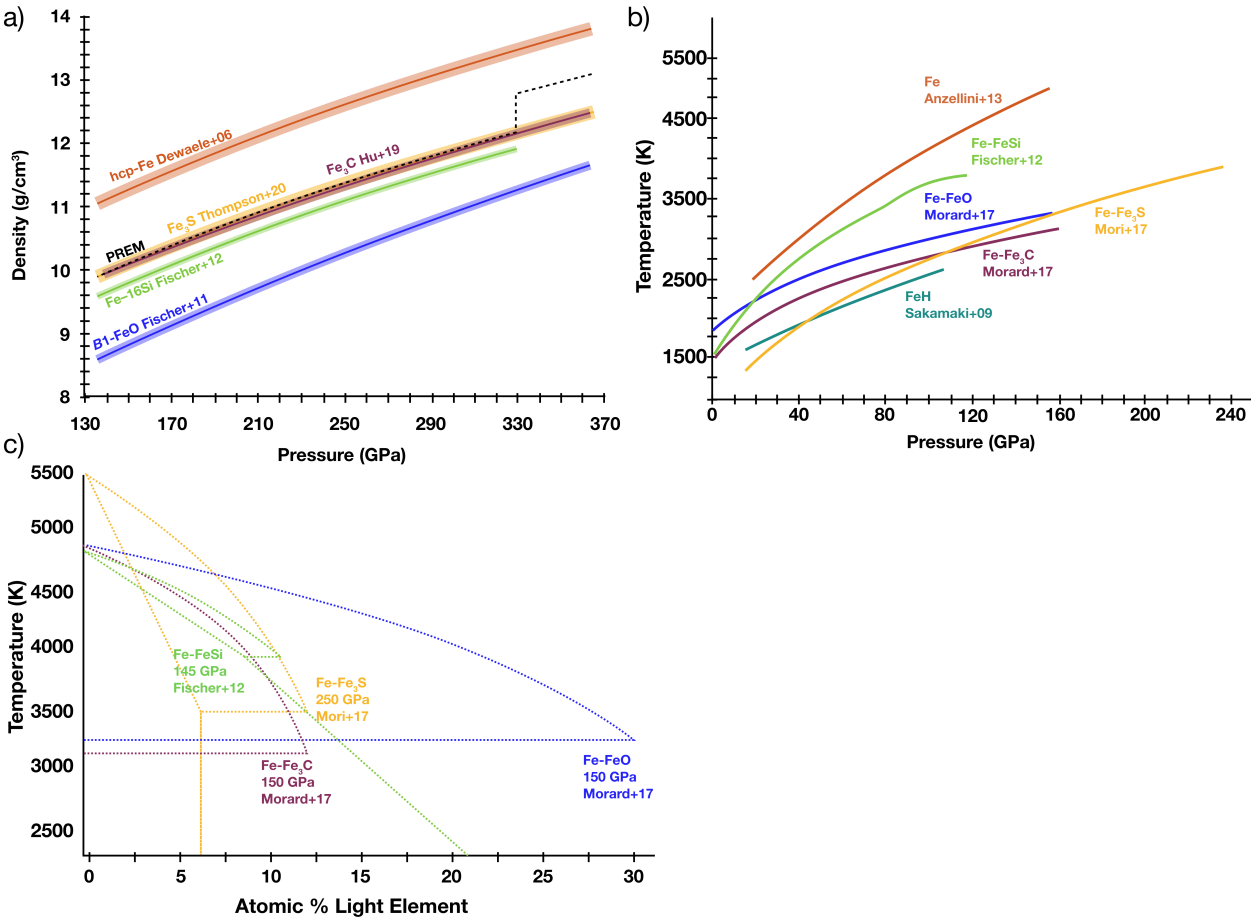

Figure 1.5. a) Iron alloy density profiles extrapolated to outer core conditions (Fischer et al. 2011; Fischer et al. 2012; Hu et al. 2019; Thompson et al. 2020), and compared with that of liquid iron (Dewaele et al. 2006) and the PREM model (Dziewonski and Anderson 1981). b) Iron alloy melting curves (Sakamaki et al. 2009; Fischer et al. 2012; Morard et al. 2017; Mori et al. 2017) with pressure compared with that of hcp-Fe (Anzellini et al. 2013). c) Fe-rich alloy binary eutectics and eutectic compositions in the 145 to 250 GPa pressure range (Fischer et al. 2012; Morard et al. 2017; Mori et al. 2017).

Thompson et al. 2020), and sulfur alone cannot match the density profile while crystallizing iron into the inner core. Equation of state studies of Fe_3C and Fe_7C_3 indicate that 5–7 wt% (20–26 at%) C is required to match the density of the outer core and ~3 wt% C (~12 at%) is required to match the density of the inner core (Litasov et al. 2013; Hu et al. 2019; Takahashi et al. 2019)

(Figure 1.5a). These outer core estimates are carbon rich of the Fe–Fe_3C eutectic at 150 GPa (Morard et al. 2017). Fe–Fe_3C eutectic compositions are trending towards more Fe-rich compositions with pressure (Morard et al. 2017), suggesting that an Fe+C core would crystallize carbide into the inner core. In the Fe-H system, equations of state of FeH_x demonstrate that 0.8–1.1 wt% H (31–38 atm%) is required to match the CMB density and 0.2–0.3 wt% (10–14 atm%) H is required to match the ICB density (Thompson et al. 2018), but the Fe–FeH_x eutectic has not been explored at core pressures and high temperatures.

Earth's core is a complex, natural system, and these Fe-alloy studies suggest that the core contains several light elements, with Si, O, S, C and H all contributing to some degree to the bulk core composition. While this work examines in detail the behavior of sulfur in Earth and planetary cores, the results contribute to our cumulative understanding of core chemistry and dynamics.

1.5. Core compositions of the terrestrial planets

Our knowledge of Earth's interior is far from complete, but better studied compared to that for our terrestrial neighbors. The model of Earth's interior that has been developed above can be combined and modified to match the limited constraints of the interior structures of Mercury, Venus and Mars. Geophysical measurements of the moments of inertia, geochemical analysis of meteorites and chemical measurements collected on NASA missions provide a basis for our understanding of the terrestrial planetary cores. While little remains known about Venus' interior, analysis of the Mercurian and Martian interiors support that sulfur is a major alloying component in their cores.

Mercury is the smallest terrestrial planet with a radius about one third that of the Earth (Figure 1.6). Interestingly, Mercury is also the densest terrestrial planet, with a Fe-rich core that accounts for nearly ¾ of the planet's radius (Anderson et al. 1987). Pressures range from 5.7 GPa at Mercury's CMB to 21 GPa at the ICB to 40 GPa at the center of the planet. The magnetic field and moment of inertia data collected by the MESSENGER mission supports the existence of a convecting liquid outer core decoupling the rotation of Mercury's core and mantle (Smith et al, 2012; Genova et al. 2019). Mercury's global magnetic field (Stevenson, 2003) combined with thermal evolution modeling based on analysis of crustal contraction on Mercury's surface is also consistent with Mercury having a liquid outer core that accounts for more than 50% of the core's radius (Hauck et al. 2004; Hauck et al. 2013). The elemental abundances collected via X-ray spectrometry measurements on Mercury's surface during the MESSENGER mission indicate that the surface contains at most 4 wt % Fe (Nittler et al. 2011). This suggests that Mercury formed in a highly reducing environment with very low FeO contents (less than half of that of Earth) (Burbine et al. 2002). Mercury's surface also contains high abundant Si and S compared to O (Nittler et al. 2011). A reducing accretion environment favors the incorporation of higher amounts of S and Si into the core (Malavergne et al. 2010), and Mercury's core is reported to potentially contain <1.5wt% S and ~14wt% Si (Namur et al. 2016; Tao and Fei 2021).

Mars is an embryo-sized terrestrial planet with a mass equal to about one tenth of Earth's mass and a core radius of about one half that of Earth (Figure 1.6). Martian core pressures range from ~20 GPa at the core-mantle boundary (CMB) to ~40 GPa at the planet's center and core-mantle boundary (CMB) temperatures have cooled from greater than 2650 K at 4.5 Ga to about

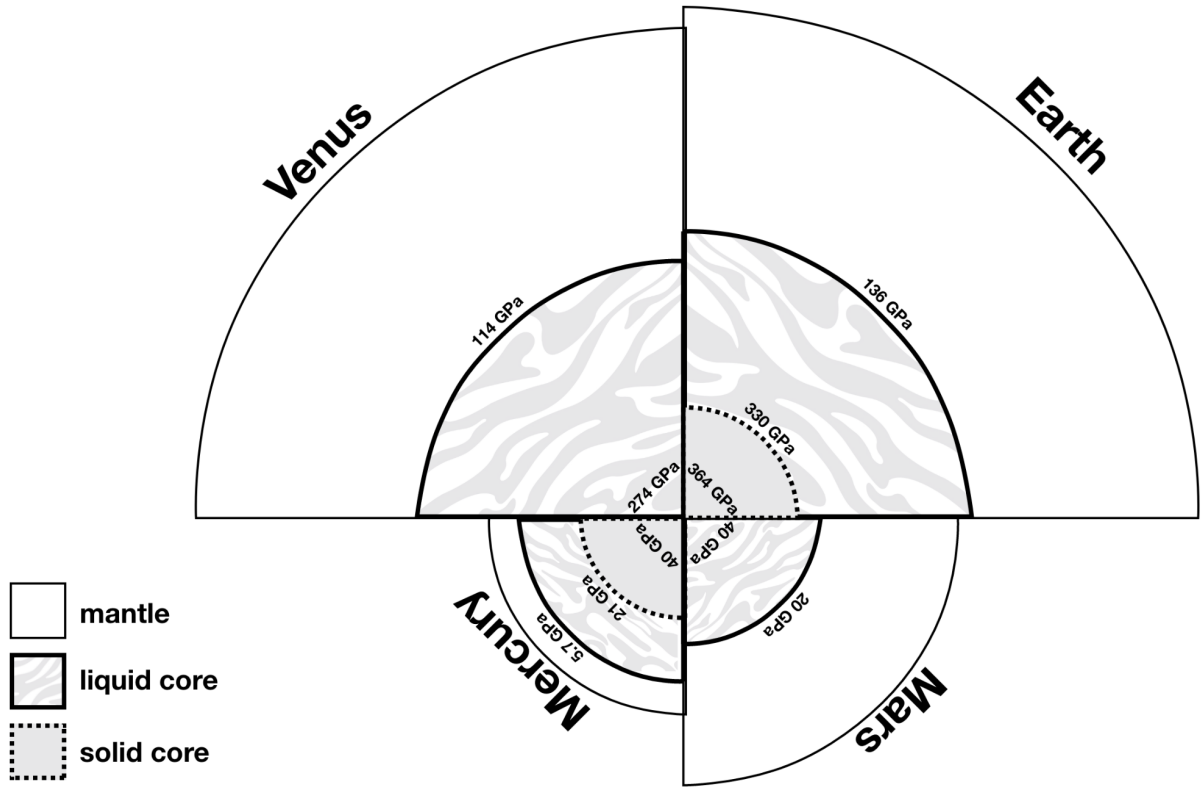

Figure 1.6. Schematic comparison of the interior structures of Earth, Venus, Mars and Mercury with core-mantle boundary, inner-core boundary, and central core pressures labeled. Visualization inspired by Nick Strobel's astronomy notes (astronomynotes.com).

2000 K at present (Fei et al. 1995) (Williams and Nimmo, 2004). Analysis of Shergotty-Nakhla-Chassigny (SNC) group meteorites thought to be rocks ejected from the surface Mars and analysis of samples collected in the Mars Exploration Rover Mission, indicate that Mars' mantle is enriched in FeO compared to Earth's and likely formed in more oxidizing conditions (Driebus and Wanke 1985; Taylor 2013). As a consequence, Mars has a small core that is likely S,O rich (Anderson 1972). Observations of early, short-lived magnetism on the Martian surface, suggest that Mars had an early, short-lived dynamo driven by the heat of core formation and not the ongoing crystallization of an inner core. The Martian core may therefore be fully molten at

present, supporting a S-rich core with liquidus temperatures lower than the current interior temperature of the Martian core (Williams and Nimmo 2004; Helffrich 2017). Comparisons of solar abundances and Fe-S melting studies at the *P-T* conditions of the Martian core, suggest up to 17 wt% S in the core (Helffrich 2017).

Less is known about Venus, but its similar size and location in the solar system to Earth indicates that Venus and Earth may have a similar core-mass fraction and core composition (Aitta 2012). Core mantle boundary pressures in Venus are 114 GPa and central core pressures are 274 GPa (Aitta 2012). Venus' core may still be fully molten, likely because of the lack of a magnetic field and heat release through plate tectonics (Nimmo et al. 2002), lending little constraint on how the core light element composition attributes to the core structure.

1.6. Iron-sulfide phase and melting relations and the need for crystallographic assessment

Geochemical and geophysical investigations of Earth and the terrestrial planets demonstrate that sulfur contributes significantly to the chemistry and formation of planetary cores (e.g., Scott and Wasson 1975; Seagle et al. 2006; Thompson et al. 2016; Thompson et al. 2020; Morard et al, 2008; Kruijer et al. 2014; Mori et al. 2017; Suer et al. 2017). While the previous sections have discussed the numerous investigations into the concentrations and melting and density behavior of iron sulfides in planetary bodies, the crystallography of iron sulfides at core-relevant *P-T-X* conditions is far less developed. Investigating iron sulfide mineralogy and coexisting phases at various pressure-temperature-composition conditions is a key factor in

evaluating core thermodynamics via the crystallization sequences occurring at the CMB and ICB. Structural phase transitions in Fe-sulfides also inform the density profiles and melting behaviors of relevant core alloys.

The lack of data on the crystallographic properties of Fe-sulfides, and iron alloys more generally, at extreme conditions, can now be addressed with the recent development of crystallographic techniques applied to high *P-T* samples (e.g., Lavina et al. 2011). Experimental investigations of iron-sulfide liquidus curves and eutectic compositions has been feasible via scanning electron microscopy on recovered high *P-T* samples for over ~30 years (e.g., Fei et al. 1997), and obtaining the volumes and bracketing the onset of melting of Fe-sulfides has been explored with *in-situ* synchrotron powder diffraction and laser heating techniques for a similar amount of time (e.g., Boehler et al. 1992). Single crystal diffraction is a mature technique, but applications of single crystal diffraction to determine the atomic arrangement of high *P-T* phases *in situ* has only been developed over the past decade (e.g., Lavina et al. 2011; Dera et al. 2013).

Applying single crystal diffraction methods to high *P-T* samples requires the synthesis of large grains at these conditions; and as the application of pressure and temperature rarely preserves or forms a single crystal, these developing methods must be capable of isolating a target grain from a multigrain synthesis. The techniques of single crystal X-ray diffraction on multigrain samples and the benefits of incorporating powder X-ray diffraction and chemical analysis techniques into these experiments are described in Chapter 2. Our current understanding of Fe-sulfide crystallography and Fe-FeS phase relations will be discussed here to provide a basis for which this thesis work will expand upon.

Fe-sulfides are known to adopt complex structures and exhibit intricate phase and melting relations (e.g., Evans 1970; Fei et al. 1995; Fei et al. 1997; Fei et al. 2000; Chen et al. 2008; Morard et al. 2008; Kamada et al. 2010; Ozawa et al. 2013; Mori et al. 2017; Tateno et al 2019). At ambient conditions, the stable Fe-rich sulfide is troilite (FeS), and it assumes a hexagonal structure (*P*-62*c*, *Z*=12) that is based on the common binary transition metal nickel-arsenide (*B*8) structure. The troilite unit cell can be viewed as a stacking of two offset NiAs-like cells along the *c* with minor shifts of Fe and S sites from their ideal positions (Evans 1970) (Figure 1.7a). With compression to 3.4 GPa, troilite transitions to the MnP-type structure (orthorhombic, *Pnma*, *Z*=4) (King and Prewitt 1982); a distortion of the NiAs structure. With further compression to 6.7 GPa, FeS transitions to a monoclinic structure (King and Prewitt 1982) and with heating at these pressures, FeS transitions to another NiAs superstructure which can be viewed as a doubling of the *B*8 structure along the *a* axis with alternating hexagonal layers of Fe and S (Fei et al. 1995). The phase relations in Fe-FeS form a simple binary in *X*-*T* space as shown at 10 GPa in Figure 1.8a (Fei et al. 1997; Chen et al. 2008) with a Fe-FeS eutectic of ~32 atm % S at ~1150 K . For further information on reading and interpreting phase diagrams, refer to Appendix 1.

The high *P*-*T* phase relations evolve from Fe+FeS to Fe+Fe_3S_2 upon pressurization to 14 GPa (Fei et al. 1995; 1997) (Figure 1.8b). The structure of Fe_3S_2 could not be determined on quench, indicating that it may break down into multiple sulfides (Fei et al. 1997). The eutectic composition in the Fe-FeS system at 14 GPa migrates towards more Fe-rich compositions (~27 atm% S) (Fei et al. 1997). Upon melting in Fe-S compositions with >27 atm% S, Fe melts to Fe_3S_2 plus liquid, and with increased heating, Fe_3S_2 + liquid melts to FeS + liquid (Figure 1.8b). This is called peritectic melting and it reveals a change in liquidus phase as the melt composition

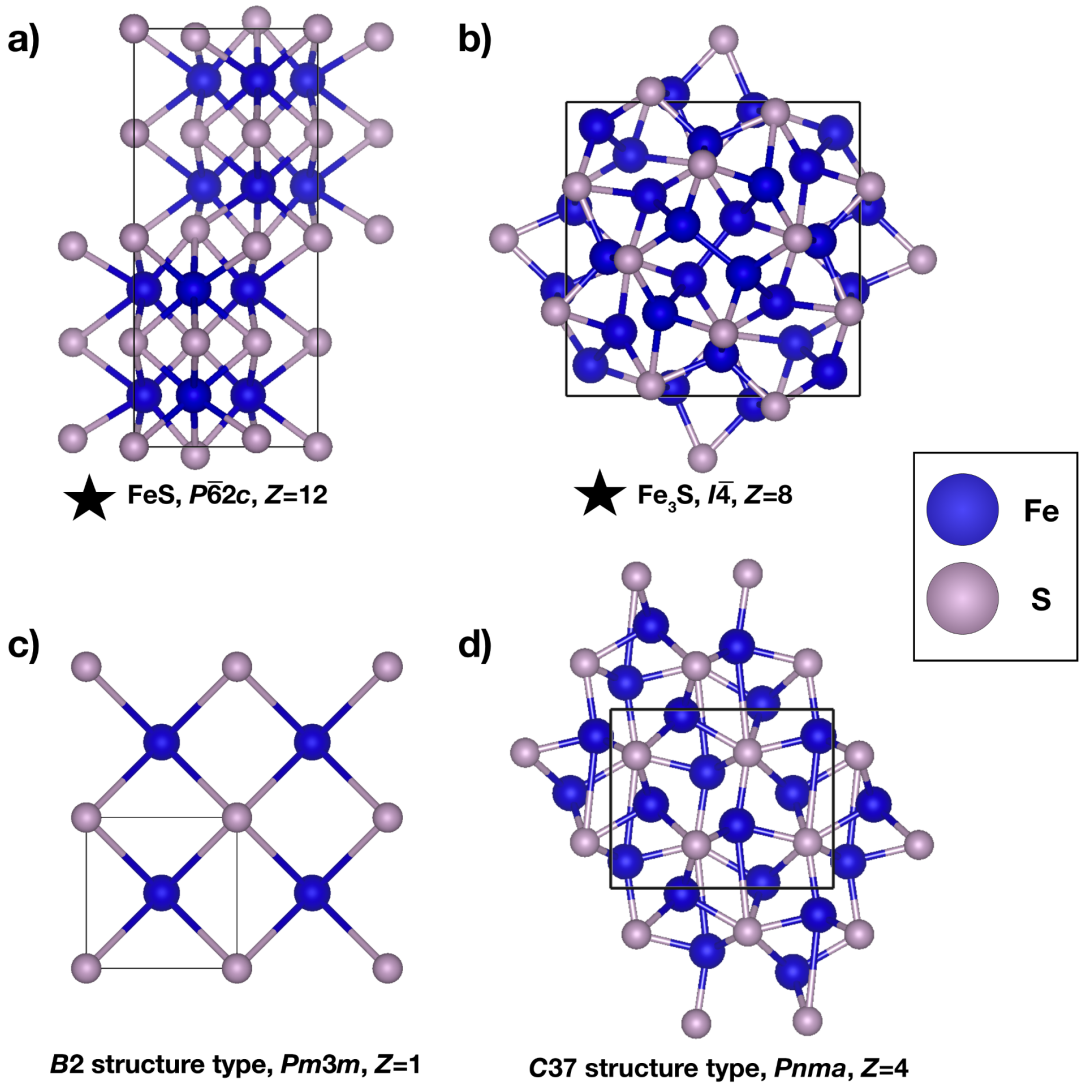

Figure 1.7. Crystal structure of a) Troilite (FeS) refined at ambient conditions (Evans 1970), b) Fe_3P-type Fe_3S synthesized at 21 GPa and high temperature and recovered to ambient conditions for structural solution and refinement (Fei et al. 2000). c) *B*2 structure reportedly compatible FeS above 250 GPa (Ozawa et al. 2013; Mori et al. 2017). d) *C*37 structure compatible with Fe_2S unit cell measured above 190 GPa (Tateno et al. 2019).

evolves upon cooling. A change in liquidus phase would relate to a change in crystallization sequence in an S-rich planetary core. On the Fe-rich side of the phase diagram, the liquidus curve

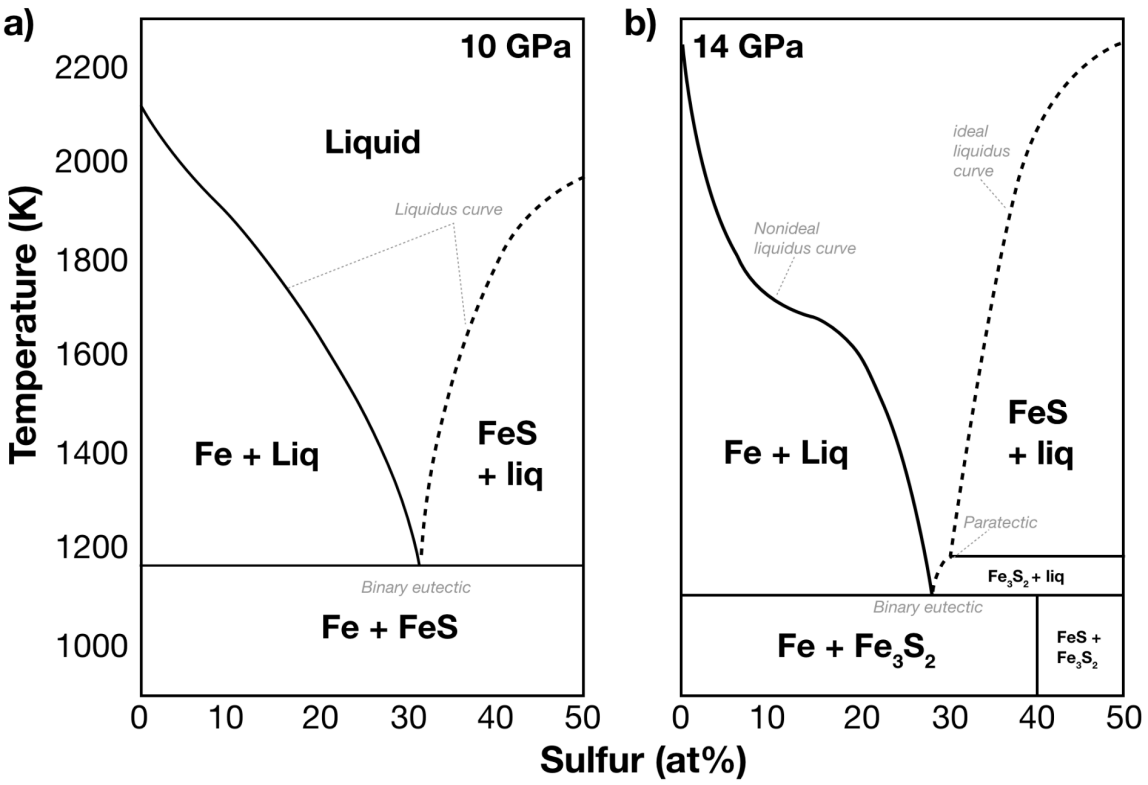

Figure 1.8. Fe-FeS phase diagram at a) 10 GPa and b) 14 GPa showing the evolution of a nonideal Fe-rich liquidus curve and the formation of the Fe_3S_2 intermediate phase (Fei et al. 1995; Fei et al. 1997; Chen et al. 2008).

evolves from nearly ideal at 10 GPa to strongly nonideal at 14 GPa (Chen et al. 2008) (Figure 1.8b). This could result in a compositional gradient in an outer core liquid and a low liquidus temperature for Fe-rich melts at these pressures. Chen et al. 2008 suggests that precipitation of Fe at varying depths in the Mercurian core may occur due to this melting behavior.

At 21 GPa, Fe_3S becomes stable coexisting with iron, and single crystal analyses conducted on Fe_3S grains recovered to ambient conditions establish that it was synthesized in a tetragonal structure (Fe_3P-type, *I*-4, *Z*=8) at 21 GPa and high temperatures (Fei et al. 2000) (Figure 1.7b, 1.9). The Fe_3P structure type is close-packed with significant Fe-Fe bonding (Rundqvist and Jellinek, 1979). Sulfur occupies sites in 9-fold coordination while Fe occupies

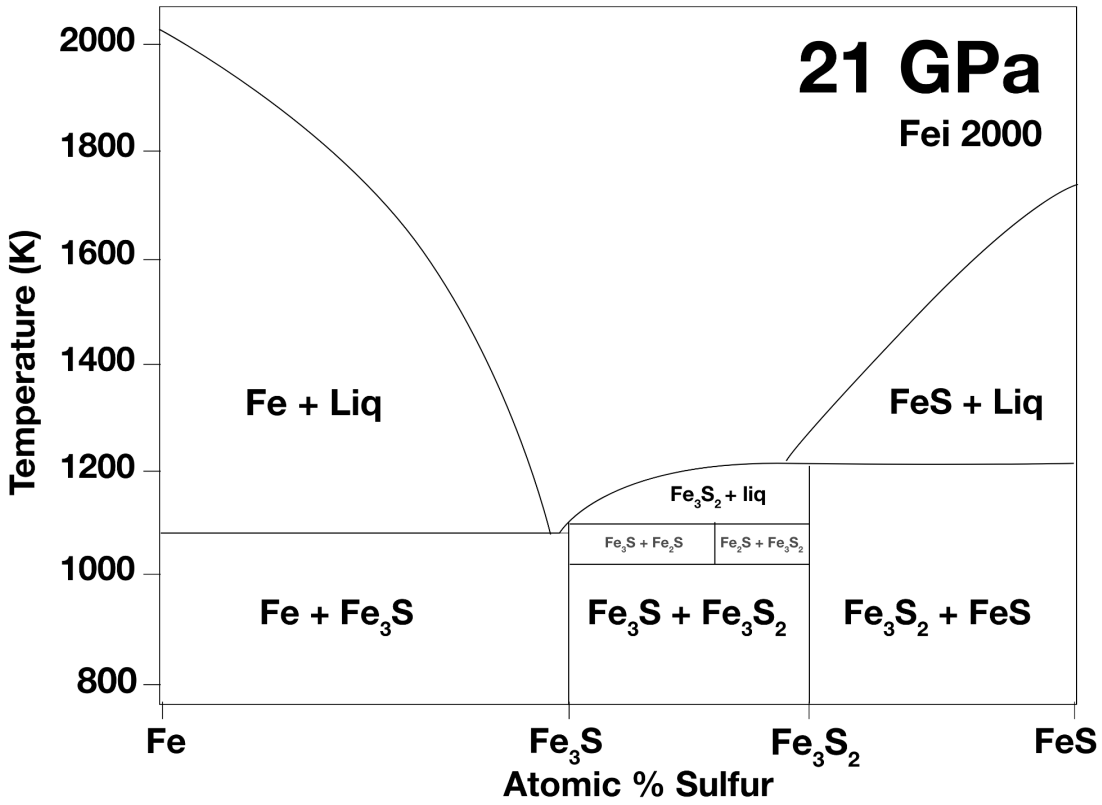

Figure 1.9. Fe-Fe-S phase diagrams at 21 GPa (Fei et al. 2000).

3 differing tetrahedrally coordinated sites: one in coordination with 4 S, one in coordination with 3 S and 1 Fe, and one in coordination with 2 S and 2 Fe (Rundqvist and Jellinek, 1979). In more sulfur-rich compositions at 21 GPa, Fe_2S, Fe_3S_2 and FeS are also reported (Fei et al. 2000) (Figure 1.9). Fe_3S melts over a limited temperature range before melting peritectically to Fe_3S_2+Fe at these pressures (Fei et al. 2000) (Figure 1.9). Transmission electron microscopy (TEM) analyses of Fe_3S_2 and Fe_2S recovered from 21 GPa and 1900 K indicate that these phases form in hexagonal unit cells, but their structures were not resolved further (Koch-Müller et al. 2002).

Figure 1.10 displays the current reported stable sulfide coexisting with iron extending to pressures related to Earth's core. Iron rich Fe-sulfide phase and eutectic melting boundaries are plotted with black dashed lines based on work reported by Fei et al. 2000; Seagle et al. 2006; Morard et al. 2008; Kamada et al. 2010; Kamada et al. 2012; Ozawa et al. 2013; Mori et al. 2017; Yokoo et al. 2019; Tateno et al. 2019; and Thompson et al. 2020. The iron phase and melting boundaries are plotted with gray dotted lines based on Anzellini et al. 2013. *I*-4 Fe_3S dominate this Fe-rich phase diagram and is reportedly stable between 21 and 250 GPa and to melting temperatures; however, single crystal analyses of Fe_3S has only been conducted at ambient conditions (Fei et al. 2000) and lattice parameters of Fe_3S have only been reported to 120 GPa (Seagle et al. 2006; Morard et al. 2008; Kamada et al. 2014; Thompson et al. 2020). Sample recovery work from >200 GPa at high temperatures shows Fe_3S-like compositions synthesized at these conditions (Ozawa et al. 2013; Mori et al. 2017; Yokoo et al. 2019), but structural information on Fe_3S is lacking in the 120–250 GPa pressure range overlapping with Earth's outer core conditions. Otherwise, the stability of iron-rich sulfides has been reported on the basis of qualitative observation in X-ray diffraction patterns.

Above 250 GPa, Fe_3S is reported to break down into a cubic, *B*2 FeS phase plus hcp-Fe at moderate temperature (Figure 1.7c, 1.9). Sample recovery from 271 GPa and 2530 K supports synthesis of an FeS stoichiometry (Ozawa et al. 2013; Tateno et al. 2019), but structural verification of this sulfide has not been conducted after high *P*-*T* synthesis. At high temperatures above ~250 GPa, FeS + Fe react at high temperatures to form an orthorhombic Fe_2S phase (Tateno et al. 2019). The diffraction angles observed for the orthorhombic Fe_2S suggest a *Pnma* space group and the unit cell measurements for Fe_2S are compatible with the Co_2Si-type

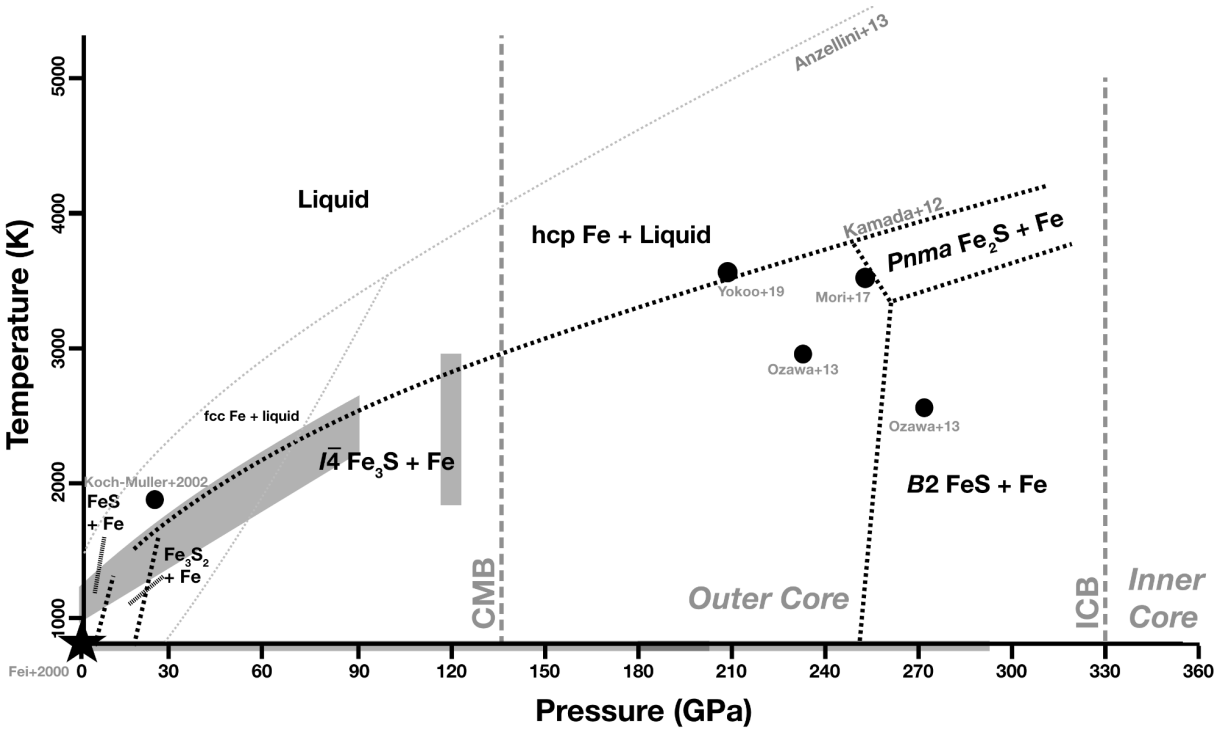

Figure 1.10. Fe-rich sulfide phase relations to Earth's inner core boundary conditions. Fe-sulfide phase boundaries are marked with black dashed lines (Fei et al. 2000; Seagle et al. 2006; Morard et al. 2008; Kamada et al. 2010; Kamada et al. 2012; Ozawa et al. 2013; Mori et al. 2017; Tateno et al. 2019; Thompson et al. 2020) and the iron phase diagram is plotted in light grey (Anzellini et al. 2013). The black circles indicate *P-T* synthesis conditions from which samples were recovered and analyzed (Koch-Müller et al. 2002; Ozawa et al. 2013; Mori et al. 2017; Yokoo et a. 2019). Black stars represent conditions where Fe-rich sulfides were crystallographically solved and refined (Evans 1970; Fei et al. 1997). Grey shaded regions show *P-T* conditions where Fe-rich sulfide lattice parameters were fit and reported. (Fei et al. 1995; Fei et al. 1997; Seagle et al. 2006; Morard et al. 2008).

structure type (*C*37, *Pnma, Z*=4) (Figure 1.7d, 1.9) (Tateno et al. 2019; Geller and Wolontis 1955). *C*37 Fe_2S is further observed on the liquidus to 306 GPa, making it an important phase to consider at Earth's inner core boundary conditions (Tateno et al. 2019). Based on these powder diffraction and chemical analyses observations (Ozawa et al. 2013; Mori et al. 2017; Tateno et al.

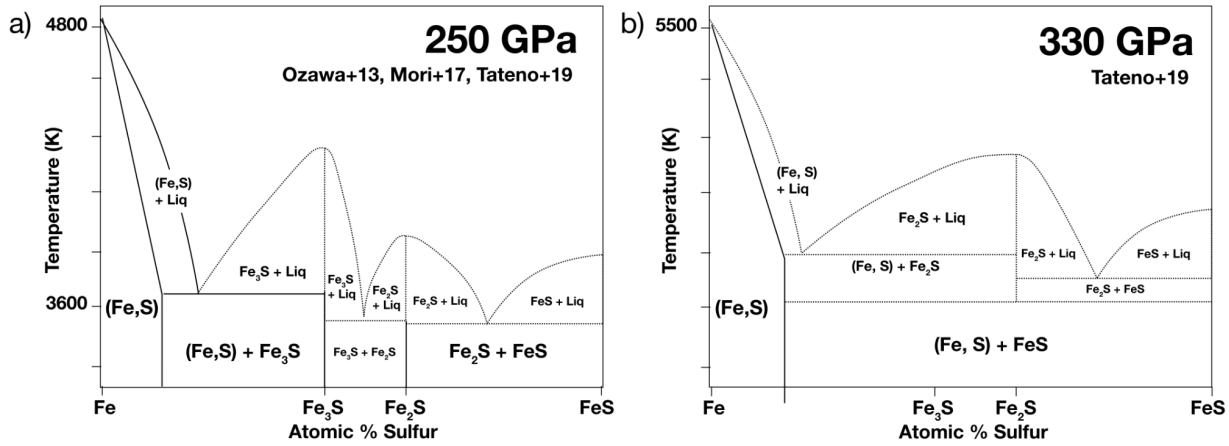

Figure 1.11. Fe-Fe-S phase diagrams at 21 GPa, 250 GPa and 330 GPa (Fei et al. 2000; Ozawa et al. 2013; Morie et al. 2017; Tateno et al. 2019).

2019), Tateno et al. 2019 approximated Fe–FeS *T-X* diagrams at 250 GPa and 330 GPa (Figure 1.11), and the change in phase relations from Fe+Fe_3S to Fe+Fe_2S is illustrated (Figure 1.11).

It is clear in Figure 1.10 that above ambient conditions, the structural details of the stable Fe-rich sulfides become limited to unit-cell parameter fittings (<120 GPa) and qualitative observations reported in X-ray diffraction patterns. The Fe-FeS *P-T-X* phase relations are rich in complexity to inner core boundary conditions, and investigations into the crystallography of Fe-rich sulfides is necessary to better characterize core crystallization sequences and dynamics. In this thesis work, I have combined powder and single crystal X-ray diffraction techniques on multigrain samples up to 200 GPa and 3500 K to examine the role of sulfur in core relevant phase relations. This work has revealed new complexities in the Fe-S system under extreme conditions and the stability of several iron sulfide phases (* indicates not previously known before this work): *C*23 Fe_2S*, *C*37 Fe_2S, Cr_2P-type Fe_2S*, *C*22 Fe_2S, $Co_{12}P_7$-type $Fe_{12}S_7$*, *I*-4 Fe_3S, and Fe_8S_3.* As tetragonal Fe_3S has been reported as the stable Fe-rich compound across the *P-T* range of our studies, our novel results highlight the importance of combining

crystallographic techniques with chemical analysis to resolve chemical and structural details of the Fe-S system at Earth and planetary core pressures.

1.7. Scope of Thesis

1.7.1. The crystal structure of Fe_2S at 90 GPa based on single-crystal X-ray diffraction techniques

To further investigate the structural properties of Fe_2S, the recently reported Fe-rich sulfide potentially stable at Earth's inner core boundary conditions, we synthesized Fe_2S and assessed its crystal chemistry in a laser-heated diamond-anvil cell at 89(2) GPa and 2380(120) K. Upon temperature quenching, crystallites of Fe_2S were identified and their structure was investigated using single-crystal X-ray diffraction techniques. Under these conditions, Fe_2S adopts the *C*23 structure (anti-$PbCl_2$, Co_2P) with space group *Pnma* (*Z*=4). This structure consists of columns of corner-sharing, FeS_4 tetrahedra and columns of edge-sharing FeS_5 square pyramids linked along edges in the *b* direction. Sulfur is in 9-fold coordination with Fe. This study marks the first high-pressure structural solution and refinement of Fe_2S synthesized in a multigrain Fe + FeS sample at 90 GPa and 2400 K and establishes the stability of *C*23 Fe_2S at these conditions. A previous powder diffraction study reports an orthorhombic Fe_2S phase with a *C*37, Co2Si-like unit cell above 190 GPa. A *C*23–*C*37 structural transition is inferred to explain the previously observed unit-cell parameters at higher pressures and temperatures.

1.7.2. Pressure-induced C23–C37 transition and compression behavior of orthorhombic Fe_2S to Earth's core pressures and high temperatures

The phase stability of orthorhombic Fe_2S was then explored to 194 GPa and 2500 K using powder and multigrain synchrotron X-ray diffraction techniques to confirm and examine the *C*23–*C*37 Fe_2S. Between 30 and 120 GPa, a *C*23-like (Co_2P, *Pnma*, *Z*=4) Fe_2S unit cell is observed and it exhibits a highly compressible *a* axis. A softening of the *a* axis occurs between 120 and 150 GPa and a relative stiffening of the *b* and *c* axes accompanies this compressibility change. Above 150 GPa, the *a* axis stiffens as the *b* and *c* axes soften and a *C*37-like (Co_2Si, *Pnma*, *Z*=4) Fe_2S unit cell is measured. On the basis of these changes in unit-cell geometry, a pressure-induced *C*23–*C*37 Fe_2S phase transition is inferred between 120–150 GPa. The *C*23 and *C*37 (*Pnma, Z*=4) structures are closely related and share the same site symmetries. Forming the *C*37 structure from the *C*23 structure requires a shortening of the *a* axis and lengthening of the *b* and *c* axes accompanied by a 4- to 5-fold coordination change. The softening of the *a* axis above 120 GPa may therefore indicate the onset of a coordination change, and the final compressibility change above 150 GPa may mark the completion of this phase transition. The presented *P*-*T* stabilities of *C*23 and *C*37 structures of Fe_2S are in agreement with and resolve the differing observations of two previous studies (Tateno et al. 2019; Zurkowski et al. in press). As *C*37 Fe_2S is observed to core-mantle boundary pressures and high temperatures, the *C*37 Fe_2S density profile through Earth's outer core was determined by fitting the *C*23 Fe_2S equation of state (<120 GPa) and applying a 1.6 % volume reduction based on the *C*37 Fe_2S volume residuals to this fit. Comparing the density of liquid *C*37 Fe_2S with that of liquid hcp-Fe (Dewaele et al. 2006) and the seismologically determined density deficit of Earth's core (Irving et al. 2018), 13.9±1.5 wt%

and 8.6±0.8 wt% sulfur would be required to match the density at the CMB and ICB respectively for a purely Fe-S core. Comparisons to eutectic melting studies indicate that sulfur is likely not the sole light alloying element in Earth's core.

1.7.3. Single-crystal synchrotron X-ray diffraction studies of cobalt phosphides as low-pressure analogs of iron sulfides: determination of the novel $Co_{12}P_7$ compound, compression of Co_2P, $Co_{12}P_7$, and CoP to 48 GPa and high temperatures, and a mechanisms for the pressure-induced C23–C37 transition in M_2X transition metal binary compounds

Between 25 and 120 GPa, Fe_2S adopts the structure that Co_2P assumes at ambient conditions. The structural properties of the Co-P system were therefore investigated to 48 GPa and high temperatures using single crystal X-ray diffraction techniques to better understand the behavior of metal-rich sulfides in Earth and planetary interiors. Co_2P is stable at moderate temperatures to 48 GPa in the *C*23 (anti-$PbCl_2$ type, αCo_2P, *Pnma, Z*=4) structure. Upon heating at 30 GPa to 1880 K, αCo_2P transitions to the *C*22 structure (Fe_2P type, βCo_2P, *P*-62*m*, *Z*=3). The α–β Co_2P phase transition has been reported previously between 1440 and 1660 K at ambient pressures, indicating a positive α–β pressure-temperature phase boundary for Co_2P to at least 30 GPa. αCo_2P compresses anisotropically with a significantly more compressible *a* axis compared to the *b* and *c* axes. Structure solution and refinement of αCo_2P show that this compression behavior is mostly driven by bond angle distortion. A discontinuity in axial compression is observed above 35 GPa where the *a* axis becomes more compressible and the *b* and *c* axes stiffen

and the Co1-tetrahedral site is observed to compress faster towards the next nearest P site. This compression behavior shapes the αCo_2P structure towards a *C*37, Co_2Si-type structure. The Co-phosphides show analogous phase stability and compressional behavior to higher pressure Fe-phosphides and sulfides relevant to Earth and planetary cores and the structural information discussed in this work may be key in building a system for comparison between these structures relevant to core crystallization.

In these experiments, two other cobalt phosphides were observed: CoP and the novel $Co_{12}P_7$. $Co_{12}P_7$ was synthesized at 27 GPa and 1740 K, and at 48 GPa and 1790 K, and decomposes to Co_2P + CoP below 18 GPa. $Co_{12}P_7$ adopts a structure initially proposed for $Cr_{12}P_7$ (space-group type $P\bar{6}$, Z =1), consisting of chains of edge-sharing CoP5 square pyramids and chains of corner-sharing CoP4 tetrahedra. This arrangement leaves space for trigonal–prismatic channels running parallel to the *c* axis. Coupled disordering of metal and phosphorus atoms has been observed in this structure for related $M_{12}P_7$ (*M* = Cr, V) compounds, but all Co and P sites are ordered in $Co_{12}P_7$. All atomic sites in this crystal structure are situated on special positions. CoP was synthesized in the *B*31 structure (MnP-type structure, *Pnma, Z*=4) to 18 GPa and 1740 K upon compression to 27 GPa and heating to 1750 K.

1.7.4. Phase stability of Fe_3S, Fe_2S and the novel $Fe_{12}S_7$ to 125 GPa based on single-crystal X-ray diffraction techniques: implications for terrestrial planetary core crystallization

The structural stability of Fe_3S, Fe_2S and $Fe_{12}S_7$ was explored using single-crystal X-ray diffraction techniques in a laser heated diamond anvil cell between 100 and 125 GPa and

quenched from high temperatures. For an $Fe_{80}S_{20}$ composition, in agreement with previous studies, Fe_3S is observed to crystallize in the tetragonal Fe_3P-type structure with recrystallized hcp-Fe. In a $Fe_{66}S_{34}$ starting composition, Fe_2S and $Fe_{12}S_7$ co-crystallize. The novel $Fe_{12}S_7$ is observed in the $Co_{12}P_7$ structure and was synthesized across the pressure and temperature range probed in this study. Fe_2S was determined at high temperatures to adopt the Fe_2P-type, *C*22 structure. Grains of orthorhombic *C*23 Fe_2S were also observed when quenching from more moderate temperatures. Previous studies support that the *C*23 Fe_2S structure is likely the lower temperature polymorph of the *C*22 Fe_2S phase. At 125 GPa, in the expected *C*23–*C*22 transitional temperature range, Fe_2S was quenched in a body-centered, Cr_2P-type structure. This structure has only been observed in the Cr and (Cr, Mn) systems and is reportedly a low temperature distortion of the *C*22 structure. The formation of the Cr_2P-type Fe_2S structure may be a metastable phase assumed during the shifting of sulfur sites between the *C*23 and *C*22 structures. These results warrant further *in-situ* investigation into the equilibrium phase transitions in Fe_2S with temperature at high pressures. The Fe-S phases discussed provide thermodynamic and structural insight into the crystallization sequences potentially occurring in rocky planetary cores, including Venus and light element rich exoplanets. Recent reports that solid solution of Si into Fe-S phases may extend the stability field of Fe_2S in Fe-rich systems, may also indicate that these findings are applicable to Mercurian core crystallization sequences.

1.7.5. Experimental evidence of a disordered trigonal iron-rich sulfide at Earth's outer core conditions and analogous observations in the Fe-P system

The phase stability of Fe_3S was then investigated with powder and single crystal methods in the 145-200 GPa pressure range after high temperature synthesis, to structurally characterize the Fe-rich Fe-S system in Earth's outer core. As the lower pressure properties of the Co-P system provided key insight into the high *P-T* Fe-S system, the Fe-P system was also examined to 70 GPa in this study, as a low-pressure analog for characterizing Fe-S structural properties. In the pressure range of 145–195 GPa hcp-Fe is observed to recrystallize at high temperatures with a set of reflections that cannot be described by tetragonal Fe_3S (*I*-4). Indexing of the reflections in the reciprocal space establishes that the high temperature phase adopts a trigonal unit cell marked by an elongated *c* axis ($c/a \sim 4.4$). A trigonal phase with analogous unit cell parameters was indexed after compression and heating of Fe-P samples between 36 and 67 GPa. The trigonal Fe-P phase becomes unstable on decompression below 16 GPa at room temperature in agreement with previous observations. Diffraction from the Fe-S and Fe-P trigonal isomorphs exhibit diffuse scattering, likely related to positional disorder and suggestive of a complex atomic arrangement. Refinements of the powder diffraction patterns reveal that the average structure of these disordered phases can be described by the related trigonal Ni_8P_3 (*R*3*c*) or $Fe_{12}As_5$ (*R*32) structures. Attempts to solve the disordered Fe-P and Fe-S structures using single crystal techniques support that the average structure is in agreement with these analogs and the stoichiometry is approximately $Fe_{11}X_4$. Transition-metal binary compounds with 71–73% metal content generally adopt these complex hexagonal or trigonal structures as a result of atomic clustering from increased metal-metal interactions. The stability of the Fe-P trigonal phase above

16 GPa should be considered in the analysis of meteorite thermodynamic histories as well as the dynamics of the Mercurian and Martian cores, and the coexistence of the Fe-S trigonal phase with iron to 200 GPa and high temperatures may directly influence the electronic and thermodynamic properties of Earth's complex core.

1.7.6 Observations of a hexagonal $Fe_X(S, O)$ phase at Earth's outer core pressures and high temperatures.

In this ongoing project, we expanded the chemical complexity of our experiments from the binary Fe-S system to the ternary Fe-S-O system to begin comparing the structural properties and phase relations of the ternary system to the respective Fe-S and Fe-O binary studies. We explored the Fe-S-O phase relations to 180 GPa and 3700 K, using a combination of *in-situ* X-ray diffraction techniques and chemical analysis of recovered samples, and the next steps of this project include conducting multigrain diffraction experiments at these conditions. From our powder diffraction results, we observe, we observe *C*37 Fe_2S coexisting with *B*1 FeO and hcp-Fe at moderate temperatures in the 150–180 GPa pressure range, and with increasing temperature, *C*37 Fe_2S + hcp Fe react to form the trigonal phase, in agreement with the results from Chapter 7. At the highest temperatures in these Fe-S-O experiments, an additional set of peaks is observed to grow into the pattern as peaks associated with the trigonal phase and Fe decrease in intensity. The phase was indexed to a hexagonal structure related to the *B*8 (NiAs type) structure. Iron likely occupies the hexagonal closed packed lattice and Fe + (O, S) likely occupies the primitive hexagonal sublattice. An experiment recovered from 172 GPa and 3300 K suggests that the *B*8-like phase is Fe-rich with contributions from both oxygen and sulfur. As this phase has not been

observed in the Fe-FeO or Fe-FeS system alone, these results suggest the importance of S + O in stabilizing this phase and have important implications for the chemistry of multicomponent planetary cores such as that of Earth's. Further experiments aiming to constrain the S, O content using multigrain techniques and further chemical analysis is needed to expand on these implications.

2. Experimental techniques for investigating iron-sulfide mineralogy at high *P-T*

2.1. X-ray diffraction from a crystal

This section provides background on the theory of X-ray diffraction as it applies to the techniques used in this work. Additional information on these topics may be found in comprehensive texts such as Ladd and Palmer 2003, Giacovazzo 2011, Girolami 2015, Stout and Jenson 1989; and succinct guides for geoscience applications including Lavina et al. 2014 and Bykova, 2015.

The monochromatic X-ray diffraction techniques used in this work are built on the interactions of X-rays with the electrons that make up the crystal lattice. When an X-ray intersects an electron, the charged electron will oscillate along with the electric field component of the X-ray path. The electron, accelerated by the electric field, spherically emits X-rays of a frequency and wavelength characteristic of the transfer of energy from the incident beam. As atoms contain electron clouds, the scattering power, or *atomic form factor,* for an atom within a crystal structure will depend on its electron density and the scattering angle. Scattered X-rays from each electron will remain fully in phase only along the forward direction of the X-ray beam and will become increasingly out of phase at high scattering angles.

For the next-simplest case of two adjacent atoms in the path of an X-ray beam, a diffraction signal is obtained if the scattered X-rays from each atom arrive at a detector in phase. It follows that the path length difference for the incident and scattered X-rays from each atom

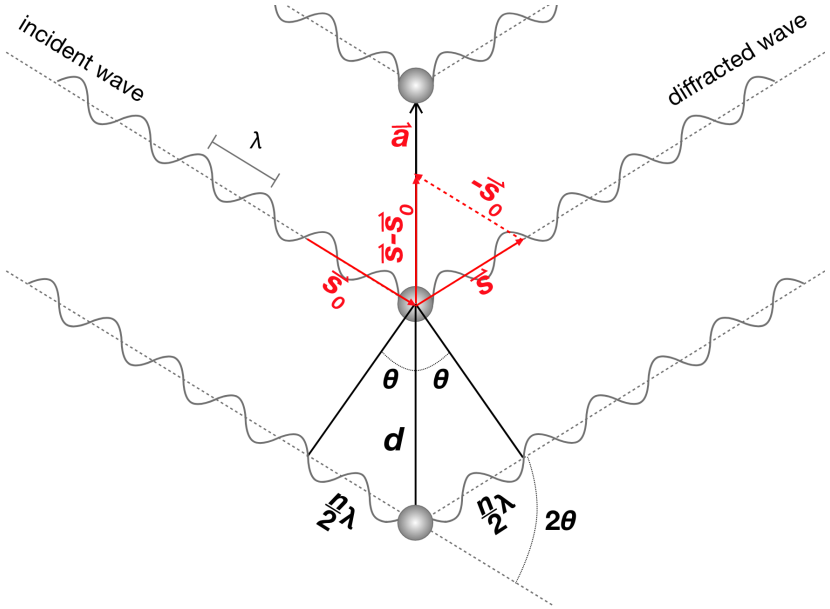

Figure 2.1. Schematic diagram of Bragg's Law showing the geometrical relationship between the angle of coherent scattering of X-rays of wavelength, λ, with integer pathlength difference, *n*, from two atomic sites separated by distance, *d*. The equivalent Laue relationship is also shown relating the difference in direction of the incident and diffracted X-ray beam to the interatomic spacing vector, $\overline{a}$, by an integer number of wavelengths.

must be an integer number of wavelengths, and this principle can be geometrically represented by Bragg's Law (Figure 2.1),

$$n\lambda = 2d\sin\theta$$

The angles of diffraction can be calculated for two scatterers (Figure 2.1) given the wavelength of the X-ray beam and the distance between the sites (*d*). The value *n* denotes the integer number of wavelengths that an X-ray must travel to remain in phase with the ray scattered from the adjacent site.

This relationship can also be conceptualized in vector form using the Laue equation:

$$\overline{a}\bullet(\overline{s}-\overline{s}_0) = h\lambda,$$

where the projection of the interatomic-distance vector $\overline{a}$ onto the vector representing the change in direction of the incoming and outgoing X-rays (described by incoming unit vector $\overline{s}_0$ and

outgoing unit vector $\bar{s}$), must equal an integer number, h, of wavelengths (Figure 2.1). These diffraction conditions may also be satisfied for a row of any number of scatterers if they are all separated by the same interatomic distance ($|a|$ or d in Figure 2.1). Diffraction from a row of equally spaced atomic sites forms a series of concentric diffraction cones with angles that satisfy the diffraction conditions.

Building up to a 2-D plane of atoms extending in directions denoted a and b, the same principles apply for each row of atoms in the a and b directions; however, constructive interference will only be detected at the angles where the cones of diffraction from each row intersect. Similarly, with a 3-D lattice, whose axes are described by the directions $\bar{a}$, $\bar{b}$, and $\bar{c}$, constructive interference will only be detected where the sets of diffraction cones along each direction intersect and all three Laue equations are satisfied:

$$\bar{a}\bullet(\bar{s}-\bar{s}_0) = h\lambda$$
$$\bar{b}\bullet(\bar{s}-\bar{s}_0) = k\lambda$$
$$\bar{c}\bullet(\bar{s}-\bar{s}_0) = l\lambda$$

All diffracted rays from a crystal may be assigned an integer set of indices h, k, l (called *Miller indices*) associated with the pathlength difference for the scattered rays. Combining the Laue equations above:

$$\bar{s}-\bar{s}_0 = (h\bar{a}^{-1} + k\bar{b}^{-1} + l\bar{c}^{-1})\lambda,$$

all diffraction angles for a crystal can be described by a linear combination of the Miller indices and the reciprocal unit cell vectors, also denoted ($\bar{a}^*, \bar{b}^*, \bar{c}^*$). If the unit vectors $\bar{s}$ and $\bar{s}_0$ are normalized to the wavelength:

$$(\bar{s}-\bar{s}_0)/\lambda = (h\bar{a}^* + k\bar{b}^* + l\bar{c}^*),$$

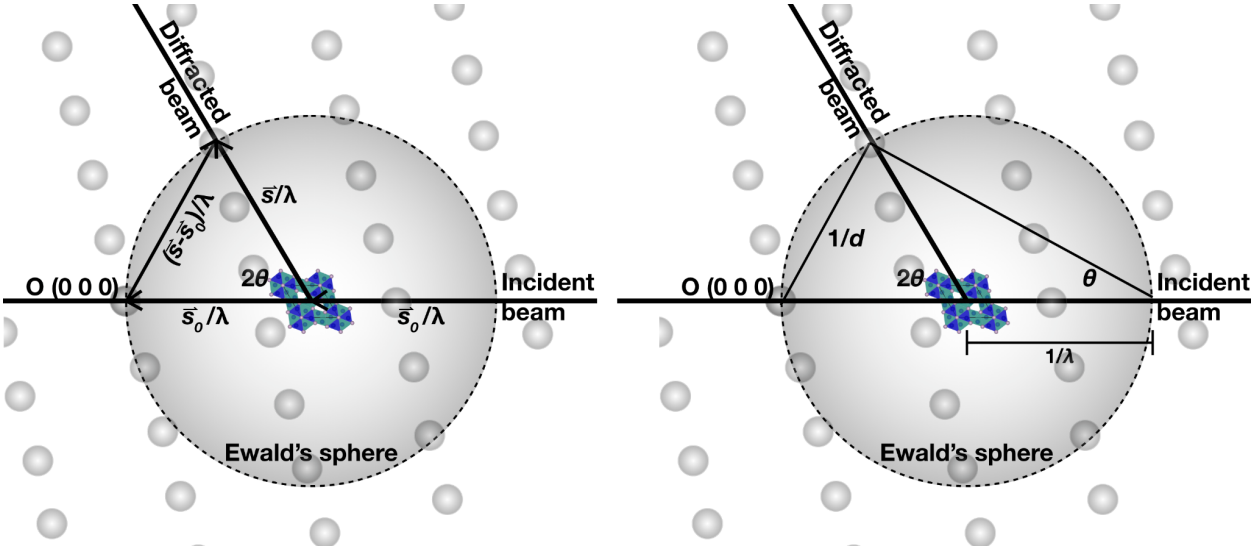

Figure 2.2. The Ewald sphere construction describes all points that satisfy the condition for diffraction described by the Laue equations (left) as well as Bragg's Law (right).

a spherical surface construction can be drawn, called the Ewald Sphere, which describes all points that satisfy this condition for diffraction (Figure 2.2). As these diffraction conditions are met at specific orientations of the crystal, rotating the crystal in the path of the X-ray beam will bring more orientations of the lattice into the condition for diffraction defined by the surface of the Ewald's sphere construction.

The Ewald's sphere can be related to Bragg's Law as the angle between $\overline{s}/\lambda$ and $\overline{s}_0/\lambda$ is equal to 2θ, and $(\overline{s}-\overline{s}_0)/\lambda$ is equal to $2\sin\theta/\lambda$ or d_{hkl}^{-1} (Figure 2.2). With a given collection of diffraction angles, the *d* spacings can be calculated and input into the equation above to determine the reciprocal lattice dimensions ($\overline{a}^*$, $\overline{b}^*$, $\overline{c}^*$) and crystal system (see Appendix 2), and to assign a set of *hkl* for each reciprocal lattice vector. This procedure is called *lattice indexing,* as the diffraction angles observed in an experiment define the cell geometry.

Each reciprocal lattice reflection detected during an experiment will have an intensity characteristic of the types of atoms contributing to the scattering. As mentioned previously, each atom within a lattice has an atomic form factor, f, that is dependent on its electron density and scattering angle; however, scattered waves from atomic sites with differing electron densities will have amplitudes and phases that will interfere at least partially deconstructively when combined. The *structure factor*, F_{hkl}, is used to represent the combined scattered wave from all atoms contributing to a diffraction reflection:

$$F_{\mathrm{hkl}} = \sum_{\mathrm{j}} f_j \exp[2\pi i \, (hx_j + ky_j + lz_j)]$$

A wave scattered from atom j with atomic form factor, f_{j} can be described with a phase, ϕ_{j} equal to $2\pi(hx_j + ky_j + lz_j)$, where (x_j, y_j, z_j) are the atomic coordinates of atom j. The intensity of the wave described by a structure factor is equal to the square of its amplitude:

$$I_{tot} = F^{2}_{\mathrm{hk}} = (\sum_{\mathrm{j}} f_j \cos\phi_{\mathrm{j}})^2 + (\sum_{\mathrm{j}} f_j \sin\phi_{\mathrm{j}})^2$$

Structure factors and intensities can be calculated for any given lattice vector if the atom types and positions are known; however, the phases of reflections cannot be determined from a given reflection intensity due to the complex nature of the structure factor. This is called the *phase problem.* Inherent to characterizing crystal structures is therefore the determination and refinement of a structure model that best matches the measured reciprocal lattice vectors and their intensities.

The first step in finding a structure model for a given set of structure factors is assessing the symmetry of the reciprocal lattice, called the *Laue class.* Reflections detected from a set of integers *hkl* and *-h-k-l* have structure factors that are complex conjugates, such that their measured intensities will be the same amplitude and opposite phases. These reflections are called

Friedel pairs. Because Friedel pairs theoretically have the same amplitude of intensity, their intensities are merged to improve estimates of reflection intensities and errors for a given dataset. If a large difference in intensity is observed from these symmetry-equivalent reflections, this may suggest that the *Laue class* is incorrect. The complex conjugate relationship of the F_{hkl} for Friedel pairs gives rise to inversion centers inherent to diffraction patterns thus differentiating the symmetry of the diffraction pattern from the crystal symmetry elements, or *space group*.

Evaluating the reflections that are *systematically absent* helps to narrow down the possible space groups that best match the collected structure factors, as the presence of certain translational symmetry elements in the unit cell causes the complete destruction of scattered waves. There are 230 crystallographic space groups and given a set of coordinates within a unit cell $x, y, z,$ each space group has a set of positions produced by applying the associated symmetry elements to these coordinates. Inputting these coordinates into the structure factor calculations provides *reflection conditions* for each space group, to which a set of indexed reflections can be compared.

As diffraction patterns have inversion centers due to the relationship of Friedel pairs, alternative techniques may be used to constrain whether the crystal itself is centrosymmetric (has an inversion center) or noncentrosymmetric (does not have an inversion center). Of the 230 crystallographic space groups, 92 and 138 are centrosymmetric and noncentrosymmetric, respectively. For a given coordinate x_j, y_j, z_j in centrosymmetric crystal, a site must also exist across the inversion center at $-x_j, -y_j, -z_j$. According to the relationship $\phi_j = 2\pi(hx_j + ky_j + lz_j)$, these two sites exhibit opposite phases, thus canceling the complex component of the structure factor. Even though phases cannot be directly measured from reflection intensities, this

characteristic for diffraction from centrosymmetric crystals limits the range of intensities typically measured. Examining the distribution of reflection intensities in a given dataset can help narrow down the assignment of a centrosymmetric or non-centrosymmetric space group.

A diffraction pattern and the electron density distribution or atomic arrangement of a crystal are related via a Fourier transform relationship:

$$\rho_{xyz} = (1/V_{cell}) * \sum_{hkl} F_{hkl} \exp[-2\pi i (hx + ky + lz)],$$

where locations of maximal ρ_{xyz} designate atomic positions. The electron density distribution within a crystal takes the form of a cosine wave, because values of electron density throughout the unit cell must be positive and real. Unfortunately, due to the phase problem, the crystal structure solution processes applied in this work utilize likely phase relationships for strong reflections with related Miller indices, and iteratively assign and modify the phases to find an electron density distribution that best matches the measured reflections.

With a starting set of atomic coordinates and atom types output by the structure solution algorithm, the structure model is then refined. After each model adjustment, a new electron density distribution is determined, and F^2 values are calculated across the reciprocal space and compared to the experimentally measured F^2_{hkl}. The atomic coordinates, site occupancies and displacement parameters, from thermal and static vibrational effects, are adjusted to minimize the difference between calculated and observed F^2 values and thus optimize the structure model.

The fundamentals of monochromatic X-ray diffraction used to characterize crystal structures discussed above most readily apply to cases of single crystal samples. The high pressure and temperature conditions targeted in this work; however, result in multigrain synthesis of Fe-sulfides, and data collection procedures are limited by pressure generation in a diamond-

anvil cell. The techniques of single-crystal X-ray-diffraction collection and analysis must be modified to account for these complexities, and in the remainder of this chapter, the procedure for sample loading, pressure generation, sample heating and data collection and analysis utilized for the multigrain Fe-sulfides samples will be explained.

2.2. Sample preparation and loading

2.2.1. Starting material

Two types of samples are typically loaded for conducting powder and multigrain experiments in the diamond anvil cell. For synthesis of compounds that are not stable at ambient conditions (e.g., Fe_2S and Fe_3S) and for phase relation studies, the ambient sample is a foil pressed from a powder. Differing starting compositions probed in this work were made by mixing Fe (99.9+%, <10 μm, Alfa Aesar) powder with iron sulfide (FeS, 99.99%, Alfa Aesar) powder and FeO (FeO, 99.5%, Alfa Aesar) in the desired ratios. Fe-FeS compositions, mixed for multigrain experiments, were homogenized in a mortar and pestle for 1 hour in alcohol, dried and then mixed dry for a short duration to reset any density settling during alcohol evaporation. Fe-S-O mixtures, produced for phase relation studies, were homogenized in alcohol in a ball mill for 1.5-3 hours at 20 Hz, dried and then ball milled dry for a short duration to reset any density segregation. The ball mill produces a fine grained, well homogenized powder but incorporates oxygen into the sample by oxidizing the iron powder during the rapid milling process. Final Fe-S-O starting compositions were measured by scanning electron microscope as described in Section 2.5.3 at the University of Chicago to determine the final oxygen content. For experiments aimed at synthesizing sulfide grains, in purely Fe-S systems, a mortar and pestle

was used for homogenizing the starting material to minimize oxidation of the iron powder. With crystal synthesis experiments, the sample is mapped with X-ray diffraction to find regions with optimal grain growth, and so homogeneity of the starting material is not critical; whereas, equilibrium phase relation studies can only be interpreted if the starting composition is homogenous and well constrained.

For single crystal experiments in which the target phase is stable at ambient conditions, single crystals of the starting material are used. A portion of this work was conducted on 10-30 μm Co_2P (Alfa Aesar, 99.9%) and Fe_3P crystals (Alfa Aesar, 99.5%).

2.2.2. Sample loading

Foils of the starting material are obtained by pressing powders between two ungasketed diamond anvils. Sample foils are loaded into 120–25 μm diameter sample chambers that were drilled from rhenium gaskets preindented to 28–40 GPa. Samples are loaded in KCl, KBr, NaCl, SiO_2, or Ne pressure media (Figure 2.3a). Those that are loaded in neon are first dried at 100ºC for 30 minutes and subsequently filled with compressed Ne gas at the GSECARS gas loading system (Rivers et al. 2008). Due to the hygroscopic nature of the alkali halide pressure media, loaded samples are dehydrated after 100ºC for 30 minutes prior pressurization. Pressure is determined from the hcp-Fe, Ne, or KCl equations of state (Dewaele et al. 2006; Fei et al. 2007, Dewaele et al. 2012).

The same type of gasket is prepared for single crystal loadings, but instead of a foil, 3–4 single crystals are loaded into the sample chamber and separated by 3–5 μm. A ruby ball is then placed next to the crystals as a pressure calibrate, and a copper or tungsten foil may. The sample

chamber was loaded with compressed neon gas as a pressure transmitting medium (Rivers et al. 2008). Pressure was determined from the ruby fluorescence scale and the Ne equation of state (Mao and Bell, 1976; Fei et al. 2007).

2.3. Pressure generation

Pressure is generated in a diamond anvil cell equipped with two opposing diamond anvils. As pressure is a function of force over area, with sufficiently small opposing diamond tips, called *culets*, multi-megabar pressures can be achieved simply by applying force via spring loaded screws (Figure 2.3a, c). Three types of diamond anvil cells were used in this thesis work: Mao symmetric cells (height ~ 3.5 cm), Mao short symmetric cells (height ~ 2.7 cm), and BX-90 cells (Kantor et al. 2012). For powder diffraction, the sample does not need to be rotated and therefore the cell does not need a wide angular opening (Figure 2.3b), but the cell does need to maintain alignment at high pressures. Symmetric diamond anvil cells routinely achieve high pressures and are the standard for powder diffraction experiments. Type-1 standard cut diamond anvils are used with culet sizes ranging from 300-50 μm (Figure 2.3b). For culet sizes less than or equal to 150 μm, diamonds with culets that bevel to 300 μm are used to provide support for the small culets. The diamonds are mounted onto standard cut tungsten carbide or cubic-boron nitride (CBN) seats (Figure 2.3b). As CBN seats only partially absorb the X-rays, samples loaded in a standard symmetric cell with a CBN seat placed upstream (closer to the X-ray source) can achieve angular access only limited by the aperture of the diamond and the opening of the cell

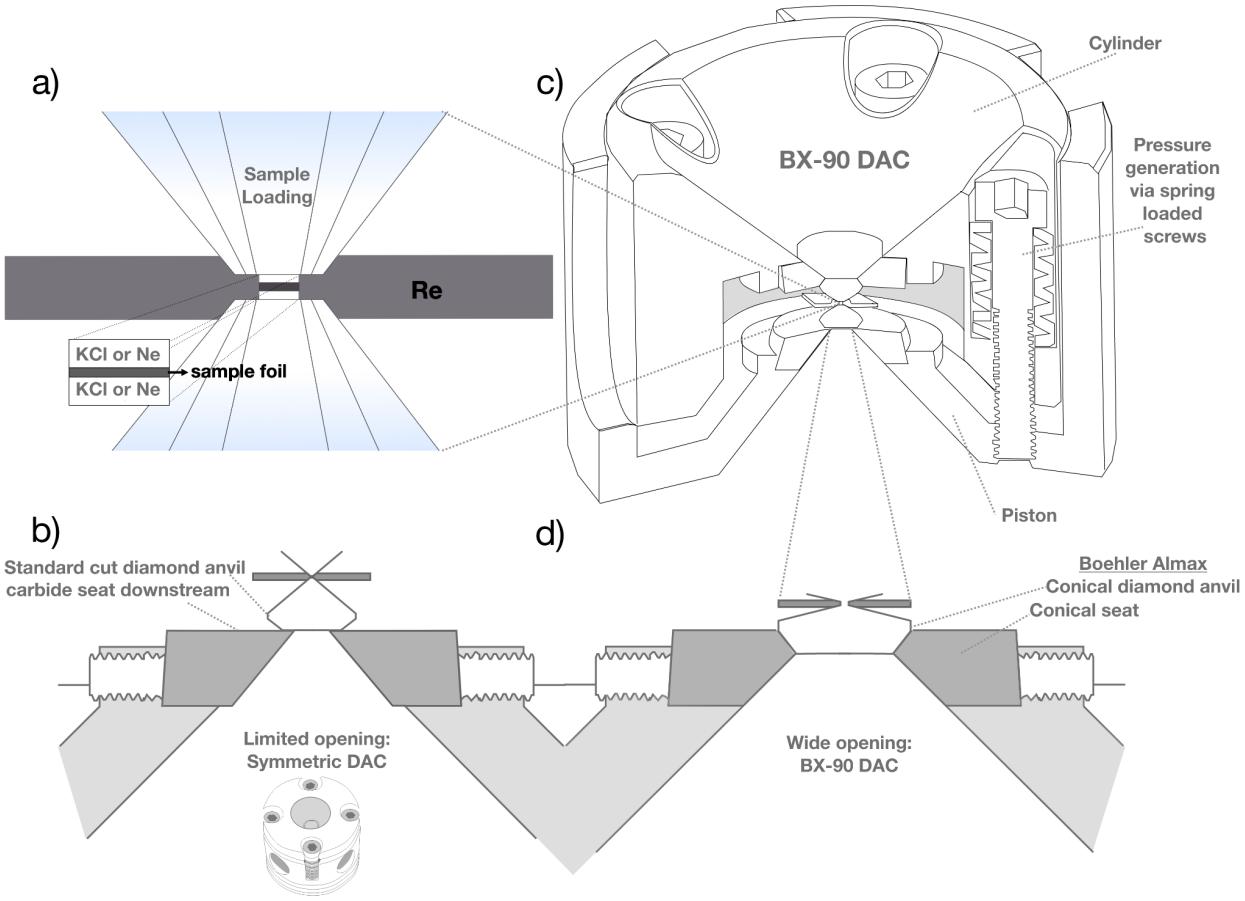

Figure 2.3. a) Rendering of the samples loaded in the diamond anvil cell. Sample foils or single crystals and pressure media are loaded in a sample chamber drilled from an indented rhenium gasket. Pressure is generated by closing the cell and applying force to the culets (300-50 μm diameter). b) Schematic of the limited angular opening of a symmetric diamond anvil cell equipped with standard cut diamonds and a carbide seat rendered based on Kantor et al. 2012. c) Drawing of the BX-90-type diamond anvil cell modified from Kantor et al. 2012 to represent the model of cell used in the current studies. The cylinder and piston of the DAC are labeled and the pressure-generating spring-loaded screws are identified. d) Schematic of the wide angular opening allotted by conical diamonds and seats loaded into a BX-90-type cell rendered based on Kantor et al. 2012.

downstream (closer to detector) (Figure 2.3b). An absorption correction must be applied to the diffraction intensities to account for the interaction of the X-ray source with the CBN seat prior

to entering the sample chamber. Information on applying this absorption correction can be found in Section 2.5.2.3 and Supplementary file SF2a.

For crystallographic work, where the cell must be rotated across wide angular range, BX-90-type (70º angular opening) diamond anvil cells (Kantor et al. 2012) (Figure 2.4c) and short symmetric diamond anvil cells (70º angular opening) equipped with type-I conical anvils and conical seats (Figure 2.4d) are used. Conical diamonds are designed to have a wide aperture (70º) and are cut with conical supports that fit into a matching seat (Figure 2.4d) (Boehler and Hantsetters 2004). Short symmetric cells also have a wide opening, due to their shortened height (~2.7 cm) compared to the standard model (~3.5 cm). If a short symmetric cell is equipped with conical diamonds, the 60–65º angular range can be achieved during diffraction collection. As a consequence of the short height of the cell, however, alignment is more challenging to maintain because the piston and cylinder are smaller (<1cm of contact length) and offer less friction to hold alignment at high pressures.

2.4. High P-T synchrotron X-ray diffraction

2.4.1. X-ray diffraction collection during laser heating

X-ray diffraction experiments conducted in this work took place at beamlines 13-ID-D and 13-BM-D of the Advanced Photon Source, Argonne National Laboratory. Diffraction measurements at 13-ID-D are collected with a 2 μm by 3 μm FWHM incident X-ray beam at 37 keV or 42 keV on a CdTe 1M Pilatus or MarCCD detector. Diffraction measurements at

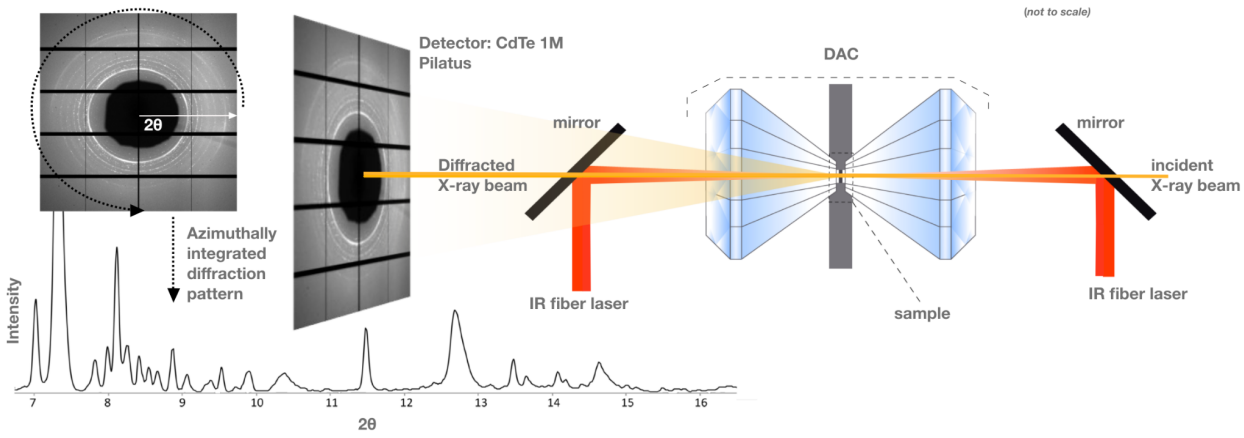

Figure 2.4. Diagram of the laser heating and X-ray diffraction set up at Sector 13 ID-D of the Advanced Photon Source, Argonne National Laboratory. The sample can be heated from both sides while collecting X-ray diffraction measurements. X-ray diffraction detection is shown here via a CdTe 1M Pilatus detector. X-ray diffraction patterns are integrated azimuthally and the raw and 2-D patterns are monitored during laser heating to assess grain growth and changes in phase and melting relations at high P-T.

13-BM-D are collected with a 3 μm by 8 μm full width half maximum (FWHM) incident X-ray beam at 37 keV with a Perkin-Elmer-16 inch amorphous silicon digital X-ray detector.

In-situ laser heating during X-ray diffraction takes place at beamline 13-ID-D (GeoSoilEnviroCARS) of the Advanced Photon Source, Argonne National Laboratory (Figure 2.4). The X-ray beam is aligned with the lasers using the fluorescence of the sample (Prakapenka et al. 2008). Samples are then laser-heated from both sides using fiber lasers shaped with ~10 μm flat tops (Prakapenka et al. 2008) (Figure 2.4). Temperature is measured spectroradiometrically based on a gray body approximation fit to the thermal emission from the central 6 μm of the laser-heated spot (Heinz and Jeanloz, 1987). A 3% correction is then applied to account for the thermal gradient through the sample chamber (Campbell et al. 2007, 2009).

Heating cycles typically last ~15–45 minutes at target pressure prior to quenching. Samples are heated up to 4 times in different locations of the sample chamber at differing

pressure steps. During heating and synthesis of iron sulfide crystallites, samples cannot be rotated to obtain additional reflections. Instead, X-ray diffraction patterns are integrated azimuthally using the Python-based program, Dioptas (Prescher and Prakapenka 2015), and the raw and 2-D patterns are monitored during laser heating to assess grain growth and changes in phase and melting relations at high *P-T* (Figure 2.4).

2.4.2. Single crystal X-ray diffraction collection techniques

For experiments aimed at assessing the crystal structure of synthesized phases, the target grains must be identified within the sample chamber, aligned with the beam and rotated under the X-ray beam. These experiments are conducted at beamlines 13-ID-D and 13-BM-D. Upon quenching high temperatures at high pressures, 10 x 10 μm diffraction maps are typically collected in 2 μm steps. At each map location, the sample may be rotated across a small angular range (≤ ±10º) so that the regions of the laser-heated area that exhibit the largest grain growth (showing high intensity, spotty XRD) of the target phase may be efficiently identified.

At selected locations, rotation images are collected across a ±30º angular range in 0.25–0.5º steps with exposure times of 1-4 s to measure a sufficient amount of the reciprocal space for crystal structure solution and refinement. As shown in Figure 2.5, 60º of the Ewald sphere can be accessed during these rotational scans (Figure 2.5). For multigrain synthesis experiments at high pressures, the quenched high-pressure samples consist of agglomerates of grains (Figure 2.5), and crystallites of the target phases must be identified in reciprocal space and separated from the reflections attributable to powder starting material, the rhenium gasket, the crystallized neon pressure medium, and diamond. The CrysAlisPro single crystal software is used to examine the

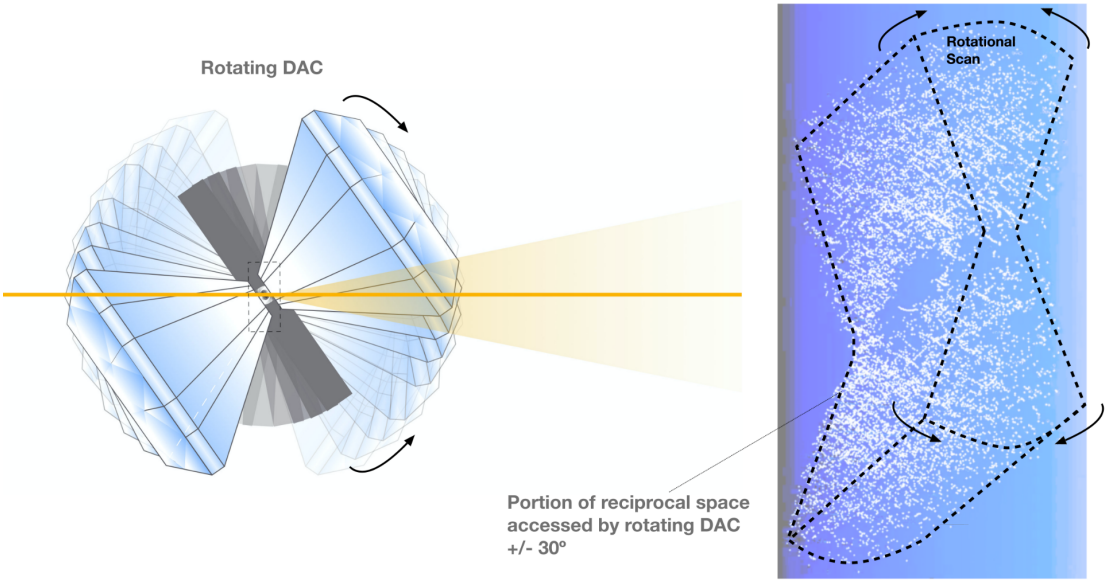

Figure 2.5. Visualization of the rotation of the diamond anvil cell during single crystal X-ray diffraction experiments and the portion of the Ewald's sphere accessed across the scan.

diffraction reflections in reciprocal space and identify and isolate grains of the target phases (Rigaku OD 2018). For an isolated lattice, the CrysAlisPro software is then used to index the reflections to determine the lattice parameters, integrate the intensities, and calculate the structure factors for the target crystallite in the reciprocal space (Rigaku OD 2018).

2.4.3. A note on technique nomenclature used in this work

The Fe-sulfide samples synthesized in this work are multigrain, and cannot be described as powder or single crystal samples; however, the diffraction patterns collected during heating without rotation, often called powder patterns, and the diffraction patterns collected with rotation after quenching, often called single crystal diffraction, are all critical to the assessment of iron sulfide phase relations and crystallography. Throughout this work, the terms *powder* and *single*

crystal diffraction will signify the type of techniques used and not the material properties of the overall samples.

2.5. Data analysis

2.5.1. Phase and melting relations, analyzing powder patterns

During *in-situ* laser-heated X-ray diffraction experiments, powder diffraction patterns are collected approximately every 200–300 K. The peaks observed at each temperature represent diffraction from the coexisting phases during heating. For identification of phases whose structures are known, .jcpds or .CIF files encoded with the unit-cell parameters, diffraction angles, intensities and equation of state behavior, are read into Dioptas. To determine the lattice parameters of the known phases present, the integrated diffraction patterns are processed with *Fityk* (Wojdyr 2010) and the fitted peak positions and their associated Miller indices of the target phase are input into the appropriate lattice geometry equations (Appendix 2). In this work, observations of unidentified structures in powder patterns were subsequently targeted in single crystal experiments.

Regarding phase and melting relation analysis with powder X-ray diffraction, a few visual points are important to identify. The observed loss of peaks of an identified phase and the simultaneous growth of a new set of peaks, suggests a phase transition. When this is observed, the first observation of the peaks associated with the new phase should be noted as the *P-T* condition of the transition. If two phases are observed to diminish as a new set of peaks grows in, this likely reveals a reaction of two phases to form a product phase. Again, the first observations

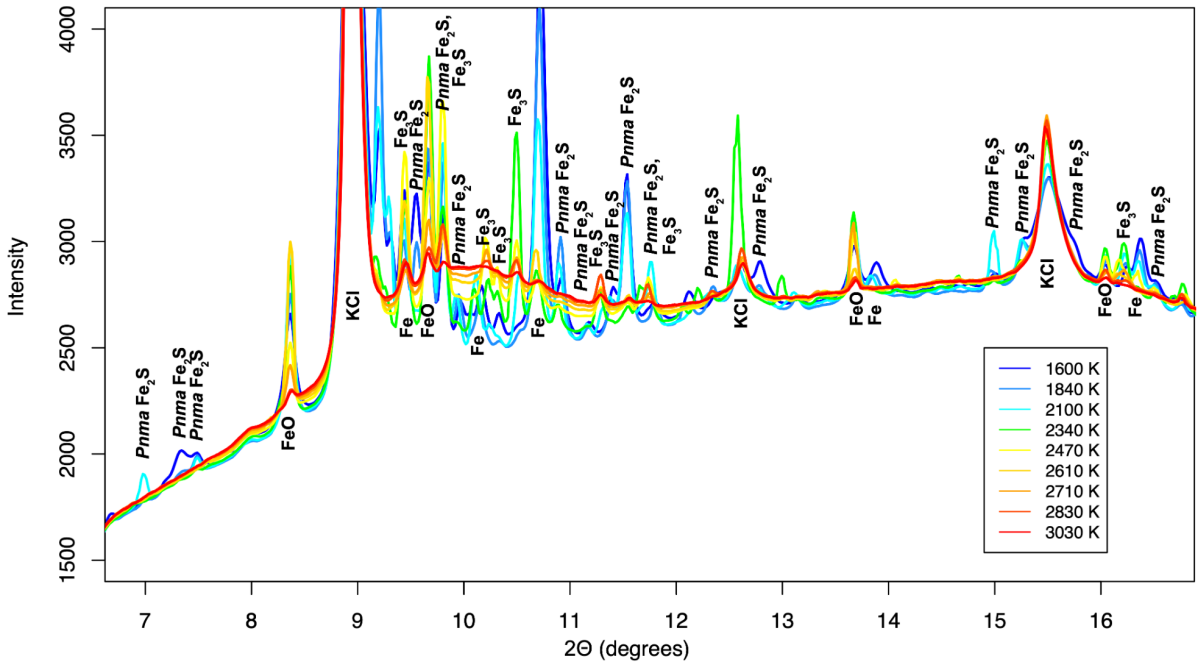

Figure 2.6. Superimposed diffraction patterns collected during heating in an Fe–12S–5O starting composition. The diffraction patterns are color coded for temperature. The reaction of Fe_2S+Fe to form Fe_3S can be observed at ~2100 K and the first signal of melting occurs at ~2340 K.

of the peaks associated with the reaction product mark the transition conditions. For example, the reaction of Fe + Fe_2S to form Fe_3S is observed at 74 GPa and 2100 K based on the first observations of the Fe_3S peaks at high *P-T* as shown in Figure 2.6 (aqua colored pattern). When melting occurs, a set of peaks will diminish in intensity simultaneously as an increase in background of the diffraction signal is observed as a result of increased thermal vibrations and disorder of the liquid structure. As the amount of constructive interference producing diffraction is greatest at low angles, the increase in background due to disorder of the melt is distinct in the 9–12º 2θ range. The first observation of this increased background, marks the first melt, and the eutectic temperature. In Figure 2.6, diffuse scattering from the liquid is observed around 2340 K (green diffraction pattern). The peaks associated with hcp-Fe are simultaneously observed to

decrease in intensity at these temperatures, indicating that Fe is the first phase to melt for this sample composition.

Even when phases are unknown and require single crystal X-ray diffraction to characterize, the powder diffraction patterns collected during high temperature synthesis are critical for assessing the *P-T* stability field of the phase and the phases with which it coexists. In the case of examining Earth's core crystallization sequences, it is particularly important to identify whether the phase equilibrates with iron at high *P-T*. This can be identified by checking that peaks of iron are present in the integrated diffraction pattern and that iron looks recrystallized in the raw pattern. As shown in Figure 2.7, recrystallized iron is identified as isolated reflections that are higher intensity compared to the powder starting material. As powder iron and recrystallized iron will overlap in the 2-D diffraction pattern, the recrystallized iron looks like bright spots on a low intensity ring. Figure 2.7 shows a diffraction pattern collected at 155(3) GPa and quenched from 3230(130) K with the crystallization of an unknown iron sulfide coexisting with recrystallized iron. These observations indicate that this unknown sulfide could be relevant to Earth's outer core thermodynamics.

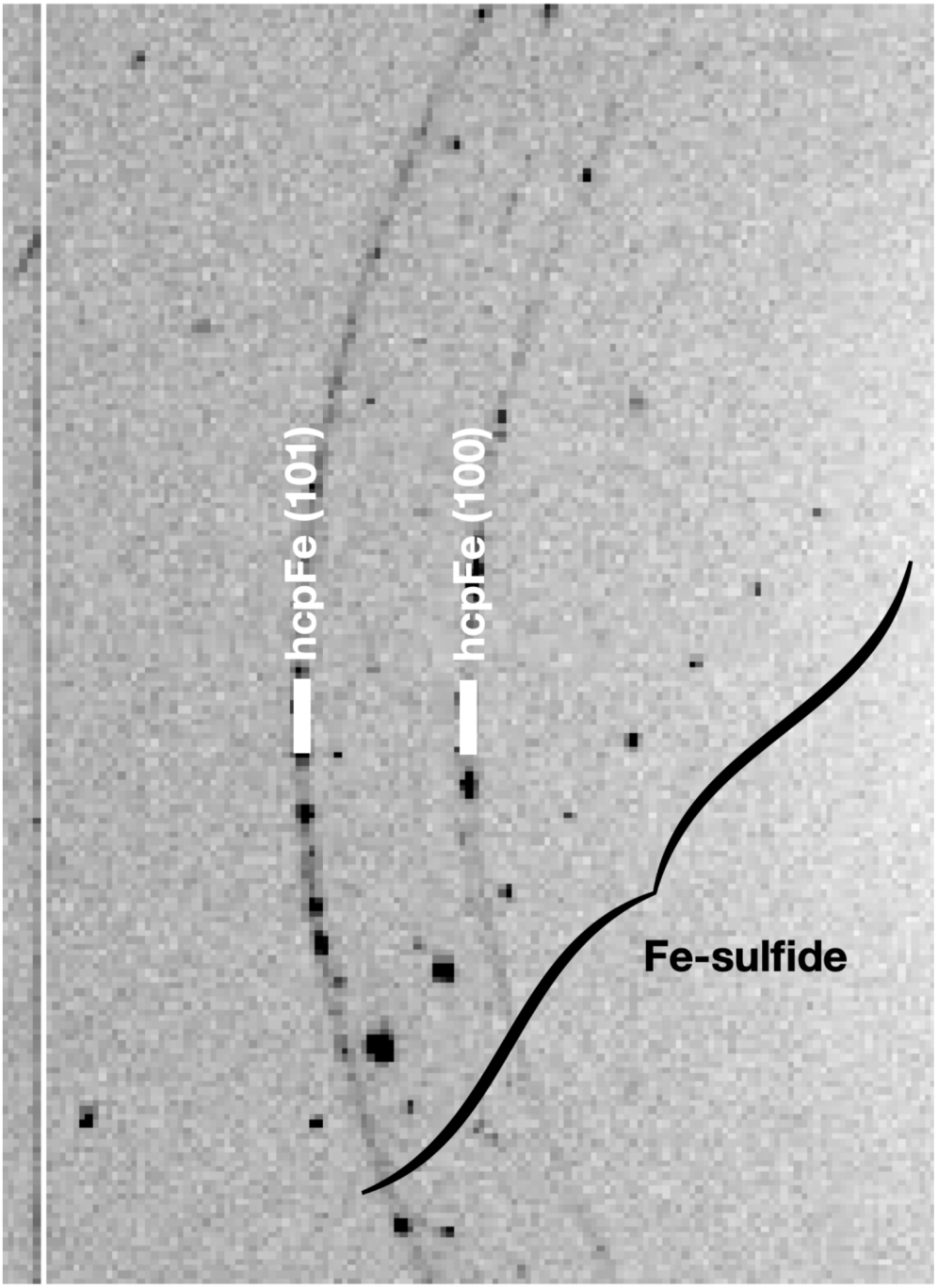

Figure 2.7. Diffraction pattern collected at 155(3) GPa and quenched from 3230(130) K showing the crystallization of an unknown iron sulfide coexisting with recrystallized iron. Sharp, high intensity reflections of iron are observed overlain on the lower intensity iron powder diffraction, indicating that the iron starting powder has reacted with the starting FeS material at high temperatures and recrystallized in equilibrium with the high P-T iron sulfide labeled.

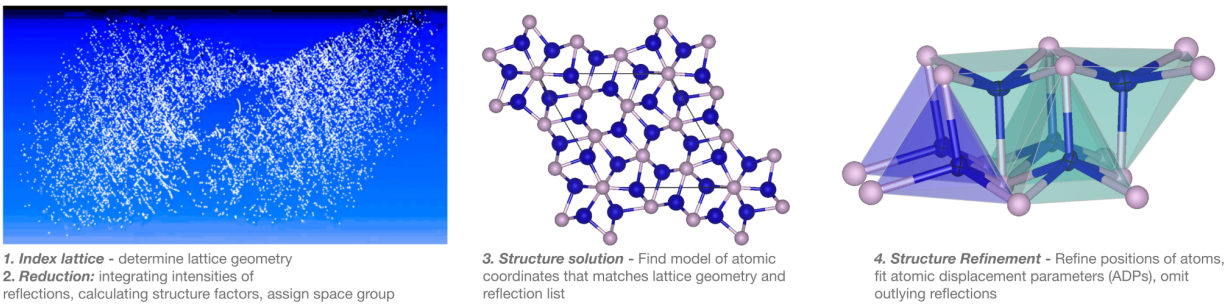

Figure 2.8. Images representing the structure analysis process with single crystal X-ray diffraction data. 1. The crystal lattice is indexed in the reciprocal space. 2. The diffraction intensities are then corrected and integrated across the angular scan. From this the structure factors are calculated. 3. A solution model for the observed structure factors and lattice symmetry is determined using the *ShelXT* program (Sheldrick 2015a) and 4. Atomic coordinates, site occupancies and atomic displacement parameters are refined to best match the observed structure factors. At this step, anomalous reflections may be omitted.

2.5.2. Crystal structure characterization using single crystal analysis techniques

Determining the crystal structure for a phase synthesized at high *P-T* conditions is a process involving: *indexing, integration, reduction, solution,* and *refinement* (Figure 2.8). As the foundational physics used in these steps were described in Section 2.1, this section aims to discuss the application of these principles to the high *P-T* data collected in this work. A thorough manual for conducting these analyses is given in Appendix A2c, a concise list of directions is also provided in supplemental file SF2a, and further detail on these methods can be found in Lavina et al. 2014 and Bykova 2015.

2.5.2.1. Lattice indexing

Structural analysis of a synthesized crystallite begins with the determination of its lattice parameters and orientation. Once several reflections of the target crystallite were identified and isolated in the reciprocal space, the auto indexing tool in CrysAlisPro was used to the find

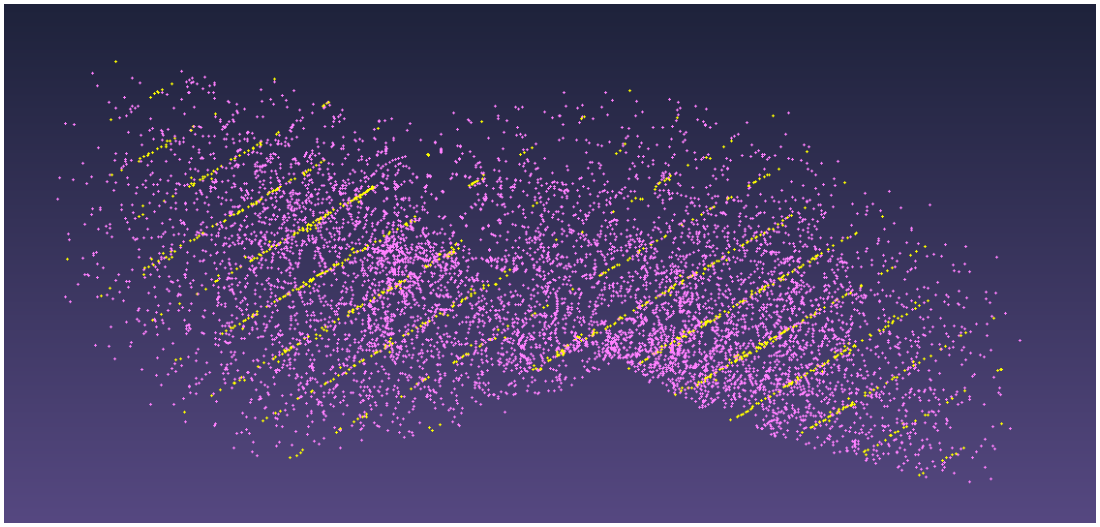

Figure 2.9. Image an Ewald's sphere from an experiment run at 45 GPa and quenched from high temperature. An auto-indexed lattice (yellow) is shown among the other detected reflections.

possible unit-cell geometries from the identified reciprocal lattice vectors. For a given unit-cell geometry, CrysAlisPro searches for all possible reciprocal lattice vectors in the dataset and assigns Miller Indices to them (Figure 2.9).

2.5.2.2 Integration and reduction

During the *integration* step, the intensity and uncertainty in intensity are determined for each reflection. Obtaining intensity uncertainties is critical for assessing the quality of a structural model. Measured intensities are not just generated from the crystallite itself, and some corrections must be applied to the intensities based on known factors. This is called data *reduction.* The following equations incorporate these corrections to determine the corrected intensities and their standard deviations based on these corrections made during the data reduction process:

$$\boldsymbol{\sigma}(I(hkl)) = (I(hkl) + \mathrm{r}B + r^2B)^{0.5}$$

$$|F(hkl)|^2 = I(hkl)/(L * p * T * D)$$

First the background must be distinguished from the intensity of a reflection over the angular range that the reflection is present in a scan. This can be described in the standard deviation $\boldsymbol{\sigma}(I(hkl))$ above, where $I(hkl)$ represents the intensity of the reflections, r represents the ratio of time spend measuring the intensity versus the background, and B represents the background intensity. These reflection intensities may then be merged with their Friedel pairs. These corrected intensities $I(hkl)$ are further corrected for the Lorentz (L), polarization (p), transmission (T) and decay (D) factors and the final corrected and scaled intensities, $|F(hkl)|^2$ with standard deviations, $\boldsymbol{\sigma}(I(hkl))$ are output.

The Lorentz factor, L, corrects for any intensity artifacts due to the time that a reciprocal lattice point spends passing through the Ewald's sphere during rotation of the sample. This may depend on the shape or mosaicity (degree of imperfection of the lattice) of the crystal as well as the angular size of the step scan and angle of scattering. The polarization factor, p, depends on the polarization of the incident beam and the scattering angle of the diffracted beam. The synchrotron X-ray diffraction used in this work is polarized and filtered to be monochromatic. The transmission factor, T, is a correction for the absorption of X-rays by the crystal and depends on the path lengths the X-rays travel and the absorbing power of the atoms within the crystal. The absorption coefficient of a crystal, μ can be easily calculated from the wavelength of the incident beam and the composition of the crystal (Hubbell and Seltzer 2004) then multiplied by the size of the crystal to approximate the absorption correction. For data reduction conducted in

this work, the absorption correction was calculated during the finalization of the structure factors in *CrysAlisPro* using a *multi-scan* method where changes in absorption correction are calculated across a rotational scan by comparing the intensity of the same reflections or Friedel pairs. The decay correction, *D*, applies if the crystal decomposes during collection and was not necessary for the short timescales of synchrotron X-ray diffraction collection and iron sulfide samples used in this work.

Along with these intensity corrections, a scale factor, accounting for the volume of the crystal and the intensity of the X-ray source, must be applied to the observed intensities and their standard deviations to obtain the structure factors. Without knowing the crystal structure, the absolute scale factor can be estimated based on the estimated intensities of scattered X-rays at $2\theta = 0$, and during crystal structure refinement, an overall scale factor is refined.

The data quality may be assessed after the integration and reduction process by comparing the difference in structure factors observed for symmetry equivalent reflections (R_{int}) and the ratio of structure factors and their uncertainties (R_{sigma}):

$$R_{int} = \Sigma| F^2_{obs} - (\overline{F})^2_{obs}| / \Sigma F^2_{obs},$$

$$R_{sigma} = \Sigma\boldsymbol{\sigma}(F^2_{obs}) / \Sigma F^2_{obs},$$

where $\overline{F}$ is equal to the average intensity for a sum of symmetry equivalent reflections. During data reduction, the R_{int} and R_{sigma} values were minimized by adjusting the reduction parameters to best account for the reflections and background in the dataset (Appendix A2c). The lattice geometry and the structure factors calculated using the optimized integration and reduction parameters were then deemed ready for structure solution and refinement.

2.5.2.3. Structure solution and refinement

Crystal structure solution was carried out using ShelXT (Sheldrick 2015a) or by applying known structure models, and structure refinement was conducted using ShelXL (Sheldrick 2015b). The logic behind the algorithms employed in these programs is discussed in Section 2.1., and instructions on the use of these programs, as they pertain to this work, are given in Appendix A4.

With a starting structure model, ShelXL was run repeatedly as one additional parameter was freed per refinement run. The atomic coordinates were refined first, followed by the ADPs. The vibration of an atomic site can be described as spherical via isotropic displacement parameters or as an ellipse via anisotropic displacement parameters. Each structure was refined with anisotropic displacement parameters only if sufficient reflections were obtained. A ratio of 6 reflections per refined parameter is acceptable to consider the fitted parameter statistically meaningful for describing the experimental structure factors. Statistical tests were also used to determine whether anisotropic displacement parameters are meaningful to the refinement output (Hamilton, 1965). Typically, the data quality of high *P-T* crystallites in a LHDAC is not sufficient to resolve statistically meaningful site occupancies, but in the final steps of the refinement process, the site occupancies were allowed to refine to check that their values did not change significantly. Little change in site occupancy values suggests that the proposed stoichiometry is correct.

Structure factors measured in microdiffraction in the LHDAC show some well-known limitations, such as limited resolution and redundancy, reflections overlapped by parasitic

scattering, diamond diffraction (Loveday et al. 1990) and, more notably, variable volume of illuminated crystal during rotation. During each refinement process, several outlier reflections were omitted based on their anomalous calculated versus measured structure factors. Discussion on reflection omission in this work is given in Appendix A4.

After each adjustment of the structure model, the quality of fit of the model to the experimental data is described by the following output values:

$$R_1 = \Sigma||F_{obs}| - |F_{calc}||/ \Sigma|F_{obs}|$$

$$wR_2 = \{\Sigma [w(F^2_{obs} - F^2_{calc})^2] / \Sigma [w(F^2_{obs})^2] \}^{0.5}$$

$$\text{GooF} = \{ \Sigma [w(F^2_{obs} - F^2_{calc})^2] / (n-p) \}^{0.5}$$

The w variable represents the weighting scheme applied to minimize the difference between observed and calculated structure factors. *ShelXL* suggests a weight based on the refined model that may be applied on the final refinement run. The n parameter indicates the number of independent reflections and p represents the number of refined parameters in the model. Typically R_1 values <0.1, wR$_2$ values <0.15 and GooF values ~ 1 were considered to demonstrate a well refined structure model for high pressure multigrain data analyzed. The procedure of assessing and minimizing these refinement parameters for the structure models reported are explained in further detail in Appendix A4.

2.5.3. Chemical analysis

Following powder and single-crystal X-ray diffraction experiments, select samples were decompressed to ambient conditions and recovered for chemical analysis at the University of Chicago using the TESCAN LYRA3 focused ion beam (FIB) and scanning electron microscope (SEM), equipped with an Oxford OmniProbe 400 micro-manipulator, Oxford OmniGIS gas injection system, and two Oxford Xmax 80 mm silicon drift detectors (SDD) for energy dispersive X-ray microanalysis. The recovered samples were first sectioned along the compression axis using the FIB. Samples were thinned to ~5 μm then attached to a copper TEM grid, for further thinning and polishing to 0.2 - 0.8 μm final thickness. Analyses of the recovered Fe-S-O foils were performed using an energy dispersive X-ray spectrometer (EDX; Oxford Instruments) on the SEM at 4–10 keV accelerating voltage. Bulk compositions of the quenched melts were determined by collecting an area average of the melted region, and point analyses of individual phases were averaged to obtain the compositions of solid grains. Oxygen measurements were facilitated by the SDD, which resolves the Fe Lα and O Kα peaks. Iron contents were determined from Fe Lα counts, allowing use of the 4–5 keV accelerating voltage for greater spatial resolution.

3. The crystal structure of Fe_2S at 90 GPa based on single-crystal X-ray diffraction techniques

Collaborators: Barbara Lavina[b,c], Stella Chariton[c], Sergey Tkachev[c], Vitali B. Prakapenka[c], Andrew J. Campbell[a]

[a]University of Chicago, Department of the Geophysical Sciences, 5734 S Ellis Ave, Chicago, IL 60637, USA
[b]X-ray Science Division, Advanced Photon Source, Argonne National Laboratory, Argonne, IL 60439, USA
[c]Center for Advanced Radiation Sources, University of Chicago, 9700 South Cass Avenue, Building 434A, Argonne, IL 60439, USA

Citation: Zurkowski, C.C., Lavina, B., Chariton, S., Tkachev, S., Prakapenka V.B. and Campbell A.J., in press. The crystal structure of Fe_2S at 90 GPa based on single-crystal X-ray diffraction techniques. Am. Mineral. https://doi.org/10.2138/am-2022-7973

3.1. Introduction

Fe_2S has emerged as a relevant Fe-rich sulfide, particularly in the context of the high *P*-*T* conditions of Earth's core (Tateno et al. 2019). Two structures have been reported for Fe_2S in the pressure range of 22–306 GPa. TEM analysis of a sample recovered from 22 GPa and 1900 K indicates that Fe_2S assumes the *C*22, Fe_2P-type structure at these conditions (Koch-Müller et al. 2002). At high temperatures between 190 and 306 GPa, Fe_2S has been observed to take an orthorhombic lattice, with unit-cell parameters compatible with the *C*37 structure (Co_2Si type, *Pnma*, *Z*=4) (Tateno et al. 2019). These results are supported by *ab-initio* calculations predicting a *Pnma* Fe_2S phase to 400 GPa at 300 K (Bazhanova et al. 2017). A recent examination of the analogous Fe_2P system reveals a pressure-induced *C*23-*C*37 transition above 42 GPa (Nakashima et al. 2020), supporting that the *C*37 structure is a high-pressure polymorph in these Fe_2X (*X* = S, P) compounds. Furthermore, as the phase relations observed in the iron phosphide system tend to serve as low-pressure analogs to the iron sulfide system (e.g., Rundqvist 1962; Ono et al. 2006;

Dera et al. 2008; Gu et al. 2016; Tateno et al. 2019), the *C*23 and *C*37 structures observed in Fe_2P may reflect higher pressure phase relations in Fe_2S.

While experimental and calculated results demonstrate that Fe_2S is an important compound to further investigate in relation to Earth's core chemistry, an examination into the crystallography of Fe_2S at high pressures has not been carried out. In the current study, crystallites of Fe_2S were synthesized in a Fe+FeS starting foil in a laser-heated diamond-anvil cell at 90 GPa and 2400 K, and its crystal structure was determined based on single-crystal X-ray diffraction techniques. Structural solution and refinement of atomic fractional coordinates indicate that the equilibrium phase is a *C*23, Co_2P-type Fe_2S. These results suggest a *C*23-*C*37 transition in Fe_2S at higher pressures.

3.2. *Materials and methods*

Starting Fe-S compositions for these experiments were made by mixing Fe (99.9+%, <10 μm, Alfa Aesar) powder with iron sulfide (FeS, 99.99%, Alfa Aesar) powder in a ratio of 1g Fe to 1.75 g FeS in an agate mortar and pestle. The pressure was generated in a BX-90-type (70º angular opening) diamond anvil cell (Kantor et al. 2012) using Type-I conical anvils with 150 μm beveled culets and conical seats. Foils of the starting material were loaded along with a ruby ball into a sample chamber that was drilled through the rhenium gasket. The sample was subsequently flushed with a neon pressure transmitting medium (Rivers et al. 2008). During compression, the ruby fluorescence scale and the Ne equation of state were used to measure pressure (Mao and Bell 1976; Fei et al. 2007). Due to the high compressibility of neon, the sample chamber diameter shrunk to ~15 μm at target pressure.

X-ray diffraction experiments were conducted at beamline 13-ID-D (GeoSoilEnviroCARS) of the Advanced Photon Source, Argonne National Laboratory. For further experimental details pertaining to this beamline, refer to Section 2.4. The sample was heated 3 times in different locations of the sample chamber with the goal of maximizing Fe_2S grain growth and data collected after the final heating cycle is reported herein. Upon quenching, a 10 x 10 μm diffraction map was collected in 2 μm steps to determine the regions of the laser-heated area that exhibited the largest grain growth (showing high intensity, spotty XRD) of the target phase. At selected locations, rotation images were collected across a ±30º angular range in 0.5º steps with exposure times of 4 s.

Quenched multigrain samples consisted of agglomerates of Fe_2S crystallites (up to ~4 μm in diameter) with a few grains of hcp-Fe in more Fe-rich regions of the starting foil. Diffraction rings from the Re were also detected due to the size of the sample chamber at target pressures, but the volumes of Fe and Fe_2S observed do not support Re reaction with the sample. Grains of the target Fe_2S phase were identified in reciprocal space and separated from the reflections attributable to iron, rhenium, neon, and diamond. Each grain of Fe_2S was processed using the single crystal analysis methods described in Section 2.5.2. A summarization of the experimental conditions and instrument parameters used in this study are given in the supplemental CIF file, SF3a.

3.3. Results and discussion

Heating experiments were conducted at 89(2) GPa. Upon quenching from 2380(120) K, several grains, within a 100 μm^2 region around the laser-heated spot, were identified in the reciprocal space and indexed to an orthorhombic lattice. The grains were found to have similar unit-cell parameters (Table 3.1), and a selected grain, based on the number of reflections and reduction parameters (Table 3.2), has the unit-cell lengths: 5.066(2) Å, 3.285(2) Å, and 6.125(2) Å. Analysis of systematic absences constrains a *Pnma* space group and density considerations suggest 4 formula units per cell Fe_2S.

Despite the limited opening of the DAC and conical seats used to obtain the high *P-T* synthesis conditions; the scattering overlap from diamond, rhenium, and other crystallites in the multigrain sample; and the variation in the volume of the crystal in the path of the beam during the rotational scans, the solution and refinement of all grains at 89 GPa indicate that the synthesized Fe_2S crystallites adopt the *C*23 structure (anti-$PbCl_2$/Co_2P-type, *Z*=4) (Rundqvist 1960) (Figure 3.1). The structural solution and refinement model are robust and repeatable, considering the good agreement of the refined atomic fractional coordinates for each grain (Table 3.4). After data reduction, 190–260 measured reflections and 82–147 independent reflections were observed for each Fe_2S crystallite, and 0–4 outlying reflections were identified based on anomalous differences in observed versus calculated structure factors and omitted in the final structure calculations (Table 3.2). Due to the limited reflections collected in these high-pressure measurements, not all sites could be refined with anisotropic displacement parameters (Table 3.4). Instead, when sufficient reflections were observed, the Fe sites were refined with anisotropic displacement parameters while the S site was refined with isotropic displacement

Table 3.1. Unit-cell parameters indexed for the 6 grains of C23 Fe_2S analyzed in this study.

Pnma Fe_2S grains indexed	**Grain 1: C132, 90 GPa, Map 16**	**Grain 2: C132, 90 GPa, Map 23**	**Grain 3: C132, 90 GPa, Map 31**	**Grain 4: C132, 90 GPa, Map 32**	**Grain 5: C132, 90 GPa, Map 32**	**Grain 6: C132, 90 GPa, S1**
a (Å) *b* (Å) *c* (Å)	5.066(2), 3.286 (2), 6.124 (2)	5.066 (2), 3.285 (2), 6.125 (2)	5.07 (2), 3.279 (1), 6.140 (1)	5.089 (1), 3.27 (1), 6.105 (1)	5.06 (2), 3.283 (1), 6.148 (2)	5.078 (3), 3.289 (2), 6.123 (3)
V (Å^3), (Z=4)	101.9 (1)	101.9 (1)	102.0 (3)	101.6 (3)	102.2 (4)	102.3 (1)
μ (mm^{-1})	2.49	2.49	2.49	2.5	2.49	2.48

Table 3.2. Reduction and refinement parameters for the 6 grains of C23 Fe_2S analyzed in this study.

Sample Name	**Grain 1: C132, 90 GPa, Map 16**	**Grain 2: C132, 90 GPa, Map 23**	**Grain 3: C132, 90 GPa, Map 31**	**Grain 4: C132, 90 GPa, Map 32**	**Grain 5: C132, 90 GPa, Map 32**	**Grain 6: C132, 90 GPa, S1**
Reduction						
No. of measured, independent and observed [I > 2σ(I)] reflections	220, 116, 110	231, 119, 114	214, 82, 76	206, 98, 91	193, 81, 68	260, 147, 134
R_{int}, R_{sigma}	0.0147, 0.0188	0.0127, 0.0162	0.0221, 0.0213	0.0423, 0.0488	0.0679, 0.0460	0.0096, 0.0116
$(\sin\theta/\lambda)_{max}$ (Å^{-1})	0.877	0.877	0.852	0.856	0.851	0.862
Refinement						
$R[F^2 > 2\sigma(F^2)]$, $wR(F^2)$, S	0.027, 0.069, 1.15	0.028, 0.076, 1.14	0.033, 0.087, 1.10	0.060, 0.168, 1.18	0.055, 0.148, 1.11	0.080, 0.189, 1.06
No. of reflections	116	119	82	98	81	147
omitted reflections	(525)			(218), (802), (801), (811)	(243)	(444), (443)
No. of parameters	10	15	10	10	10	10
$\Delta\rho_{max}$, $\Delta\rho_{min}$ (e Å^{-3})	1.10, −1.25	1.28, −1.15	0.73, −1.44	1.60, −1.68	1.90, −2.10	5.12, −3.36

parameters (Table 3.4). Otherwise, all sites were refined with isotropic displacement parameters (Table 3.4). Within 1%, all sites for all grains are fully occupied. A CIF file of the refined solution model is provided in Supplementary Material. The uniformity of unit-cell parameters and site occupancies suggest invariable stoichiometry and structure from grain to grain.

The *C*23 Fe_2S structure can be viewed as corner-sharing columns of FeS_4 tetrahedra and columns of edge-sharing FeS_5 square pyramids linked along edges in the *b* direction (Figure 3.1a). The Fe1, Fe2, and S3 sites occupy Wyckoff position 4*c* with point symmetry *m* (Table 3.4). Sulfur is coordinated by 9 iron atoms (Figure 3.1b, Table 3.3). The Fe1, Fe2, and S

Table 3.3. Interatomic distances, polyhedra volumes and distortion indices (Baur, 1974) measured in the coordination polyhedra of *C*23 Fe_2S at 89(2) GPa.

Polyhedron	Sites	Interatomic Distance (Å)	Polyhedra Volume (Å^3)	Distortion Index
FeS_5			8.462	0.042
	Fe1–S3	2.110(2)		
	Fe1–S3	2.190(1)		
	Fe1–S3	2.190(1)		
	Fe1–S3	2.359(1)		
	Fe1–S3	2.359(1)		
FeS_5			4.263	0.012
	Fe2–S3	1.994(2)		
	Fe2–S3	2.047(2)		
	Fe2–S3	2.066(1)		
	Fe2–S3	2.066(1)		
SFe_9			20.016	0.050
	S3–Fe2	1.994(2)		
	S3–Fe2	2.047(2)		
	S3–Fe2	2.066(1)		
	S3–Fe2	2.066(1)		
	S3–Fe1	2.110(2)		
	S3–Fe1	2.190(1)		
	S3–Fe1	2.190(1)		
	S3–Fe1	2.359(1)		
	S3–Fe1	2.359(1)		

coordination environments observed differentiate this structure from the *C*37, Co_2Si-type structure. M_2X compounds in the *C*37 structure have the same space group and site symmetries as compounds with the *C*23 structure, but *C*37 phases have one 10-fold coordinated *X* site and two 5-fold coordinated *M* sites (Geller and Wollontis 1955; Rundqvist 1960; Hyde et al. 1992) while *C*23 phases have one 9-fold coordinated *X* site, one 4-fold coordinated *M* site, and one 5-fold coordinated *M* site. S–Fe interatomic distances in *C*23 Fe_2S range from 1.994(2) Å to

2.357(1) with the tenth closest Fe atom at 3.077(3) Å, supporting 9-fold coordination of Fe around the S sites. Fe-S distances in the FeS_4 tetrahedra range from 2.110(2) Å to 2.359(1) Å with the next nearest S atom at 3.063(3) Å, supporting 4-fold coordinated Fe site. The interatomic distances measured in Fe_2S at 89(2) GPa are given in Table 3.3. These bond lengths are comparable to those measured in Fe_3S, FeS, and FeS_2 (Brostigen and Kjekshus 1969; Lennie et al. 1995; Fei et al. 2000) considering the degree of compression of the Fe-S bond at 89 GPa.

The integration of the diffraction patterns collected in each rotational scan shows the presence of *C*23 Fe_2S crystallites, and Re and Ne (Figure 3.3). Unit-cell volumes and site occupancies of the Fe_2S grains analyzed (Table 3.4), verify that Re did not react into the sample. Rhenium diffraction, likely from the gasket-hole edge, is an outcome of the small hole size at these high pressures. Fe_2S in the raw diffraction patterns appears as spotty Debye rings, showing a range of grain sizes formed at the synthesis conditions (Figure 3.3, red tick marks). In the integrated patterns, Fe_2S accounts for nearly all of the lower-intensity peaks, compared to Ne and Re (Figure 3.3). An additional peak at around $2\Theta \sim 9.1^{\circ}$ remains unidentified (Figure 3.3), but it appears as a weak powder ring in the raw patterns, indicating that it is not diffraction from the synthesized *C*23 Fe_2S crystallites. In Figure 3.3b and 3.2c, a few additional reflections are marked as unidentified. No additional lattice-types were identified in the reciprocal space, indicating that these unidentified diffraction spots are not associated with *C*23 Fe_2S and are not a part of a well-formed crystal lattice in the sample chamber. The calculated diffraction lines for *C*23 Fe_2S based on the single-crystal analyses are shown in red below the integrated diffraction pattern in Figure 3.3 and higher intensity miller indices are labeled. The calculated *hkl* values, d-spacings, 2Θ values, and Q values are provided in supplemental file SF3b.

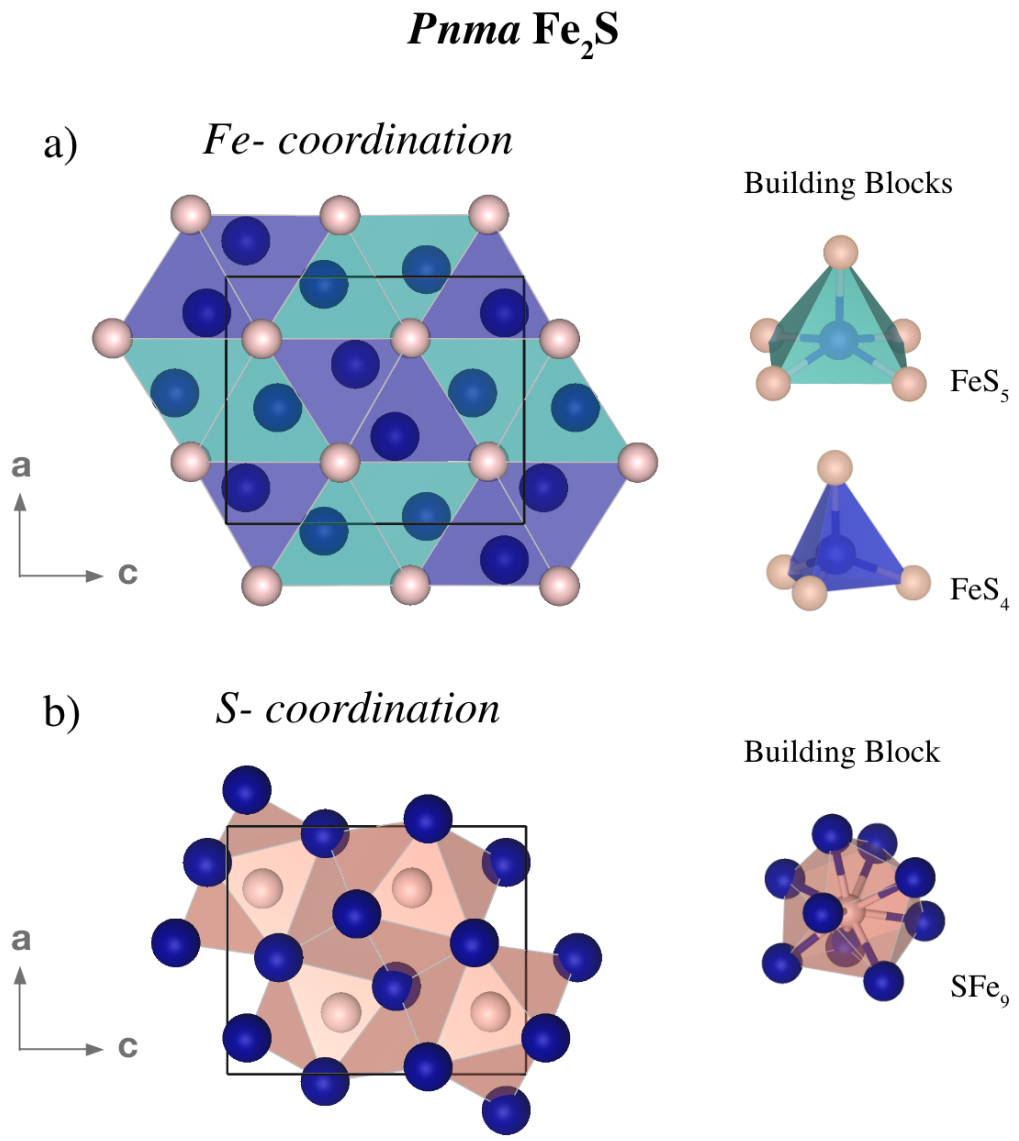

Figure 3.1. *C*23 Fe_2S, synthesized at 89(2) GPa and 2380(112) K with iron atoms in dark blue and sulfur atoms in light pink. a) Polyhedral view of Fe_2S showing Fe-coordination polyhedra. In this view, the unit cell is composed of FeS_4 tetrahedra and FeS_5 square pyramids in a 1:1 ratio. The tetrahedral and square pyramid building blocks are shown on the right. b) Polyhedral view of Fe_2S showing S-coordination polyhedra. In this view, the unit cell is composed of SFe_9 polyhedra. The SFe_9 building block is shown on the right.

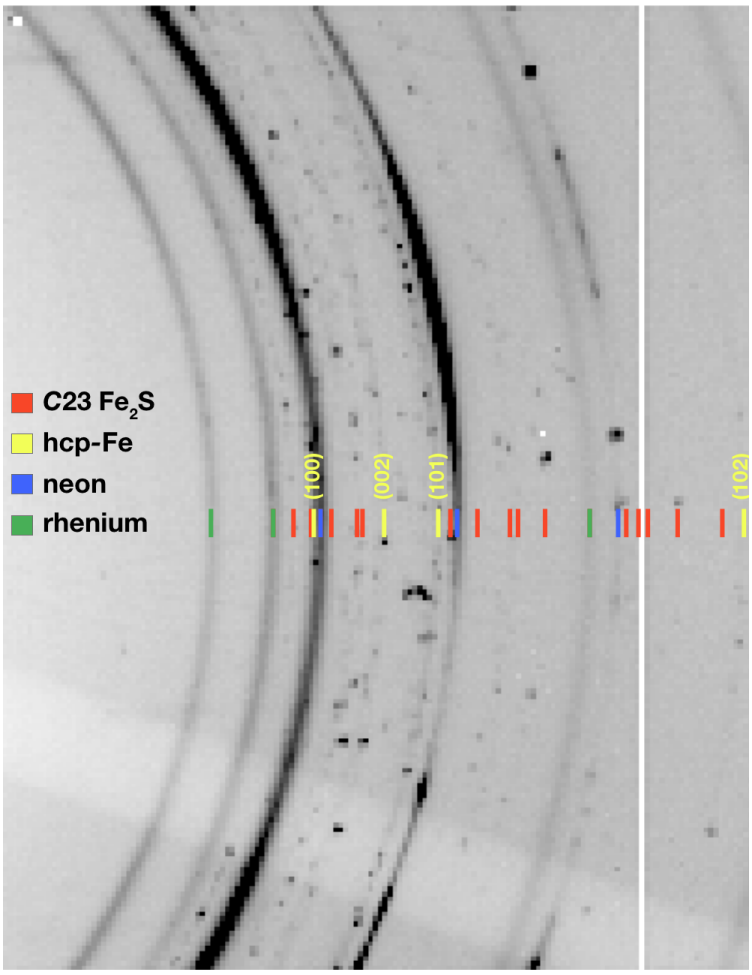

Figure 3.2. Zoomed-in raw X-ray diffraction pattern at 89(2) GPa produced by combining the images collected across ±30º rotation in 0.5º steps with 4 s exposure per image. Reflections of hcp-Fe are identified with their corresponding Miller Indices. *C*23 Fe_2S, neon and rhenium are also labeled.

At the sample locations where grains 3–6 were identified (Table 1), crystallites of Fe are also observed, indicating a more iron-rich region of the starting material. In the cases where Fe is present in the diffraction patterns, it is observed in the hcp-phase and identified based on diffraction from the (100), (002), (101), (102), (110), (112), and (201) planes. Sharp, high-intensity spots overlain on faint rings at the hcp-Fe diffraction angles indicate recrystallized iron coexisting with Fe_2S (Figure 3.2). At other locations, such as the locations where grains 1 and 2

were identified (Table 1), all of the initial Fe has reacted with FeS to form Fe_2S, such that no diffraction from hcp-Fe are observed (Figure 3.3). If these sample locations where hcp-Fe is not observed are associated with more S-rich regions of the starting material, then the additional unidentified reflections (Figure 3.3b, c) may indicate the presence of a coexisting sulfide that is more S-rich than Fe_2S. Further experiments, aimed at assessing the equilibrium phase relations are required to explain these observations.

Fe_2S has previously been reported to take an orthorhombic structure in the pressure range of 190–306 GPa and up to 3600 K with unit-cell parameters compatible with the *C*37 structure (Tateno et al. 2019). This *C*37 Fe_2S structure was proposed without verification from single-crystal techniques, but insight can be gained from the systematic comparison of the Co_2 P and Co_2Si unit cells, which can serve as analogs of the Fe_2S polymorphs. At ambient conditions, *C*23 Co_2P has a longer *a* axis and shorter *b* and *c* axis than that of *C*37 Co_2Si (Rundqvist 1960), and Co_2P has a *c/a* ratio of 1.16 while Co_2Si has a *c/a* ratio of 1.44 (Rundqvist 1960; Geller and Walantis 1955). Between 190 and 300 GPa, Tateno et al. 2019 report Fe_2S *c/a* ratios in the 1.35–1.40 range, and at 90 GPa, the current study reports a Fe_2S *c/a* ratio of 1.21. These relative unit-cell analyses support that the *C*37 Fe_2S is the stable phase at higher pressures (Tateno et al. 2019), while the structural solution and refinement carried out in this study establishes that Fe_2S adopts the *C*23 structure at 90 GPa.

Table 3.4. Atomic fractional coordinates and thermal parameters refined for 6 grains of *C*23 Fe_2S.

Grain 1: C132, Map 16										
atom	**x**	**y**	**z**	**U11**	**U22**	**U33**	**U23**	**U13**	**U12**	**Ueq**
Fe1 coordinate	0.96985	0.25000	0.67373	0.00459	0.00351	0.00391	0.00000	-0.00046	0.00000	0.00401
error	0.00016	0.00000	0.00013	0.00050	0.00073	0.00029	0.00000	0.00024	0.00000	0.00021
Fe2 coordinate	0.85317	0.25000	0.06621	0.00355	0.00361	0.00339	0.00000	0.00043	0.00000	0.00352
error	0.00016	0.00000	0.00011	0.00046	0.00073	0.00033	0.00000	0.00023	0.00000	0.00021
S3 coordinate	0.75181	0.25000	0.38073	0.00313						
error	0.00022	0.00000	0.00019	0.00000						
Grain 2: C132, Map 23										
atom	**x**	**y**	**z**	**U11**	**U22**	**U33**	**U23**	**U13**	**U12**	**Ueq**
Fe1 coordinate	0.97004	0.25000	0.67398	0.00736	0.00323	0.00546	0.00000	0.00043	0.00000	0.00535
error	0.00018	0.00000	0.00015	0.00054	0.00078	0.00033	0.00000	0.00027	0.00000	0.00023
Fe2 coordinate	0.85289	0.25000	0.06609	0.00563	0.00481	0.00468	0.00000	0.00021	0.00000	0.00504
error	0.00018	0.00000	0.00013	0.00055	0.00085	0.00037	0.00000	0.00025	0.00000	0.00024
S3 coordinate	0.75178	0.25000	0.38063	0.00526						
error	0.00025	0.00000	0.00023	0.00000						
Grain 3: C132, Map 31										
atom	**x**	**y**	**z**	**U11**	**U22**	**U33**	**U23**	**U13**	**U12**	**Ueq**
Fe1 coordinate	0.96989	0.25000	0.67357	0.00426						
error	0.00073	0.00000	0.00021	0.00041						
Fe2 coordinate	0.85293	0.25000	0.06657	0.00353						
error	0.00092	0.00000	0.00020	0.00045						
S3 coordinate	0.75250	0.25000	0.38114	0.00362						
error	0.00141	0.00000	0.00036	0.00053						

Table 3.4. ***continued***

Grain 4: C132, Map 32										
atom	**x**	**y**	**z**	**U11**	**U22**	**U33**	**U23**	**U13**	**U12**	**Ueq**
Fe1 coordinate	0.97051	0.25000	0.67189	0.01203	0.01873	0.01026	0.00000	-0.00040	0.00000	0.01367
error	0.00032	0.00000	0.00024	0.00100	0.01140	0.00089	0.00000	0.00042	0.00000	0.00366
Fe2 coordinate	0.85383	0.25000	0.06602	0.01305	0.01816	0.01029	0.00000	0.00036	0.00000	0.01383
error	0.00031	0.00000	0.00020	0.00095	0.01012	0.00097	0.00000	0.00042	0.00000	0.00323
S3 coordinate	0.74995	0.25000	0.38069	0.01248						
error	0.00048	0.00000	0.00039	0.00088						
Grain 5: C132, Map 32										
atom	**x**	**y**	**z**	**U11**	**U22**	**U33**	**U23**	**U13**	**U12**	**Ueq**
Fe1 coordinate	0.96844	0.25000	0.67326	0.00336						
error	0.00119	0.00000	0.00035	0.00069						
Fe2 coordinate	0.85388	0.25000	0.06652	0.00400						
error	0.00139	0.00000	0.00036	0.00076						
S3 coordinate	0.75449	0.25000	0.38072	0.00267						
error	0.00235	0.00000	0.00057	0.00089						
Grain 5: C132, S1										
atom	**x**	**y**	**z**	**U11**	**U22**	**U33**	**U23**	**U13**	**U12**	**Ueq**
Fe1 coordinate	0.97023	0.25000	0.67244	0.00876	0.00892	0.00940	0.00000	-0.00083	0.00000	0.00903
error	0.00030	0.00000	0.00024	0.00099	0.00088	0.00102	0.00000	0.00039	0.00000	0.00065
Fe2 coordinate	0.85389	0.25000	0.06609	0.00624	0.00989	0.00973	0.00000	0.00009	0.00000	0.00862
error	0.00028	0.00000	0.00024	0.00100	0.00092	0.00111	0.00000	0.00036	0.00000	0.00065
S3 coordinate	0.75126	0.25000	0.38134	0.00874						
error	0.00035	0.00000	0.00053	0.00069						

3.4. Implications

Upon pressurization to 90 GPa and heating to 2400 K, Fe_2S was synthesized and its structure was determined using single-crystal X-ray diffraction techniques on a multigrain Fe+FeS starting material. Structural solution and refinement of 6 crystallites prove that Fe_2S takes a *C*23 structure (*Pnma, Z*=4) at these conditions. While Earth's core-mantle boundary (CMB) pressure is 136 GPa, exceeding the pressure conditions of the current study, broad understanding of stable iron sulfide phases is important to assess the behavior of Fe,S-rich systems relevant to Earth's core. Moreover, the C23 Fe_2S phase may be important in the crystallization sequences within smaller terrestrial planets. Future experiments at lower pressures, may elucidate the stability of Fe_2S versus Fe_3S and Fe_3S_2 at conditions related to the Martian and Mercurian core. A recent multi-anvil press study revealed that Si may expand the stability field of Fe_2S at the conditions of the Mercurian inner core boundary (ICB), but no structure information was obtained for this Fe_2(S, Si) phase (Tao et al. 2021).

In relation to Earth's core, Fe_2S has been observed at Earth's mid-outer-core pressures (190–306 GPa) to have a unit-cell with geometry compatible with a *C*37 structure (Tateno et al. 2019). Analogous to the Fe_2P system (Nakajima et al. 2020), Fe_2S may therefore undergo a *C*23–*C*37 transition within the 89–190 GPa range. Future crystallographic work, tracking the coordination of Fe_2S within this pressure range is needed to determine the *C*23 and *C*37 *P-T* stability fields. This analysis would reveal the structure of Fe_2S at Earth's CMB pressures and high temperatures and help characterize the density profile of Fe_2S throughout the conditions of the outer core (136–330 GPa, ~4000–6000 K). As both *C*23 Fe_2S and *C*37 Fe_2S take the space group *Pnma* with *Z*=4, the results from this work and that of Tateno et al. 2019 remain in

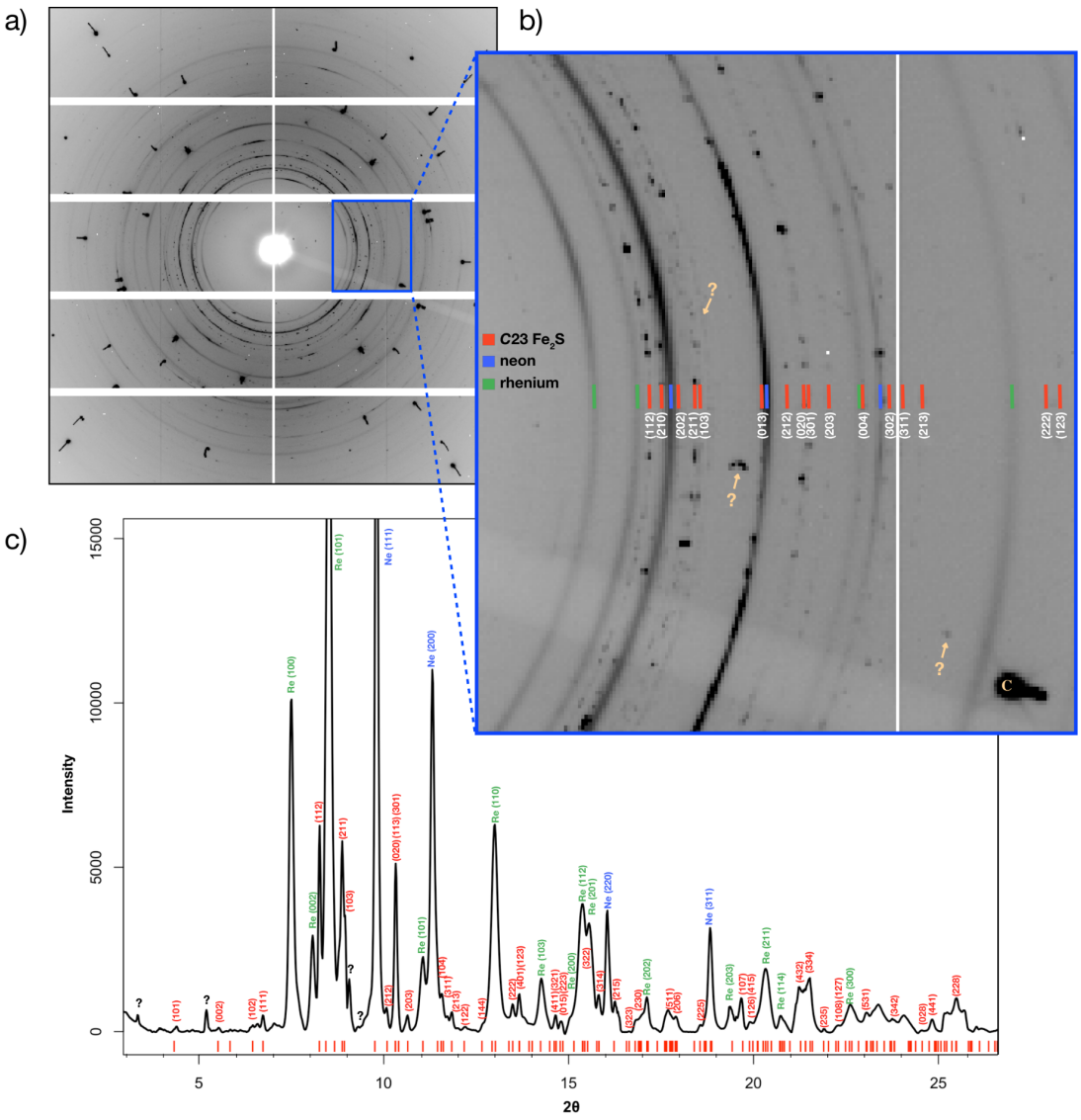

Figure 3.3. a) Raw X-ray diffraction pattern at 89(2) GPa produced by combining the images collected across ±30º rotation in 0.5º steps with 4 s exposure per image. b) Zoomed-in portion of the raw diffraction images. Red tick marks indicate the diffraction angles of *C*23 Fe_2S and the respective Miller Indices labeled. Diffraction angles associated with neon (blue) and rhenium (green) are also labeled and rings or spots that were not indexed to these phases are labeled with a question mark (?). The high intensity spot, labeled with a "C," is a diamond reflection. c) Integrated X-ray diffraction pattern with the calculated d-spacings based on the *C*23 Fe_2S analyses shown as the red tick marks below the pattern. Selected higher intensity Fe_2S peaks are labeled with their corresponding Miller indices. Peaks associated with Re and Ne are labeled in green and blue respectively. Unknown peaks are labeled with a question mark. Scattering from diamond has been masked out of the integrated pattern. The Miller indices, intensities, d-spacings, 2Θ values and Q values calculated for *C*23 Fe_2S are given in supplementary file SF3b.

agreement with *ab-initio* calculations on Fe_2S (Bazhanova et al. 2017) and set a framework for future structural exploration of Fe_2S.

To further underscore the importance of investigating Fe_2S at conditions relevant to Earth's core, this work demonstrates the cocrystallization of hcp-Fe with *C*23 Fe_2S at 90 GPa and 2400 K (Figure 3.2). *C*23 Fe_2S is, therefore, the stable sulfide in Fe-rich compositions at these *P-T* conditions, in contrast to previous interpretations of Fe_2S coexisting with Fe at high temperatures only above 250 GPa (Ozawa et al. 2013; Tateno et al. 2019). While the focus of this study was not on the Fe-S phase relations, observations of Fe_2S and Fe crystallizing at high pressures and temperatures necessitates consideration of Fe_2S in the Fe-rich thermodynamics occurring in Earth's core.

This work marks the first characterization of the lattice geometry and atomic fractional coordinates of Fe_2S based on data collected at high pressures and quenched from high temperatures. Synthesis of Fe_2S with increasing pressure and temperature will provide key insight into the material properties of Fe-rich sulfides in Earth's core and, based on the current results, single-crystal X-ray diffraction is an effective technique for probing the iron-sulfide phases that stabilize at these extreme conditions.

4. Pressure-induced *C*23–*C*37 transition and compression behavior of orthorhombic Fe_2S to Earth's core pressures and high temperatures

Collaborators: Barbara Lavina[b,c], Nigel M. Brauser[a], Anne H. Davis[a], Stella Chariton[c], Sergey Tkachev[c], Eran Greenberg[c†], Vitali Prakapenka[c], Andrew J. Campbell[a]

[a]University of Chicago, Department of the Geophysical Sciences, 5734 S Ellis Ave, Chicago, IL 60637, USA
[b]X-ray Science Division, Advanced Photon Source, Argonne National Laboratory, Argonne, IL 60439, USA
[c]Center for Advanced Radiation Sources, 9700 South Cass Avenue, Building 434A, Argonne, IL 60439, USA
[†]Now at Applied Physics Department, Soreq Nuclear Research Center (NRC), Yavne 81800, Israel

4.1. Introduction

As Fe_2S is observed coexisting with Fe on the liquidus at pressures related to Earth's outer core, investigating its material properties has become the focus of recent investigations (Tateno et al. 2019; Zurkowski et al. in press, Chapter 3). Tateno et al. 2019 measured the volume of Fe_2S between 190 and 306 GPa and determined that its unit-cell parameters and diffraction angles are compatible with an orthorhombic unit-cell with space group *Pnma.* In particular, the *c*/*a* ratio measured for Fe_2S is similar to that of the Co_2Si structure type (*C*37, *Pnma*, *Z*=4) (Geller and Wolontis, 1955) (Figure 4.1). The recent crystallographic analyses of Fe_2S synthesized at ~90 GPa and 2400 K established that Fe_2S assumes a *C*23 structure at these conditions (Co_2P-type, *Pnma*, *Z*=4) (Zurkowski et al. in press) (Figure 4.1). The *C*23 and *C*37 structure types are routinely compared on the basis of their differing relative unit cells and coordination environments (e.g., Rundqvist 1960; Shoemaker and Shoemaker, 1965; Rundqvist and Nawapong, 1966; Jeitschko and Altymeyer, 1990; Nakajima et al. 2020). The *C*23 and *C*37 structures have the same site symmetries, space group and formula units per cell, but the *C*37

structure is distinct from the *C*23 structure based on its relatively larger *b* and *c* axes and shorter *a* axis (Figure 4.1). The *C*23 structure is composed of MX_4 tetrahedra and MX_5 square pyramids while the *C*37 structure is composed of MX_5 dipyramids and MX_5 square pyramids (Figure 4.1). The additional *M*–*X* bond in the *C*37 MX_5 dipyramid compared to the *C*23 MX_4 tetrahedra is oriented along the *a* direction. The *C*37 structure can therefore be seen as a distortion of the *C*23 structure: the *C*37 structure forms from the *C*23 structure by shortening the *a* axis and lengthening the *b* and *c* axes, resulting in a 4- to 5-fold coordination change with the next nearest *X* site along the *a* direction.

A *C*23–*C*37 pressure-induced transition has recently been reported in Fe_2P around 42 GPa (Nakajima et al. 2020), suggesting that pressure plays a role in shaping the Co_2P structure type into the Co_2Si structure type. As the Fe-P system has been shown to be a low-pressure analog to the Fe-S system (e.g., Gu et al. 2016), a pressure-induced *C*23–*C*37 transition may likewise occur in Fe_2S at higher pressures, as is suggested by the observations of *C*23 Fe_2S at 90 GPa (Zurkowski et al. in press) and a *C*37-like Fe_2S cell above 190 GPa (Tateno et al. 2019).

This work investigates the compression behavior of orthorhombic Fe_2S using powder and multigrain X-ray diffraction techniques between 29 and 194 GPa and to 2500 K. A *C*23-like Fe_2S phase is observed between 30 and 120 GPa and at high temperatures. Between 120 and 150 GPa, a softening of the *a* axis and relative stiffening of the *b* and *c* axes is measured, and, above 150 GPa, a *C*37-like unit-cell of Fe_2S is observed. A sharp *C*23–*C*37 transition is not observed; instead, the *C*23 Fe_2S unit-cell evolves towards a *C*37 structure with pressure and this behavior intensifies in the 120–150 GPa pressure range, likely as a result of the onset of a 4- to 5-fold coordination change on the FeS_4 tetrahedral sites. Fe_2S is observed in this study to coexist with

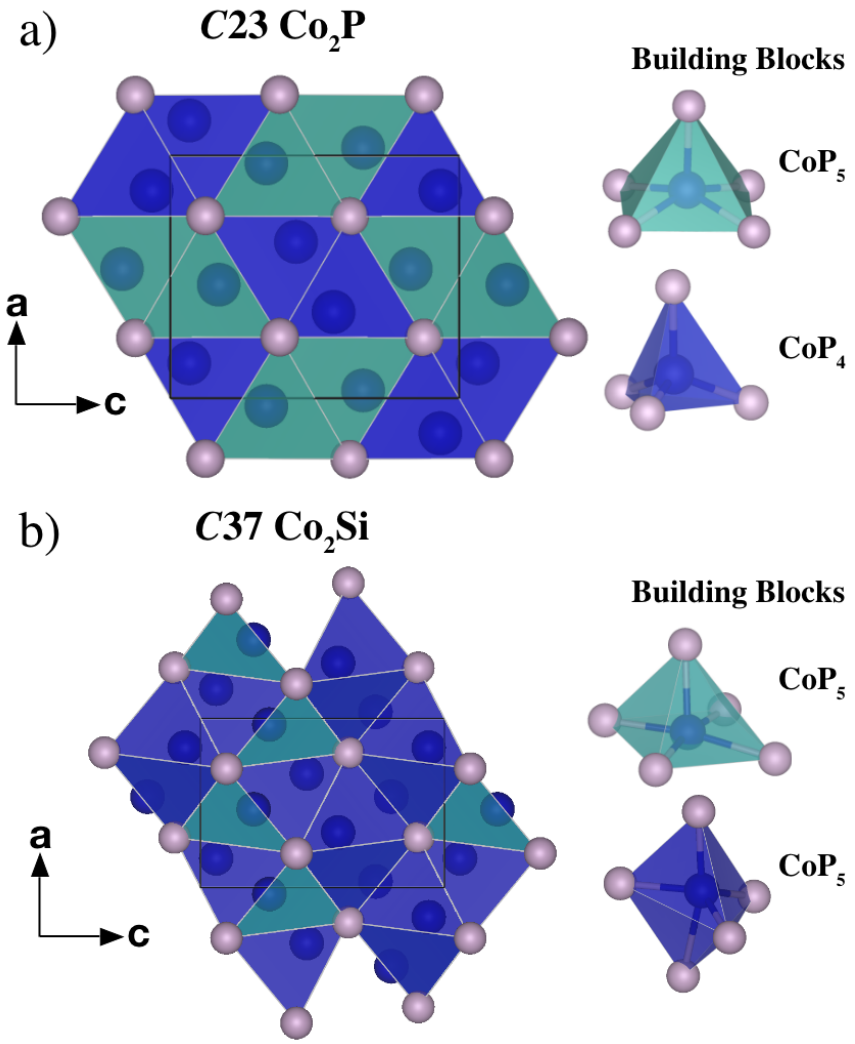

Figure 4.1. Comparison between the a) C23, Co_2P-type and b) C37, Co_2Si type structures (Geller and Wolontis, 1955; Rundvist, 1960) that are inferred in this Fe_2S study. The C23 structure is composed of CoP_5 square pyramid (green) and CoP_4 tetrahedral (blue) building blocks. The C37 structure is composed of CoP_5 square pyramid (green) and CoP_5 dipyramid (blue) building blocks.

hcp-Fe, and, as the *C*23–*C*37 Fe_2S transition occurs around core-mantle boundary pressures and high temperatures, this transition in Fe_2S is important to consider in the context of Earth's core chemistry and dynamics. A thermal equation of state (EoS) is presented for *C*23 Fe_2S to 120 GPa and a volume reduction is applied to characterize the *P-V-T* behavior of *C*37 Fe_2S above 150

GPa. Comparing the calculated density of *C*37 Fe_2S with that of hcp-Fe (Dewaele et al. 2006) and the seismologically determined densities at CMB and ICB conditions (Dziewonski and Anderson, 1981; Irving et al. 2018), the sulfur content of a purely Fe-S core is presented.

4.2. Materials and methods

In this study, Fe_2S was observed in experiments on Fe-rich Fe-S and also Fe-S-O compositions. Previous single crystal analyses of Fe_2S at 90 GPa and 2400 K (Zurkowski et al. in press) indicate that Fe_2S forms in an oxygen-free system with all sites occupied by sulfur. Observations of Fe_2S in FeO saturated compositions are therefore included in this study, as differences in measured Fe_2S volumes are not discernible between the Fe-S and Fe-S-O compositions. Starting powders for these experiments consisted of Fe (99.9+%, <10μm, Alfa Aesar), iron sulfide (FeS, 99.99%, Alfa Aesar) and iron oxide (FeO, 99.5%, Alfa Aesar) powders. Two Fe-FeS compositions were weighed: Fe–12.5S, Fe–23S (dashed notation indicates wt%). The Fe-FeS compositions were homogenized in a mortar and pestle for 1 hour in alcohol, dried and then mixed dry for a short duration to reset any density settling during alcohol evaporation. Fe-S-O mixtures were homogenized in alcohol in a ball mill for 1.5–3 hours at 20 Hz, dried and then ball milled dry for a short duration to reset any density segregation. The final Fe-S-O starting compositions were measured by SEM: Fe–13S–5O, Fe–17S–5O, Fe–6S–12O, Fe–3O–7S, and Fe– 4O–8S.

Sample foils were loaded into rhenium gaskets preindented to 28-40 GPa with 120–25 μm diameter sample chambers. Samples were loaded in KCl, KBr, NaCl, SiO_2, or Ne pressure media

and were dried at 100ºC for 30 minutes prior to gas loading or pressurization. Type I diamonds and tungsten carbide or cBN seats or Boehler-Almax diamonds with conical seats were used with symmetric or BX-90 type (Kantor et al. 2012) cells. The culet sizes ranged from 300–50 μm.

Angle-dispersive X-ray diffraction experiments were conducted with *in-situ* laser heating, as described in Section 2.4, at Argonne National Laboratory, Sector 13 ID-D (GSECARS) of the Advanced Photon Source. The experimental procedure for *in situ* laser heating and XRD collection conducted in the experiments in this chapter follows that described in Section 2.41. Upon quenching from high temperatures samples loaded in wide opening cells were probed using single crystal X-ray diffraction techniques as described in Section 2.4.2.

Powder diffraction data were integrated using Dioptas (Prescher and Prakapenka, 2015). Peaks were fitted using Fityk (Wojdyr, 2010) and lattice parameters from each measurement were obtained on the basis of an orthorhombic Fe_2S cell. For runs where rotational scans were performed, data from individual grains of Fe_2S were indexed using CrysAlisPro (Rigaku OD, 2018). Further details on the powder and single crystal data processing methods used can be found in Section 2.5.

4.3. Results

Between 30 and 194 GPa and upon heating to subsolidus temperatures, in all compositions examined, hcp-Fe (and FeO, if oxygen was present) was observed in the diffraction patterns coexisting with a set of diffraction angles that cannot be accounted for by the tetragonal Fe_3S phase that is reported to be stable at higher temperatures in this pressure range (e.g., Ozawa

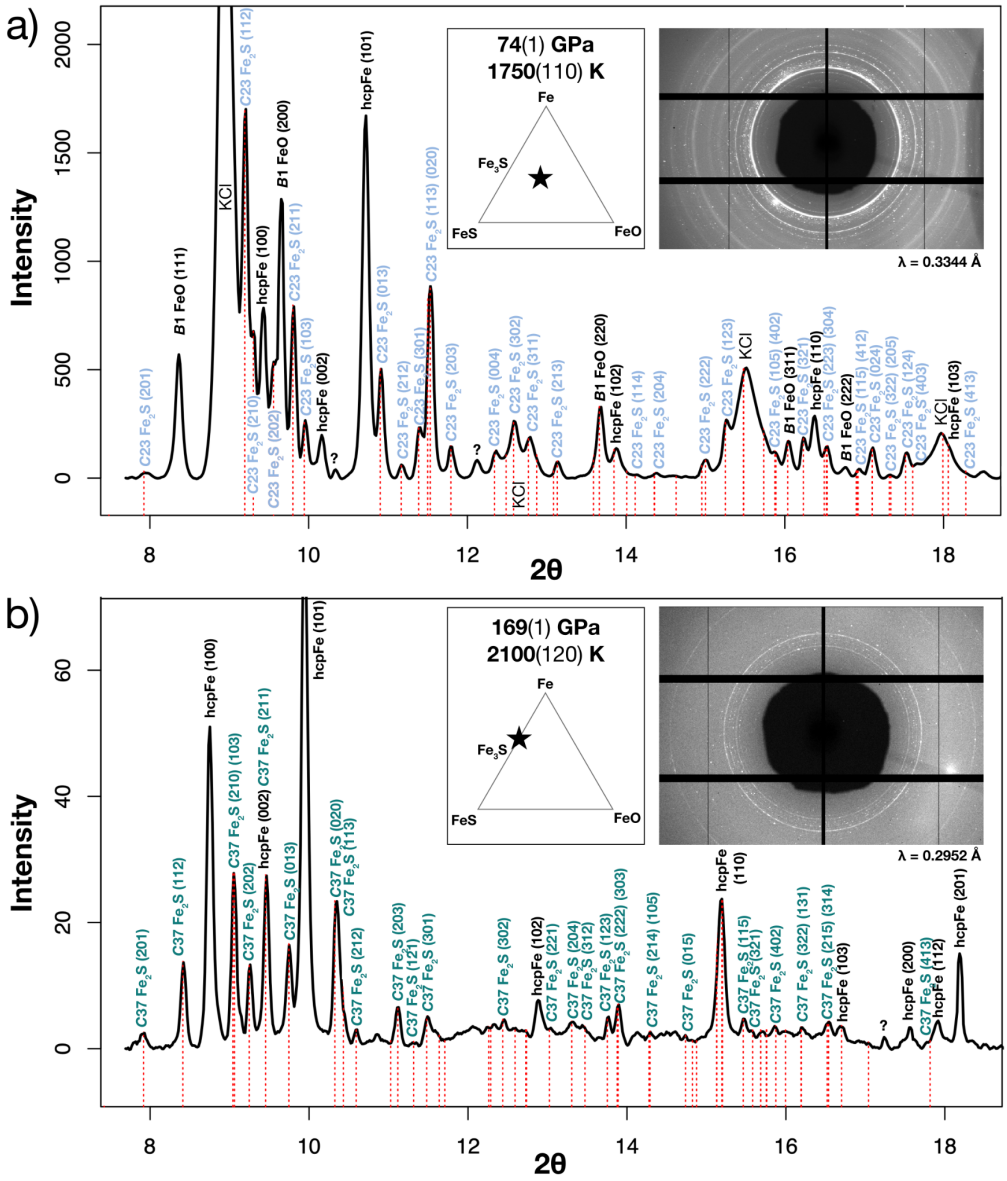

Figure 4.2. Integrated X-ray diffraction patterns exemplifying the observations of Fe_2S at high *P-T*. a) At 74(1) GPa and 1750(110) K, Fe_2S is observed coexisting with hcp-Fe and *B*1 FeO in a KCl medium. The Fe–12S–5O (wt%) starting composition is shown by the star in the ternary. The calculated diffraction angles based on this fit are plotted as the red dashed vertical lines, and prominent peaks of *C*23 Fe_2S are labeled with their corresponding Miller indices in light blue. Two low intensity unidentified peaks are marked by the question mark (?) and may represent the initial peaks of the higher temperature Fe_3S phase. b) At 169(1) GPa and 2100(120) K, Fe_2S is observed coexisting with hcp-Fe in a SiO_2 pressure medium. The starting composition is Fe–12.5S (wt%) and given by the star in the ternary. The calculated *C*37 Fe_2S diffraction angles are plotted as the red dashed vertical lines and prominent peaks of *C*37 Fe_2S are labeled with their

Figure 4.2. ***continued***
corresponding Miller indices in emerald green. One unidentified peak at around 17.5º 2Θ is distinguishable from the background and marked by the question mark.

et al. 2013; Seagle et al. 2006; Thompson et al. 2020) (Figure 4.2). The peaks were instead indexed to an orthorhombic lattice with a volume equal to 4 formula units of Fe_2S. As shown in the example provided in Figure 4.2a, the diffraction angles measured for Fe_2S at 74(1) GPa and 1750(110) K fit to an orthorhombic unit-cell with parameters: a = 5.253(2)Å, b = 3.328(2) Å, and c = 6.222(3) Å. This cell is compatible with that reported for $C23$ Fe_2S at 90 GPa (Zurkowski et al. in press). In contrast, at 169(1) GPa and 2100(120) K (Figure 4.2b), Fe_2S is observed with unit cell parameters: a = 4.561(3) Å, b = 3.281(3) Å, and c = 6.145(5) Å, in agreement with the $C37$-like Fe_2S unit-cell geometry reported by Tateno et al. 2019 at ~190 GPa.

The high temperature observations of Fe_2S in P-T space are shown in Figure 4.3. The light blue data points indicate the stability of a $C23$-like Fe_2S, including the data from Zurkowski et al. *in press*, and the emerald green data points indicate the stability of $C37$ Fe_2S, including the data from Tateno et al. 2019. The split blue-green data points represent the region where the measured Fe_2S unit-cell is transitional between the $C23$ and $C37$ structures. The observed $C23$ and $C37$ unit cells suggest that the structural evolution of Fe_2S is more sensitive to pressure than temperature (Figure 4.3).

The $C23$, transitional, and $C37$ Fe_2S phase fields plotted in Figure 4.3 were determined based on the evolution of the measured unit cell parameters with pressure (Figure 4.4, including the data by Zurkowski et al. *in press,* and Tateno et al. 2019). Between 29 and 306 GPa, Fe_2S exhibits pronounced anisotropic compression, wherein the a axis is more compressible than the b

and *c* axes (Figure 4.4a). A more rapid softening of the *a* axis and relative stiffening of the *b* and *c* axes is observed above ~120 GPa, indicating a change in compressibility of the structure. Stiffening of the *a* axis and softening of the *b* and *c* axis is further observed above ~150 GPa, marking another structural change in Fe_2S (Figure 4.4a). The Fe_2S unit-cell geometries reported by Zurkowski et al. *in press* and Tateno et al. 2019 support the trend observed in Figure 4.4a; namely a *C*23 Fe_2S cell between 30 and ~120 GPa and a *C*37 Fe_2S unit cell above ~150 GPa. Between these pressures, the unit cell geometry is transitional between these two relative unit cells.

The compressional behavior of Fe_2S can also be viewed in terms of the *c*/*a* ratio trend and systematically compared to the *c*/*a* ratio of the Co_2P and Co_2Si structure types (Figure 4.4b). The relative unit cells of M_2X and MX_2 structures with these site symmetries have been routinely compared and grouped into Co_2P- and Co_2Si-branches of the $PbCl_2$ family in previous studies (e.g., Rundqvist 1960; Shoemaker and Shoemaker, 1965; Rundqvist and Nawapong, 1966; Jeitschko and Altymeyer, 1990; Nakajima et al. 2020). At ambient conditions, Co_2P and Co_2Si have *c*/*a* ratios of 1.19 and 1.44 respectively (dashed horizontal lines in Figure 4b), and here we take these values as characteristic of their two structure types, and associated with the difference in their cation coordinations. Up to 112 GPa, the Fe_2S *c/a* ratio shows a nearly linear trend increasing from around 1.14 at 29 GPa to 1.22 at 112 GPa, similar to that of the *C*23 structure (Figure 4.4b). Between 159 GPa and 306 GPa, the Fe_2S *c*/*a* ratios show an approximately linearly increasing trend with *c*/*a* ratios ranging from 1.34–1.40, more like that of the *C*37 structure type (Figure 4.4b). In the intermediary pressure range, the data trend along an S-shaped curve joining the <120 GPa and >150 GPa values, revealing a transitional pressure range where

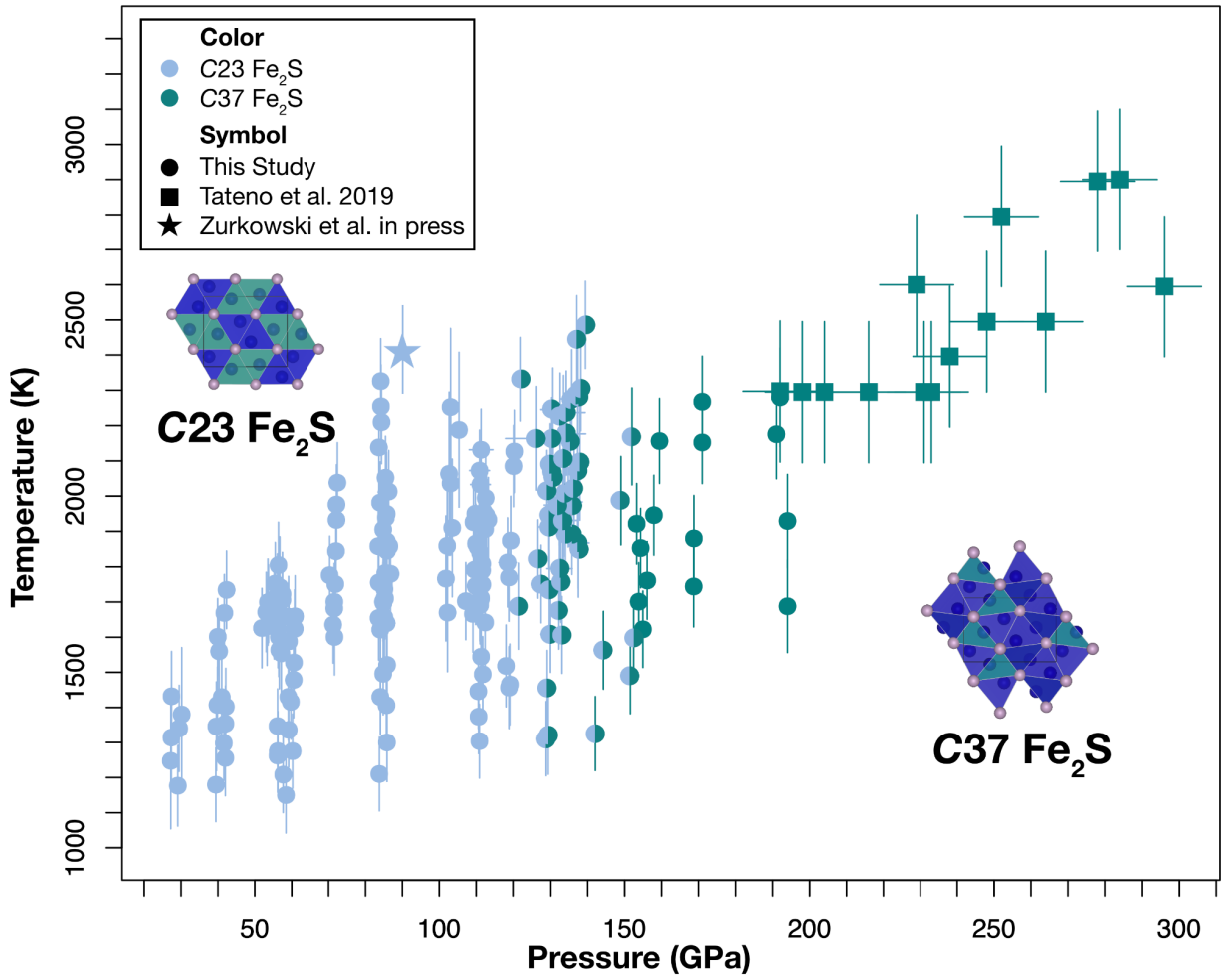

Figure 4.3. The phase stability of *C*23 and *C*37 Fe_2S in pressure-temperature space. The blue circles indicate observations of a *C*23-like unit cell of Fe_2S in this study. The blue star at 89 GPa and 2380 K refers to the single crystal study by Zurkowski et al. *in press* in which the structure of Fe_2S was determined to be *C*23 after temperature quenching from these conditions. The emerald circles represent observations of a *C*37-like unit cell of Fe_2S in this study. The emerald squares refer to the Tateno et al. 2019 study, where a *C*37 Fe_2S unit cell was measured above 190 GPa. The split blue/green data between 110 and 150 GPa indicate the observations of a transitional *C*23–*C*37 Fe_2S unit-cell.

Fe_2S is more rapidly evolving from a *C*23- to a *C*37-like unit cell. The inflection point in this trend occurs around 142 GPa, marking the cut-off pressure between the *C*23 and *C*37 structures of Fe_2S in this transitional pressure range (Figure 4.4).

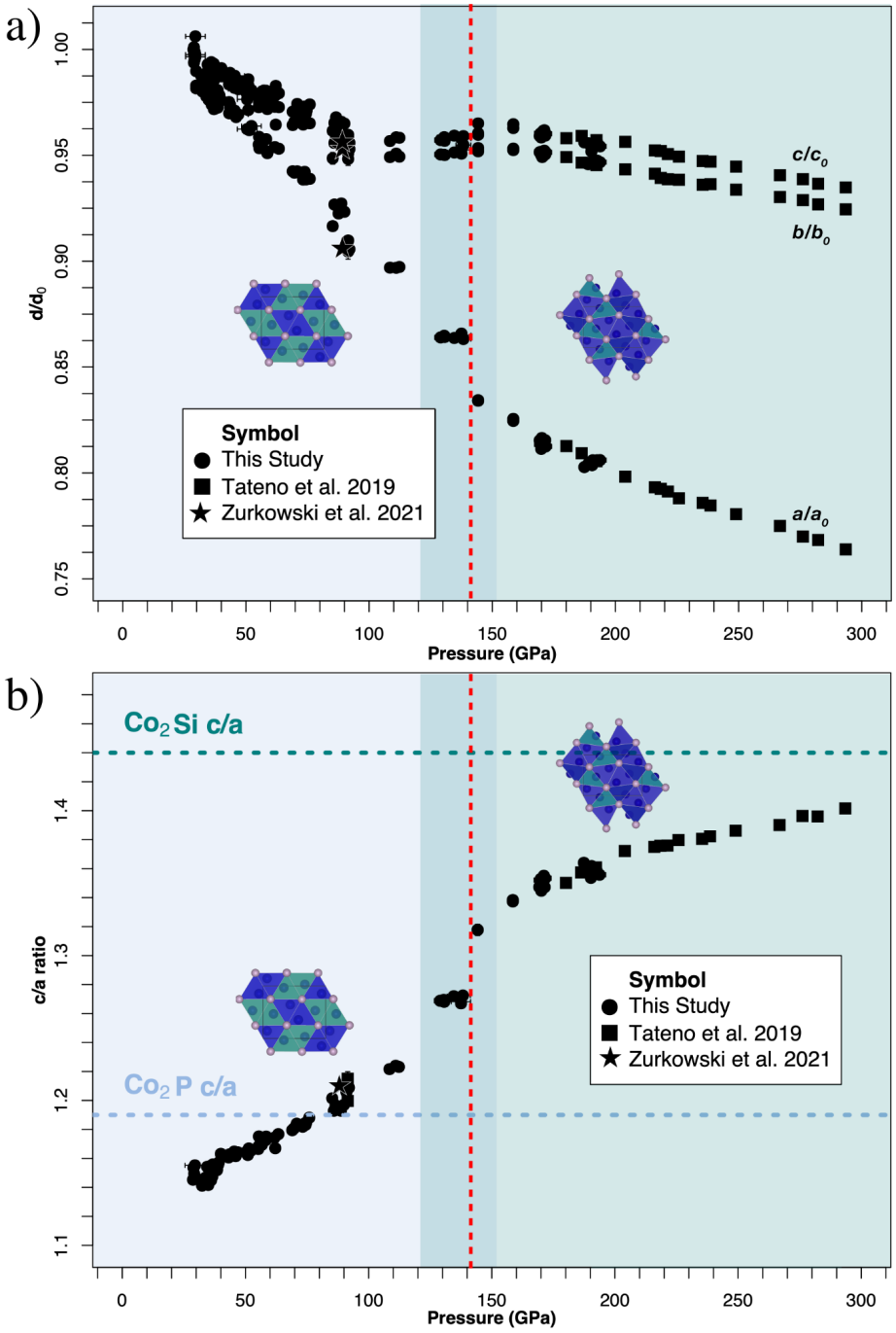

Figure 4.4. a) Relative lattice parameters measured for Fe_2S in this study (circles) along with the data reported by Tateno et al. 2019 (squares) and Zurkowski et al. in press (stars). The shaded regions encompass the data that is more compatible with a Co_2P-like unit-cell (light blue shading) and data more compatible with a Co_2Si-like unit-cell (green shading). The shaded regions overlap where the relative lattice parameters measured along the *a* axis soften as the *b* and *c* axes stiffen between ~110-150 GPa, indicating a potential transitional pressure range between these two structure types. The red, vertical dashed line represents this *C*23–*C*37 cut-off. b) *C/a* ratio measured for Fe_2S in this study (circles) along with the data

Figure 4.4. ***continued***
reported by Tateno et al. 2019 (squares) and Zurkowski et al. *in press* (star). The horizontal dashed lines indicate the c/a ratio determined for Co_2P (light blue) (Rundqvist, 1960) and Co_2Si (emerald green) (Geller and Wolontis, 1955). The shaded regions encompass the data that is more compatible with a Co_2P-like *c/a* ratio (light blue shading) and data more compatible with a Co_2Si-like *c/a* ratio (green shading). As the c/a ratios measured evolve smoothly from Co_2P-like to Co_2Si-like, the shaded regions overlap in the potentially transitional pressure range. The inflection point in this S-shaped *c*/*a* ratio trend occurs around 142 GPa, differentiating the more *C*23-like and *C*37-like unit-cells of Fe_2S. The red, vertical dashed line represents this *C*23–*C*37 cut-off.

The measured volumes of Fe_2S between 29 and 194 GPa are plotted in Figure 4.6 along with the Fe_2S volumes reported by Zurkowski et al. *in press* and Tateno et al. 2019. As Fe_2S is observed to undergo a change in compressibility above 120 GPa and again above 150 GPa (Figure 4.4), a thermal equation of state was fit only to the *C*23 Fe_2S volumes measured below the first compressibility change (<120 GPa, Figure 4.4). The *C*23 Fe_2S *P*-*V* data were fitted to a Mie-Grüneisen EoS given in Equation 4.1. The $P_{300}(V)$ term in Equation 4.1 (expanded in Equation 4.2) is a third-order Birch-Murnaghan EoS (Birch, 1952) fit to the room temperature *P*-*V* data via the isothermal bulk modulus, K_0; pressure derivative, K'; and zero-pressure volume, V_0. High temperature data were fitted using the Grüneisen parameter (γ, Equation 4.3) and the Debye model of vibrational energy relating thermal energy *E* with γ and Debye temperature (θ_D, Equation 4.4). To decrease the number of fitted parameters, anharmonic and electronic contributions to thermal pressure were not included, and the one bar Grüneisen parameter, γ_0, was fit to our high temperature data with θ_0 and q fixed to 400 K and 1, respectively.

$$P(V, T) = P_{300}(V) + (\gamma/V)[E(\theta_D, T) - E_{300}(\theta_D, 300)] \quad 4.1$$

$$P_{300}(V) = 3K_0 f(1 + 2f)^{2.5} * (1 + 1.5(K' - 4)f), f = 0.5 * ((V/V_0)^{(-2/3)} - 1) \quad 4.2$$

$$\gamma = \gamma_0 (V/V_0)^q \quad 4.3$$

$$\theta_D = \theta_0 ex[\gamma_0(1 - (V/V_0)^q/q] \quad 4.4$$

The *C*23 Fe_2S equation of state was fitted with $V0$ = 20.6(3) cm3/mol, $K0$ = 138(22) GPa, K' = 5.6(7), and γ_0 = 2.59(8). The covariance in the EoS parameters are plotted in Figure 4.5. The room temperature, 1000 K, 2000 K and 3000 K isotherms calculated from this EoS fit are plotted in Figure 4.6. Pressure residuals for the *C*23 Fe_2S data (<120 GPa) show a root mean square value of ~1.5 GPa (Figure 4.6b). The pressure residuals for the Fe_2S measurements in the 120–194 GPa range (triangles, Figure 4.6) and those reported by Tateno et al. 2019 were calculated based on the EoS and plotted in Figure 4.6b. These data are not well described by the *C*23 Fe_2S equation of state, supporting the observed structural changes in Fe_2S above 120 GPa.

As *C*37 Fe_2S is only observed above 150 GPa, the low-pressure data necessary for adequately describing its EoS parameters are lacking. To characterize the *P-V-T* behavior of *C*37 Fe_2S, we assume here that its compressional and thermal behavior are identical to the *C*23 phase, with only a different volume V_0. The volume residuals observed for *C*37 Fe_2S above 150 GPa show an average 1.6% decrease in volume compared to the *C*23 Fe_2S EoS (Figure 4.7). As the *C*23 and *C*37 structure types are closely related and low pressure (<150 GPa) data for *C*37 Fe_2S is not available, a *C*37 Fe_2S EoS was constructed by applying this volume change to the *C*23 Fe_2S equation of state, while keeping the K_0, K', and γ_0 parameters fixed. The resulting modified equation of state is plotted with the *C*37 data (>150 GPa) in Figure 4.8. The 120–150 GPa pressure range was not included in this volume change calculation, as a phase transition is likely

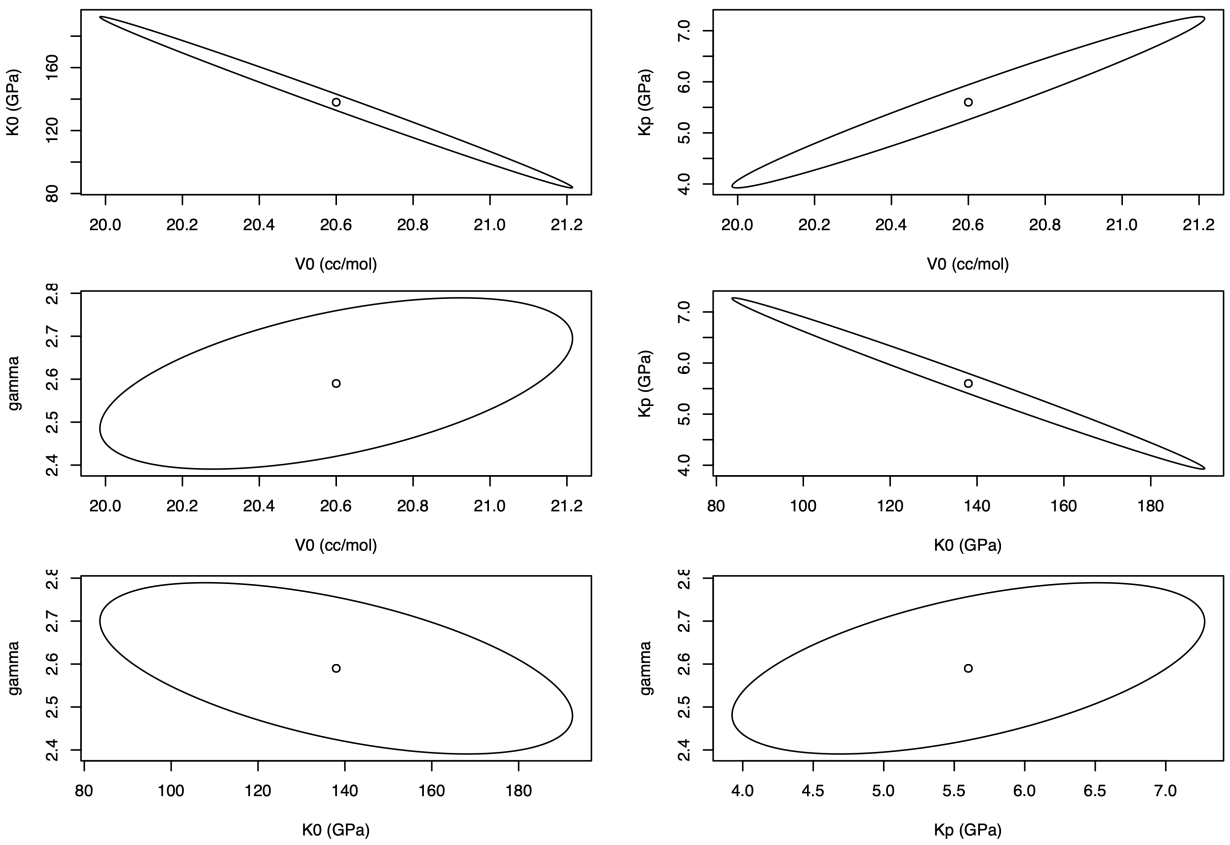

Figure 4.5. Covariance ellipses showing the relationships between the *C*23 Fe_2S EoS parameters fit in the current study.

occurring. Future decompression work on *C*37 Fe_2S to lower pressures is necessary to more accurately characterize its *P-V-T* relationship.

The 300 K *C*37 Fe_2S data reported in the Tateno et al. 2019 study show anomalously high volumes compared to the high temperature *C*37 Fe_2S volumes measured in this study (Figure 4.6). In the Tateno et al. 2019 study, Fe_2S was synthesized at high pressures and temperatures, quenched, and decompressed at 300 K in an MgO pressure medium, a significantly harder medium compared to Ne, KCl or NaCl mediums used to collect the room temperature data reported in this study. The greater room temperature Fe_2S volumes measured in the Tateno et al.

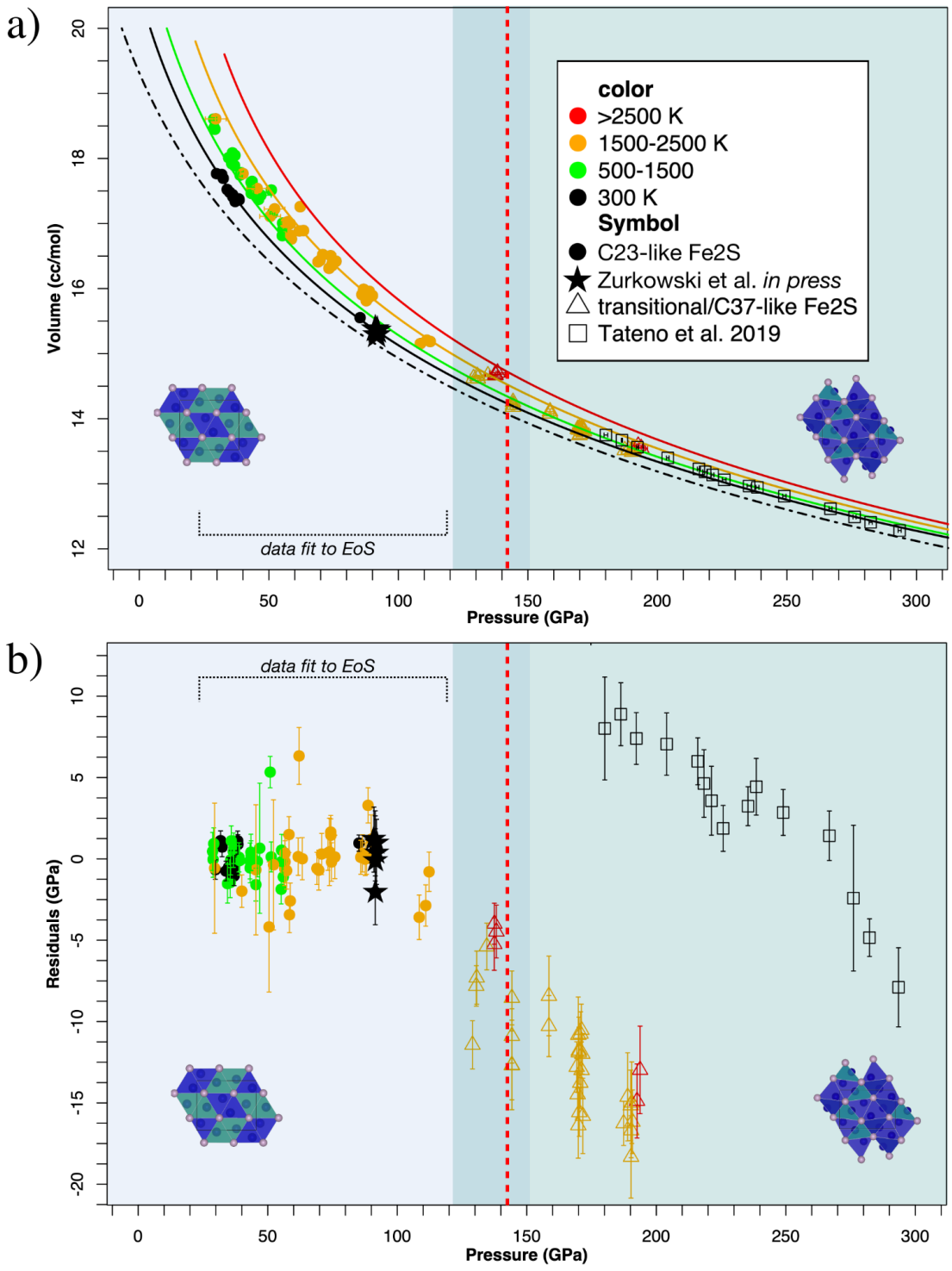

Figure 4.6. a) *P-V* data for Fe_2S (color coded for temperature) collected in this study (circles, triangles), Zurkowski et al. in press (stars), and Tateno et al. 2019 (squares). The 300 K (black), 1000 K (green), 2000 K (orange) and 3000 K (red) isotherms (solid lines) were calculated based on the thermal EoS fit to *C*23 Fe_2S data collected up to 120 GPa in this study and the study by

Figure 4.6. ***continued***
Zurkowski et al. in press (~90 GPa, stars). The dashed line, labeled "data fit to EoS," brackets the Fe_2S volumes included in the EoS fit. For comparison, the Bazhanova et al. 2017 calculated 300 K EoS for *Pnma* Fe_2S (dashed-dot line) is included. The shaded regions represent the pressure ranges where *C*23-like (light blue), transitional (blue green), and *C*37-like (light green) Fe_2S structures are observed. The red vertical dashed line represents this *C*23–*C*37 cut-off determined in Figure 4.4 b) Residuals to the EoS fit are plotted with an r.m.s. of ~1.5 for the fitted *C*23 Fe_2S data (<120 GPa) (filled circles). The plotted open triangles depict the difference in pressure calculated from this EoS versus measured pressure for the Fe_2S data in the transitional and *C*37 Fe_2S pressure range. The black squares show the same comparison for the data reported by Tateno et al. 2019.

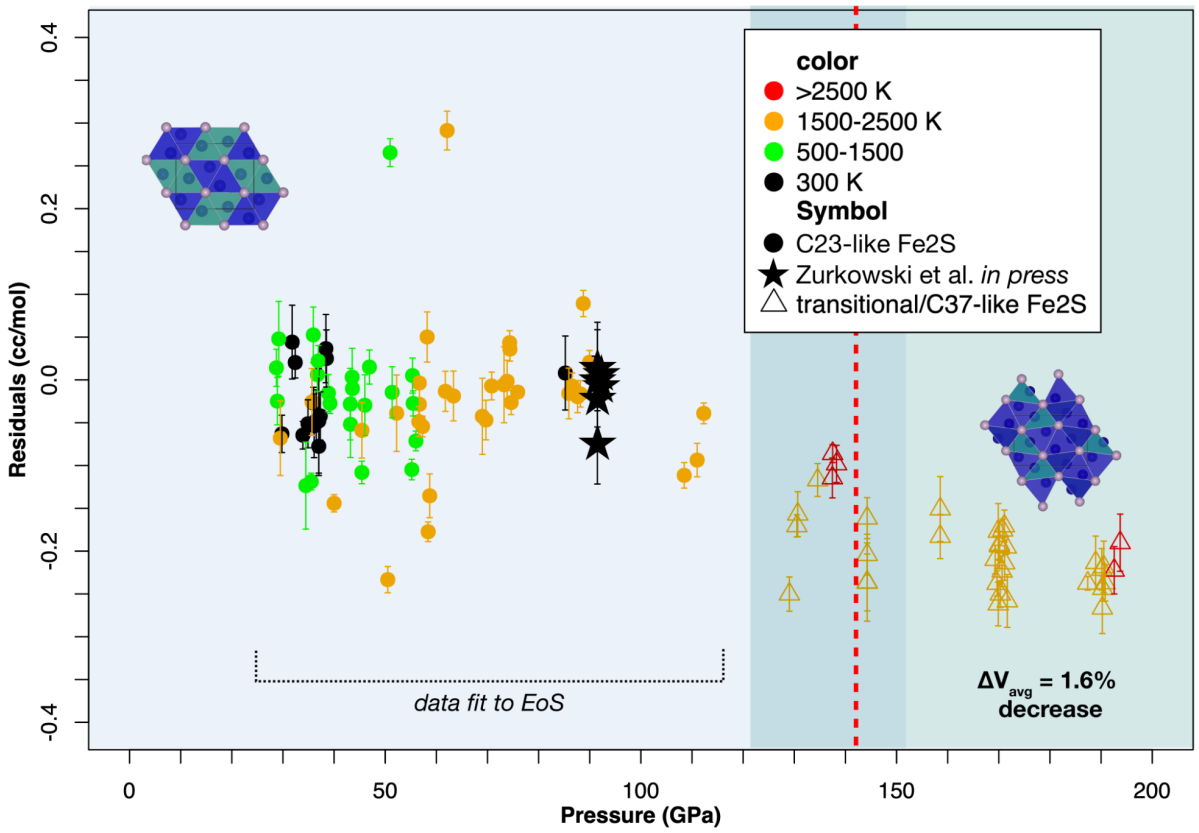

Figure 4.7. Volume residuals to the EoS fitted to *C*23 Fe_2S (<120 GPa, light blue shaded region, filled circles). The plotted open triangles represent the difference in volume calculated from this EoS versus measured volume for the Fe_2S data in the transitional (120-150 GPa, blue-green shading) and *C*37 Fe_2S (>150 GPa, light green shading) pressure range. A 1.6% decrease in volume is observed for the *C*37 Fe_2S (>150 GPa) data. The red dashed vertical line was determined in Figure 4.4to be the *C*23-*C*37 cut off.

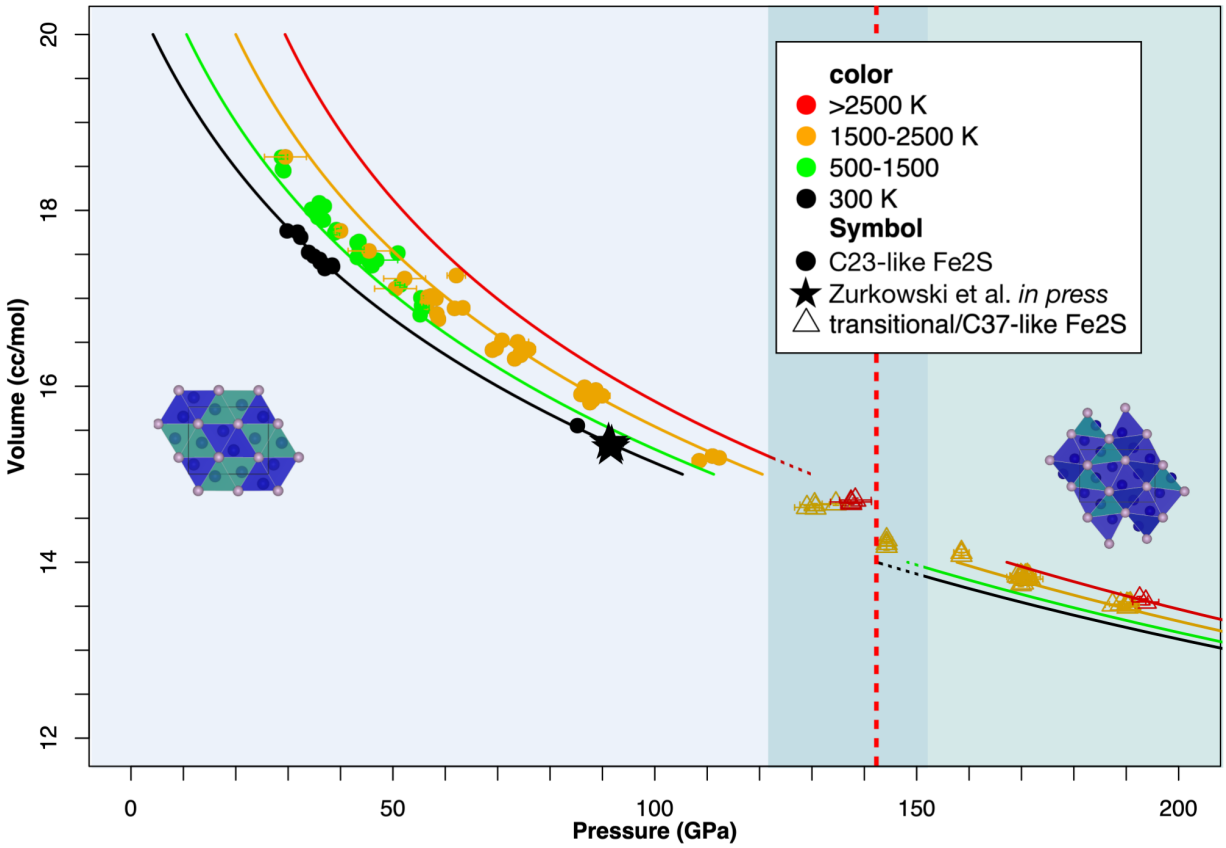

Figure 4.8. *P-V* data collected on *C*23 Fe_2S (<120 GPa, light blue shaded region), *C*37 Fe_2S (>150 GPa, green shaded region) and the transitional cell (120-150 GPa, blue-green shaded region) in this study up to 194 GPa and to 2500 K. The equation of state fit to the *C*23 Fe_2S data is plotted up to 120 GPa and is color coded for temperature. The *C*37 Fe_2S volume residuals for this equation of state show an average 1.6% volume reduction in Fe_2S above 150 GPa. This volume reduction was applied to the *C*23 Fe_2S equation of state, keeping K_0, K', and γ_0 fixed, and plotted above 150 GPa. The overlap in the *C*23 (blue) and *C*37 (green) shaded regions in the 120-150 GPa pressure range indicates the pressure range where *C*23-like Fe_2S transitions to the *C*37-like structure. This pressure range was not included in the volume reduction calculation. The red, vertical dashed line represents the *C*23–*C*37 cut-off determined in Figure 4.

2019 study may be a consequence of the more nonhydrostatic aspect of the ceramic medium compared to alkali halide and noble gas media.

4.4. Discussion

A pressure-induced *C*23–*C*37 transition, analogous to the current study, has been reported previously in other M_2X compounds including PbF_2 at 10 GPa and Fe_2P at 42 GPa (Haines et al. 1998; Nakajima et al. 2020). These lower pressure studies observe the *C*23–*C*37 M_2X transition to occur over a few GPa, whereas changes in compressibility of Fe_2S bracket a *C*23–*C*37 Fe_2S transition across ~30 GPa pressure range above 120 GPa. The difference in chemistry and the higher transition pressures observed in Fe_2S compared to PbF_2 and Fe_2P may play a role in the difference in behavior across the transition, but further room temperature compression experiments are needed to better characterize the structural changes in these phases during the respective *C*23–*C*37 transitions.

Based on the systematic comparison between the *C*23 and *C*37 structures (Figure 4.1), a highly compressible *a* axis and the onset of bonding between Fe and the next nearest S site along the *a* direction is necessary for a *C*23–*C*37 pressure-induced transition. The unit-cell compression of Fe_2S reported in this study demonstrates this pronounced behavior (Figure 4.4). The high compressibility of the *a* axis in *C*23 Fe_2S shapes the Fe_2S unit cell towards a *C*37-like geometry up to ~120 GPa. Above these pressures, a softening is observed along the *a* axis accompanied by a relative lengthening of the *b* and *c* axes. This may represent the onset of new atomic interactions and a coordination change that is complete above ~150 GPa, where stiffening of the *a* axis and softening of the *b* and *c* axes is observed (Figure 4.4a). The 120–150 GPa pressure range discussed in Figure 4.4, is likely to represent the transitional pressure range where a coordination change occurs to form *C*37 Fe_2S. Examining the *c/a* ratio trend in Fe_2S supports these observations and reveals an inflection point around 142 GPa, where below this pressure,

Fe_2S lattices more compatible with *C*23 structure are observed and, above these pressures, Fe_2S lattices more compatible with *C*37 structure are observed. Further crystallographic analysis is required to better characterize the atomic arrangement of Fe_2S across this transition, but the compression behavior observed in Fe_2S exhibits distinct structural changes in Fe_2S across the 30 to 300 GPa pressure range (This study; Tateno et al. 2019; Zurkowski et al. 2021) .

Interestingly, the *C*23–*C*37 Fe_2S transitional pressure range (120–150 GPa) encompasses core-mantle boundary pressures. As Fe_2S is observed in this study coexisting with hcp-Fe at moderate temperatures, further experimental work is required to understand how the *C*23–*C*37 Fe_2S transition affects the thermodynamics and phase relations in Fe-rich systems at core-mantle boundary conditions. Furthermore, anisotropic compression is also observed in the *C*37-like Fe_2S cell where the *a* axis is more compressible than the *b* and *c* axes (this study, Tateno et al. 2019), and future experiments at higher pressures may reveal further pressure-induced transformations in Fe_2S. The *C*37-like Fe_2S phase is observed in Fe-rich systems on the liquidus at 306 GPa (Tateno et al. 2019), making the structural behavior of this phase relevant to the thermodynamics of solidification at Earth's inner core boundary.

To constrain the possible sulfur contribution to the density of Earth's core, the density profile of Fe_2S was calculated using the *C*37 EoS determined by applying a 1.6% volume decrease to the *C*23 Fe_2S EoS fit in this study and extrapolated throughout the core. As the *C*37 Fe_2S phase is stable at core mantle boundary pressures and high temperatures, the *C*37 Fe_2S density profile extrapolated through the core provides an important addition to previous Fe-sulfide EoS studies (e.g., Fei et al. 2000; Kamada et al. 2014; Seagle et al. 2006; Tateno et al. 2019). The densities of Fe_2S calculated at CMB and ICB conditions were then combined with

that of hcp-Fe (Dewaele et al. 2006) and compared to the seismologically determined CMB density reported by Irving et al. 2018 and the ICB density reported by the PREM model (Dziewonski and Anderson, 1981). Results from the Irving et al. 2018 study of the outer core is used for the CMB density calculations in this study, as this work reported elastic parameters that better predict the observed normal mode frequencies and body wave models for the outer core. A CMB density and pressure of 10.05 g/cm^3 and 135.8 GPa (Irving et al. 2018) and an ICB density and pressure of 12.8 g/cm^3 and 328.9 GPa (Dziewonski and Anderson, 1981) was implemented into our calculations, respectively. An adiabatic temperature profile for the outer core (Birch, 1952), a 1% volume increase from solid to liquid iron alloy (Anderson, 2003), and a CMB temperature set at 4000 ± 500 K (Anderson, 2003) was assumed. The inner core boundary temperature, calculated along the hcp-Fe adiabat, was determined to be 5200 ± 500 K.

Figure 4.9 shows the adiabatic density profiles of *C*37 Fe_2S (this study) (blue) and hcp-Fe (Dewaele et al. 2006) (red), compared to the density profile for the outer core and inner core (Dziewonski and Anderson, 1981; Irving et al. 2018). Comparing these density trends, 13.9 ± 1.5% S is required to match CMB density and 8.6 ± 0.8 wt% S is required to match the ICB density. Previous iron sulfide equations of state studies conclude that 11–16 wt% S is required to match the density deficit at the CMB (e.g., Seagle et al. 2006; Thompson et al. 2016; Thompson et al. 2020) and 6.9 ± 0.9 wt% S is required to match the ICB density deficit (Kamada et al. 2014). Within error, the calculated CMB and ICB sulfur concentrations reported in this study are in good agreement with these previous works.

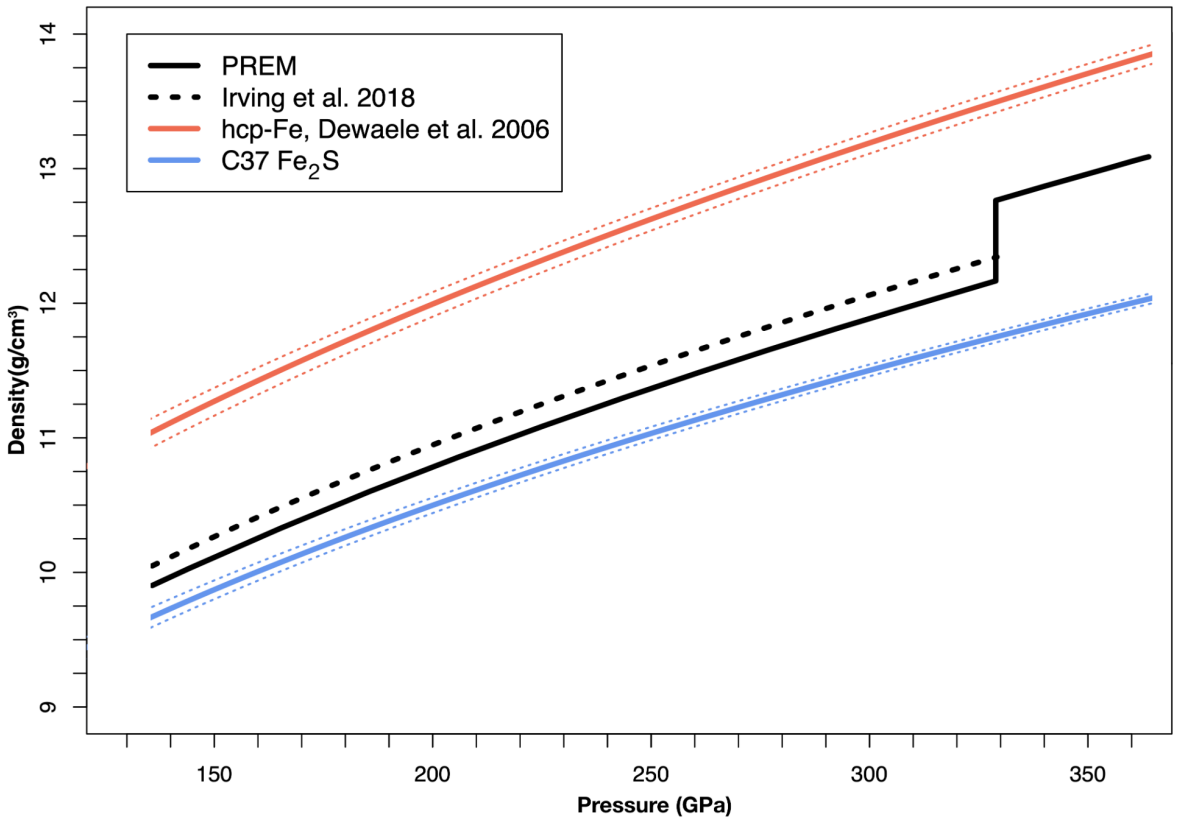

Figure 4.9. Calculated adiabatic density curves for liquid *C*37 Fe_2S (blue) and liquid hcp-Fe (red) (Dewaele et al. 2006) plotted with the density profiles of the outer core based on the PREM model (Dziewonski and Anderson 1981) (solid black line) and Irving et al. 2018 (dashed black line).

From the density extrapolations presented, it is apparent that the curvature of the liquid Fe_2S and Fe and the liquid outer core density profiles do not match, indicating that the density and sound velocities of a purely Fe-S core would not satisfy geophysical constraints. Furthermore, melting studies of the Fe-Fe_3S system report 5.7 ± 0.3 wt% S in the eutectic liquid at 250 GPa, and the eutectic liquid composition is likely more Fe-rich at ICB conditions (Mori et al. 2017; Tateno et al. 2019). Results from this work combined with that of Kamada et al. 2014 predict 6.9–8.6 wt% S to match the density at the inner core boundary, suggesting that the S-content of the core may be on the S-rich side of the Fe-liquidus field (Mori et al. 2017; Tateno et

al. 2019). As crystallization of an Fe-sulfide inner core from an Fe-rich liquid violates the observed density profile and geophysical constraints for the core, sulfur is likely not the sole light-alloying element in Earth's Fe-rich core and other light elements, including O, Si, C and H, may be present.

4.5. Conclusions

The phase stability of orthorhombic Fe_2S was investigated between 29 and 194 GPa and up to 2500 K, and a *C*23–*C*37 Fe_2S phase transition is observed in the 120–150 GPa pressure range. Upon compression to ~120 GPa, a *C*23-like unit cell of Fe_2S is measured, in agreement with previous studies (Zurkowski et al. in press). In this pressure range, the *a* axis compresses significantly more than the *b* and *c* axes. Between 120 and 150 GPa, a softening of the *a* axis and relative stiffening of the *b* and *c* axes is observed, as the orthorhombic Fe_2S cell evolves towards a *C*37-like geometry. Above 150 GPa, the *a* axis stiffens as the *b* and *c* axes soften and a *C*37-like Fe_2S cell is measured, in agreement with the study by Tateno et al. 2019. As a *C*23–*C*37 transition occurs as a result of a relative shortening of the *a* axis and a 4- to 5-fold coordination change, the Fe_2S compression behavior in the 120-150 GPa pressure range, likely indicates the onset of the *C*23–*C*37 transition. This Fe_2S *c/a* ratio trend reveals an inflection point and *C*23–*C*37 cut-off pressure of ~142 GPa. Across the pressure and temperature range examined in this study, Fe_2S is observed coexisting with hcp-Fe, and the *C*23–*C*37 phase transition is observed around core-mantle boundary pressures; making these structures potentially relevant to Earth's core chemistry. As the *C*37 Fe_2S structure is the high *P-T* phase, a *C*37 Fe_2S EoS was determined by applying a 1.6% volume reduction to the fitted *C*23 Fe_2S thermal EoS. Comparing the density

of *C*37 Fe_2S extrapolated through Earth's outer core with that of hcp-Fe (Dewaele et al. 2006) and the seismologically determined density deficit of Earth's core (Irving et al. 2018), 13.9±1.5 wt% and 8.6±0.8 wt% sulfur would be required to match the density at the CMB and ICB respectively. Sulfur likely cannot be the sole light alloying element in Earth's core, due to the sulfur content required to match the core seismological profiles compared to the eutectic melting behavior in the Fe-S system at core pressures. This study supports that Earth's core is likely a multicomponent Fe-rich alloy and characterizes the pressure-induced *C*23–*C*37 Fe_2S transition around core-mantle boundary pressures.

5. Single-crystal synchrotron X-ray diffraction studies of cobalt phosphides as low-pressure analogs of iron sulfides: determination of the novel $Co_{12}P_7$ compound, compression of Co_2P, $Co_{12}P_7$, and CoP to 48 GPa and high temperatures, and a mechanisms for the pressure-induced *C*23–*C*37 transition in M_2X transition metal binary compounds

Collaborators: Barbara Lavina[b, c], Stella Chariton[c], Sergey Tkachev[c], Vitali Prakapenka[c], Andrew J. Campbell[a]

[a]University of Chicago, Department of the Geophysical Sciences, 5734 S Ellis Ave, Chicago, IL 60637, USA
[b]Center for Advanced Radiation Sources, 9700 South Cass Avenue, Building 434A, Argonne, IL 60439, USA
[C] X-ray Science Division, Advanced Photon Source, Argonne National Laboratory, Argonne, IL 60439, USA

Citation: Zurkowski, C., Lavina, B., Chariton, S., Tkachev, S., Prakapenka, V. and Campbell, A. (2020). The novel high-pressure/high-temperature compound $Co_{12}P_7$ determined from synchrotron data. Acta Crystallographica Section E: Crystallographic Communications, 76(10), 1665–1668. https://doi.org/10.1107/S2056989020012657

5.1. Introduction: cobalt phosphides as low pressure iron-sulfur analogs

The ambient pressure thermodynamic properties of cobalt phosphides have been examined extensively (Okamoto and Massalski, 1990; Schlesinger, 2002; Prins and Bussell, 2012; Pramanik et al. 2017; Fujii et al. 1988; Reehuis and Jeitschko, 1989), but limited studies have been conducted on the high pressure-temperature (*P*-*T*) behavior of cobalt phosphides (e.g., Qian et al. 2011; Zurkowski et al. 2020). Notably, phase transitions in Co-rich phases such as Co_2P and CoP tend to precede in pressure the phase relations observed in the Fe-S and Fe-P

systems. Co-phosphides can therefore serve as important low-pressure analogs for the high-pressure behavior of Fe-rich sulfide and phosphide phases relevant to Earth and planetary cores.

Co_2P adopts the orthorhombic, *C*23 structure (*Pnma*, *Z*=4, Co_2P-type) at ambient pressures and temperatures (*P-T*) (Rundqvist 1960) and transforms into a hexagonal *C*22 structure (*P*-62*m*, *Z*=3, Fe_2P-type) (Rundqvist and Jellinek 1959) at high temperatures (Ellner and Mittemeijer 2001). The *C*23 and *C*22 unit cells are depicted in Figure 5.1. A description of the *C*23 structure can be found in Chapters 3 and 4 and the *C*22 structure is composed of the same polyhedral building blocks with columns of corner sharing CoP_4 tetrahedra and columns of edge sharing CoP_5 square pyramids links along edges in the *c* direction (Figure 5.1). Both the *C*23 and *C*22 structures have been identified in Fe_2P at ambient pressures and high temperatures (Britvin et al. 2002, 2017, 2019; Litasov et al. 2020) and Fe_2S above 20 GPa at high temperatures (Koch-Müller et al. 2002; Zurkowski et al. in press; Zurkowski et al. submitted, Chapter 4). The *C*23–*C*22 high temperature phase boundary has not been investigated with pressure in the Co-P, Fe-P or Fe-S systems, despite being potentially relevant to the high temperature conditions of terrestrial planetary cores.

Fe_2S has recently been identified to adopt the Co_2P-type structure (*C*23, *Pnma*, $Z = 4$) between 25 and 120 GPa (Zurkowski et al. in press; Zurkowski et al. submitted, Chapter 4) and exhibits anomalous compression behavior. To 120 GPa, *C*23 Fe_2S expresses a highly compressible *a* axis, and the structure transitions to a *C*37-like unit cell (Co_2Si-type, *Pnma*, $Z = 4$) between 120 and 150 GPa (Zurkowski et al. submitted, Chapter 4). Furthermore, *C*37 Fe_2S is the plausible Fe-rich sulfide at Earth's inner core conditions (Tateno et al. 2019), making the structural properties of the *C*37 structure important to further characterize in relation to core

thermodynamics. A *C*23–*C*37 transition is also observed in Fe_2P at 42 GPa (Nakajima et al. 2020). The *C*23 and *C*37 structures are closely related, as discussed in Chapter 4, but the structural mechanisms and role of pressure in forming the *C*37 atomic arrangement from the *C*23 structure has been speculated upon (Chapter 4) but not resolved crystallographically. Despite Co_2P adopting the *C*23 structure at ambient conditions, making it a good candidate for a single crystal X-ray diffraction study assessing the mechanisms for anisotropic compression behavior in the *C*23 structure and the details of the *C*23–*C*37 transition, crystal structure analysis of Co_2P with pressure has not been conducted.

At ambient conditions, CoP takes an orthorhombic, *B*31 structure (*Pnma, Z*=4), isomorphic with FeP at ambient conditions and FeS above 3.4 GPa (King an Prewitt 1982; Gu et al. 2011; Ono et al. 2006; Ono et al. 2008). The *B*31 structure is an orthorhombic distortion of the *B*8 structure which is observed in FeS at 250 GPa and at moderate temperatures in Fe-rich compositions (Tremel et al. 1986; Ozawa et al. 2013; Mori et al. 2017). The *B*8 structure is one of the most common structure types in transition metal diatomic stoichiometries and serves as the framework for many *MX* and M_2X compounds (e.g., Tremel et al. 1986). The *B*31 structure is shown in Figure 5.1 and is made up of MX_6 distorted octahedra that form edge sharing columns, linked along edges along the *b* direction (Rundqvist, 1962). Examining the behavior of *B*31 CoP with pressure may provide insight into the material properties of Fe, S, P phases relevant to Earth's outer core pressures, and transition metal chemistry more broadly.

This study investigates the stability of *C*23 Co_2P (also referred to as αCo_2P), *C*22 Co_2P (also referred to as βCo_2P), and *B*31 CoP, and reports a new phase, $Co_{12}P_7$, to 48 GPa and high temperatures using single crystal X-ray diffraction techniques. We present a room temperature

equation of state for αCo_2P to 48 GPa and reveal a highly compressible *a* axis, analogous to what is reported in previous Fe_2P and Fe_2S studies. By determining accurate atomic coordinates for αCo_2P to 48 GPa, the anisotropic compression behavior was resolved to be predominantly attributable to the pressure-induced distortion of bond angles oriented along the *a* axis. As a result of the high compressibility of the *a* axis and relative stiffening of *b* and *c* axes, the *C*23 Co_2P structure compresses towards a Co_2Si-like structure, supporting observations of a *C*23–*C*37 pressure induced transition in M_2X compounds and supporting that the *C*23–*C*37 phase transition may evolve over a pressure range (Zurkowski et al. submitted, Chapter 4). We then demonstrate the stability of βCo_2P quenched from 31 GPa and 1870 K, indicating that the βCo_2P phase is a high *P-T* Co_2P polymorph and a positive α–β Co_2P phase-boundary slope with pressure. We present a crystal structure refinement model for the hexagonal, ordered $Cr_{12}P_7$-type, $Co_{12}P_7$ phase synthesized at 25 GPa and 48 GPa and high temperatures and present room temperature equation of state of $Co_{12}P_7$. Peak broadening observed on decompression below 15 GPa may reveal phase instability below these pressures.We finally present room temperature compression of *B*31 CoP to 35 GPa. The structural properties of Co_2P, $Co_{12}P_7$ and CoP determined in this study offer insight into the chemical and material properties of analogous Fe-(P, S) systems at Earth and planetary core conditions.

5.2. *Materials and methods*

Pressure was generated in a BX-90-type diamond anvil cell (DAC) with 300 μm culet, Boehler-Almax type diamonds on conical seats. Sample chambers were drilled out of pre-indented rhenium gaskets; 10–30 μm Co_2P crystals (Alfa Aesar, 99.9%) were loaded into the

sample chambers along with a ruby ball for pressure calibration. Sample chambers were loaded with compressed neon gas as a pressure transmitting medium (Rivers et al. 2008), and pressure was determined from the ruby fluorescence scale and the Ne equation of state (Mao and Bell, 1976; Fei et al. 2007). Two loadings were prepared for this study with several crystals placed in the sample chamber of each loading.

Single crystal X-ray diffraction (SXD) took place at beamlines 13-BM-D and 13-ID-D of the Advanced Photon Source, Argonne National Laboratory, following the methodology described in Section 2.4. X-ray diffraction data was collected upon compression and decompression in ~5 GPa steps between ambient conditions and 48 GPa. At each pressure step, diffraction data was collected in 8 x 8 μm maps to locate suitably large grains. At each map location, the sample was rotated across a ±10º range as diffraction images were collected in 0.5º steps at a rate of 2–4s per step, and at selected map locations, demonstrating optical grain growth, diffraction images were collected across a ±30° omega range in 0.5° step with 2-4 s exposure times. Samples were heated at select pressures, and when available, diffraction data was collected during heating to monitor grain growth. *Ex-situ,* single sided laser heating took place at the DAC laboratory at Sector 13 and *in-situ,* double sided laser heating took place at 13-ID-D. During *ex-situ* heating, temperature measurements were not obtained. For *in-situ* heating, the temperature measurement procedure described in Section 2.4.1 was applied. All single crystal data was processed following Section 2.5.

5.3. Results and discussion

5.3.1. Synthesis of αCo$_2$P, βCo$_2$P, Co$_{12}$P$_7$ and CoP

Four cobalt phosphides were identified in experiments conducted between ambient conditions and 48 GPa and 1750 K in a Co$_2$P + CoP starting composition: αCo$_2$P (Co$_2$P-type, *Pnma, Z* = 4), CoP (*B*31, *Pnma*, *Z* = 4), ßCo$_2$P (Fe$_2$P-type, *P*-62*m*, *Z*=3), and a hexagonal Co$_{12}$P$_7$ (Figure 5.1, Table 5.1). At ambient conditions, grains of αCo$_2$P and CoP were identified, indicating that the starting material was not purely composed of Co$_2$P. Upon compression to 14.7(1) GPa and quenching from high temperatures, only grains of αCo$_2$P and CoP were observed. With further compression and heating to 26.9(8) GPa and 1740(110) K, grains of αCo$_2$P coexist with grains of hexagonal phase with unit cell parameters, a = 8.142(3) Å and c = 3.2559(9) Å and a volume equal to 1 formula unit-per cell Co$_{12}$P$_7$. A grain of CoP was also identified, possibly indicating incomplete reaction of Co$_2$P and CoP to form Co$_{12}$P$_7$ across the thermal gradient of the sample chamber. ßCo$_2$P was synthesized at 1870(90) K at 30.7(8) GPa, marking the first synthesis of the ßCo$_2$P phase at high pressures and supporting that ßCo$_2$P is a high *P-T* Co$_2$P polymorph. Grains of Co$_{12}$P$_7$ or CoP may have been present in the sample chamber, but were not detected under the sample volume probed. Grains of αCo$_2$P and Co$_{12}$P$_7$ were observed to 48.2(5) GPa up to 1790(200) K. On decompression, a sample was heated at 17.5(1) GPa to 1740(110) K where grains of αCo$_2$P and CoP formed, suggesting reversal of the CoP+Co$_2$P→ Co$_{12}$P$_7$ reaction. Furthermore, a differing grain of Co$_{12}$P$_7$ was decompressed at room temperature to ambient conditions, and a significant decrease in reflections from Co$_{12}$P$_7$

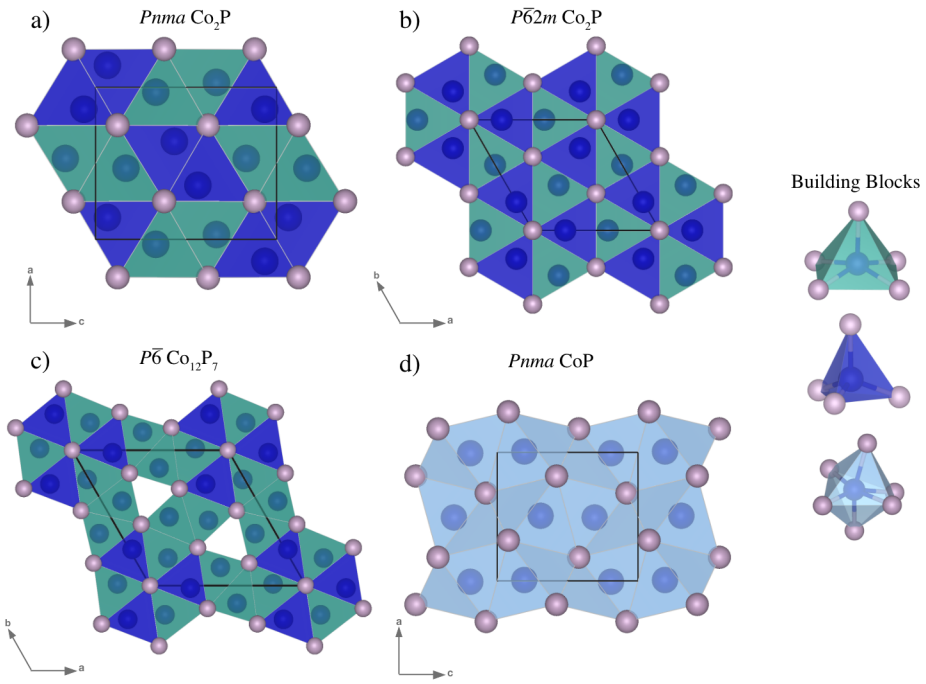

Figure 5.1. Crystal structures of a) *C*23Co_2P, b) *C*22 Co_2P, c) *P*-6 $Co_{12}P_7$ and d) *B*31 CoP observed in this study. The Co_2P polymorphs and $Co_{12}P_7$ are composed of CoP_4 and CoP_5 building blocks while CoP is composed of CoP_6 distorted octahedra.

Table 5.1. Structural details of the phases observed in this study with unit cell parameters measured 30(1) GPa and 300 K provided for comparison.

Phase		Structural Details			Unit Cell Parameters			
		Space Group	Z	Structure type	*a* (Å)	*b* (Å)	*c* (Å)	V (Å³)
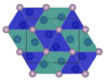	**αCo₂P**	*Pnma*	4	Co_2P	5.309(4)	3.396(2)	6.433(2)	116.0(1)
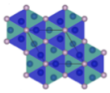	**βCo₂P**	*P*6̄2*m*	3	Fe_2P	5.539(1)		3.2854(8)	87.28(3)
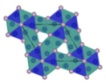	**Co₁₂P₇**	*P*6̄	1	$Co_{12}P_7$	8.097(3)		3.246(1)	184.3(1)
	**CoP**	*Pnma*	4	MnP	4.889(3)	3.1068(9)	5.371(2)	81.59(6)

Table 5.2. Experimental *P-T* conditions and synthesis products observed in this study. Regarding the column titles, "S" refers to the sample, and "q T" refers to the quench temperature if heating was conducted at that pressure step. For samples heated offline where temperature could not be measured, the quench temperature is labeled as "offline."

Beamline	S	Crystal	P (GPa)	err (GPa)	compression/ decompression	q T (K)	err (K)	phases found in sample chamber
13-BM D	S1	C1, C4, C5	amb	–	compression	–	–	aCo2P
13-BM D	S1	C5	7.5	0.8	compression	–	–	aCo2P
13-BM D	S1	C4	8.0	0.4	compression	–	–	aCo2P
13-BM D	S1	C5	13.93	0.05	compression	–	–	aCo2P
13-BM D	S1	C5	14.3	0.1	compression	–	–	aCo2P
13-BM D	S1	C5	14.1	0.5	compression	–	–	aCo2P
13-BM D	S1	C4	14.65	0.1	compression	offline	–	aCo2P, CoP
13-BM D	S1	C5	20.6	0.5	compression	–	–	aCo2P, CoP
13-BM D	S1	C4	20.85	0.7	compression	offline	–	aCo2P, CoP
13-ID D	S1	C1	26.45	0.3	compression	–	–	aCo2P, CoP
13-ID D	S1	C1	26.775	0.25	compression	1750	110	aCo2P, Co12P7
13-ID D	S1	C1	26.9	0.8	compression	1750	110	aCo2P, Co12P7
13-ID D	S1	C1	30.6	0.8	compression	–	–	aCo2P, Co12P7
13-ID D	S1	C4	30.7	0.8	compression	1870	90	aCo2P, bCo2P
13-ID D	S1	C4	30.475	0.85	compression	1870	90	aCo2P, bCo2P
13-ID D	S1	C5	31.35	1.5	compression	–	–	aCo2P
13-ID D	S1	C1	35.1	1.2	compression	–	–	aCo2P, Co12P7, CoP
13-ID D	S1	C5	35.2	0.2	compression	–	–	aCo2P
13-ID D	S1	C1	28.65	0.3	decompression	–	–	aCo2P, Co12P7
13-ID D	S1	C5	28.6	0.2	decompression	–	–	aCo2P
13-ID D	S1	C1	22.45	1.3	decompression	–	–	aCo2P, Co12P7
13-ID D	S1	C5	23.3	0.4	decompression	–	–	aCo2P

Table 5.2. ***continued***

13-ID D	S1	C5	18.55	0.3	decompression	–	–	aCo2P
13-ID D	S1	C5	17.85	0.1	decompression	1740	110	aCo2P, CoP
13-BM D	S1	C5	15.35	0.1	decompression	–	–	aCo2P
13-BM D	S1	C1	15.2	0.2	decompression	–	–	aCo2P, Co12P7
13-BM D	S1	C4	15.4	0.2	decompression	–	–	aCo2P
13-BM D	S1	C1	8.55	0.7	decompression	–	–	aCo2P, Co12P7
13-BM D	S1	C1	7.65	0.1	decompression	–	–	aCo2P, Co12P7
13-BM D	S1	C1	amb	–	decompression	–	–	aCo2P, Co12P7
13-BM D	S2	xtl2	amb	–	compression	–	–	aCo2P
13-BM D	S2	xtl2	6.7	0.5	compression	–	–	aCo2P
13-BM D	S2	xtl2	10.2	0.5	compression	–	–	aCo2P
13-BM D	S2	xtl2	14	0.5	compression	–	–	aCo2P
13-BM D	S2	xtl2	16.5	0.5	compression	–	–	aCo2P
13-BM D	S2	xtl2	17	0.5	compression	–	–	aCo2P
13-BM D	S2	xtl2	19	0.5	compression	–	–	aCo2P
13-BM D	S2	xtl2	26.5	0.5	compression	–	–	aCo2P
13-BM D	S2	xtl2	29.2	0.5	compression	–	–	aCo2P
13-BM D	S2	xtl2	32.9	0.2	compression	–	–	aCo2P
13-BM D	S2	xtl2	36	0.5	compression	–	–	aCo2P
13-BM D	S2	xtl2	39.45	0.5	compression	–	–	aCo2P
13-BM D	S2	xtl2	42.2	0.5	compression	–	–	aCo2P
13-BM D	S2	xtl2	44	0.5	compression	–	–	aCo2P
13-ID D	S2	xtl2	48.2	0.5	compression	1790	200	aCo2P, Co12P7

was detected below 15 GPa, accompanied by peak broadening, supporting phase instability below ~ 15-18 GPa.

The run conditions for each experiment conducted in this study along with the phases observed at each pressure step is provided in Table 5.2 and this data is shown in *P-T* space in Figure 5.2. While the focus of this work is not the Co-P phase-relations, our high P-T syntheses suggest that αCo$_2$P is stable between ambient pressures and 48 GPa at moderate temperatures and transitions to ßCo2P at high temperatures up to at least 31 GPa. CoP coexists with Co$_2$P to at least 17 GPa and Co$_2$P and CoP react to form Co$_{12}$P$_7$ between 18 and 48 GPa at moderate temperatures. Plausible phase boundaries are drawn in Figure 2, based on these results, but *in-situ* high temperature diffraction work is needed to determine the equilibrium CoP–Co$_2$P phase relations.

5.3.2. Crystal structure refinement of Co$_{12}$P$_7$

Grains of Co$_{12}$P$_7$ identified in the reciprocal space between between 15 and 48 GPa after high temperature synthesis were indexed to a primitive hexagonal lattice with unit cell parameters ranging from a = 8.253(5) Å, c = 3.290(2) Å at 15 GPa to a = 7.965(2) Å, c = 3.2053 Å at 48 GPa. Analysis of systematic absences indicate a *P*-6 space group with Z=1 (Figure 5.1, Table 5.3, supplemental file SF5a). Refinement of the structure model confirms that Co$_{12}$P$_7$ takes the ordered Cr$_{12}$P$_7$ structure type (Baurecht et al. 1971; Chun and Carpenter, 1979; Zurkowski et al. 2020).

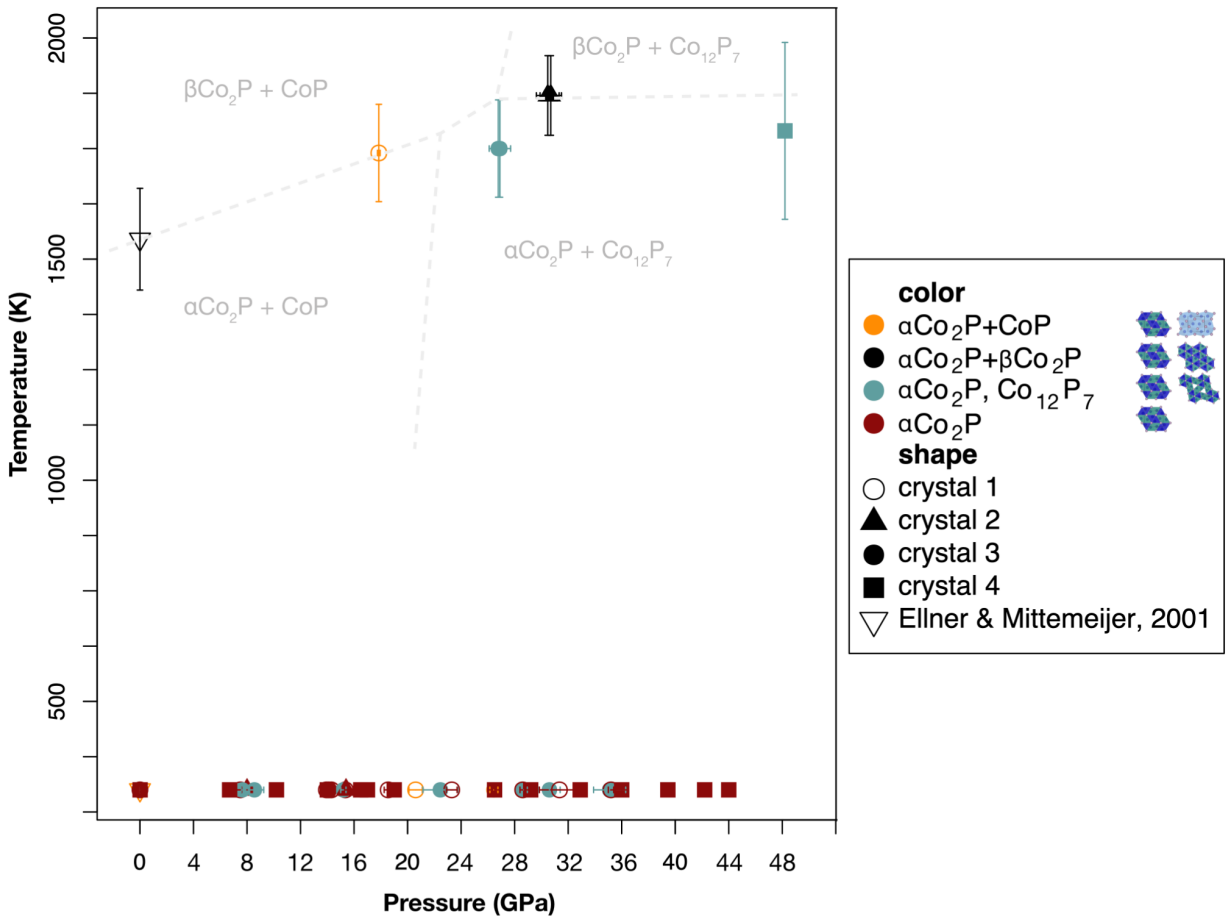

Figure 5.2. Pressure temperature run conditions for each experiment run in this study. The data plotted in this figure is given in Table 2. The color of the symbols indicate the phases observed upon quench while the shapes indicate the crystals that were examined at each P-T condition. The starting composition of some crystals must be P-rich of Co_2P as CoP and $Co_{12}P_7$ were observed forming with Co_2P for crystals 1, 3, and 4. For crystal 2, only Co_2P was observed upon quench from high P-T synthesis. The average of the $\alpha Co_2P \rightarrow \beta Co_2P$ transition at ambient pressures reported by Ellner and Mittigmeijer 2011 is shown. Plausible phase boundaries are noted in grey.

The novel $Co_{12}P_7$ structure type consists of columns of alternating tetrahedral and pyramidal polyhedra and columns of stacked triangular prismatic polyhedra extending along the *c*-axis (Figure 5.1). Metal atoms occupy half of all tetrahedral and pyramidal sites while the triangular prismatic sites are empty (Baurecht et al. 1971). The polyhedra within the unit cell can

Table 5.3. Collection, structural solution and refinement details for $Co_{12}P_7$ at 48 and 15 GPa.

	48 GPa	15 GPa
Crystal data		
Chemical formula	$Co_{12}P_7$	$Co_{12}P_7$
M_r	923.95	923.95
Crystal system, space group	Hexagonal, $P\bar{6}$	Hexagonal, $P\bar{6}$
Temperature (K)	293	293
a, c (Å)	7.9700 (14), 3.2034 (4)	8.253 (5), 3.2902 (18)
V (Å^3)	176.22 (7)	194.1 (3)
Z	1	1
Radiation type	Synchrotron, λ = 0.29521 Å	Synchrotron, λ = 0.3344 Å
μ (mm^{-1})	2.47	3.17
Crystal size (mm)	0.01 × 0.01 × 0.01	0.01 × 0.01 × 0.01
Data collection		
Diffractometer	13IDD @ APS	13BMD @ APS
Absorption correction	Multi-scan (*CrysAlis PRO*; Rigaku OD, 2018)	Multi-scan (*CrysAlis PRO*; Rigaku OD, 2018)
T_{min}, T_{max}	0.789, 1.000	0.546, 1.000
No. of measured, independent and observed [$I > 2\sigma(I)$] reflections	336, 292, 279	592, 321, 253
R_{int}	0.006	0.055
$(\sin\theta/\lambda)_{max}$ (Å^{-1})	0.874	0.762
Refinement		
$R[F^2 > 2\sigma(F^2)]$, $wR(F^2)$, S	0.037, 0.096, 1.12	0.053, 0.105, 1.11
No. of reflections	292	321
No. of parameters	32	32
$\Delta\rho_{max}$, $\Delta\rho_{min}$ (e Å^{-3})	2.35, −1.81	1.70, −1.74
Absolute structure	Flack x determined using 75 quotients $[(I^+)-(I^-)]/[(I^+)+(I^-)]$ (Parsons *et al.*, 2013)	Flack x determined using 78 quotients $[(I^+)-(I^-)]/[(I^+)+(I^-)]$ (Parsons *et al.*, 2013)
Absolute structure parameter	0.42 (6)	0.4 (2)

be described as $Co_9^P Co_3^T \square_2^{Pr} P_7$ (P = pyramidal, T = tetrahedral, Pr = trigonal prismatic) (Maaref and Madar 1981). $Co_{12}P_7$ is composed of the same polyhedral building blocks as both the *C*22 and *C*23 structures, and only differs in the ratio of tetrahedral to pyramidal sites (Maaref et al. 1981; Zurkowski et al. 2020) (Figure 5.1); where the *C*22 and *C*23 structures have a 1:1 ratio of tetrahedral and square pyramid sites and the $Co_{12}P_7$ structure has a 3:1 ratio of square pyramid to tetrahedral sites accompanied by empty trigonal sites (Zurkowski et al. 2020).

Co-P interatomic distances and polyhedral volumes are provided in Table 5.4 and Figure 5.3. Co0 atoms occupy distorted tetrahedral sites with one P atom at a short distance, two at intermediate distances and one at a long distance (Figure 2). Co1 and Co2 atoms occupy axially truncated square pyramids with two intermediate and two long interatomic distances at the base. Co3 atoms occupy a less distorted square pyramid with two elongated and two truncated bonds

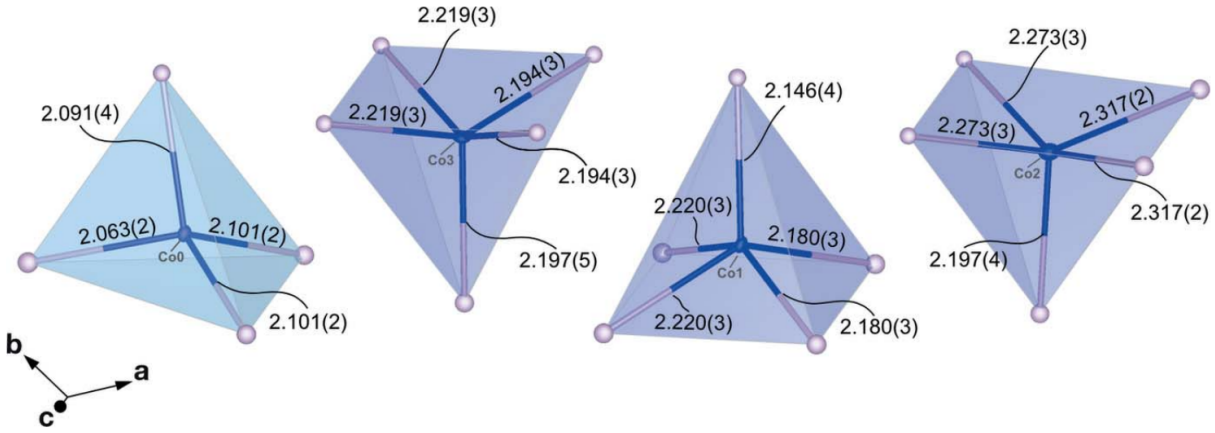

Figure 5.3. Co-P polyhedra as observed in the $Co_{12}P_7$ structure (48 GPa data set) showing varying degrees of volume and distortion, quantified in Table 5.4. CoP_4 tetrahedra are shaded in cyan and CoP_5 square pyramids are shaded in violet. Displacement ellipsoids are drawn at the 50% probability level.

at the base (Figure 5.3). The selected structural parameters for $Co_{12}P_7$ are provided in Table 5.4 are compatible with those observed in other Co-P phases such as αCo_2P and CoP (Rundqvist 1960; Rundqvist, 1962).

5.3.3. Equations of state of αCo_2P, $Co_{12}P_7$ and CoP

The volumes of *Pnma* Co_2P, $Co_{12}P_7$ and CoP were measured to 48 GPa and show smooth decreasing trends with pressure (Figures 5.4-5.6). The *P-V* datasets for each phase include measurements collected on grains with no heating history (blue symbols in Figure 5.4-5.6), grains that were heated and quenched then measured (red symbols in Figure 5.4-5.6) and grains that were compressed or decompressed after high temperature synthesis (green symbols in Figure 5.4-5.6). No systematic differences are observed in the volumes measured based on these differing heating histories, indicating invariable stoichiometries during these experiments (Figure 5.4-5.6). The *P-V* datasets for each phase were fitted to a Birch Murnaghan equation of state

Table 5.4. Selected structural parameters for $Co_{12}P_7$ at 48 GPa.

Group	Maximal Bond Length	Minimal Bond Length (Å)	Polyhedron Volume (Å^3)	Distortion Index
CoP_4 (Co0–P4, –P5, –P6)	2.102(2)	2.062(2)	4.5433	0.00656
CoP_5 (Co2–P4, –P5)	2.220(3)	2.147(4)	8.1257	0.01085
CoP_5 (Co2 –P4, –P5, –P6)	2.317(2)	2.198(4)	9.0766	0.01432
CoP_5 (Co3–P4, –P5)	2.218(3)	2.194(3)	8.3239	0.00514

(BMEoS) (Birch 1952) relating room temperature pressure (P) to the zero-pressure volume, (V_0), isothermal bulk modulus (K_0) and its pressure derivative (K') (Equation 5.1).

$$P(V) = 3K_0 f(1 + 2f)^{2.5} * (1 + 1.5(K' - 4) f), f = 0.5 * ((V/V_0)^{(-2/3)} - 1) \quad 5.1$$

*C*23 Co_2P was observed in two samples up to 48.2(5) GPa and quenched from temperatures of up to 1870(90) K. Forty-two P-V data points were collected; 34 on compression and 8 on decompression (Figure 5.4). The EoS fit to these data, given in Table 5.5, is shown by the black solid line plotted in Figure 5.4. Pressure residuals to the fit show a root mean square value of 0.9 and are given in the lower panel, supporting a single volume trend across this pressure range (Figure 5.4). Covariance matrices illustrating the relationship between V_0, K_0 and K' are given in Figure 5.5. P-V data and the fitted EoS presented in the powder diffraction study by Qian et al. 2011 are also plotted in Figure 5.4, revealing higher compressibility measured for

Table 5.5. EoS parameters fit for αCo$_2$P, Co$_{12}$P$_7$ and CoP

Phase		Equation of State Parameters		
		V_0 (cm^3 /mol)	K_0 (GPa)	K'
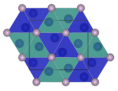	**αCo$_2$P**	19.67(2)	180(5)	5.0(3)
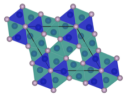	**Co$_{12}$P$_7$**	124.2(1)	222(3)	4 (fixed)
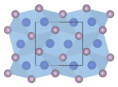	**CoP**	14.010(2)	172(2)	4 (fixed)

Co$_2$P in this previous study. The experiments conducted by Qian et al. 2011 were run in an NaCl pressure-transmitting medium whereas the current study was conducted in neon; therefore disagreements in Co$_2$P volumes measured are likely attributable to the differences in stress conditions induced by the NaCl versus neon.

Co$_{12}$P$_7$ was synthesized in one sample at 26.9(8) GPa and 1740(110) K and compressed to 35(1) GPa prior to decompression to ambient conditions. In a second sample, Co$_{12}$P$_7$ was synthesized at 48.2(5) GPa and 1790(200) K. Ten *P-V* measurements were collected in this pressure range (Figure 5.6) and all data between 18 and 48 GPa were included in the EoS fit. The measurements collected below 15 GPa were excluded from the fit because the loss of reflections, peak broadening, and larger than expected measured volumes suggest phase instability. The EoS fit to the data between 18 and 48 GPa data is given in Table 5.5 and plotted in Figure 5.6 (solid black line). K' was fixed at 4 due to the limited number of measurements particularly at low pressures. The residuals to this fit are given in the lower panel of Figure 5.6 showing root mean

square value of 0.3. Covariance in V_0 and K_0 is provided in Figure 5.7. The *P-V* data below 15 GPa are included in the Figure 5.6 for comparison to the EoS fit and the differences in measured pressure and calculated pressure for these <15 GPa data points are plotted in the lower panel.

CoP data was collected between 14.7(1) GPa and 35(1) GPa in this study. The ambient unit-cell parameters reported by Rundqvist et al. 1962 were included in the EoS fit to help constrain the low pressure behavior of this phase (Figure 5.8). When fitting K', a value of 4 was obtained. The data was then fit to a second-order Birch-Murnaghan EoS to better constrain the V_0 and K_0 parameters (Table 5.5). Pressure residuals to the equation of state with a root mean square value of 1 are plotted in the lower panel of Figure 5.8. Covariance in V_0 and K_0 for CoP is plotted in Figure 5.9.

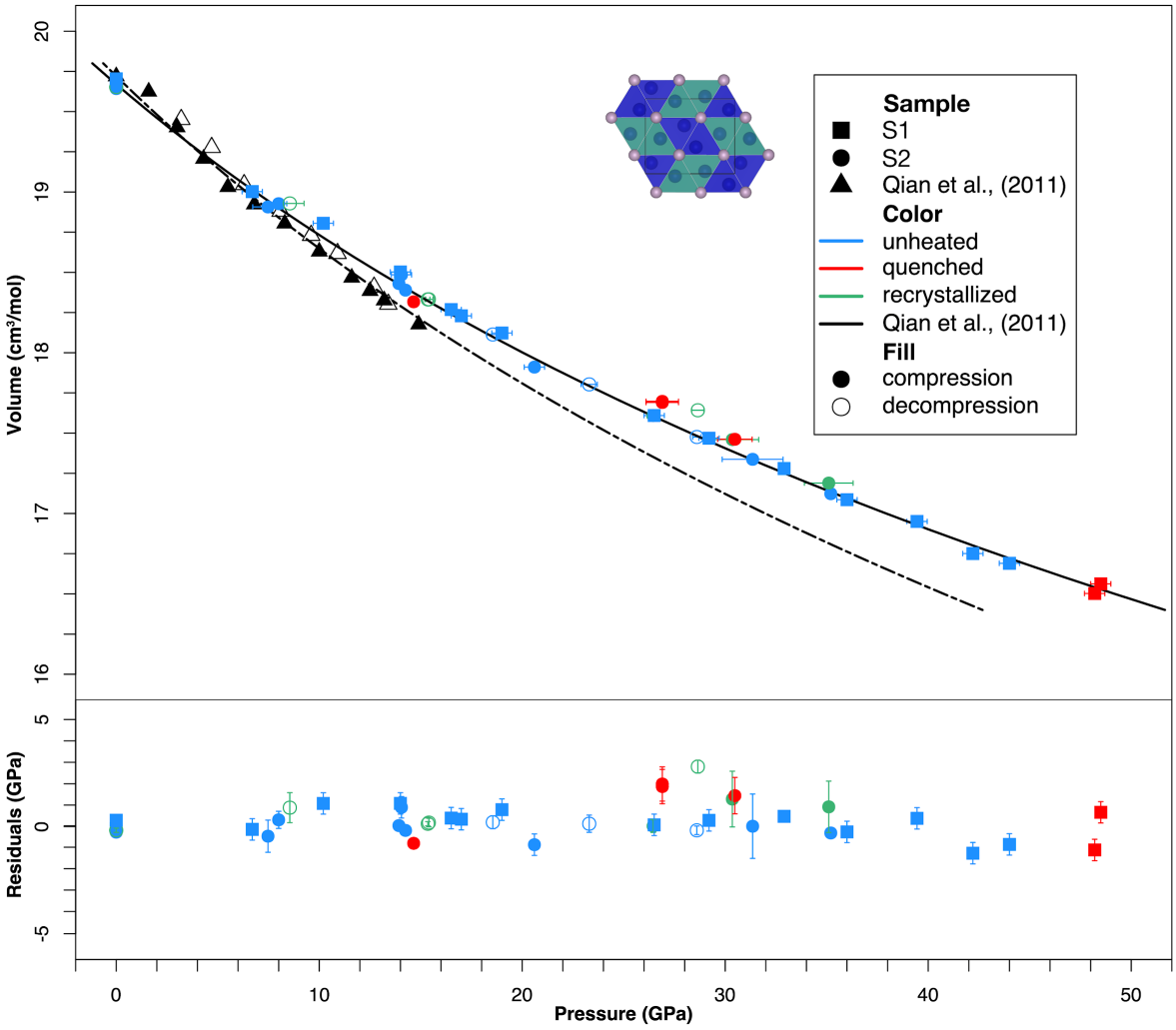

Figure 5.4. *P-V* data for αCo$_2$P collected on the two samples (S1 and S2) in this study (circles and squares) with *P-V* data collected in the powder diffraction experiments by Qian et al. 2011 included (triangles). Blue symbols indicate data collected on grains that had no heating history, the red symbols indicate data collected on grains that were heated and quenched at that pressure prior to collection and the green symbols indicate data collected on grains that were heated at a previous pressure step and further compressed or decompressed prior to collection. The solid black line indicates the 300 K compression curve calculated from the EoS fit presented in this study and the black dashed-dot line indicates the 300 K compression curve reported by Qian et al. 2011. Residuals to the EoS fit from the current study are plotted in the lower panel showing a <3 GPa difference in measured pressure versus calculated pressure across the pressure range examined.

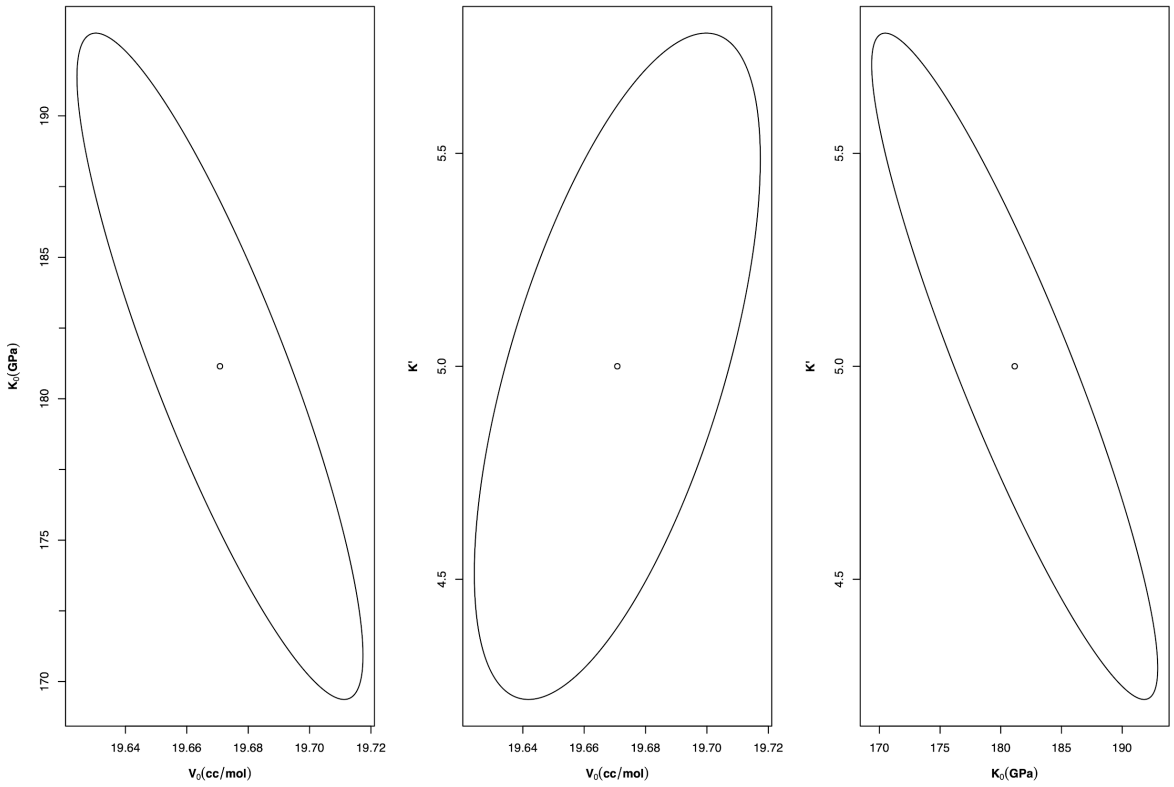

Figure 5.5. Covariance ellipses showing relationship between V_0, K_0 and K' fit in the αCo_2P EoS.

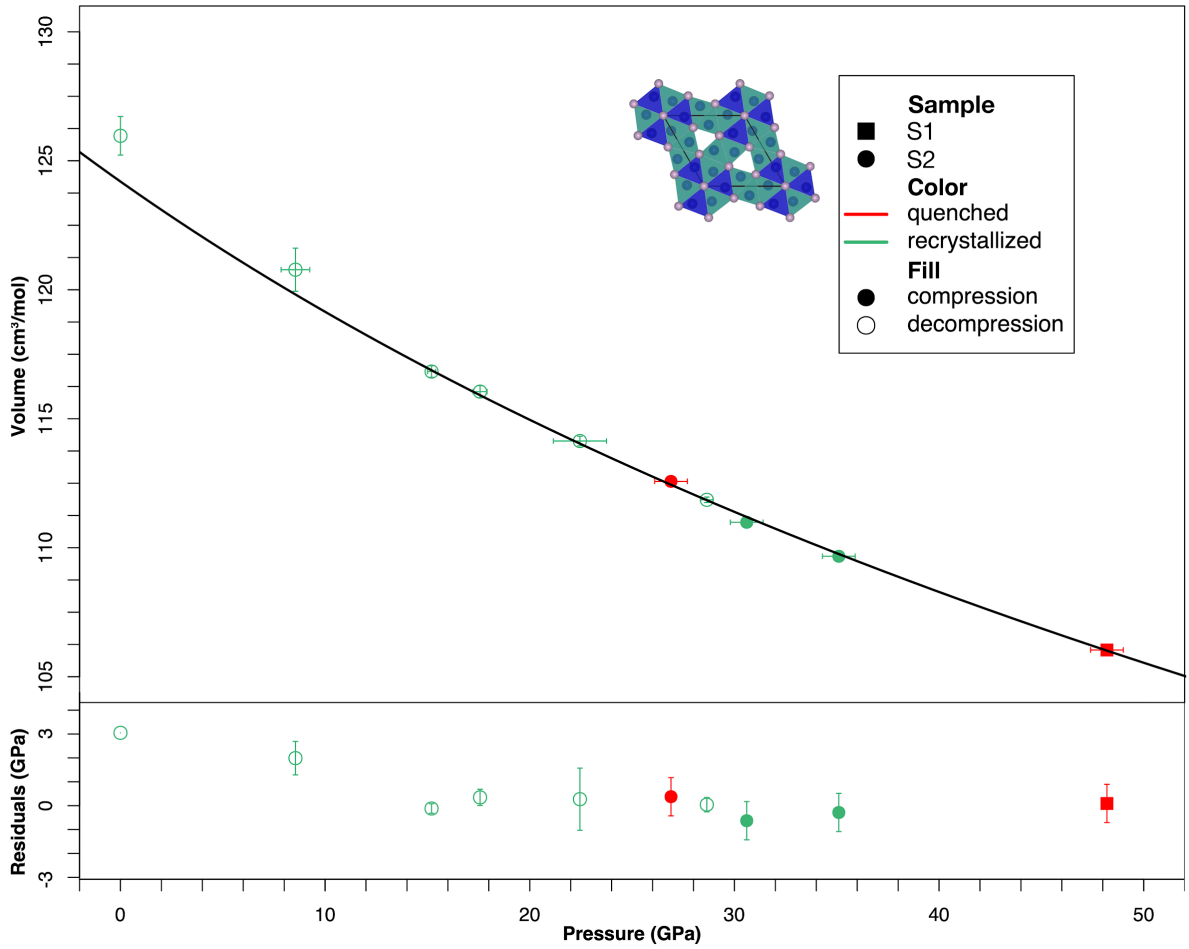

Figure 5.6. *P-V* data for $Co_{12}P_7$ collected in the two samples run (S1 and S2) in this study (circles and squares). The red symbols indicate data collected on grains that were heated and quenched at that pressure prior to collection and the green symbols indicate data collected on grains that were heated at a previous pressure step and further compressed or decompressed prior to collection. Filled symbols indicate measurements collected on compression and open symbols indicate measurements collected on decompression. The *P-V* data above 10 GPa were included in the EoS fit as loss of reflections and peak broadening indicated possible grain decomposition at lower pressures. The EoS fit to this data is plotted with the black solid line and residuals to the fit are plotted in the lower panel showing a <3 GPa difference between measured and calculated pressure across the pressure range examined. The difference in calculated pressure based on this EoS and measured pressure for the measurements at ambient and ~8 GPa are included to indicate the deviation from the fit likely due to phase instability.

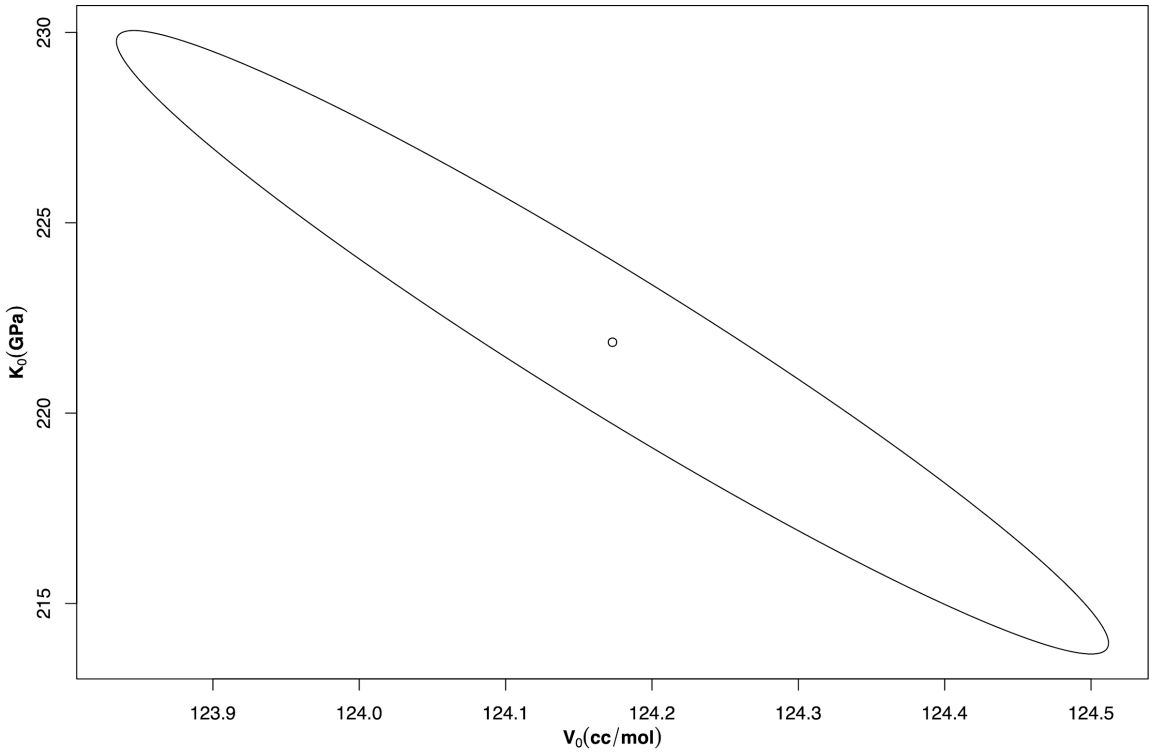

Figure 5.7. Covariance ellipse showing relationship between V_0, and K_0 the $Co_{12}P_7$ EoS.

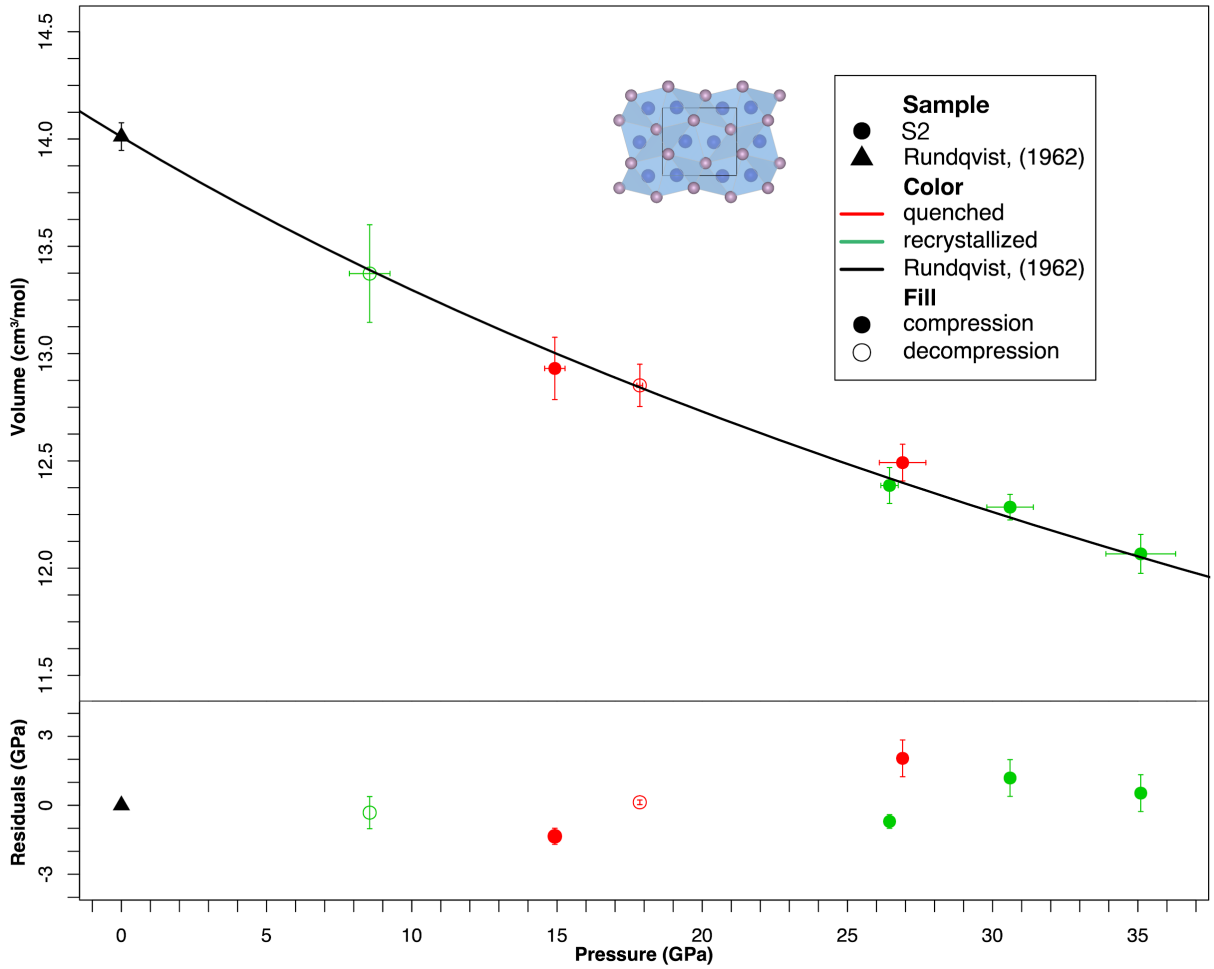

Figure 5.8. *P-V* data for CoP collected on sample S2 run in this study (circles). Grains of CoP were not observed in the ambient measurement, but this MnP-type structure of CoP was previously examined at ambient conditions by Rundqvist et al. 1962 and the ambient volume was included in this study (triangle). The red symbols indicate data collected on grains that were heated and quenched at that pressure prior to collection and the green symbols indicate data collected on grains that were heated at a previous pressure step and further compressed or decompressed prior to collection. Filled symbols indicate measurements collected on compression and open symbols indicate measurements collected on decompression. The EoS fit to this data is plotted with the black solid line and residuals to the fit are plotted in the lower panel showing a <3 GPa difference between measured and calculated pressure across the pressure range examined.

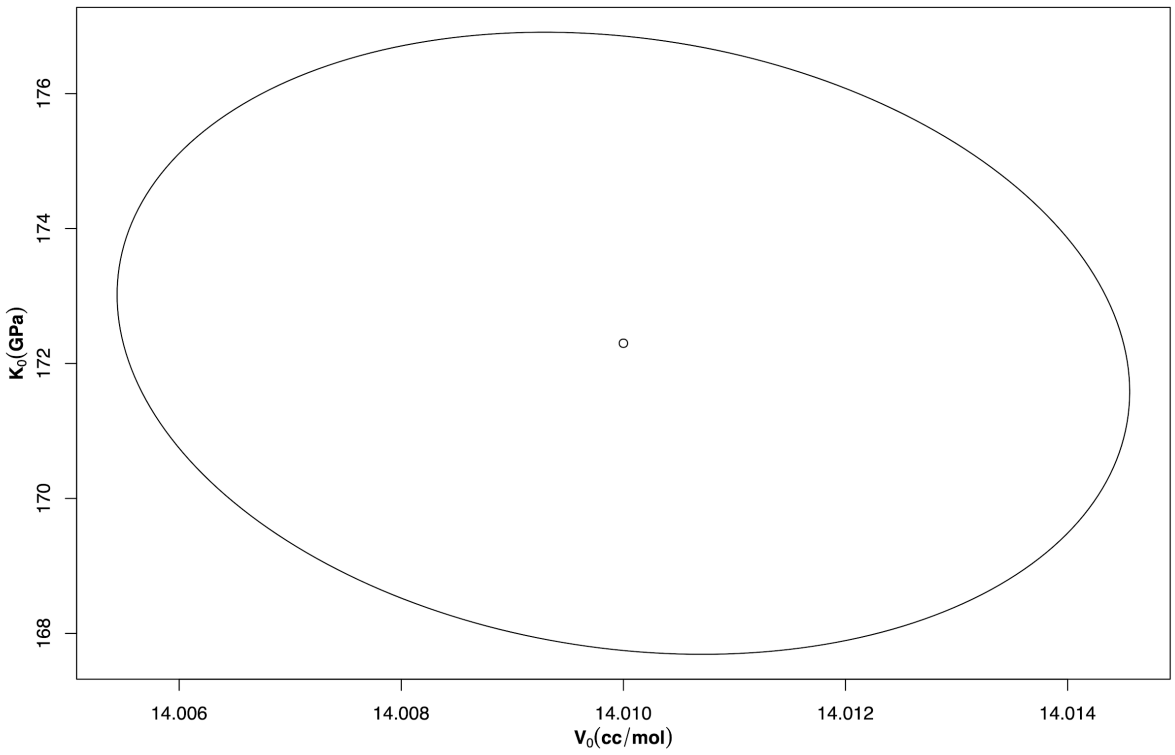

Figure 5.9. Covariance ellipses showing the relationship between V_0 and K_0 fit in the CoP EoS.

5.3.4. Compressibility of αCo$_2$P, Co$_{12}$P$_7$ and CoP

The unit-cell parameters of αCo$_2$P measured to 48 GPa reveal significant anisotropic behavior (Figure 5.10). The *a* axis is highly compressible compared to the *b* and *c* axes, analogous to what is observed in the Fe$_2$P and Fe$_2$S systems (Dera et al. 2008; Zurkowski et al. submitted, Chapter 4). Furthermore, a change in compression behavior is observed above 36 GPa where the *a* axis softens, similar to that observed in Fe$_2$S above 120 GPa (Zurkowski et al. submitted, Chapter 4). This behavior αCo$_2$P must be accompanied by a stiffening of the *b* and *c* axes, as a continuous trend in unit-cell volume with pressure is observed (Figure 5.4). The *b* axis does show stiffening above 42 GPa, but additional data is needed to better statistically characterize this behavior.

To describe the anisotropic axial compression behavior, a second-order Birch-Murnaghan equation of state was fit to the axial lengths with pressure (Angel et al. 2000; Angel et al. 2014) for data collected below 36 GPa. The resultant zero-pressure axial lengths (d_0) and linear moduli (K_0) are listed for each unit-cell parameter in Table 5. The data at ≥ 36 GPa are plotted with open symbols in Figure 5.10 to indicate that they were not included in the fit of the axial compression behavior. The results of the EoS quantify that that *a* axis is about two and three times more compressible than the *b* and *c* axes respectively in this pressure range.

Notably, an *a* axis that is significantly more compressible than the *c* axis is the necessary mechanism for shaping the Co$_2$P structure into the Co$_2$Si (*C*37 structure) with pressure, as described in Chapter 4. On the basis of relative unit-cell comparison, the Co$_2$P structure has a *c*/*a* ratio of 1.17 at ambient conditions and the Co$_2$Si structure has a *c*/*a* ratio of 1.44 at ambient

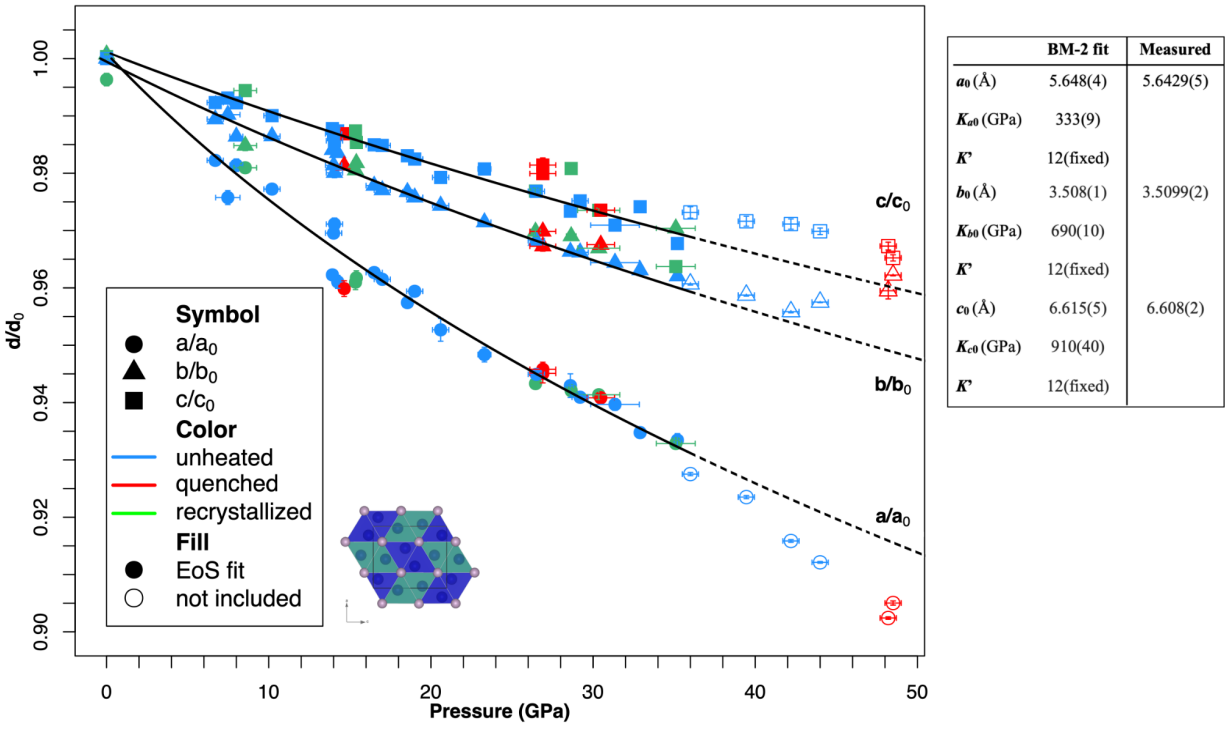

	BM-2 fit	Measured
a_0 (Å)	5.648(4)	5.6429(5)
K_{a0} (GPa)	333(9)	
K'	12(fixed)	
b_0 (Å)	3.508(1)	3.5099(2)
K_{b0} (GPa)	690(10)	
K'	12(fixed)	
c_0 (Å)	6.615(5)	6.608(2)
K_{c0} (GPa)	910(40)	
K'	12(fixed)	

Figure 5.10. Relative unit-cell parameters for αCo$_2$P with circles, triangles, and squares referring to the *a, b,* and *c* axes respectively. Blue symbols indicate data collected on grains that had no heating history, the red symbols indicate data collected on grains that were heated and quenched at that pressure prior to collection and the green symbols indicate data collected on grains formed from high *P-T* synthesis prior to compression. The compression behavior is anisotropic, with the *a* axis compressing much more than the *b* and *c* axes and a softening of the *a* axis is observed above ~35 GPa. A second-order Birch-Murnaghan equation of state was fit for each unit-cell parameter up to 35 GPa as shown on the right. This EoS fit is plotted as the black solid lines, and above 35 GPa, the EoS fit lines are dashed and the data points are unfilled to indicate that these data were not included in the EoS fit.

conditions. The *c*/*a* ratio of αCo$_2$P with pressure is plotted in Figure 5.11 and shows an approximately linearly increasing trend. Up to 48 GPa, the *c*/*a* ratio increases to ~1.26; still significantly less than that observed in a Co$_2$Si unit cell (1.44). If the αCo$_2$P *c*/*a* ratio remains roughly linear with pressure, Co$_2$P would achieve a Co$_2$Si-like relative unit cell by ~115 GPa (Figure 5.11).

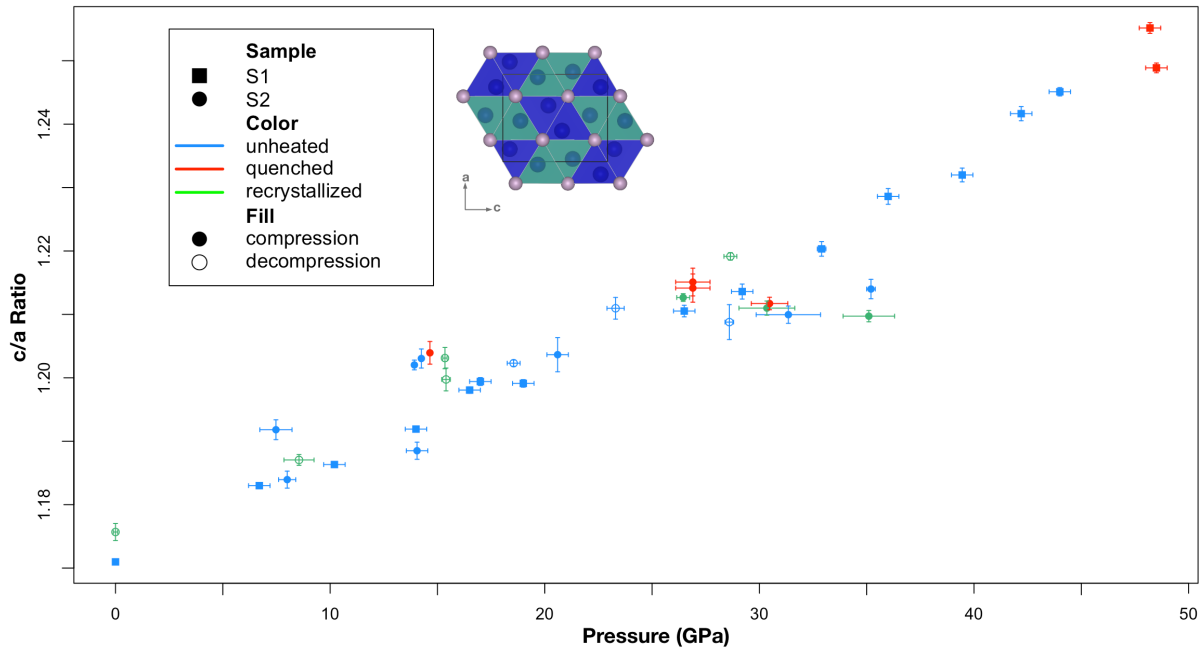

Figure 5.11. Ratio of *c* to *a* of αCo$_2$P with pressure to 48 GPa.

The relative unit-cell parameters measured for Co$_{12}$P$_7$ show nearly isotropic compression behavior up to 25 GPa and increased compression along the *a* axis above 25 GPa (Figure 5.12). Peak broadening observed upon decompression below 15 GPa may indicate phase instability in this lower pressure range; therefore, the axial compression of Co$_{12}$P$_7$ above these pressures may better characterize the compression behavior. The lattice parameters of CoP up to 35 GPa display greater compression along the *b* direction, but more data is needed to assess this compression trend (Figure 5.12).

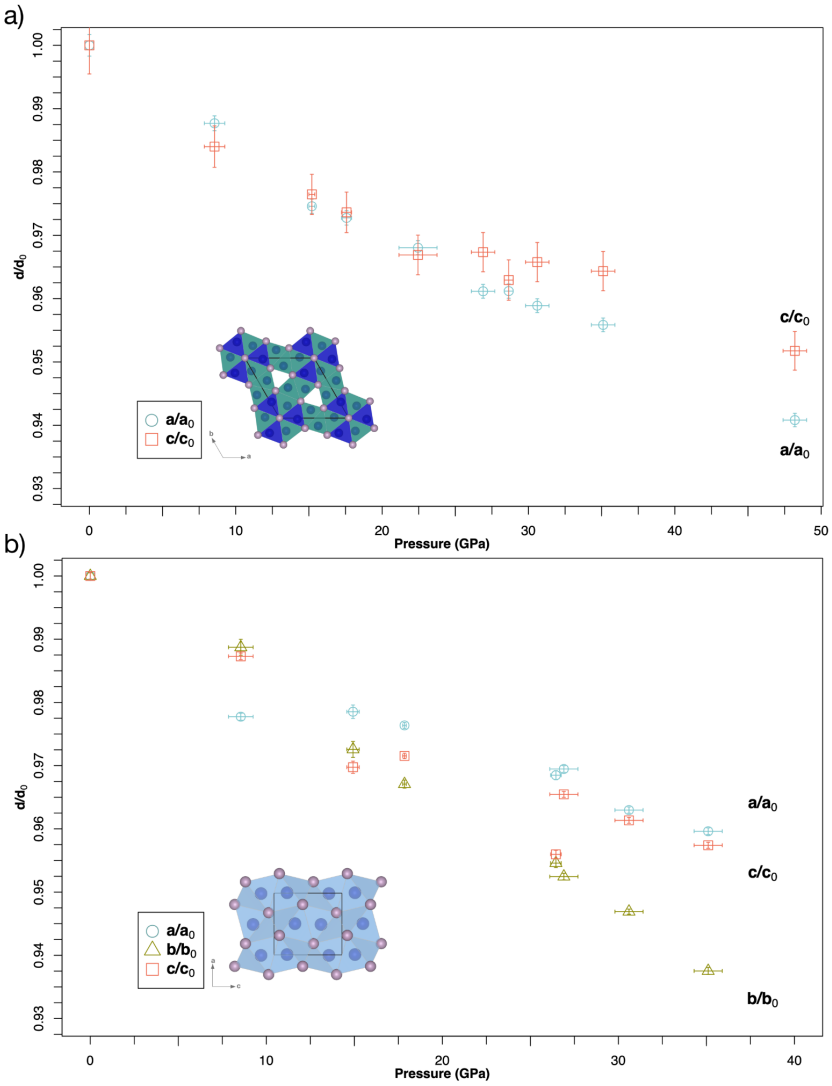

Figure 5.12. Relative lattice parameters for a) $Co_{12}P_7$ and b) CoP measured in this study.

5.3.5. Structural analysis α*Co_2P, $Co_{12}P_7$ and CoP and assessment of the anisotropic compression mechanism in* α*Co_2P.*

As the Co_2P polymorphs and $Co_{12}P_7$ and CoP phases observed in this study adopt previously determined structure types, the structure factors were reduced for each Co-phosphide and used to refine the atomic coordinates and thermal displacement parameters using the known structure models (Rundqvist and Jellinek 1959; Rundqvist 1960; Zurkowski et al. 2020;

Rundqvist 1962). In the final structural refinements, few outlying reflections were omitted and if sufficient reflections were obtained, Co-atoms were refined with anisotropic displacement parameters (Table 5.6). If fewer reflections were measured, all atoms were refined with isotropic displacement parameters (Table 5.6). All sites of each Co-phosphide are fully occupied within uncertainty, indicating that the stoichiometries of each phase do not change significantly across the *P-T* range investigated.

The change in position between the atomic coordinate in the *x* and *z* directions (parallel to *a* and *c* axes respectively) of the asymmetric unit and the ambient pressure fractional coordinates for αCo$_2$P are shown in Figure 5.13. The *y* coordinate is not plotted, as atomic positions are fixed along the *b* direction. With pressure, the Co1 sites, located inside the tetrahedral building blocks show movement in the positive *x* direction and slight movement in the negative *z* direction, resulting in movement of the Co1 site towards the edge of the tetrahedron. The Co2 sites, located inside the square pyramid building blocks, move slightly in the positive *x* direction and significantly in the positive *z* direction towards the base of the square pyramid. The P sites exhibit positive shifts in the *x* direction. In Figure 5.14, the data plotted in Figure 5.13 is shown in comparison to the difference in atomic coordinate locations for Co$_2$Si with Co$_2$P at ambient conditions. Interestingly, all atomic coordinates in αCo$_2$P are on a trajectory to migrate into coincidence with the related Co$_2$Si sites, except for the P$_x$ coordinate. At some pressure, the P sites must shift in the negative *x* direction for a *C*23–*C*37 transition to occur. This may be a consequence of a coordination or other structural change and further experiments are required to understand this behavior.

Table 5.6. Site symmetries, atomic fractional coordinates, anisotropic displacement parameters (Å) determined for αCo$_2$P, Co$_{12}$P$_7$, CoP, and βCo$_2$P.

αCo$_2$P, 30(1) GPa

Atom	Wycoff site	symmetry		x	y	z	U11	U22	U33	U23	U13	U12	Ueq
Co1	4*c*	*m*	coordinate	0.0331	0.25	0.67403	0.0083						
			error	0.0002		0.00009	0.0004						
Co2	4*c*	*m*	coordinate	0.1479	0.25	0.06275	0.0079						
			error	0.0002		0.00008	0.0004						
P3	4*c*	*m*	coordinate	0.2506	0.25	0.3767	0.0073						
			error	0.0003		0.0001	0.0005						

Co$_{12}$P$_7$, 28.7(2) GPa

Atom	Wycoff site	symmetry		x	y	z	U11	U22	U33	U23	U13	U12	Ueq
Co1	3*j*	*m*	coordinate	0.0163	0.2655	0	0.0050	0.0060	0.006	0	0	0.0023	0.0058
			error	0.0003	0.0003		0.0009	0.0008	0.001			0.0007	0.0004
Co2	3*j*	*m*	coordinate	0.1322	0.6239	0	0.0051	0.0054	0.004	0	0	0.0025	0.0051
			error	0.0003	0.0003		0.0009	0.0008	0.001			0.0007	0.0004
Co3	3*k*	*m*	coordinate	0.2139	0.2035	0.5	0.0111	0.008	0.006	0	0	0.0061	0.0077
			error	0.0003	0.0003		0.0009	0.001	0.001			0.0008	0.0004
Co4	3*k*	*m*	coordinate	0.5187	0.1358	0.5	0.0065	0.0051	0.006	0	0	0.0027	0.0060
			error	0.0003	0.0003		0.0009	0.0009	0.001			0.0007	0.0005
P5	3*k*	*m*	coordinate	0.1658	0.4504	0.5	0.0051						
			error	0.0006	0.0005		0.0007						
P6	3*j*	*m*	coordinate	0.4459	0.2817	0	0.0051						
			error	0.0005	0.0006		0.0007						
P7	1*a*	-6	coordinate	0	0	0	0.007						
			error				0.001						

CoP, 35.2(2) GPa

Atom	Wycoff site	symmetry		x	y	z	U11	U22	U33	U23	U13	U12	Ueq
Co1	4*c*	*m*	coordinate	0.5067	0.75	0.3081	0.0072						
			error	0.0002		0.0001	0.0004						
P2	4*c*	*m*	coordinate	0.1836	0.75	0.5787	0.0073						
			error	0.0003		0.0002	0.0004						

βCo$_2$P, 30(1) GPa

Atom	Wycoff site	symmetry		x	y	z	U11	U22	U33	U23	U13	U12	Ueq
Co1	3*f*	*m*2*m*	coordinate	0.601	0	0	0.023	0.058	0.006	0	0	0.029	0.025
			error	0.001			0.002	0.004	0.002			0.002	0.002
Co2	3*g*	*m*2*m*	coordinate	0.2588	0	0.5	0.019	0.034	0.017	0	0	0.017	0.022
			error	0.0008			0.002	0.003	0.003			0.002	0.002
P3	2*d*	-6	coordinate	0.333	0.667	0.5	0.015						
			error				0.002						
P4	1*a*	-62*m*	coordinate	0	0	0	0.004						
			error				0.002						

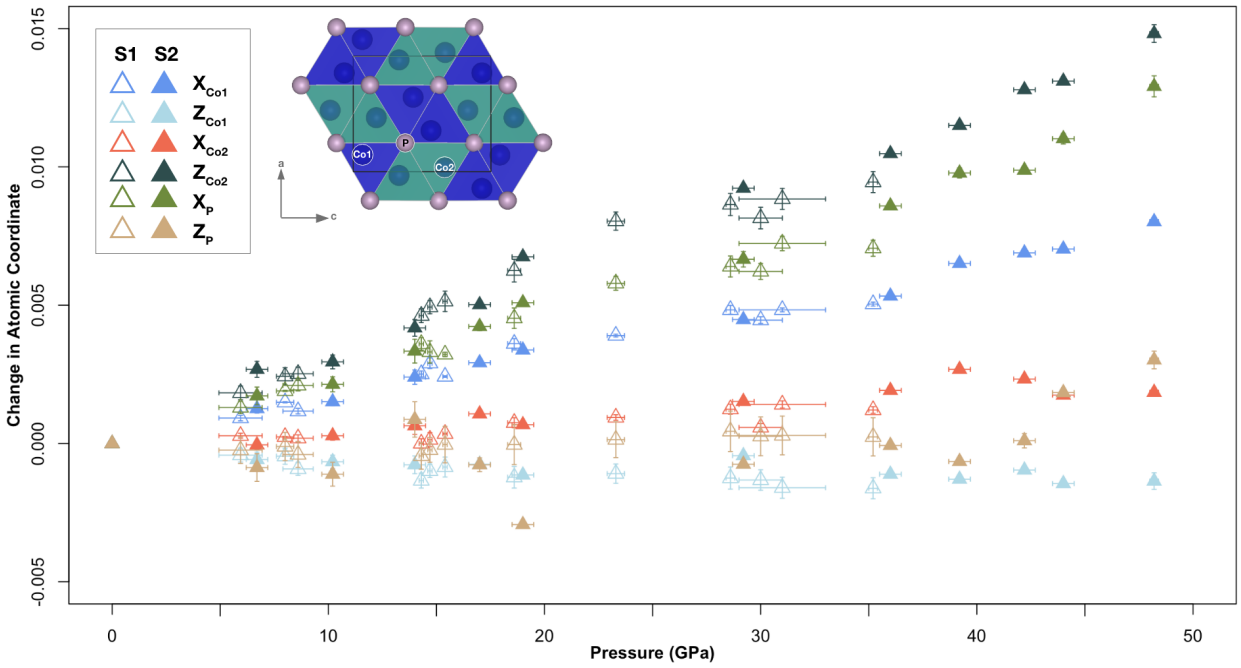

Figure 5.13. The change in *x* and *z* atomic coordinates of the αCo$_2$P from the initial, ambient pressure values for the general positions of the asymmetric unit with pressure. *X* and *z* are in the direction of the *a* and *c* axes respectively. The asymmetric unit sites are labeled in the top left. Open and closed symbols differentiate data collected on two samples, S1 and S2.

Compression of the Co-P interatomic distances within the tetrahedral and square pyramid αCo$_2$P building blocks follow expected compression behavior; namely, the longer bonds compress more relative to the shorter bonds as expected (Figure 5.15). Interestingly, the distance between the tetrahedrally coordinated Co site and the fifth nearest P site, the site required to bond with Co1 during a *C*23-*C*37 transition, shows anomalous compression behavior. In Figure 5.16, the ratio of the interatomic distance of the Co1 site and this next nearest P site (labeled "T5") to the the average interatomic distance within the CoP4 tetrahedra (labeled "AVG(T1:T4)") is plotted with pressure. Note that this T5 distance shown in Figure 5.16 is oriented mostly along the *a* direction and the highly compressible *a* axis brings the Co1 site increasingly closer to this P

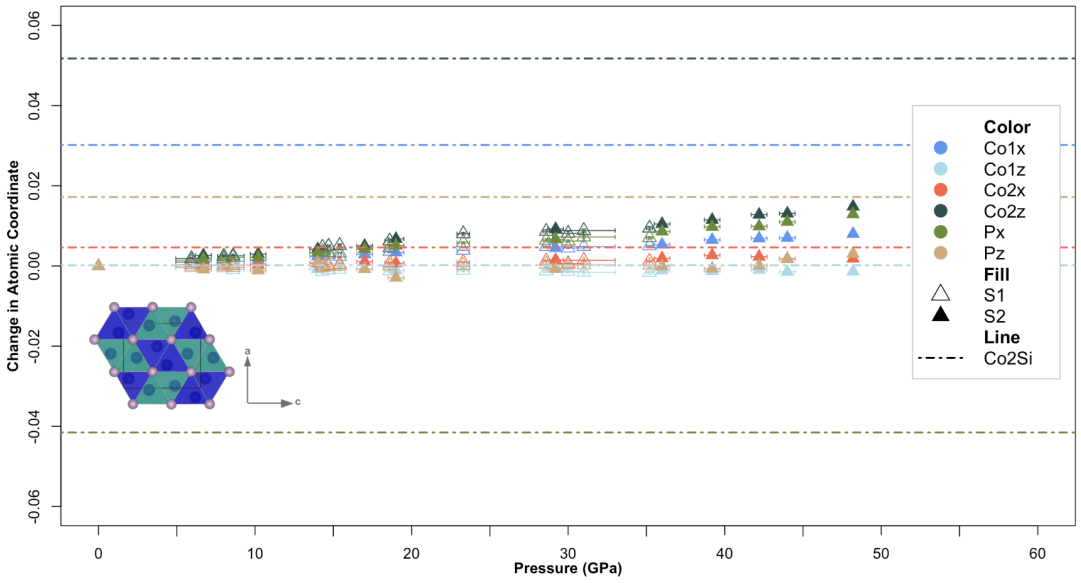

Figure 5.14. The change in atomic coordinates of the αCo$_2$P asymmetric unit with pressure compared to the shift in atomic coordinates to achieve the Co$_2$Si asymmetric unit as shown by the horizontal dashed-dot lines.

site. The T5 distance decreases steadily with pressure up to ~35 GPa, above which a discontinuity is observed and a higher compressibility of this interatomic distance is observed. This change in slope coincides with the discontinuity in axial compression (Figure 5.10), suggesting that the change in compressibility of αCo$_2$P evolves the structure more towards a *C*37 configuration.

A *y* value of 1.13 in Figure 5.16 would indicate that the ratio of the T5 distance to the average of the bond lengths in the CoP$_4$ tetrahedron is equal to that observed in the ideal Co$_2$Si structure. This value is plotted as the red dotted horizontal line in the inset of Figure 5.16 and demonstrates that the Co1 site in αCo$_2$P does not reach a configuration comparable to Co$_2$Si up to 48 GPa and still requires significant compression of this T5 distance for a *C*23–*C*37 transition to occur. The intensification of this compression behavior above 35 GPa, however, may imply

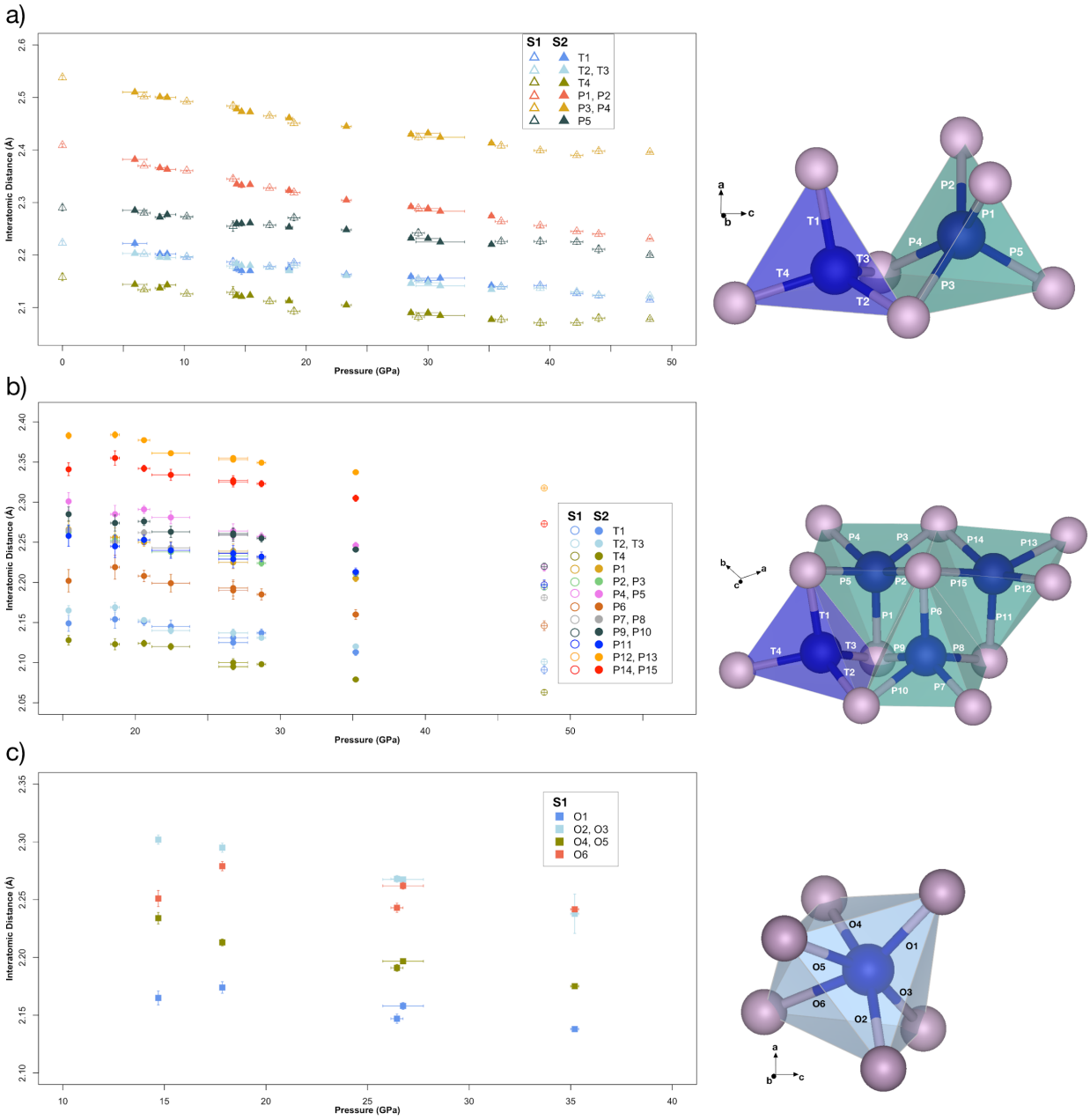

Figure 5.15. Interatomic distances measured in the CoP_4 and CoP_5 or CoP_6 building blocks for αCo_2P, $Co_{12}P_7$ and CoP with pressure.

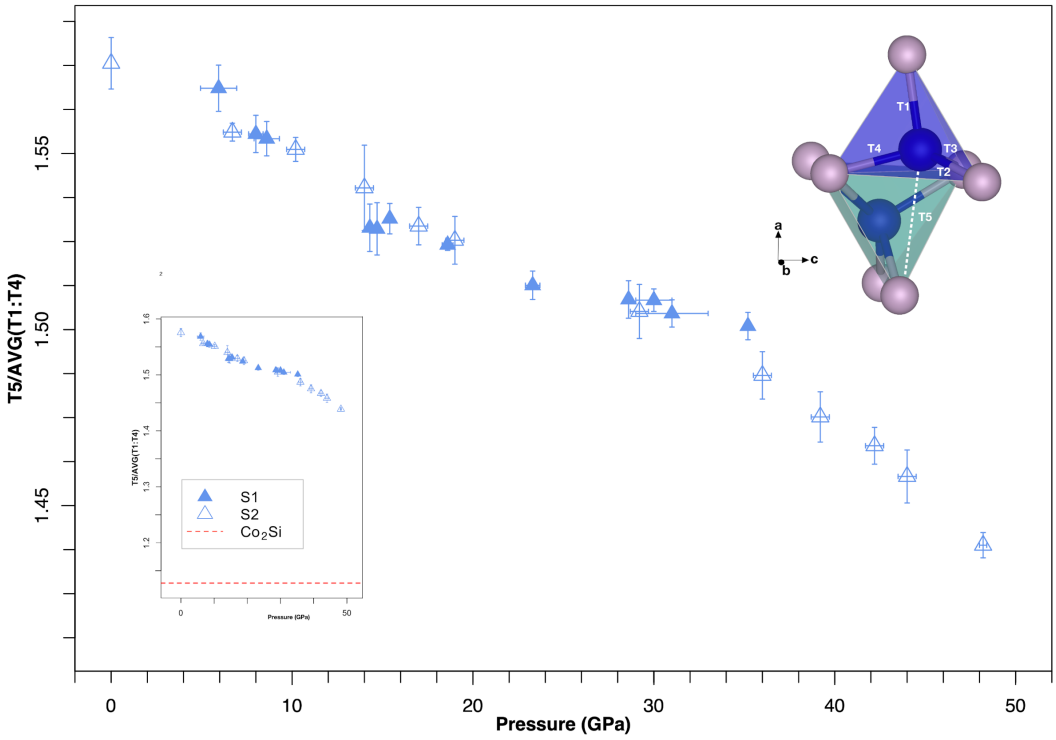

Figure 5.16. The interatomic distance between the Co1 tetrahedral site and the next nearest P site, labeled T5, compared to the average interatomic distances within the Co1P_4 tetrahedra (T1, T2, T3 and T4). Open and closed symbols differentiate data collected on samples S1 and S2.

that the Co1 and 5th nearest P site are experiencing attractive forces and the structure is compressing towards a coordination change.

The relative bond angles within the CoP_4 and the CoP_5 building blocks of αCo_2P further exhibit the mechanisms for anisotropic compression in the αCo_2P structure (Figure 5.17). Angles within the CoP_4 unit, labeled aT1-aT6, are plotted in the top panel of Figure 5.17 and angles within the CoP_5 unit, labeled aP1-aP8 are plotted in the lower panel of Figure 5.17. Over the pressure range studied, the aT1 angle shrinks significantly with pressure. This bond angle is predominantly aligned along the *a* axis, such that the narrowing of this angle compared to the other angles in the CoP_4 tetrahedron contributes to the high compressibility of the *a* axis. Likewise, within the square pyramids, the aP1 and aP2 angles decrease the most with pressure,

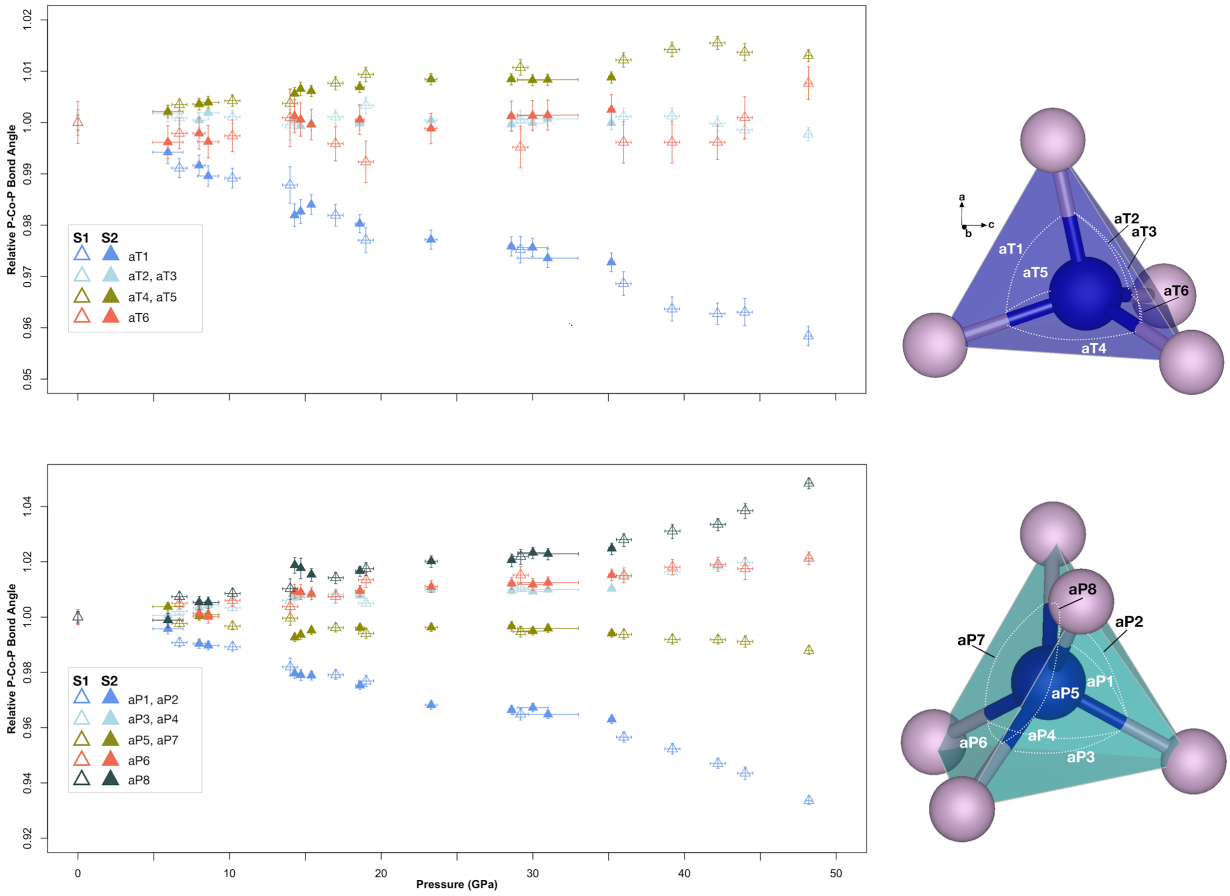

Figure 5.17. Relative bond angles with pressure within the CoP_4 tetrahedrons and the CoP_5 square pyramid building blocks of the αCo_2P structure. The aT1 angle shrinks significantly with pressure and is aligned along the *a* axis. Within the square pyramids, the aP1 and aP2 angles shrink the most with pressure and are mostly aligned with the *a* axis and the aP8 angle opens with pressure along the *a* axis. The behavior of these angles under compression distort the polyhedra and accommodate the softening along the *a* axis with pressure.

significant components of which are aligned with the *a* axis. Conversely, angles such as the aP8 angle, oriented roughly perpendicular to the *a* direction broaden with pressure. Above 35 GPa, a discontinuity is observed where the narrowing and broadening behavior of these angles becomes more pronounced and the CoP4 and CoP5 building blocks become increasingly distorted.

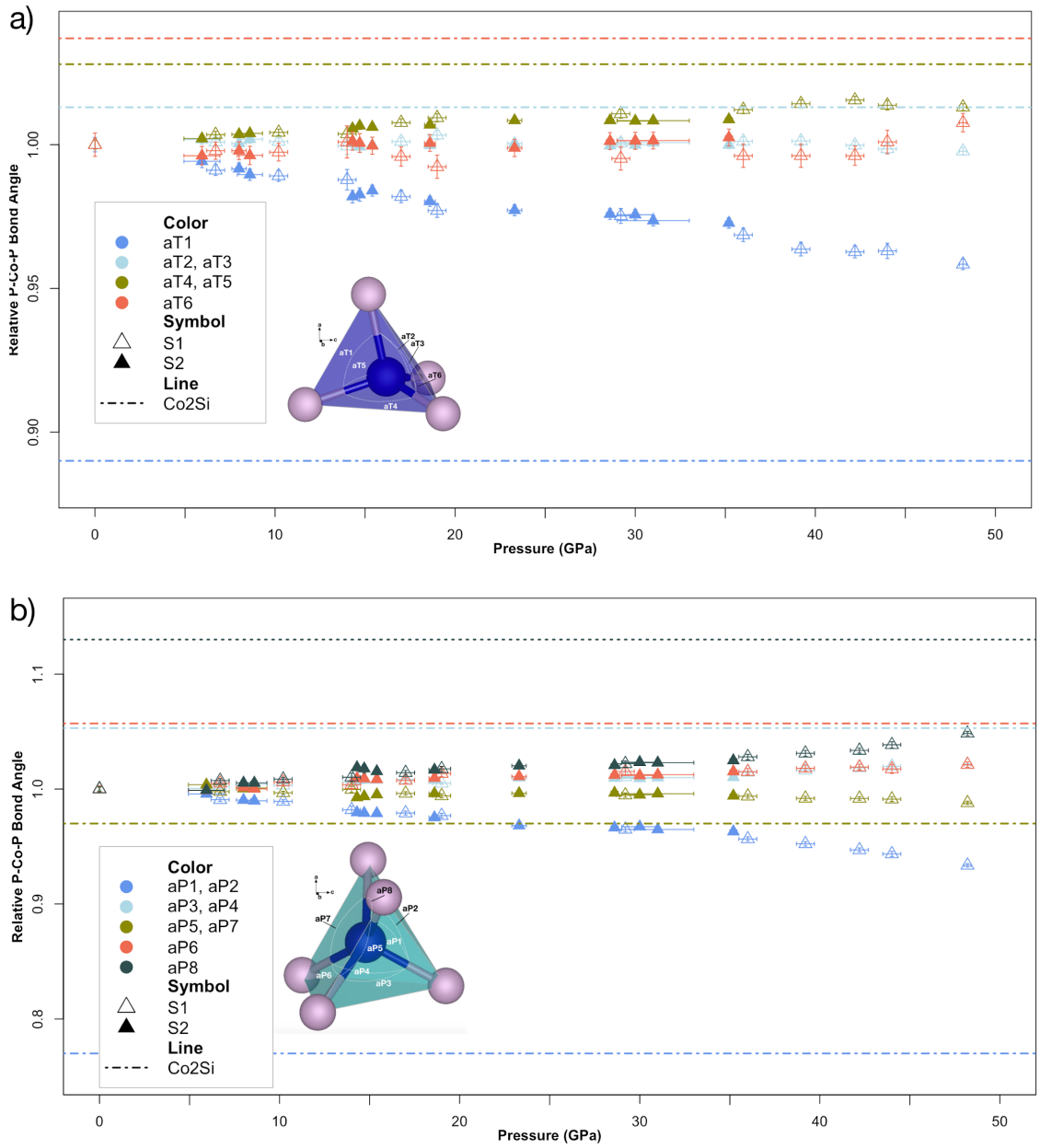

Figure 5.18. Relative bond angles within the αCo$_2$P tetrahedral and square pyramid blocks compared to the respective relative bond angles within a Co$_2$Si structure (horizontal dashed-dot lines).

Figure 5.18 shows the relative bond angles of Co$_2$Si-type structure compared to the data shown in Figure 5.17. Overall, the discontinuity in bond angle compression observed above 35 GPa brings the bond angles in Co$_2$P closer to coincidence with the Co$_2$Si structure, but

significant changes in the bond angles are still required to achieve the Co_2Si structure (Figure 5.18). Namely, the aT1 and aP8 angles must change by ~10% and the aP1, aP2 angles must narrow by ~25%. The aT6 must also begin to broaden by ~5%. The broadening of the aT6 angle is paired with the movement of the Co1 towards that edge of the tetrahedral building block (Figure 5.13, 5.17).

The bond lengths and angles determined for αCo_2P were then used to calculate the distortion indices (Bauers 1974) and bond angle variances (Robins et al. 1971) for each pressure point (Figure 5.19). The distortion index (Bauers 1974) is a measure of how each bond length within a polyhedron differs from the average and is given by equation 5.2.

$$D = \frac{1}{n}\sum_{i=1}^{n}\frac{|l_i - l_{\mathrm{av}}|}{l_{\mathrm{av}}}, \tag{5.2}$$

where n is the number of atoms coordinated to the central atom of the polyhedron, l_i is a given bond length and l_{av} is the average bond length in that polyhedron.

The bond angle variance (Robins et al. 1971) is a comparison of how each bond angle in the polyhedron differs from the ideal bond angle for that given type of polyhedron (i.e. 109.5º for a tetrahedron, 90º for a square pyramid). The bond angle variance is given by equation 5.3.

$$\sigma^2 = \frac{1}{m-1}\sum_{i=1}^{m}(\phi_i - \phi_0)^2 \tag{5.3}$$

where m is the number of bond angles in the polyhedron, ϕ_i is a given bond angle, and ϕ_0 is the ideal bond angle for that polyhedron.

These values are plotted with pressure for the tetrahedral and square pyramid building blocks of αCo_2P in Figure 5.19. The dashed lines in Figure 5.19a, b demarcate the ambient

pressure αCo_2P values while the dotted lines give the respective Co_2Si values. αCo_2P exhibits relatively constant distortion indices between ambient pressures and 35 GPa (Figure 5.19a), and above 35 GPa, the distortion index of the square pyramids and tetrahedrons begin evolving towards values that are similar to what is observed in the 1 bar Co_2Si structure (Figure 5.19a).

The bond angle variance for the square pyramids show a decreasing trend with pressure, meaning that the bond angles are getting closer to 90.º This behavior coincides with the movement in atomic coordinates where the central Co atoms are observed to move towards the base of the square pyramids with pressure (Figure 5.13). It is clear, however, that to achieve a Co_2Si structure, the bond angle variance of the square pyramids must reach a minimum beyond which they begin deviating significantly from 90º as shown by the dotted green line in Figure 5.19b. Comparatively, the Co sites within square pyramid building blocks in the Co_2Si structure do lie on the base of the square pyramid polyhedron, but the P sites are shifted such that the P site at the top of the square pyramid shifts to align with one side of the base. Therefore, change in bond angle variance to form the Co_2Si structure is attributable to the change in atomic coordinates of the P sites. This result supports the required change in direction of the P_x atomic coordinate to form the Co_2Si structure as shown in Figure 5.14.

In the tetrahedral building blocks, an increasing trend in bond angle variance is observed, meaning that the bond angles are deviating from the ideal bond angle of 109.5º with pressure (Figure 5.13). The bond angle variance of the tetrahedral sites must continue to increase to reach a Co_2Si-like configuration and it is unclear how a 4- to 5-fold coordination change on this Co1 site would affect the bond angles compared here.

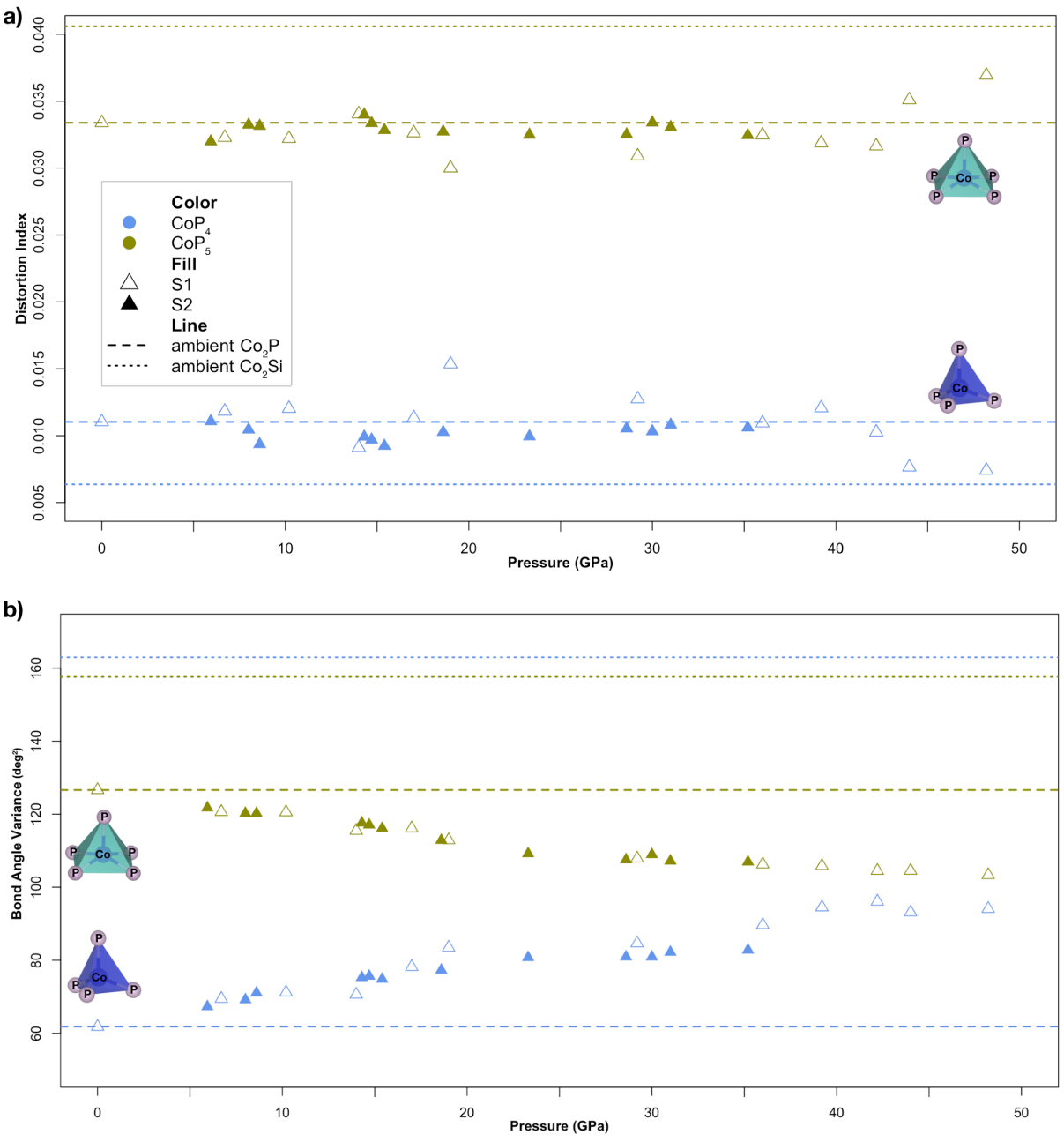

Figure 5.19. Distortion indices (Bauers 1971) and bond angles variances (Robins et al. 1974) with pressure determined for the tetrahedral and square pyramid building blocks of αCo_2P. The dashed lines indicate the ambient pressure distortion indices and bond angle variances for Co_2P and the dotted lines indicate the respective values for a Co_2Si structure.

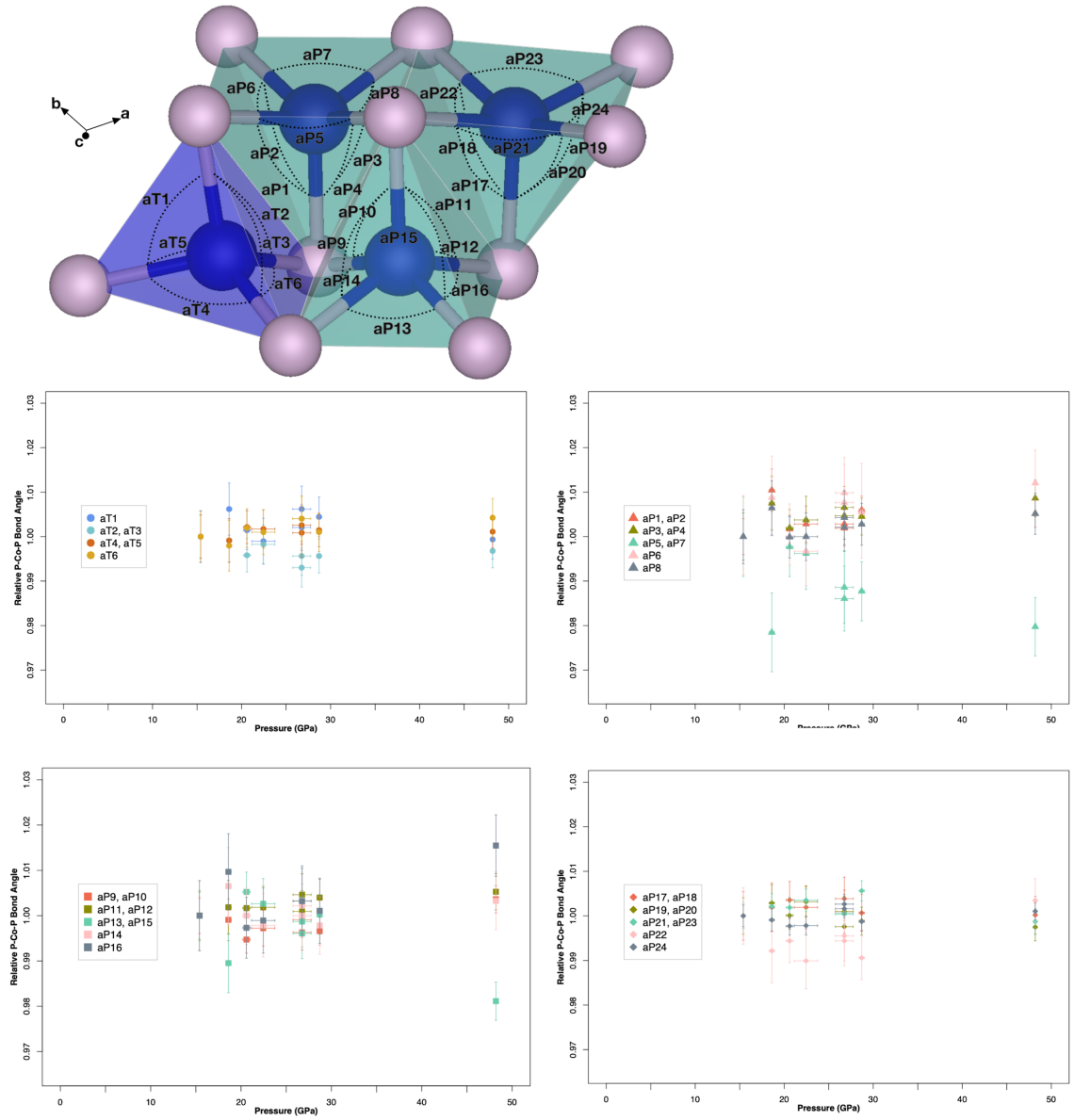

Figure 5.20. Relative bond angles calculated for $Co_{12}P_7$ between 15 and 48 GPa within the tetrahedral and three square pyramidal sites.

The atomic coordinates of $Co_{12}P_7$ and CoP were refined at 8 and 5 pressure steps respectively between 15 and 48 GPa. The Co-P bond lengths within the polyhedra of these phases show uniform compression across this pressure range (Figure 5.15b, c). The compression behavior observed for these two phases can be viewed by the distortion of the bond angles within

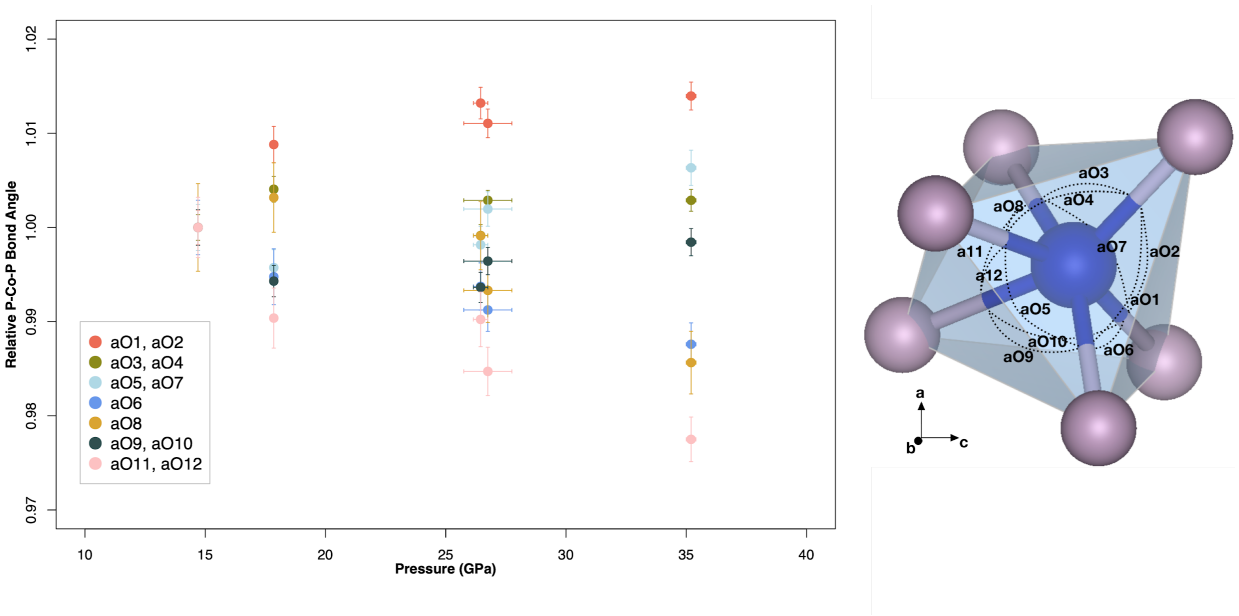

Figure 5.21. Relative bond angles calculated for CoP between 15 and 35 GPa. The CoP structure is composed of CoP_6 distorted octahedra.

the polyhedra building blocks. $Co_{12}P_7$ exhibits a more compressible *a* axis above 15 GPa, accommodated by the shrinking of two bond angles oriented along the *a* axis within one of the square pyramid building blocks (aP5, aP7 in Figure S5i). The compression along the *b* axis in the *B*31 CoP structure appears to be accommodated by the combined opening of angles predominantly oriented perpendicular to the *b* axis and closing of bond angles that lie along the *b* axis (aO1, aO2 and aO11, aO12 respectively, Figure 5.21).

5.4. Implications

The orthorhombic Co_2P structure was examined in this study as a more accessible, low-pressure analog to the high pressure behavior of Fe_2P (Dera et al. 2008) and Fe_2S (Tateno et al. 2019; Zurkowski et al. in press; Zurkowski et al. submitted, Chapter 4). Recent examinations of Fe_2P have indicated that, at low pressures and moderate temperatures, *C*23 Fe_2P exhibits high

compressibility along the *a* axis compared to the *b* and *c* axes (Dera et al. 2008). Above 42 GPa, a *C*23–*C*37 Fe_2P transition has been reported (Nakajima et al. 2020). In recent studies, *C*23 Fe_2S is shown to exhibit a highly compressible *a* axis and form into a *C*37-like unit cell between 120 and 150 GPa (Zurkowski et al. submitted, Chapter 4). The results of the current study verifies that Co_2P exhibits analogous behavior to both Fe_2S and Fe_2P and by solving and refining the structure of *C*23 Co_2P to 48 GPa, the compressibility of this structure as well as mechanism for a pressure-induced *C*23–*C*37 M_2X transitions may be discussed in more detail.

*C*23 Co_2P exhibits pronounced compression along the *a* direction that is a predominant result of distortion of the components of bond angles oriented along the *a* direction (Figure 5.17). The compression behaviors of the bond lengths and angles becomes more pronounced above 35 GPa, resulting in a softening of the *a* axis and stiffening of the *b* and *c* axes (Figure 5.10). In terms of the atomic coordinates, all sites are migrating with pressure towards the respective positions in a Co_2Si structure, except for the P_x coordinate (Figure 5.16). A change in position of this coordinate may be achieved in a coordination change in the transition to the *C*37 structure.

A graphical depiction of the *C*23–*C*37 evolution with pressure is depicted in Figure 5.22, where a unit-cell of (a) *C*23 Co_2P at ambient conditions (this study) is compared to a unit-cell of (b) *C*23 Co_2P at 48 GPa (this study) and to a unit-cell of (c) Co_2Si (Geller and Wollontis 1955). The square pyramid building blocks are shaded in green to guide the eye and the Co_2P tetrahedral building blocks are left unshaded because a 4- to 5-fold coordination change on this Co site occurs between Figure 5.22b and Figure 5.22c. Our results support that compression along the *a* direction distorts the bond angles oriented along the *a* direction and in turn shapes the αCo_2P structure towards the Co_2Si structure. The distortion of the bond angles also shifts the Co1

sites closer to the next nearest P site along the *a* direction, and *C*23 Co_2P is tending towards a CoP_4–CoP_5 coordination change across the pressure range of this study (Figure 5.22 b, c). Further experiments at still higher pressures are required to determine the pressure where this coordination change occurs.

The similarity in the αCo_2P structure under compression and the Co_2Si structure shown in Figure 5.22 is suggestive of a possible Co_2P–Co_2Si transition that evolves over a range of pressures, as is observed in Fe_2S at high pressures (Zurkowski et al. submitted, Chapter 4). However, the *C*23–*C*37 transition in Fe_2P was reported to occur over a few GPa around 42 GPa (Nakajima et al. 2020). Certain aspects of the high pressure Co_2P structure, such as distortion of the bond angles and the distortion indices based on the bond lengths, support that the Co_2P–Co_2Si transition is evolving gradually with pressure, but other aspects of the Co_2P structure, such as the movement of the P sites (Figure 5.14) and the bond angle variance in the polyhedra (Figure 5.19b), must undergo significant change to achieve the *C*37 structure. It remains unclear whether the *C*23–*C*37 transition will occur gradually with increasing pressure or if structural changes will occur more rapidly at high pressures as new atomic interactions initiate. Future work may confirm how the compression behavior of αCo_2P develops above 48 GPa and resolve the *C*23–*C*37 transition pressure for Co_2P.

The *C*23-*C*22 phase transition is observed in Co_2P at ambient conditions between 1430 and 1660 K (Ellner and Mittemeijer 2001) and at 31 GPa and 1880 K (current study), indicating a positive phase boundary slope between the stability fields of these phases. Both the *C*23 and *C*22 structures have been observed in Fe_2P and Fe_2S below 8 GPa and at 21 GPa, respectively (Dera et al. 2008; Koch Müller et al. 2002), but the high temperature stability of these phases in

the *C*22 structure has not been investigated at high pressures. In support of this observed behavior in Co_2P, *ab-initio* calculations of Fe_2P conducted by Litasov et al. 2020 indicate that *C*23 Fe_2P may be a low temperature polymorph and *C*22 Fe_2P a high temperature polymorph with a positive phase boundary slope with pressure. Future Fe_2P and Fe_2S experiments may seek to explore this phase transition as it may have important implications for the Fe-rich sulfide liquidus phase in terrestrial planetary cores and the *P-T* history of recovered iron meteorites.

The stability of Co into an ordered $Cr_{12}P_7$ structure with pressure and temperature was first established in this study, and it is evident that $Co_{12}P_7$ has the same building blocks as the *C*23 and *C*22 Co_2P structures (Figure 5.1). The $Co_{12}P_7$ unit cell has an additional P atom for every 6 unit cells of Co_2P and this change in stoichiometry results in a change in the square pyramid to tetrahedral site ratio from 1:1 for Co_2P to 3:1 for $Co_{12}P_7$. The 3:1 square pyramid to tetrahedral site ratio in $Co_{12}P_7$ is accompanied by the formation of trigonal prismatic channels along the *c* direction in $Co_{12}P_7$ (Figure 5.1). Despite the similar arrangement of polyhedral building blocks in these structures, the current compression curves of αCo_2P and $Co_{12}P_7$ indicate that $Co_{12}P_7$ is less compressible than αCo_2P and exhibits less pronounced anisotropic compression. These results reveal that the 3:1 ratio of square pyramid to tetrahedra building blocks and the trigonal channels formed in the $Co_{12}P_7$ unit cell make for an overall less compressible structure. The stability of this phase at high pressures and temperatures and the similarities in the Co_2P and $Co_{12}P_7$ structures makes the $Co_{12}P_7$ structure another potential analog to high-pressure Fe-phosphides and sulfides.

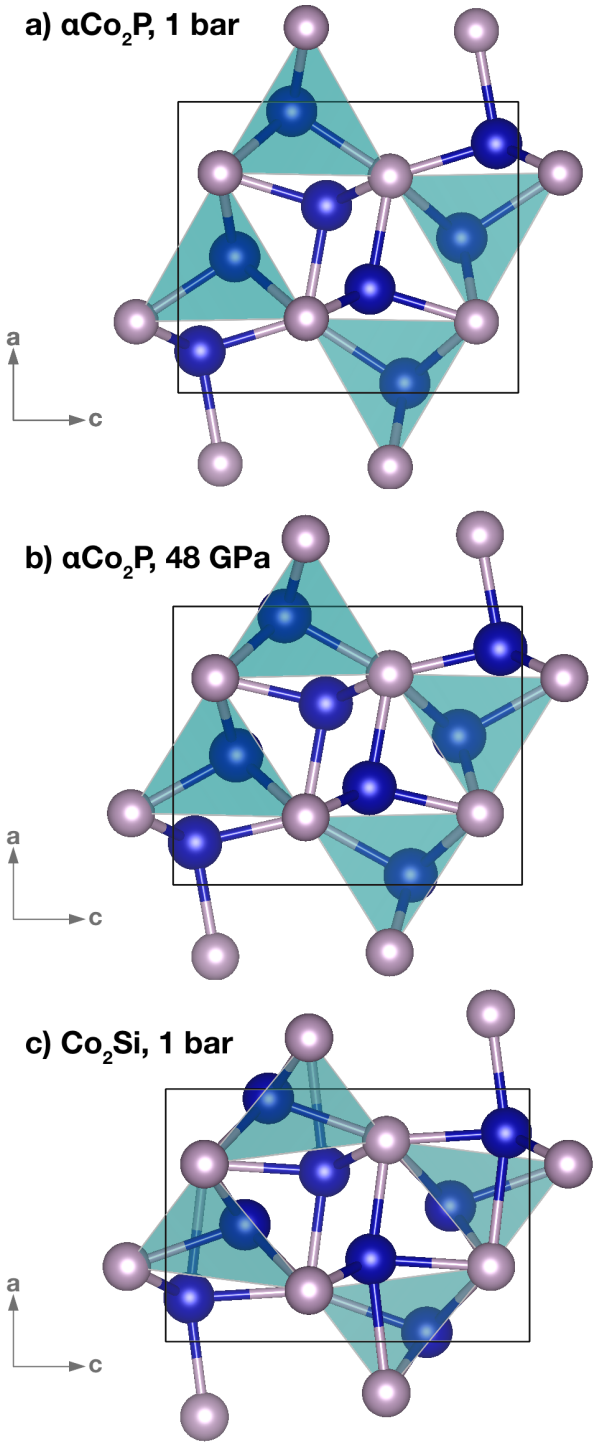

Figure 5.22. Comparison of a) the *C*23 Co_2P structure at ambient conditions, b) the *C*23 Co_2P structure at 48 GPa and c) the *C*37, Co_2Si structure viewed down the *b* axis. This visualization demonstrates how compression shapes the *C*23 structure towards a *C*37 structure.

CoP is observed to take the MnP structure with room temperature compression up to 36 GPa in the current study. The anisotropic compression along the *b* axis observed in CoP in the current study is also observed in MnP with pressure (Yu et al. 2017). CoP serves as an important analog to FeS and FeP, as the *Pnma* CoP structure characterized here between 15 GPa and 36 GPa at room temperatures is observed in FeS above 3.4 GPa and again above 35 GPa with differing magnetic properties (King and Prewitt 1982; Ono et al. 2008). These results confirm that the structural stability of CoP precedes in pressure the stability of isostructural FeS phases. As the *B*31 structure is a modification of the *B*8 structure, further examination of the CoP with pressure may provide insight into the formation and stability of the *B*8 FeS structure that has been reported at Earth's outer core pressures (Ozawa et al. 2013).

5.5. Conclusions

The Co_2P, $Co_{12}P_7$ and CoP compounds were explored to 48 GPa and 1900 K using single crystal X-ray diffraction techniques. Co_2P adopts the *C*23 structure upon compression and heating to 48 GPa and moderate temperatures. At 31 GPa and 1900 K, *C*23 Co_2P transitions to *C*22 Co_2P. $Co_{12}P_7$ is observed in the ordered $Cr_{12}P_7$ structure between 15 and 48 GPa and at moderate temperatures. *B*31 CoP was synthesized upon heating to 17 GPa. A room temperature equation of state is reported for the *C*23 Co_2P, $Co_{12}P_7$ and CoP. Notably, *C*23 Co_2P exhibits a highly compressible *a* axis, predominantly as a result of bond angle distortion and compression of bond lengths along the *a* direction. A discontinuity is observed above 35 GPa at which the *a* axis softens and the *b* and *c* axes stiffen, accompanied by an intensification of the distortion trends within the atomic arrangement of the structure. As a result, the *C*23 Co_2P structure

compresses towards a *C*37, Co_2Si-like structure as has been inferred from Fe_2P and Fe_2S powder diffraction studies. The *C*23–*C*22 high temperature Co_2P phase transition observed at 31 GPa and 1800 K establishes that the *C*22 Co_2P phase is stable to high pressures and temperature with a positive *C*23–*C*22 phase boundary slope. The *C*23, *C*22, $Co_{12}P_7$ and *B*31 structure types have been analogously observed in Fe_2S, Fe_2P, $Fe_{12}S_7$, FeP and FeS at higher pressures, supporting that these structural characterizations in the Co-P system provide a basis for systematic comparison to the higher-pressure behavior of the iron sulfides and phosphides that may play a role in the thermodynamics of Earth and planetary cores.

6. Phase stability of Fe_3S, Fe_2S and the novel $Fe_{12}S_7$ to 125 GPa based on single-crystal X-ray diffraction techniques: implications for terrestrial planetary core crystallization

Collaborators: Barbara Lavina[b,c], Stella Chariton[c], Vitali Prakapenka[c], Andrew J. Campbell[a]

[a]University of Chicago, Department of the Geophysical Sciences, 5734 S Ellis Ave, Chicago, IL 60637, USA
[b]X-ray Science Division, Advanced Photon Source, Argonne National Laboratory, Argonne, IL 60439, USA
[c]Center for Advanced Radiation Sources, 9700 South Cass Avenue, Building 434A, Argonne, IL 60439, USA

6.1. Introduction

At the extreme pressures of Earth's outer core, the iron content of the stable sulfide in Fe-saturated systems changes from 75 at% Fe in Fe_3S to ~67 at% Fe in Fe_2S (Tateno et al. 2019), prompting renewed interest in the phase stability of S-rich Fe-sulfides at high *P-T*. Recent investigations of the Fe-S–Si system at conditions related to the Mercurian core further reveal that the presence of Si expands the stability field of Fe_2S compared to Fe_3S (Tao and Fei 2021). High *P-T* studies of analog transition metal systems such as the cobalt-phosphide system have also revealed novel $M_{12}X_7$ compounds that are stabilized with pressure, in a hexagonal structure that is closely related to the *C*23 and *C*37 structures of Fe_2S (Zurkowski et al. 2020, Chapter 5). As the Fe-content of a potential $Fe_{12}S_7$ compound exists between that of the known sulfide compounds, Fe_3S_2 and Fe_2S, the stabilization of such a stoichiometry with pressure may be important in the context of S-rich exoplanetary cores.

In the current study, the structural stability of Fe_3S, Fe_2S and $Fe_{12}S_7$ was explored using single-crystal X-ray diffraction techniques in a laser heated diamond anvil cell between 100 and 125 GPa and quenched from high temperatures. Fe_3S is confirmed to adopt the tetragonal, Fe_3P-type structure at these conditions. Fe_2S is observed in the *C*23 structure (Co_2P-type, *Pnma*, *Z*=4) (Rundqvist 1960) at lower temperatures, in agreement with Zurkowski et al. in press, and transforms to the Fe_2P-type, *C*22 structure (*P*-62*m*, *Z*=3) (Rundqvist and Jellinek 1959) at high temperatures. This hexagonal phase of Fe_2S is in agreement with the relative Fe_2S unit-cell recovered from 21 GPa and 1900 K, indicating a potentially wide high temperature stability field of hexagonal Fe_2S (Koch-Müller et al. 2002). At 125(3) GPa, Fe_2S was quenched at moderate temperatures in a Cr_2P-type structure (*I*2*mm*, *Z*=12) (Artigas 1996). This structure has been previously reported as a low temperature modification of the *C*22 structure (Atrigas et al. 1996), and is closely related to the *C*22 and *C*23 structures (Blanchard et al. 2008). Synthesis of this phase may represent the structural pathway to transitioning from the *C*23 to *C*22 structure with temperature or a distortion on fast cooling from the *C*22 structure. The novel $Fe_{12}S_7$ is observed in the pressure and temperature range probed in this study and forms in the $Co_{12}P_7$ structure (*P*-6, *Z*=1) (Zurkowski et al. 2020). Results from single-crystal X-ray diffraction experiments on multigrain samples are reported and discussed in this work. The synthesis of these high *P*-*T* Fe_3S and novel Fe_2S and $Fe_{12}S_7$ phases present interesting chemical and dynamic interactions if present in an S-rich planetary and exoplanetary cores.

6.2. Materials and methods

The starting material used in this study consisted of Fe (99.9+%, <10 μm, Alfa Aesar) powder and iron sulfide (FeS, 99.99%, Alfa Aesar) mixed into two compositions: one with a ratio of 1g Fe to 1.78 g FeS (~$Fe_{66}S_{34}$) and one with a ratio of 2.1g Fe to 1 g FeS (~$Fe_{80}S_{20}$). The starting materials were homogenized in a mortar and pestle for one hour in alcohol, dried, and then mixed dry for a short time. This final dry mixing accounts for density separation during alcohol evaporation and is conducted for a short duration to limit Fe-oxidation. The final starting materials were then compressed into foils between two ungasketed diamond anvils prior to loading.

Pressure was generated using short symmetric and BX-90-type diamond anvil cells equipped with Boehler-Almax conical diamonds and seats. Diamonds with 150 μm culets that beveled to 300 μms were used. Sixty-μm sample chambers drilled out of preindented rhenium gaskets were each loaded with a sample foil placed between layers of KCl pressure transmitting medium. During compression, the equation of state of KCl (Dewaele et al. 2012) was used to monitor pressure. The agreement between measured unit-cell parameters and structural refinement models, for multiple grains of each phase in this study, support that deviatoric strain from the quenched KCl medium did not play a major role in the observed structural geometries and did not inhibit structural analysis.

Double sided laser heating of the pressurized samples was conducted at beamline 13-ID-D (GeoSoilEnviroCARS) of the Advanced Photon Source, Argonne National Laboratory following Section 2.4. Four ~30-minute heating experiments in the 100–125 GPa pressure range were carried out in this study. Run 1 was conducted on the $Fe_{66}S_{34}$ starting composition at

Table 6.1. Experimental conditions and instrument parameters used for the diffraction data collected in this study.

	Run 1	Run 2	Run 3	Run 4
Starting composition (at %)	$Fe_{66}S_{34}$	$Fe_{66}S_{34}$	$Fe_{80}S_{20}$	$Fe_{80}S_{20}$
Pressure (GPa)	105.3(9)	125(1)	101(3)	118(2)
Synthesis Temperature (K)	2400(120)	2260(140)	2670(240)	2390(220)
Synthesis Beamline	13IDD @ APS	13IDD @ APS	13IDD @ APS	13IDD @ APS
Collection Temperature (K)	296	296	296	296
Collection Station	13IDD @ APS	13IDD @ APS	13BMD @ APS	13BMD @ APS
Radiation type	synchrotron	synchrotron	synchrotron	synchrotron
λ (Å)	0.2952	0.2952	0.3344	0.3344
Beam size (FWHM) *horizontal* x *vertical* (μm)	2 x 3	2 x 3	5 x 8	5 x 8
Detector	CdTe 1M Pilatus	CdTe 1M Pilatus	Perkin-Elmer 16" amorphous silicon digital	Perkin-Elmer 16" amorphous silicon digital
omega range (°), step size (°), exposure time (s)	±30, 0.5, 2	±30, 0.5, 2	±30, 0.5, 2	±30, 0.5, 2

105.3(9) GPa and quenched from 2400(120) K. The sample was then pressurized to 125(1) GPa and heated to 2260(140) K prior to quenching in Run 2. A $Fe_{80}S_{20}$ sample was compressed in Run 3 to 101(3) GPa and heated to 2640(240) K, then compressed to 118(2) and heated to 2390(220) K in Run 4. A summarization of the experimental conditions and instrument parameters used in this study is given in Table 6.1.

Upon quenching at each pressure, X-ray diffraction was conducted at beamlines 13-ID-D and 13-BM-D (GeoSoilEnviroCARS) of the Advanced Photon Source, Argonne National Laboratory following Section 2.4. Around the center of the laser heated spots, 10 x 10 μm

diffraction maps were collected in 3 μm steps to assess the regions of optimal grain growth. Centered at selected map locations, angular scans were collected and the single crystal diffraction data containing grains of Fe_3S, Fe_2S and $Fe_{12}S_7$ grains was processed following Section 2.5. Due to the small size of the sample chambers, ~30 μm at target pressures, diffraction from the rhenium gasket was also observed in the rotational scans.

6.3. Results and discussion

6.3.1. *Synthesis and indexation of the target phases*

The *P-T* synthesis conditions for this study are provided in Table 6.1 and visualized *P-T* space in Figure 6.3. Upon quenching the $Fe_{66}S_{34}$ sample at 105.3(9) GPa in Run 1, grains associated with two differing hexagonal lattices were synthesized at the center of the laser heated spot (Figure 6.1a, Table 6.2). One set of grains was indexed to a hexagonal unit cell with parameters a = 5.326(7) Å and c = 3.125(3) Å, compatible with 3 formula units of Fe_2S. The second set of hexagonal grains was indexed to a unit cell with a = 7.794(2) Å and c = 3.1234(8) Å, compatible with 1 formula unit of $Fe_{12}S_7$. A few grains of an orthorhombic lattice, compatible with C23 Fe_2S, were also observed (Zurkowski et al. in press). After quenching the $Fe_{66}S_{34}$ sample 125(3) GPa from 2260(240) K (Run 2, Table 6.1), the heated region was predominately comprised of grains of $Fe_{12}S_7$ and a body-centered orthorhombic lattice with parameters a = 5.382(1) Å, b = 6.103(4) Å, c = 9.098(4) Å (Figure 6.1b, Table 6.2). The volume of this phase matches 12 formula units of Fe_2S. One grain of hexagonal Fe_2S and a few grains of C23 Fe_2S were also observed within the heated region. In Runs 3 and 4 between 101 and 118 GPa in the

$Fe_{80}S_{20}$ composition (Table 6.1), only grains indexed to a tetragonal lattice were observed with a = 8.227(4) and c = 4.062(4) at 101(3) GPa and a = 8.166(2) Å and c = 4.010(2) Å at 118(2) GPa, matching to 8 formula units of Fe_3S (Figure 6.1c, Table 6.2). Diffraction from KCl, Re and hcp-Fe are also observed and are labeled in each frame of Figure 6.1. Iron is observed as low intensity, uniform rings at high temperature in the $Fe_{66}S_{34}$ composition (Runs 1, 2; Figure 6.1a, b), likely indicating diffraction from the outer, unreacted regions of the sample chamber probed by the tails of the X-ray beam. The sharp reflections observed near the hcp-Fe (100) and (101) diffraction angles in Run 1 and 2 (Figure 6.1a, b) are attributable to the Fe_2S and $Fe_{12}S_7$ phases as labeled. Fe_3S was synthesized with recrystallized hcp-Fe (Figure 6.1c).

6.3.2. Solving and refining the target phases

After each heating cycle, the samples are multigrain (Figure 6.1), allowing for single crystal analysis of the synthesized Fe-S phases. Several components of high P-T synthesis do limit the capability to structurally solve and refine these crystal structures; namely, limited angular sample access in the diamond-anvil cell, overlap in diffraction angles of target phases with diffraction from other grains, rhenium, and the KCl insulator, and the amount of the grain illuminated by the X-ray beam. Despite these challenges, sufficient reflections were obtained for each Fe-sulfide phase and each phase was structurally solved and refined (Table 6.2). For the refinement models shown in Table 6.2, an independent-reflection-to-parameter ratio greater than 6 was maintained, demonstrating that sufficient reflections were collected for the number of parameters in the refinement models at these high-pressure conditions (e.g., Lavina et al. 2014).

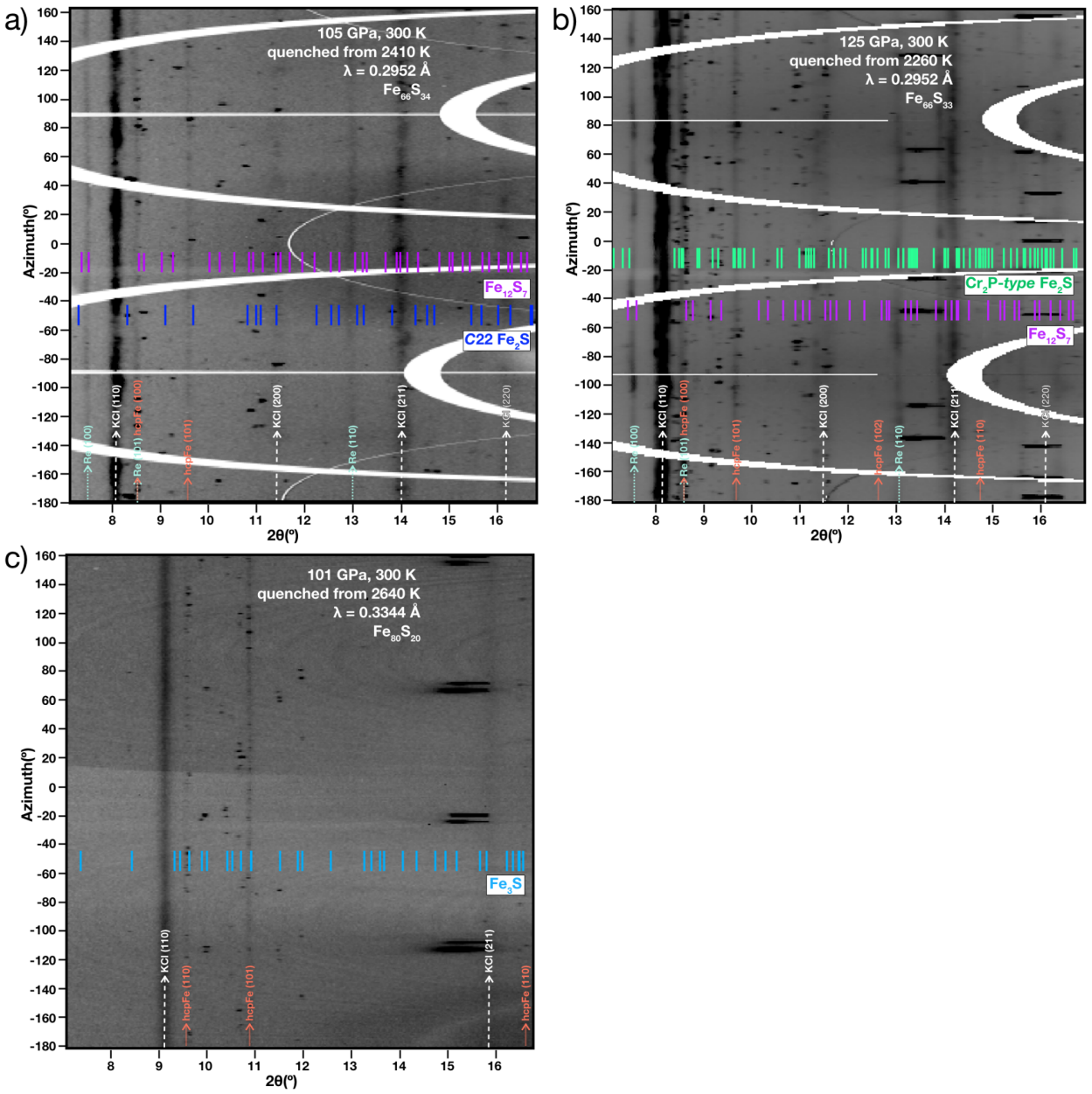

Figure 6.1. Raw diffraction patterns collected after temperature quenching in a) Run 1, b) Run 2, and c) Run 3 labeled with the synthesized Fe-sulfides characterized in this study. a) After quenching from 105.3(9) GPa and 2400(120) K in the $Fe_{66}S_{34}$ starting composition, the pattern is dominated by reflections from *C*22 Fe_2S and $Co_{12}P_7$-type $Fe_{12}S_7$. b) After temperature quenching from 125(3) GPa and 2260(140) K in the $Fe_{66}S_{34}$ starting composition, reflections from Cr_2P-type Fe_2S and $Co_{12}P_7$-type $Fe_{12}S_7$ are observed. c) Fe_3S formed in the Fe_3P-type structure was observed after quenching from 2670(240) K at 101(3) GPa in the $Fe_{80}S_{20}$ composition. Diffraction from KCl, Re and hcp-Fe are labeled. Iron is observed as low intensity, uniform rings at high temperature in the $Fe_{66}S_{34}$ composition, likely indicating diffraction from the outer regions of the sample chamber probed by the tails of the X-ray beam.

Table 6.2. Experimental, reduction and refinement parameters for each grain analyzed

Phase	**$Co_{12}P_7$-type $Fe_{12}S_7$**		**C22 Fe_2S**			**Cr_2P-type Fe_2S**	
Sample Name	**C133 P1 map 26**	**C133 P2 map 26**	**C133 P1 map 33**	**C133 P1 map 26**	**C133 P2 map 37**	**C133 P2 map 36**	**C133 P2 map 37**
Synthesis							
Run #	1	2	1	1	2	2	2
Pressure (GPa)	105.3(9)	125(1)	105.3(9)	105.3(9)	125(1)	125(1)	125(1)
Synthesis Temperature (K)	2400(120)	2260(140)	2400(120)	2400(120)	2260(140)	2260(140)	2260(140)
Symmetry	Hexagonal, *P*-6, Z=1		Hexagonal, *P*-62*m*, Z=3			Orthorhombic, *I*2*mm*, *Z*=12	
a (Å)	7.794(2)	7.706(3)	5.340(3)	5.326(7)	5.282(5)	5.382(1)	5.380(3)
b (Å)						6.103(4)	6.08(1)
c (Å)	3.1234(8)	3.103(1)	3.133(2)	3.125(3)	3.062(4)	9.098(4)	9.08(1)
V (Å^3)	164.33(8)	159.57()	77.38(9)	76.8(2)	74.0(2)	298.8(2)	296.9(7)
Reduction							
No. of measured, independent and observed [I > 2σ(I)] reflections	386, 263, 226	357, 285, 229	142, 83, 79	135, 80, 69	128, 72, 71	304, 259, 218	251, 217, 191
R_{int}, R_{sigma}	0.014, 0.014	0.011, 0.0210	0.031, 0.017	0.058, 0.456	0.014, 0.015	0.037, 0.039	0.024, 0.031
Refinement							
$R[F^2 > 2\sigma(F^2)]$, $wR(F^2)$, S	0.048, 0.148, 1.16	0.039, 0.109, 1.05	0.041, 0.092, 1.33	0.056, 0.128, 1.11	0.059, 0.160, 1.30	0.077, 0.193, 1.131	0.057, 0.148, 1.066
No. of reflections	263	285	83	80	72	259	217
No. of parameters	32	32	11	11	11	26	26
$\Delta\rho_{max}$, $\Delta\rho_{min}$ (e Å^{-3})	2.60, -1.70	2.26, -1.64	1.15, -1.19	1.31, -1.89	2.17, -2.25	2.40, -2.88	2.18, -2.12
Deviation from full site occupancy	≤6%	≤6%	≤2%	≤7%	≤3%	≤13%	≤18.0%

Table 6.2. ***continued***

Phase	**C23 Fe_2S**				**Fe_3P-type Fe_3S**	
Sample Name	**C133 P1 map 33**	**C133 P2 map 26**	**C133 P2 map 26**	**C133 P2 map 38**	**C140 P1 map 19**	**C140 P2 map 13**
Synthesis						
Run #	1	2	2	2	3	4
Pressure (GPa)	105.3(9)	125(1)	125(1)	125(1)	101(3)	118(2)
Synthesis Temperature (K)	2400(120)	2260(140)	2260(140)	2260(140)	2640(240)	2390(220)
Symmetry	Orthorhombic, *Pnma*, *Z*=4				Tetragonal, *I*-4, *Z=8*	
a (Å)	5.08(1)	4.995(4)	4.940(2)	5.006(3)	8.227(4)	8.166(2)
b (Å)	3.290(2)	3.277(2)	3.280(6)	3.253(2)		
c (Å)	6.146(8)	6.095(2)	6.1522(6)	6.100(7)	4.062(3)	4.010(2)
V (Å^3)	102.77()	99.8(1)	99.7(2)	99.3(1)	274.9(3)	267.4(2)
Reduction						
No. of measured, independent and observed [I > 2σ(I)] reflections	191, 110, 88	221, 123, 106	164, 89, 81	214, 110, 101	345, 273, 166	309, 251, 150
R_{int}, R_{sigma}	0.026, 0.033	0.019, 0.0213	0.0317, 0.0273	0.0186, 0.0178	0.167, 0.219	0.110, 0.197
Refinement						
$R[F^2 > 2\sigma(F^2)]$, $wR(F^2)$, S	0.062, 0.166, 1.05	0.048, 0.123, 1.04	0.066, 0.158, 1.07	0.038, 0.102, 1.175	0.076, 0.161, 0.770	0.054, 0.119, 0.688
No. of reflections	110	123	89	119	273	251
No. of parameters	10	10	10	19	17	17
$\Delta\rho_{max}$, $\Delta\rho_{min}$ (e Å^{-3})	2.83, -2.20	1.82, -2.03	1.63, -1.90	1.37, -1.66	2.24, -2.05	1.56, -1.45
Deviation from full site occupancy	≤5%	≤8%	≤1%	≤3%	≤5%	≤2%

The structures were refined with anisotropic displacement parameters on the metal atoms if enough reflections were collected and a significant improvement to the refinement model was observed. Alternatively, in the case of limited reflections or when adding anisotropic displacement to the metal sites did not result in a change in the refinement output, all sites were refined with isotropic displacement parameters. The errors on metal site occupancies are provided in Table 6.2 for each refinement model and support the reported stoichiometries for the Fe-sulfides analyzed. CIF files for refinement of each new phase in this work (*C*22 Fe_2S, Cr_2P-type Fe_2S, $Fe_{12}S_7$) is provided in the supplementary files SF6a-c.

6.3.3. Structural properties and stability of the Fe_2S polymorphs

The hexagonal Fe_2S phase is observed to dominate the diffraction patterns in Run 1 after quenching from high temperatures at 105.3(9) GPa, and few hexagonal Fe_2S lattices were identified in Run 2 after quenching from more moderate temperatures at 125(3) GPa. During reduction of the reflections indexed to the hexagonal Fe_2S phase for isolated lattices forms Runs 1 and 2, the structure factors observed and systematically absent were determined to be compatible with a *P*-62*m* space group. A *C*22 (Fe_2P-type, *Z*=3) structure solution was then refined to the data with *R*1 values ranging from ~4-6% (Table 6.2). This structure, shown in Figure 6.2a, is composed of two Fe-sites: one 4-fold coordinated and one 5-fold coordinated. Sulfur is in 9-fold coordination with Fe. The FeS_4 and FeS_5 polyhedra are arranged into columns of edge sharing square pyramids (green) and columns of corner sharing tetrahedra (blue) linked along edges in the *c* direction (Figure 6.2a). The square pyramid and tetrahedral building blocks

are symmetric (Figure 6.5). In the square pyramids, all bond lengths making up the bases are equal length and the tetrahedra are composed of two sets of equal length bonds.

In Run 1, a few grains of Fe_2S were identified in the *C*23 structure Co_2P-type, *Pnma*, *Z*=4) (Figure 6.2b, Figure 6.3) in agreement with the structure reported by Zurkowski et al. in press. In Run 2, several *C*23 Fe_2S grains were observed, as the synthesis temperatures were lower (2260(140) K, Table 6.2). The *C*23 structure is reported in analogous systems as a lower temperature M_2X polymorph of *C*22 M_2X phases (Ellner and Mittemeijer 2001), suggesting that synthesis temperatures in Runs 1 and 2 may have been bracketing the *C*23–*C*22 phase boundary. The *C*23 structure similarly consists of columns of edge sharing FeS_5 square pyramids and columns of corner sharing tetrahedra linked along edges in the *b* direction (Figure 6.2b); however, the polyhedral building blocks in the *C*23 structure are less symmetric compared to *C*22 Fe_2S. The bases of the square pyramid building blocks have two sets of equal length bonds and the tetrahedra have two bonds with equal length and two bonds of differing lengths (Figure 6.5). The *C*23 structure has been described to assume the *C*22 structure by modifying shifting chains of *X* sites for M_2X compounds (Chenevier et al. 1987).

In Run 2 at 125(3) GPa and quenched from 2260(120) K and within the same location of the sample (Run 2, Map 26, Table 6.2), two *C*23 Fe_2S grains were observed with distinct differences in lattice parameters (Table 6.2). The grains have the same volume within error, but one grain has a shorter *a* axis and longer c axis compared to the other two grains (Table 6.2). This may reflect some deviatoric strain in the sample chamber, as some fluctuation in the lattice parameters are observed in grains analyzed at a different sample locations (Map 28, Table 6.2),

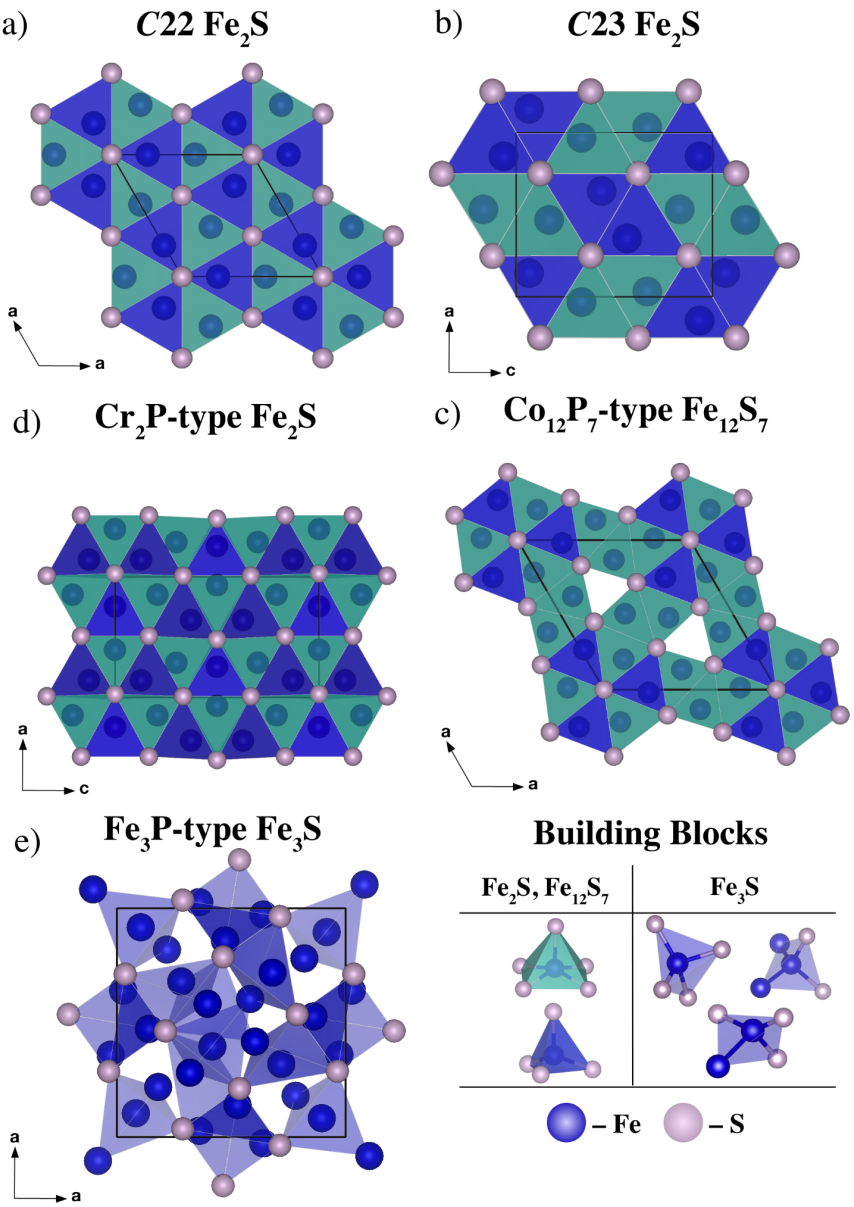

Figure 6.2. Solved and refined structures of the Fe-sulfides observed in this study. a) Hexagonal Fe_2S is observed to adopt the *C*22, Fe_2P-type structure (*P*-62*m*, *Z*=3) which is composed of columns of edge sharing FeS_5 square pyramids (green) and columns of corner sharing tetrahedra (blue) linked along edges along the *c* direction. b) At lower temperatures, grains of orthorhombic Fe_2S in a *C*23, Co_2P-type structure (*Pnma*, *Z*=4) structure are observed. This structure is composed of columns of edge sharing FeS_5 square pyramids (green) and columns of corner sharing tetrahedra (blue) linked along edges along the *b* direction. c) Hexagonal $Fe_{12}S_7$ is observed in the $Co_{12}P_7$-type structure (*P*-6, *Z*=1) which is composed of columns of edge sharing FeS_5 square pyramids (green) and columns of corner sharing tetrahedra (blue) linked along edges along the *c* direction. This structure has the same building blocks and similar arrangement to both the *C*22 and *C*23 Fe_2S structures, but $Fe_{12}S_7$ has an increased ratio of square pyramid to

Figure 6.2. ***continued***
tetrahedral building blocks, resulting in the formation of as trigonal channels along the *c* direction. d) Fe_2S is also observed to assume the *C*37 structure (Co_2Si-type, *Pnma, Z*=4), a distortion of the *C*23 structure, marked by an increased *c*/*a* ratio and increased coordination on the tetrahedral building block. This structure is composed of columns of corner sharing FeS_5 pyramids and columns of edge sharing square pyramids with columns linked along faces in the *b* direction. d) Fe_3S takes the Fe_3P-type (*I*-4, *Z*=8) structure which can be viewed as an arrangement of three 4-fold iron sites with successive incorporation of Fe-Fe bonding.

but the most pronounced distortion is observed between the two grains in map 26 (Table 6.2). The distortion of these grains along the *a* and *c* axes is compatible with the recent observations of a *C*23–*C*37 Fe_2S transition occurring in this pressure range (Zurkowski et al. submitted, Chapter 4). The *C*37 structure (Co_2Si-type, *Pnma*, Z=4) (Geller and Wolontis, 1955) has the same site symmetries as the *C*23 structure, but is marked by a shorter *a* axis and longer *c* axis and increased coordination with the next nearest neighbor along the *a* direction. As described in Chapter 4, between the 120–150 GPa pressure range, the *C*23 Fe_2S relative unit cell more rapidly evolves to be more *C*37 like, suggesting the onset of the coordination change and new atomic interactions. The small but distinct difference in the relative unit cell of the two unit-cells of *C*23 Fe_2S in this study may reflect this transition and the unit cells' sensitivity to pressure at these conditions. Figure 6.4 reports the difference in the polyhedra of two grains analyzed in Map 26 (Table 6.2) and illustrates the proximity of the next nearest S neighbor. The grain labeled "xtl2," with the shortened a axis and longer c axis, also exhibits a shortened distance between tetrahedrally coordinated Fe and the next nearest S neighbor along the a direction. The dashed bonds in Figure 6.4, with bond lengths labeled in red, illustrate the coordination change required to form the *C*37 structure, and the shortening of this distance between the two grains supports an evolution of the *C*23 to the *C*37 structure.

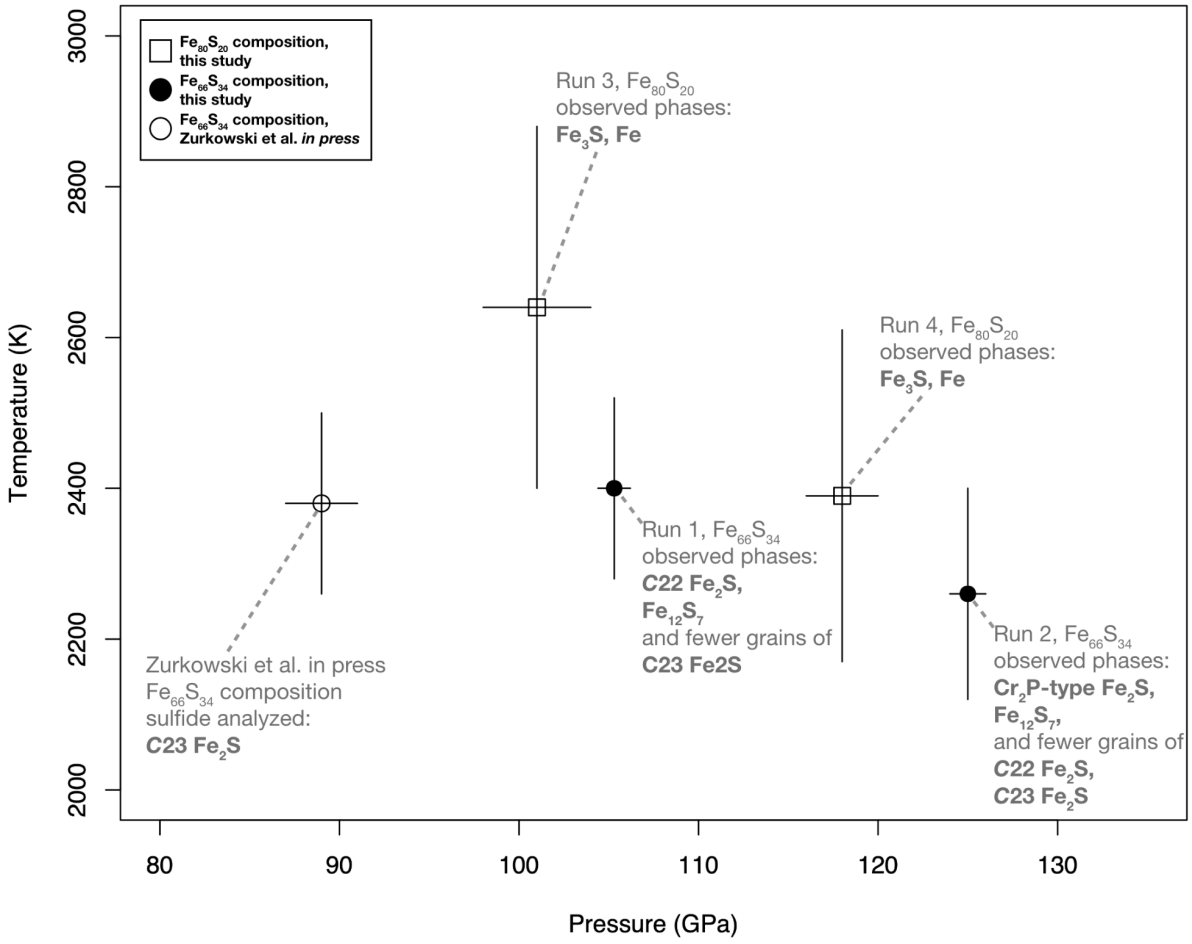

Figure 6.3. Pressure-temperature synthesis conditions in this study compared to that reported by Zurkowski et al. in press. At each synthesis conditions, the Run #, starting composition and observed phases are noted.

In Run 2 at 125(3) GPa and quenched from 2260(120) K in the $Fe_{66}S_{34}$, the presence of *C*23 and a few *C*22 Fe_2S grains within the heated region suggests that the quenching temperature was near the *C*23–*C*22 boundary; however, the diffraction patterns mainly consist of a larger, body-centered orthorhombic Fe_2S lattice (Figure 6.1b, Table 6.2). The unit cell for each grain identified was indexed to an *I*2*mm* space group with 12 formula units per cell volume equal to Fe_2S. The structure was solved and the refinement model revealed that Fe_2S assumes the Cr_2P structure at these conditions (Figure 6.2c). This structure is a slight distortion of the *C*22

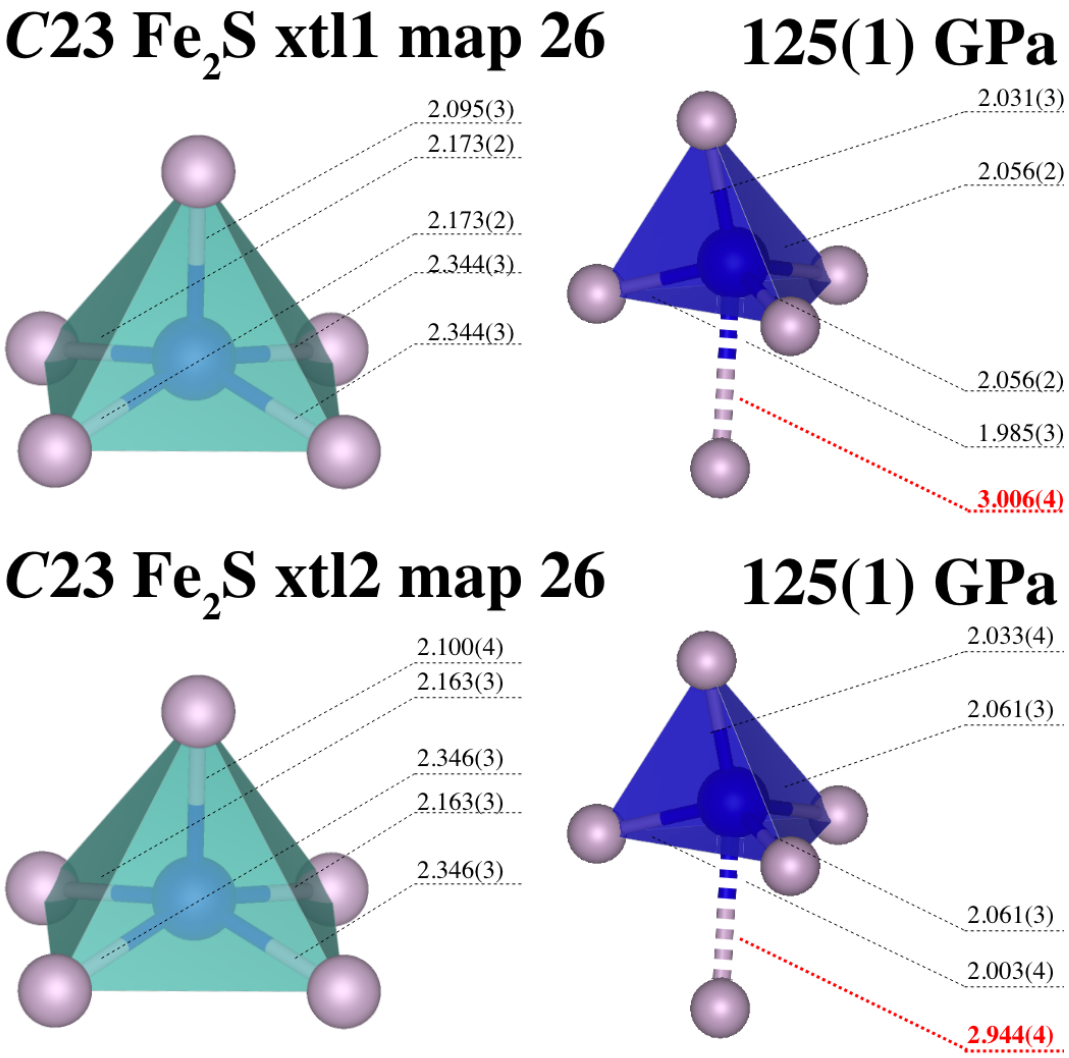

Figure 6.4. Comparison of coordination polyhedra and next nearest P neighbor observed in the *C*23 Fe_2S grains analyzed at 125 GPa

structure and a loss of symmetry is observed in the polyhedra building blocks, resulting in four 5-fold Fe sites and two 4-fold Fe sites (Figure 6.5). Three of the FeS_5 polyhedra maintain a square base, but the bond lengths differ between them. The fourth square pyramid has a base, similar to that of the pyramid polyhedra observed in the C23 structure, that is composed of two sets of equal interatomic distances (Figure 6.5). The polyhedra are also arranged into columns of edge sharing square pyramids and columns of corner sharing tetrahedra, linked along edges in

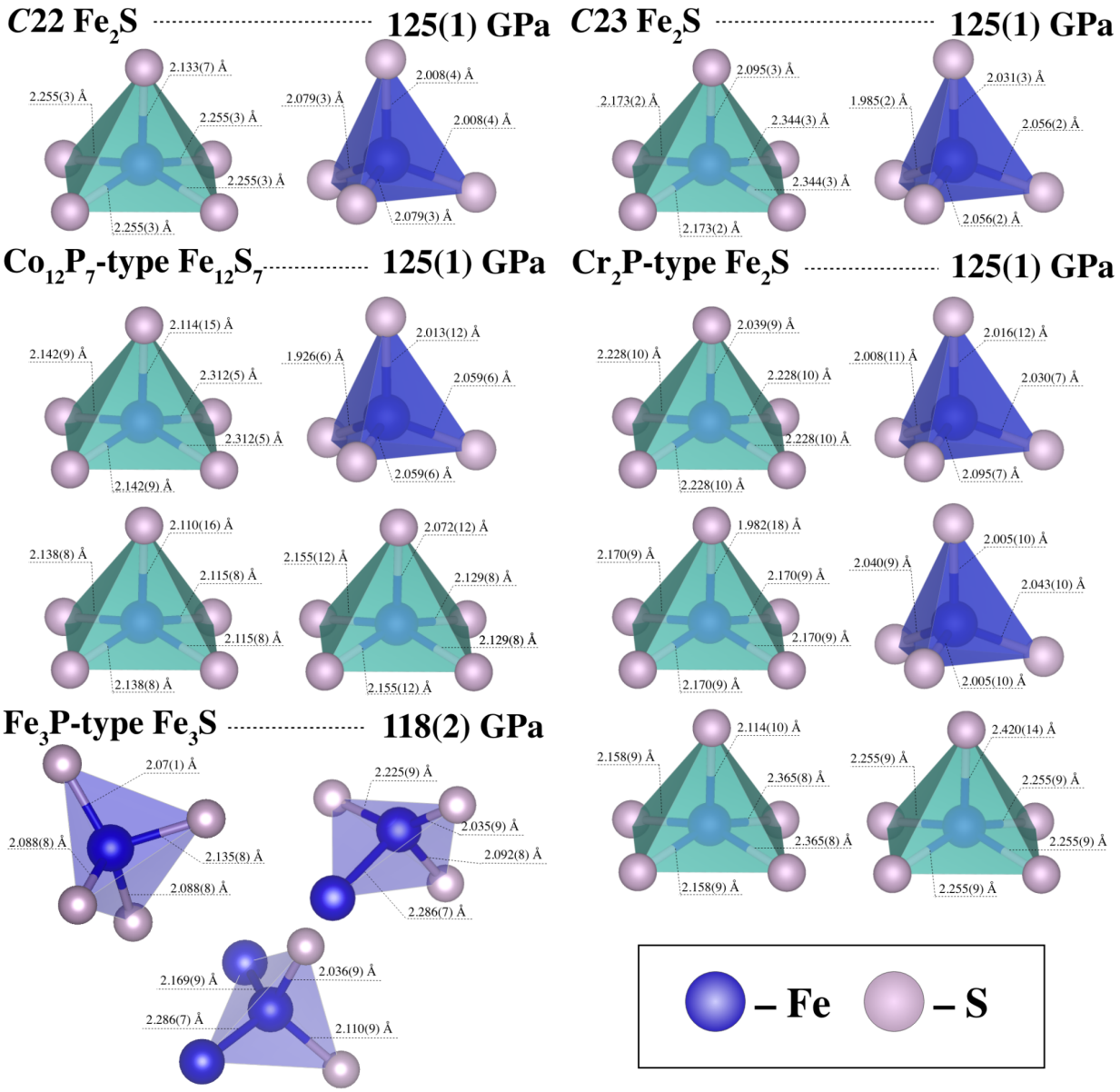

Figure 6.5. Coordination polyhedra with labeled interatomic distances for *C*22 Fe_2S, *C*23 Fe_2S, Cr_2P-type Fe_2S, $Co_{12}P_7$-type $Fe_{12}S_7$ and Fe_3P-type Fe_3S at select pressures.

the b direction. However, unlike the *C*23 and *C*22 structures, the Fe-sites are not uniform within the columns.

Cr_2P has previously been reported as a low temperature modification of the *C*22 structure (Artigas et al. 1996). The quenching temperature, 2260(140) K at 125(3) GPa in Run 2, is lower

than the quenching temperature in Run 1 (Table 6.1), supporting that this may be a low temperature modification of the *C*22 structure. The presence of this phase along the expected *C*23–*C*22 phase boundary complicates the thermodynamics of these Fe_2S phase relations. A few possibilities may be considered regarding the structure stability of Cr_2P-type Fe_2S and each would benefit from future *in-situ* investigation of the Fe_2S phase relations at these conditions. One option is that grains of the *C*22 Fe_2S phase distorted on temperature quenching to the Cr_2P-like configuration and the body centered Fe_2S polymorph is not an equilibrium phase. Alternatively, as the polyhedral building blocks of the Cr_2P-type Fe_2S are intermediate between the *C*23 and *C*22 structures, the presence of this Fe_2S polymorph may represent the sequence of transformation as the sulfur chains shift between the *C*23 and *C*22 structures. In this case, the structure may also be metastable. Finally, the Cr_2P-type Fe_2S could become stable at high pressures and the synthesis conditions may represent a pressure-induced phase boundary. Further *in-situ* work is needed to assess the equilibrium crystallization sequence upon cooling from the *C*22 structure, to assess the metastability of this phase in the context of the *C*23–*C*22 transition, and to assess the phase boundaries in the Fe_2S phase diagram at high *P*-*T*. The deviation from full occupancy for the Fe and S sites refined in the Cr_2P-type Fe_2S structure models (Table 2) are larger than that observed for the other phases examined in this study, suggesting that the Cr_2P-type Fe_2S grains were were not as well formed and may be metastable. Of the transition metal M_2X compounds, the Cr_2P-type structure (*I*2*mm*, *Z*=12) has only previously been observed in Cr_2P and $(Cr, Mn)_2P$ (Artigas et al. 1996; Lomnitskaya 2001), making this the first observation of this structure in Fe_2X compounds.

6.3.4. Structural properties and stability of $Fe_{12}S_7$

$Fe_{12}S_7$ is observed in all heating cycles in the $Fe_{66}S_{34}$ starting composition (Runs 1 and 2, Table 6.2). $Fe_{12}S_7$ adopts a hexagonal structure with a *P*-6 space group and was solved and refined to the $Co_{12}P_7$ structure (*Z*=1) (Zurkowski et al. 2020) (Figure 6.2d) which can be viewed as an ordered $Cr_{12}P_7$ structure (Chun and Carpenter 1987). This structure is related to the *C*22, *C*23 and Cr_2P-type Fe_2S structures, in that it is also made up of columns of edge sharing FeS_5 square pyramids (green) and columns of corner sharing tetrahedra (blue) linked along edges along the *c* direction. $Fe_{12}S_7$ has an increased ratio of square pyramid to tetrahedral building blocks compared to the Fe_2S polymorphs, resulting in the formation of as trigonal channels along the *c* direction (Figure 6.1c). $Fe_{12}S_7$ has three distinct square pyramid sites (Figure 6.5), and each column of FeS_5 square pyramids extending along the *c* direction is occupied by one site.

This structural framework was first observed in the Th_7S_{12}, $Cr_{12}P_7$ and $V_{12}P_7$ compounds, where disordering of the metal sites raises the symmetry to $P6_3/m$ (Zachariasen, 1949; Olofssen and Ganglberger 1970; Chun and Carpenter 1979). To check whether the $Fe_{12}S_7$ phase is ordered ($Co_{12}P_7$-type, *P*-6) or disordered ($Cr_{12}P_7$-type, $P6_3/m$), the error on site occupancies was assessed. Within 6% error, all sites within $Fe_{12}S_7$ are fully occupied (Table 2), supporting that $Fe_{12}S_7$ is more compatible with the $Co_{12}P_7$ structure type at these conditions (Zurkowski et al. 2020). Previous studies have shown that Fe, Ni and Co do not occupy the $Cr_{12}P_7$ structure at ambient conditions (Dharhi 1996), likely because, compared to Cr and V, these transition metals do not preferentially occupy structures with predominantly 5-fold sites. The recent work on synthesizing $Co_{12}P_7$ (Zurkowski et al. 2020), demonstrated that, with pressure and temperature, Co will occupy an ordered $Cr_{12}P_7$ structure ($Co_{12}P_7$-type, *P*-6) while maintaining a 3:1 ratio of 5-

fold to 4-fold Co sites. The same behavior is observed here in the Fe-S system, where $Fe_{12}S_7$ is stable in the $Co_{12}P_7$ structure at high pressures and quenched from high temperatures. This work along with Zurkowski et al. 2020 establish pressure and temperature as mechanisms for stabilizing Fe and Co into this structure. The observed interatomic distances in $Fe_{12}S_7$ in this study are comparable with those observed in $Co_{12}P_7$, and with that of the Fe_2S polymorphs (Zurkowski et al. 2020) (Figure 6.5).

6.3.5. Structural properties and stability of Fe_3S

In agreement with previous diffraction studies at these conditions (e.g., Kamada et al. 2010; Thompson et al. 2020), Fe_3S is observed to crystallize in the Fe_3P structure type (*I*-4, Z = 8) at 101(3) and 118(2) GPa and high temperatures in an $Fe_{80}S_{20}$ composition (Runs 3 and 4, Table 6.2; Figure 6.2e) (Aronnson 1955 and references therein). This tetragonal structure is a more closed packed structure compared to the other structures discussed in this work with Fe-Fe bonding (Blanchard et al. 2008). In terms of the Fe coordination, isomorphic M_3X structures have been described as having 3 tetrahedrally coordinated *M* sites (Blanchard et al. 2008). Applying this framing to Fe_3S (Figure 6.6), one Fe-site is coordinated tetrahedrally by S atoms at a maximum distance of 2.135(8) Å, the second Fe site is coordinated by 3 S atoms and 1 Fe atom at a maximum distance of 2.286 (7) Å, and the third Fe site is coordinated by 2 S and 2 Fe atoms a maximum distance of 2.286 (7) Å (Figure 6.5). More generally, within a radius of 2.6 Å from each Fe site; 4 S and 8 Fe surround the first Fe site, 3 S and 9 Fe surround the second, and 2 S and 10 Fe surround the third. Sulfur is coordinated by 9 Fe sites. These values are based on the structure refinement conducted at 118(2) GPa (Run 4, Table 6.2) and the measured interatomic

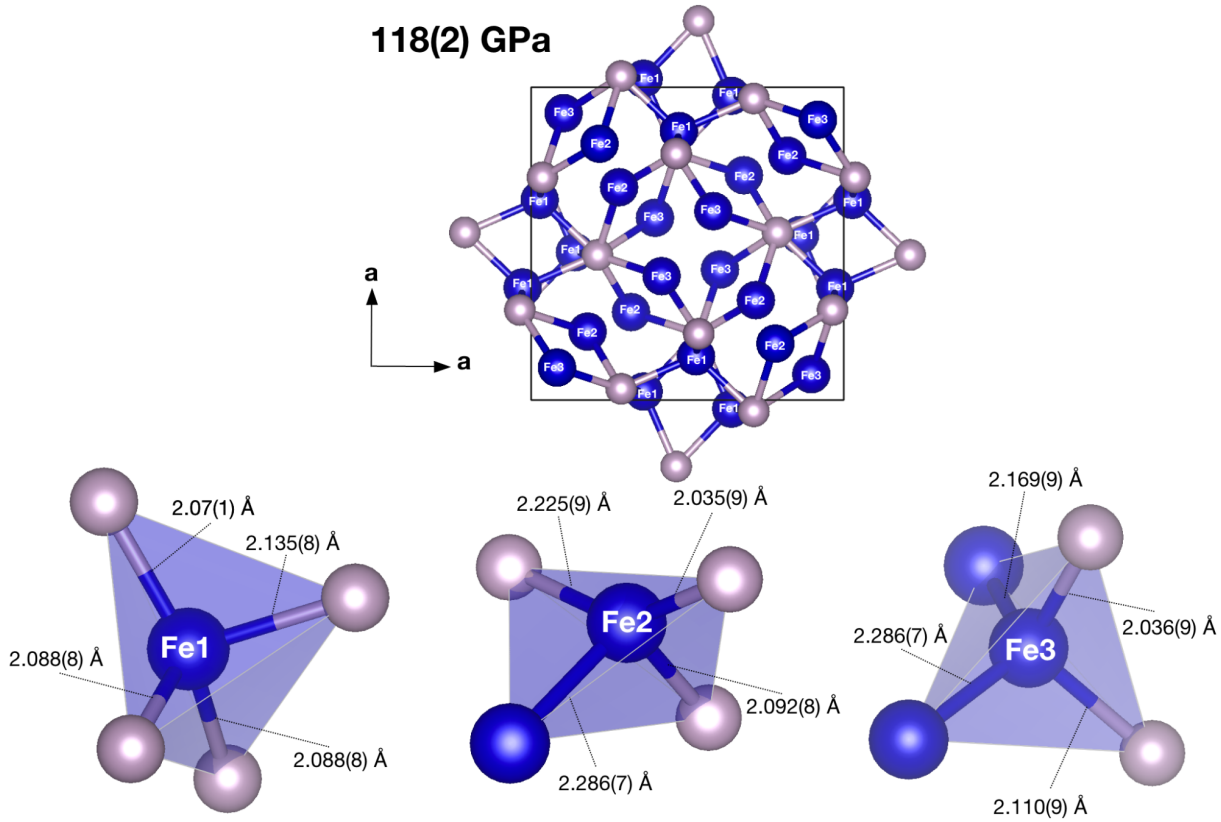

Figure 6.6. Fe_3S structure with Fe sites labeled. The Fe sites can be pictured as three differing tetrahedral building blocks as shown below.

distances are comparable to reports on other transition metal M_3X structures (e.g., Aronnson 1955; Rundqvist 1979) and comparable to the Fe_2S and $Fe_{12}S_7$ phases analyzed in this study (Figure 6.5).

6.4. Implications

This work has demonstrated that within Fe-rich systems with 16–25 wt% sulfur, a series of Fe-S phase relations are observed. In the range of 16–22 wt% sulfur, Fe_3S and Fe_2S are likely to be the relevant sulfides and in the range of 22–25 wt% sulfur, Fe_2S and $Fe_{12}S_7$ are the relevant sulfide compounds between ~100 and 130 GPa. A possible phase diagram incorporating these

subsolidus relations at 125 GPa is given in Figure 6.7, and further melting relations studies are needed to constrain the eutectic melting temperature and compositions and liquidus curves for these phase relations. The melting temperature of Fe and FeS along with the melting behavior of the Fe–Fe_3S system and the concentration of S in solid Fe are incorporated into the phase diagrams based on previous works (Boehler, 1992; Kamada et al. 2012; Anzellini et al. 2013; Mori et al. 2017) (Figure 6.7).

These results may be applied to the core chemistries on terrestrial planets and exoplanets. In particular, Venus is described to have a CMB pressure of 114 GPa and a central pressure of 274 GPa with a similar light element fraction compared to that of Earth' core (Aitta 2012). Venus is likely to have a fully or partially molten core, as the planet lacks the cooling mechanisms accompanied by plate tectonics (Nimmo et al. 2002). Venus' stagnant lid lends to uncertainty in the role of light elements on the structure and crystallization temperature of the current core, but as further constraints on Venus' core S-content are determined, the diagram initiated based on this study may directly apply (Figure 6.7). If Venus were to have a similar light element content to that of Mars (11–17wt%, Hefflrich 2017; red line in Figure 6.7), this work suggests two differing core scenarios. On the low sulfur content end of this range, a gravitationally unstable Fe_3S inner core and Fe-rich liquid outer core would form and on the S-rich side of this range, the core may crystallize an Fe_3S-rich inner core with an Fe_2S-rich liquid outer core (Figure 6.7). These scenarios can also be applied to Venus-sized exoplanets, and with more S-rich compositions, Fe_2S and $Fe_{12}S_7$ become critical phases in the core crystallization sequences.

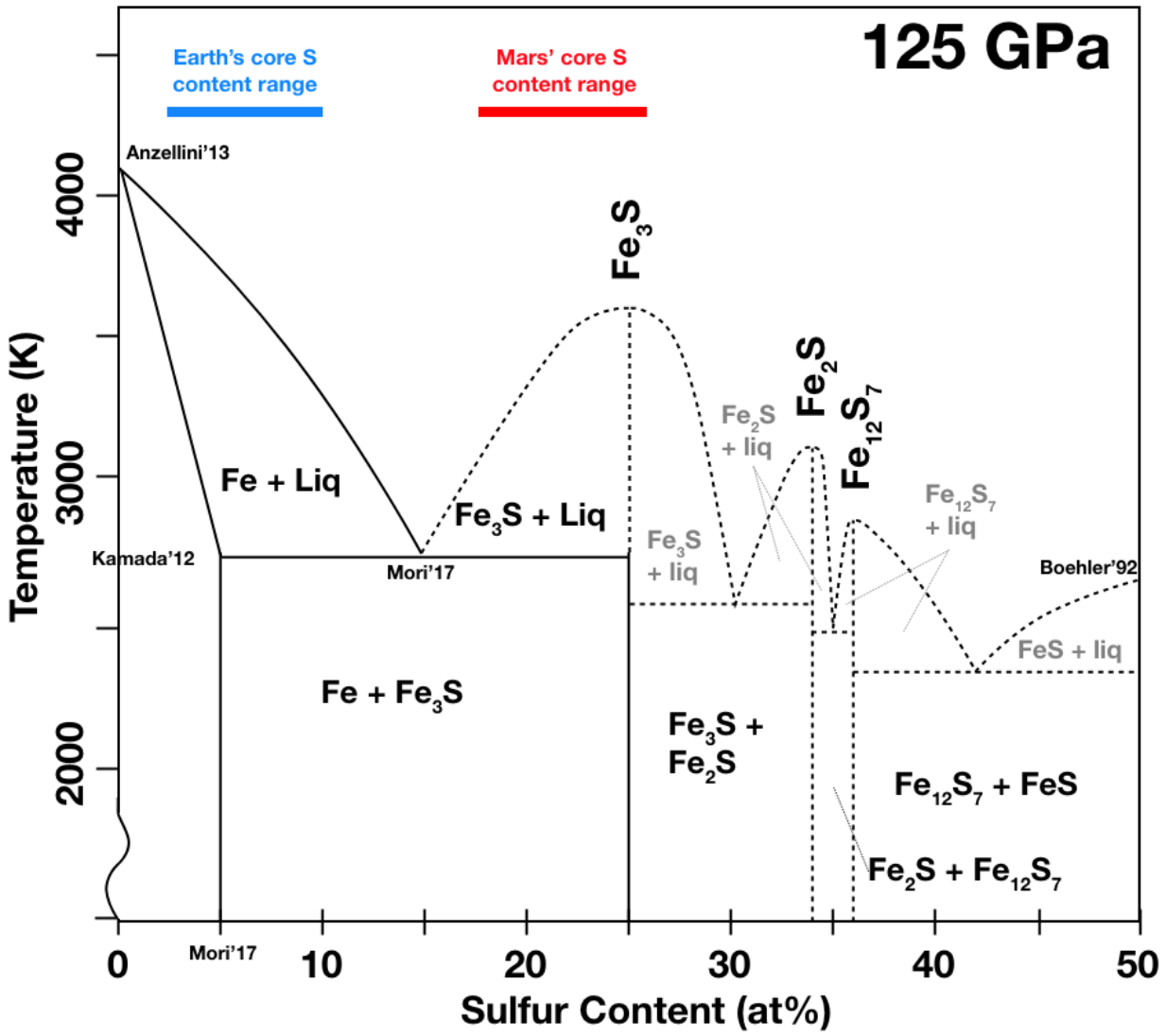

Figure 6.7. A possible phase diagram for the Fe-FeS system at 125 GPa based on the sulfides observed in this study. Fe and FeS melting temperatures were taken from Anzellini et al. 2013 and Boehler 1992. Eutectic melting temperature in the Fe–Fe_3S system (~2750 K) is from Kamada et al. 2012. Eutectic melt composition (~16 at% S) in the Fe–Fe_3S system and S content in solid Fe at 125 GPa is from Mori et al. 2017. The dotted lines and grey labels indicate possible phase relations in more S contents greater than 25 at%, based on the current study. For comparison, the S range reported for Earth's core, based on cosmochemical analyses and melting experiments (McDonough 2003; Mori et al. 2017) and the S range reported for Mars' core, based on chemical analyses of SNC meteorites and modeling (Helffrich 2017 and references therein).

A recent study has also demonstrated that the presence of Si expands the stability field of Fe_2S on the liquidus at 24 GPa (Tao and Fei 2021). Future experimental work investigating the phase stability of Fe_2(S, Si) is needed and may verify whether the phase relations observed here in Fe_2S are viable high-pressure analogs to the Fe_2(S, Si) phase relations. The Fe_2S structures presented in this study may have direct implications on the Mercurian outer core structure.

For the above core crystallization scenarios, this study elucidates the structures that may contribute to inner core formation or outermost core crystallization. To the degree that these phases are present in Venus-sized cores of varying compositions, Fe_3S would crystallize in the tetragonal, Fe_3P-type structure and $Fe_{12}S_7$ would crystallize in the hexagonal, $Co_{12}P_7$-type structure. The structural stability of Fe_2S is strongly temperature dependent in this pressure range. At low temperatures Fe_2S forms in the orthorhombic *C*23 structure and at high temperatures, Fe_2S is observed in the *C*22 structure. Fe_2S is also observed to distort to the body-centered Cr_2P-type structure at temperatures along the *C*23–*C*22 boundary, suggesting that this structure may be adopted as the sulfur sites are shifting between the *C*23 and *C*22 phases. Further *in situ* work is needed to demarcate the equilibrium phase boundaries for these polymorphs. With this, it likely remains that the *C*22 Fe_2S is the relevant high temperature phase to consider in the crystallization of S-rich, Venus-sized cores.

Fe_2S has been recovered from 19 GPa and 1900 K and was confirmed to adopt the *C*22 structure upon synthesis (Koch-Müller et al. 2002). These results indicate a wide stability field for the *C*22 Fe_2S structure at high temperatures. This structure type is relevant in analogous Fe-S–Si systems in the context of Mercury's core (Tao and Fei 2021). For example, to the degree

that Mercury may be forming an Fe_2S layer at the core-mantle boundary of Mercury (Tao and Fei 2021), $Fe_2(S, Si)$ may be depositing as *C*22 crystals depositing in this region.

Recent studies have also reported that Fe_3S breaks down above 250 GPa to Fe + Fe_2S (Ozawa et al. 2013; Mori et al. 2017), and Fe_2S becomes the stable Fe-rich sulfide on the liquidus to 306 GPa (Tateno et al. 2019). Continuing to characterize the liquidus phases of Fe_2S polymorphs in this pressure range and up to Earth's inner core boundary is critical. The results discussed in Chapter 4, as well as the Tateno et al. 2019 study demonstrate that *C*23 Fe_2S transitions to *C*37 Fe_2S with pressure. Even though these structures are closely related, the high temperature behavior of the *C*37 structure has not been extensively investigated as has been done for the *C*23 structure (this chapter, Zurkowski et al. *in press*). Here the *C*23 Fe_2S grains transition at high temperature to the *C*22 structure by shifting some S sites and possibly forming the intermediary Cr_2P structure; however, the coordination increase that occurs in the *C*23–*C*37 transition may interrupt this transition when the *C*37 structure is heated to high temperatures (>150 GPa). Analog high temperature analysis of *C*37 Co_2Si at ambient conditions (Geller and Wolontis 1955) or *C*37 Fe_2P above 40 GPa (Nakajima et al. 2020) may elucidate the temperature driven transitions in these structure types. Melting studies of Fe_2S may also be beneficial for determining the likelihood of a phase transition in *C*37 Fe_2S phase at inner core boundary pressures prior to melting temperatures.

6.5. Conclusions

The phase stability of Fe-rich sulfides was probed in Fe-S compositions (20–34 at% S) between 100 and 125 GPa using single crystal X-ray diffraction techniques on quenched multigrain samples. In a starting composition with 34 at% S, two compounds are observed: Fe_2S and $Fe_{12}S_7$. At low temperatures, Fe_2S is observed in the *C*23 structure, in accordance with previous studies and at high temperatures Fe_2S is observed to adopt the Fe_2P-type, *C*22 structure. This high temperature phase transition agrees with observations in analogous systems. At 125 GPa and from moderate temperatures, a distortion of the *C*22 Fe_2S phase was temperature quenched and determined to adopt the body-centered orthorhombic Cr_2P-type structure. These observations may indicate the structural transition sequence from the *C*23–Cr_2P-type–*C*22 structure with temperature as these structure types are all closely related and future *in-situ* work is required to determine the equilibrium stability of these phases. $Fe_{12}S_7$ is observed to take the $Co_{12}P_7$ type structure across the pressure and temperature range examined for the 34 at% S starting composition. The $Fe_{12}S_7$ structure is also closely related to the Fe_2S polymorphs. Fe_3S was determined to adopt the Fe_3P structure when synthesized in the Fe + 20at% S starting composition, in agreement with previous studies. Observations of these compounds and structures at these conditions provide insight into the thermodynamics that may be applicable to Venus' core, terrestrial exoplanetary cores as well as the potentially low-pressure analog Fe-S–Si system related to Mercury's core. Depending on the degree of light element incorporation into a terrestrial planet during late stage planet formation, rocky planetary cores with sulfur contents in the range of ~16–25 wt% S could result in a wide range of core chemical structures and dynamics.

7. Experimental evidence of a disordered trigonal iron-rich sulfide at Earth's outer core conditions and analogous observations in the Fe-P system

Collaborators: Barbara Lavina[b,c], Stella Chariton[b], Sergey Tkachev[b], Vitali Prakapenka[b], Andrew J. Campbell[a]

[a]University of Chicago, Department of the Geophysical Sciences, 5734 S Ellis Ave, Chicago, IL 60637, USA
[b]Center for Advanced Radiation Sources, 9700 South Cass Avenue, Building 434A, Argonne, IL 60439, USA
[c]X-ray Science Division, Advanced Photon Source, Argonne National Laboratory, Argonne, IL 60439, USA

7.1. Introduction

Crystallographic assessment of Fe_3S at high pressures and temperatures is limited in Earth's core pressure range. Unit cell parameters for Fe_3S have only been reported to 120 GPa at high temperatures (Seagle et al. 2006; Morard et al. 2008; Thompson et al. 2020; Zurkowski et al. submitted, Chapter 4) and single crystal analyses of quenched Fe_3S at 100 and 120 GPa confirm that it adopts the tetragonal structure to these conditions (Zurkowski et al. submitted, Chapter 4). Unit-cell geometry and the atomic arrangement of Fe_3S in the 120 – 250 GPa range has not been reported, but sample recovery experiments demonstrate that an Fe_3S-like compound does form at high temperatures at 200 GPa, 236 GPa, 254 GPa (Ozawa et al. 2013; Mori et al. 2017; Yokoo et al. 2019). Above ~250 GPa, Fe_3S breaks down at low temperatures into a *B*2 FeS + Fe phase assemblage, and FeS+Fe react at high temperatures to form *C*37 Fe_2S on the liquidus to 306 GPa (Ozawa et al. 2013; Mori et al. 2017; Tateno et al. 2019). Across Earth's core pressures and high temperatures, Fe_3S is likely the relevant compound throughout the top of the outer core and Fe_2S is likely the relevant compound in the deeper regions of the outer core and to

the inner core boundary (Kamada et al. 2010; Ozawa et al. 2013; Mori et al. 2017; Tateno et al. 2019; Yokoo et al. 2020; Zurkowski et al. submitted, Chapter 4).

While geochemical models of Earth's core suggest that phosphorus is lower in abundance compared to sulfur (McDonough 2003), iron phosphides are significant components of iron meteorites, pallasites, lunar meteorites and some chondrites (e.g., Olsen and Fredriksson 1966; Buseck 1969; Brandstätter et al. 1991; Britvin et al. 2002). Several Fe-P phases have been identified in meteorites including (Fe, Ni)$_3$P schreibersite (Fe$_3$P-type, *I*-4, *Z*=8), Fe$_2$P allabogdanite (Co$_2$P-type, *Pnma*, *Z*=4) and Fe$_2$P barringerite (Fe$_2$P-type, *P*-62*m*, *Z*=3) (Buseck 1969; Litasov et al. 2020) and investigations into the *P*-*T* stability fields of these phases provide important insight into the thermodynamic history of meteorites and their parent bodies. Previous examinations of the phase stability of Fe$_3$P report findings that are not fully in agreement. With room temperature compression of Fe$_3$P, onset of a phase transition has been reported above 15 GPa (Scott et al. 2007). The transition was later confirmed with heating at 21 GPa (Scott et al. 2008), but structural details for this phase were not reported. Later, *I*-4 Fe$_3$P was reported stable to 64 GPa at room temperature and the first order transition was not observed (Gu et al. 2014). With subsequent heating to 1650 K at 64 GPa, Fe$_3$P transitioned to a phase that was indexed to a primitive tetragonal cell (Gu et al. 2014). A more recent work also reported no structural transition in *I*-4 Fe$_3$P up to 111 GPa (Lai et al. 2020).

Ion-phosphides also serve as low-pressure analogs to Fe-sulfides. Fe$_3$P is stable at ambient conditions, Fe$_3$(P$_{0.87}$ S$_{0.13}$) is stable at 8 GPa and Fe$_3$S is stable at 21 GPa (Fei et al. 2000; Gu et al. 2016). Fe$_2$P is observed in the barringerite structure at ambient pressures and high temperatures (Rundqvist and Jellinek 1959; Britvin 2002) and is observed in Fe$_2$S between 21

and 125 GPa at high temperatures (Koch-Müller et al. 2002; Zurkowski et al. submitted, Chapter 4). Fe_2P is observed in the allabogdanite structure at moderate temperatures above 8 GPa, while Fe_2S adopts the Co_2P-type structure between 25 and 120 GPa at moderate temperatures (Zurkowski et al. 2021; Zurkowski et al. submitted, Chapter 4). Further investigation into the lower pressure behavior of Fe-phosphides may provide structural information on core-relevant Fe-sulfide phases.

In the current study, the high temperature structural stability of Fe_3S was assessed between 145–200 GPa, and the analogous properties of Fe_3P were investigated from ambient conditions to 70 GPa using powder and single crystal X-ray diffraction techniques in a laser heated diamond anvil cell. Upon heating an $Fe_{80}S_{20}$ composition between 145 and and 195 GPa, *C*37 Fe_2S + Fe are observed to react to form a new trigonal structure marked by an elongated *c* axis ($c/a \sim 4.4$). Large crystallites of this trigonal phase are observed coexisting with recrystallized hcp-Fe to 193 GPa and 3200 K. Between 35 and 70 GPa, Fe_3P adopts an analogous trigonal phase ($c/a \sim 4.4$). The trigonal Fe-P phase was decompressed in neon to ambient conditions and was observed to decompose between below 16 GPa in agreement with previous studies (Scott et al. 2007; 2008). A room temperature equation of state is presented for the Fe-P trigonal phase between 16 and 67 GPa. Assessment of the rotational scans of the Fe-S and Fe-P samples reveal diffuse scattering from positional disordering. Refinements of the Fe-S and Fe-P powder diffraction patterns agreeably show that either the Ni_8P_3 (*R*3*c*) or $Fe_{12}As_5$ (*R32*) structure types can account for the average structures of the trigonal Fe-S and Fe-P phases. Ni_8P_3 and $Fe_{12}As_5$ adopt similar trigonal structures and are characterized by atomic clustering resulting from significant metal-metal interactions. Attempts at solving the disordered Fe-S and Fe-P

structures using single crystal techniques support that the average structure is related to the Ni_8P_3 and $Fe_{12}As_5$ structure types with an $Fe_{11}X_4$ stoichiometry. The trigonal Fe-P phase may contribute to the convection or inner core crystallization in the Mercurian and Martian cores, respectively, while the high *P-T* stability of trigonal Fe-S phase coexisting with iron may directly contribute to the crystallization sequences, thermal conductivity and density profiles in the upper regions of Earth's outer core.

7.2. Materials and methods

Experiments targeting multigrain synthesis in the Fe-S system consisted of mixtures of Fe (99.9+%, <10μm, Alfa Aesar) and iron sulfide (FeS, 99.99%, Alfa Aesar) in Fe+12.5 wt% S ($Fe_{80}S_{20}$), Fe + 23 wt% S ($Fe_{67}S_{33}$) compositions. The Fe-FeS compositions were homogenized in ethanol in a mortar and pestle for 1 hour then mixed dry for a short interval to reset any density settling during alcohol evaporation. Fe-P experiments were conducted on an Fe_3P starting material (99.5% Alfa Aesar).

Pressure was generated using BX-90 type (Kantor et al. 2012) diamond anvil cells (DAC) with type 1 Boehler-Almax conical diamonds and seats, and Mao symmetric type DACs with Type 1 standard cut diamonds mounted on tungsten carbide of cBN seats. Diamond culets ranged from 300-50 μm in diameter. Two types of samples were loaded in the DACs: powder foils of $Fe_{80}S_{20}$, $Fe_{67}S_{33}$, or Fe_3P were loaded in a solid pressure media and single crystals of Fe_3P were loaded in neon.

Angle dispersive X-ray diffraction and *in-situ* X-ray diffraction experiments were conducted at Argonne National Laboratory, sectors 13 ID-D and 13 BM-D, of the Advanced

Photon Source, and laser heating was conducted during XRD collection at sector 13-ID-D. Powder diffraction patterns collected were processed using Dioptas (Prescher and Prakapenka, 2015) and GSAS-II (Toby and Von Dreele 2013). Pressure determined using the equation of state of hcp-Fe (Dewaele et al. 2006) and neon (Fei et al. 2007). Further experimental details can be found in Section 2.4.

Upon quenching sample locations showing high intensity, spotty diffraction patterns were chosen for single crystal X-ray diffraction collection. At chosen map locations, single crystal X-ray diffraction rotational images were collected. Processing of the single crystal X-ray diffraction data was processed using the methodology discussed in Section 2.5.

7.3. Results and discussion

7.3.1. Phase relations in the Fe-S system between 145 and 195 GPa and to high temperatures

Upon heating the $Fe_{67}S_{33}$ and $Fe_{80}S_{20}$ compositions between 145 and 195 GPa, *C*37 Fe_2S is observed to crystallize with + hcp-Fe at moderate temperatures (Figure 7.1a). At 184 GPa and 2150(120) K in the $Fe_{80}S_{20}$ composition, the *C*37 Fe_2S diffraction angles were indexed to a unit cell with parameters a = 4.562(1) Å , b = 3.277(1) Å, c, = 6.146(2) Å , in agreement with previous studies (Zurkowski et al. submitted, Chapter 4; Tateno et al. 2019). With continued heating above 2150 K at 184 GPa, a new set of reflections is observed in the diffraction patterns and the diffraction angles associated with *C*37 Fe_2S decrease in intensity (Figure 7.1a, Figure 7.2). The peak intensities of the high temperature phase vary during heating up to 3210 K and the

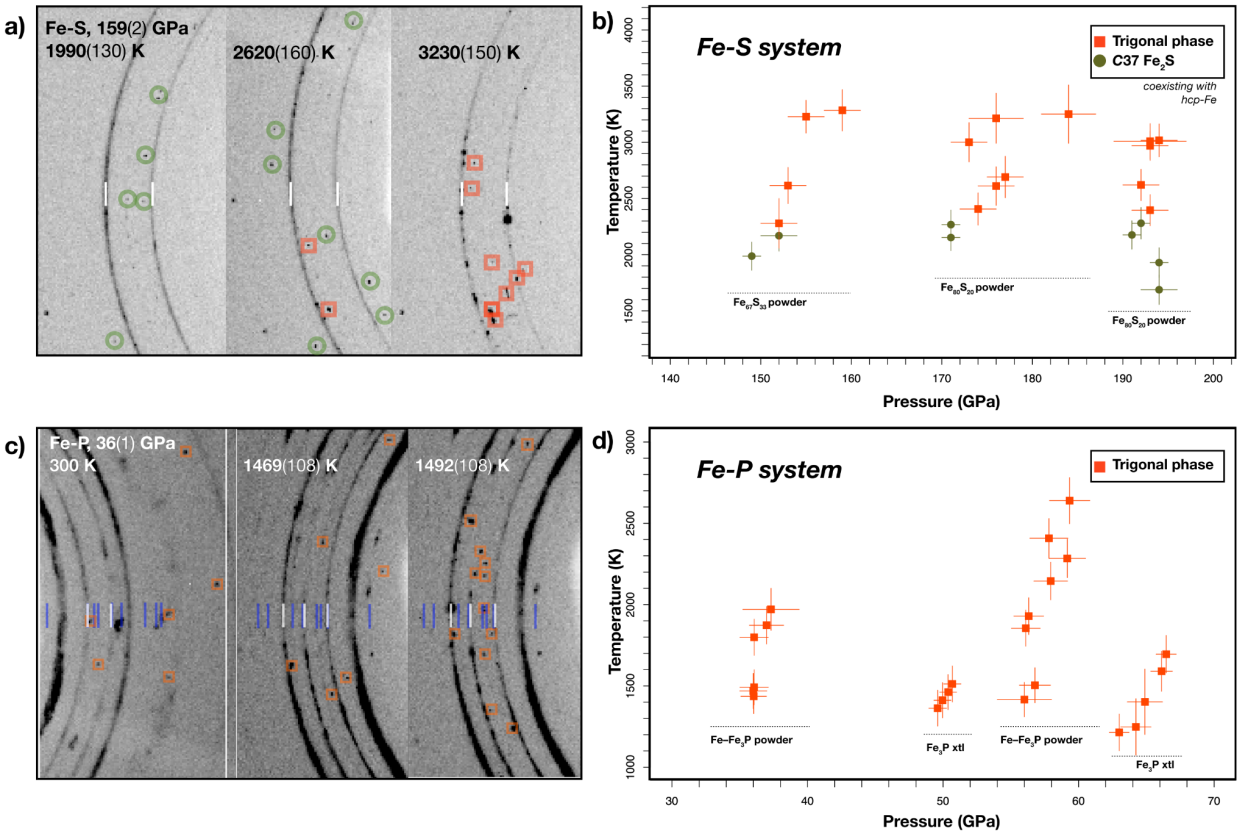

Figure 7.1. a) Diffraction images of the $Fe_{67}S_{33}$ sample with heating at 159(2) GPa. Crystallization of *C*37 Fe_2S (green circles) coexisting with iron (white lines) is observed at low temperatures, and the crystallization of the trigonal phase (red squares) with recrystallized iron occurs at high temperatures. b) Pressure-temperature plot of the stable Fe-sulfide coexisting with hcp-Fe between ~148 and 200 GPa and to ~3500 K based on the current experiments. c) Diffraction images of an Fe+Fe_3P sample in KCl with heating at 36(1) GPa. At room temperatures, crystallization from the trigonal phase is observable, and with heating, diffraction from Fe_3P decreases in intensity as the trigonal phase stabilizes. d) Pressure-temperature plot of the stable Fe-phosphide observed between ~35 and 70 GPa and to ~2800 K based on the current experiments. As the trigonal phase is observed to begin crystallizing at room temperatures, the trigonal phase is observed in this P-T range. The starting material for each sample is labeled under each heating cycle for the Fe-S and Fe-P phase diagrams to demonstrate that compatible observations were made across multiple experiments.

raw diffraction images become spotty (Figure 7.2, Figure 7.3), indicating that large crystallites form (Figure 7.3). Peak intensities observed in integrated powder diffraction patterns vary due to the limited orientations of the synthesized grains (Figure 7.3, Figure 7.2).

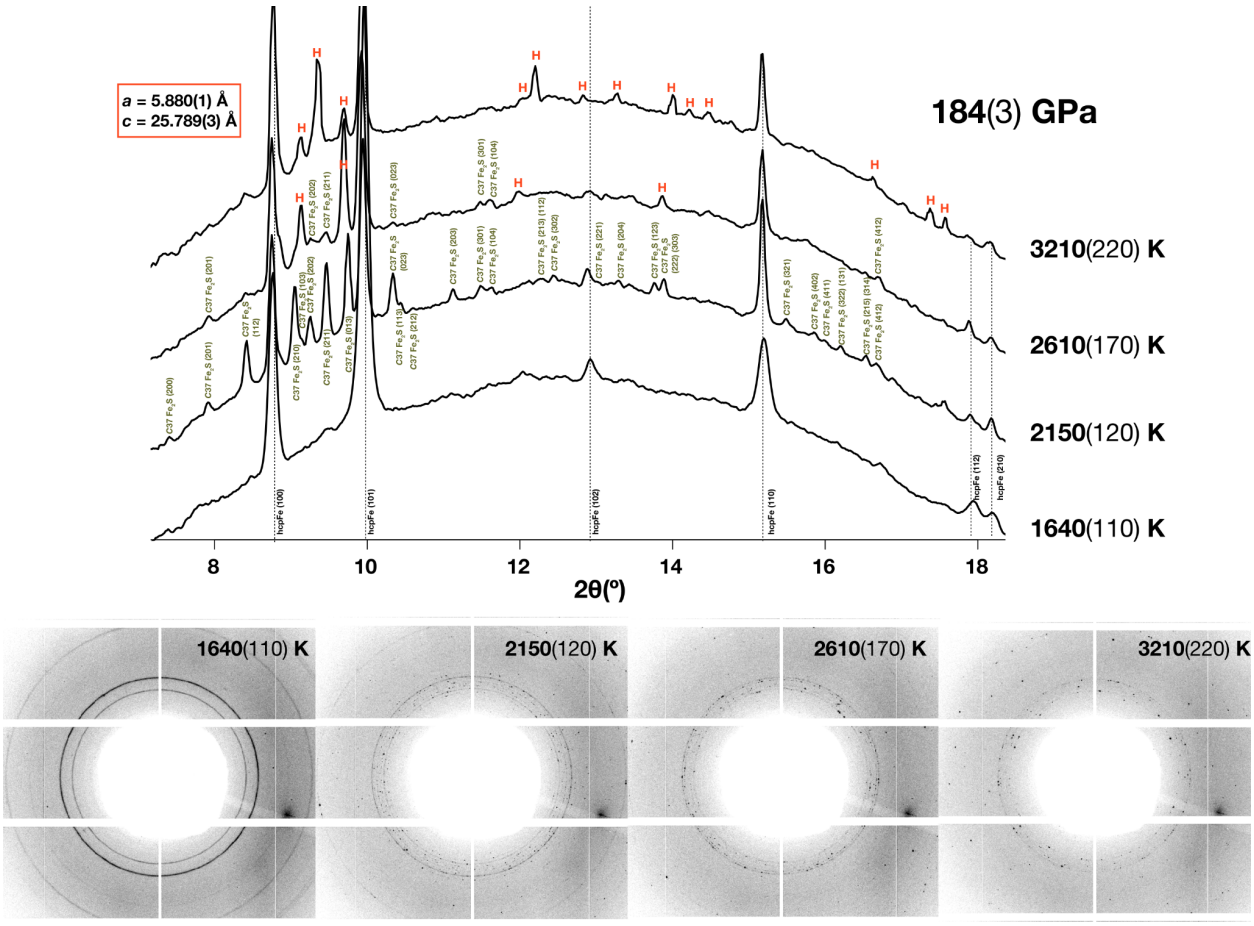

Figure 7.2. X-ray diffraction collected at 184(3) GPa and to high temperatures on the $Fe_{80}S_{20}$ starting composition embedded in SiO_2. Upon heating to 2150(120) K, *C*37 Fe_2S crystallizes with hcp-Fe. With continued heating, *C*37 Fe_2S becomes unstable and new peaks appear (labeled "H") coexisting with hcp-Fe above 2610(170) K and to at least 3210(220) K. Upon quenching the sample and collecting rotational scans, crystallites of the high temperature phase were indexed in the reciprocal space to a trigonal unit cell with a = 5.880(1) Å and c = 25.789(3) Å.

The phase boundary between the *C*37 Fe_2S + Fe and this high temperature phase was bracketed by the first observations of diffraction reflections from the new sulfide in the raw diffraction patterns (Figure 7.1a). Between 145 and 195 GPa, the first reflections of the high temperature phase are observed between 2100 and 2400 K, with a shallow positive phase boundary slope (Figure 7.1b), and at the highest temperatures, no reflections from *C*37 Fe_2S are observed (Figure 7.1a). The high-temperature-sulfide + hcp-Fe phase assemblage was observed

between to 195 GPa and to ~3250 K (Figure 7.1b). Additional experiments are required to further characterize the *P-T* relationship of this phase boundary, but it is compatible with observations of *C*37 Fe_2S on the liquidus by 306 GPa (Tateno et a. 2019).

The high temperature phase forms with recrystallized hcp-Fe, as shown by the spotty (100) and (101) hcp-Fe rings in Figure 7.3. Recrystallization of high intensity hcp-Fe with this phase is observed in both the $Fe_{67}S_{33}$ and $Fe_{80}S_{20}$ compositions, indicating that the phase is either iron poor of the $Fe_{67}S_{33}$ composition or that iron-rich locations of the $Fe_{67}S_{33}$ sample material were probed. As the starting materials for this study were not ball-milled, thus limiting iron oxidation while sacrificing sample homogeneity, the sample compositions may vary between sample locations in the DAC. For these reasons, the stoichiometry of the phase is not inferred from the starting material and the *T-X* phase and melting relations at each pressure step were not the focus of the current study. Instead, the equilibration of this high temperature phase with recrystallized hcp-Fe is emphasized, indicating that the probed samples are in an Fe-saturated phase field.

As the large crystallites of the synthesized high temperature sulfide are quenchable (Figure 7.3), they are good candidates for experiments and analyses utilizing single crystal X-ray diffraction techniques (SXD). Upon quenching both Fe-S sample compositions from high temperature synthesis conditions between 145 and 195 GPa, the samples were rotated across a ±17º or ±20º angular range depending on the geometry of the cell used in each experiment (Table 1). The integrated rotational scans for each pressure step are composed of large, high intensity reflections that crystallized with iron from the Fe-rich starting powder foil (Figure 7.4 a, b). The diffraction reflections were then mapped in the reciprocal space and lattices of the high

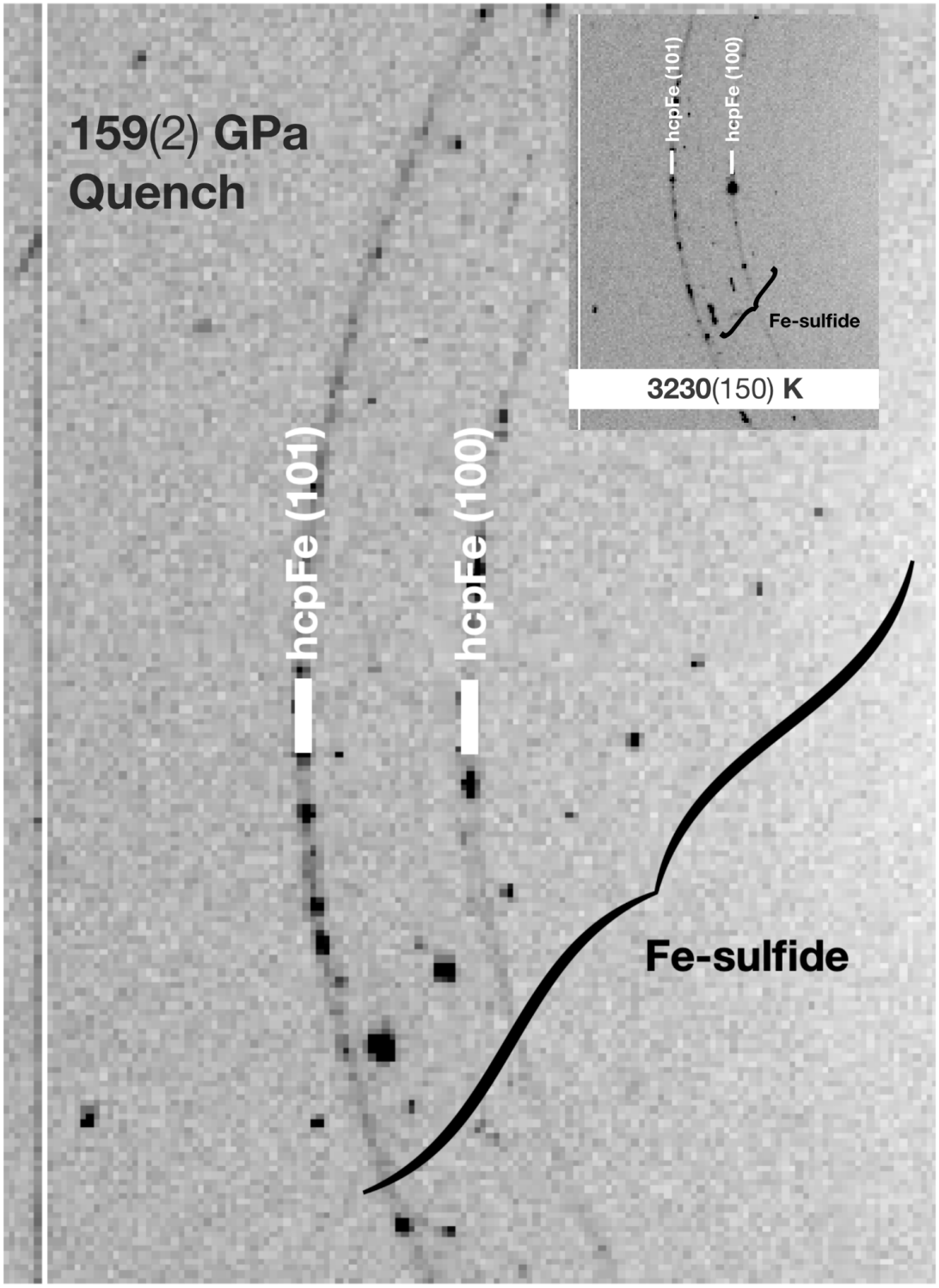

Figure 7.3. View of a crystallite of the high temperature Fe-sulfide phase coexisting with recrystallized hcp-Fe after synthesis at 159(2) GPa and 3230(130) K (inset). The spotty rings corresponding to the hcp-Fe (100) and (101) planes demonstrate that iron equilibrated at 159(2) GPa and 3230(130) K.

temperature phase were identified and indexed. Despite the limited angular range, 84–189 reflections were obtained for each Fe sulfide grain. At 193 GPa, a Fe sulfide lattice (Figure 7.4c) was indexed to a trigonal unit cell with a = 5.8400(7) Å and c = 25.583(2) Å. Compatible unit cells were measured between 145 and 195 GPa and in some experiments, several trigonal grains were identified in the limited rotational scans (Table 7.1). One measurement at 136.4(5) GPa after synthesis at 159(2) GPa and 3230(150) K shows a compatible a axis but a c axis that is ~2.75 times longer than expected (Table 7.1). These indexing results suggest ordering may cause a longer c-axis in this lower pressure measurement, but future work at these *P-T* conditions may elucidate the details ordering within this structure. Agreement between the measured lattice parameters for the trigonal phase in the higher-pressure experiments conducted supports that the same phase is observed across the high *P-T* range of this study. The trigonal unit cell geometry also confirms that the synthesized Fe-S trigonal phase coexisting with hcp-Fe at these *P-T* conditions cannot be described by the tetragonal Fe_3S structure previously reported on the basis of powder diffraction analyses at these conditions (e.g., Kamada et al. 2010; Kamada et al. 2012; Ozawa et al. 2013; Mori et al. 2017), and no lattices of tetragonal Fe_3S were identified in the current investigations.

Table 7.1. Experimental details and measured lattice parameters for each observation of the trigonal phase in the Fe-P and Fe-S systems. Each lattice listed was indexed in the reciprocal space and the rotational scan range (*ω)* and number of reflections (# ref.) used for indexing are provided. In two experiments, sample synthesis at high temperatures was conducted without collecting temperature measurements. For these runs, the synthesis condition is noted as "high T, not measured."

				Room temperature collection						Synthesis conditions	
Sample name	Starting material	Beamline	medium	P GPa	*a* Å	*c* Å	V Å^3	*ω* (º)	# ref.	*P* GPa	*T* K
C129_P140_map71	Fe67S33	13 ID-D	SiO2	136.4(5)	5.957(4)	71.89(4)	2209(2)	34	84	159(2)	3230(150)
C129_P150_map9	Fe67S33	13 ID-D	SiO2	144.2(8)	5.939(3)	25.99(6)	794(2)	34	76	high T, not measured	
C129_P150_map9	Fe67S33	13 ID-D	SiO2	144.2(8)	5.923(1)	26.004(6)	789.9(3)	34	146	high T, not measured	
C137_P1_map25	Fe80S20	13 ID-D	SiO2	159(1)	5.890(3)	25.837(7)	776.2(5)	40	108	184(3)	3250(260)
C137_P1_map25	Fe80S20	13 ID-D	SiO2	159(1)	5.880(1)	25.789(3)	772.0(2)	40	108	184(3)	3250(260)
C137_P1_map25	Fe80S20	13 ID-D	SiO2	159(1)	5.876(2)	25.884(8)	774.0(4)	40	116	184(3)	3250(260)
C137_P1_map25	Fe80S20	13 ID-D	SiO2	159(1)	5.883(3)	25.85(1)	774.6(7)	40	126	184(3)	3250(260)
C137_P1	Fe80S20	13 ID-D	SiO2	159(1)	5.897(3)	25.90(1)	775.1(6)	40	116	184(3)	3250(260)
C137_P1	Fe80S20	13 ID-D	SiO2	159(1)	5.878(1)	25.784(3)	771.6(2)	40	149	184(3)	3250(260)
C137_P2_34	Fe80S20	13 ID-D	SiO2	179(1)	5.8400(7)	25.583(2)	755.7(1)	40	189	193(4)	3010(160)
C130_61GPa_map24	Fe3P xtl	13 ID-D	Ne	59.0(4)	6.2564(9)	27.219(4)	922.7(4)	60	293	66.5(7)	1700(110)
C130_61GPa_map24	Fe3P xtl	13 ID-D	Ne	59.0(4)	6.2569(9)	27.222(4)	922.2(4)	60	303	66.5(7)	1700(110)
C130_58GPa	Fe3P xtl	13 ID-D	Ne	60.25(7)	6.2563(9)	27.218(4)	922.6(2)	60	304	66.5(7)	1700(110)
C130_54GPa_S2	Fe3P xtl	13 ID-D	Ne	54.5(1)	6.256(3)	27.41(2)	929.1(8)	60	272	66.5(7)	1700(110)
C130_51GPa	Fe3P xtl	13 ID-D	Ne	52.41(8)	6.274(2)	27.455(5)	935.9(4)	60	494	66.5(7)	1700(110)
C125_45GPa_map35	Fe3P xtl	13 ID-D	Ne	45.46(8)	6.325(1)	27.545(4)	954.2(3)	60	1123	50.7(6)	1510(110)
C125_45GPa_map35	Fe3P xtl	13 ID-D	Ne	45.46(8)	6.326(1)	27.583(5)	955.8(3)	60	1136	50.7(6)	1510(110)

Table 7.1. ***continued***

C125_45GPa_map35	Fe3P xtl	13 ID-D	Ne	45.46(8)	6.330(2)	27.583(5)	957.2(4)	60	1136	50.7(6)	1510(110)
C125_45GPa_map42	Fe3P xtl	13 ID-D	Ne	45.0(1)	6.3228(3)	27.536(1)	953.32(8)	60	673	50.7(6)	1510(110)
C125_45GPa_map42	Fe3P xtl	13 ID-D	Ne	45.0(1)	6.3240(5)	27.575(2)	955.1(1)	60	740	50.7(6)	1510(110)
C125_45GPa_map42	Fe3P xtl	13 ID-D	Ne	45.0(1)	6.3205(4)	27.564(1)	953.6(1)	60	619	50.7(6)	1510(110)
C125_30GPa_map	Fe3P xtl	13 ID-D	Ne	33(1)	6.5006(3)	27.949(1)	991.62(9)	60	433	high T, not measured	
C125_30GPa_map	Fe3P xtl	13 ID-D	Ne	33(1)	6.3677(3)	27.931(1)	990.04(8)	60	433	high T, not measured	
C125_decompress	Fe3P xtl	13 BM-D	Ne	37.9(6)	6.347(3)	27.83(1)	970.8(8)	60	181	50.7(6)	1510(110)
C125_decompress	Fe3P xtl	13 BM-D	Ne	37.9(6)	6.367(6)	27.76(2)	975(1)	60	91	50.7(6)	1510(110)
C125_decompress	Fe3P xtl	13 BM-D	Ne	37.9(6)	6.368(5)	27.72(2)	974(1)	60	285	50.7(6)	1510(110)
C125_decompress	Fe3P xtl	13 BM-D	Ne	30.3(8)	6.432(4)	28.08(2)	1006(1)	60	319	50.7(6)	1510(110)
C125_decompress	Fe3P xtl	13 BM-D	Ne	23.5(6)	6.499(4)	28.25(1)	1017.6(9)	60	394	50.7(6)	1510(110)
C125_decompress	Fe3P xtl	13 BM-D	Ne	23.5(6)	6.457(7)	28.30(2)	1022(2)	60	201	50.7(6)	1510(110)
C125_decompress	Fe3P xtl	13 BM-D	Ne	16.5(6)	6.521(4)	28.81(2)	1061(1)	60	309	50.7(6)	1510(110)
C125_decompress	Fe3P xtl	13 BM-D	Ne	11.4(5)	6.60(1)	29.32(3)	1104(2)	60	76	50.7(6)	1510(110)
C134_P1_map25	Fe3P foil	13 ID-D	KCl	31.2(2)	6.3984(7)	28.026(2)	993.6(2)	60	688	37(2)	1970(130)
C134_P1_map25	Fe3P foil	13 ID-D	KCl	31.2(2)	6.3987(5)	27.96(1)	991.3(5)	60	551	37(2)	1970(130)
C134_P2_map33	Fe3P foil	13 ID-D	KCl	49.8(8)	6.3986(5)	27.96(1)	991.3(5)	60	547	59(1)	2640(140)

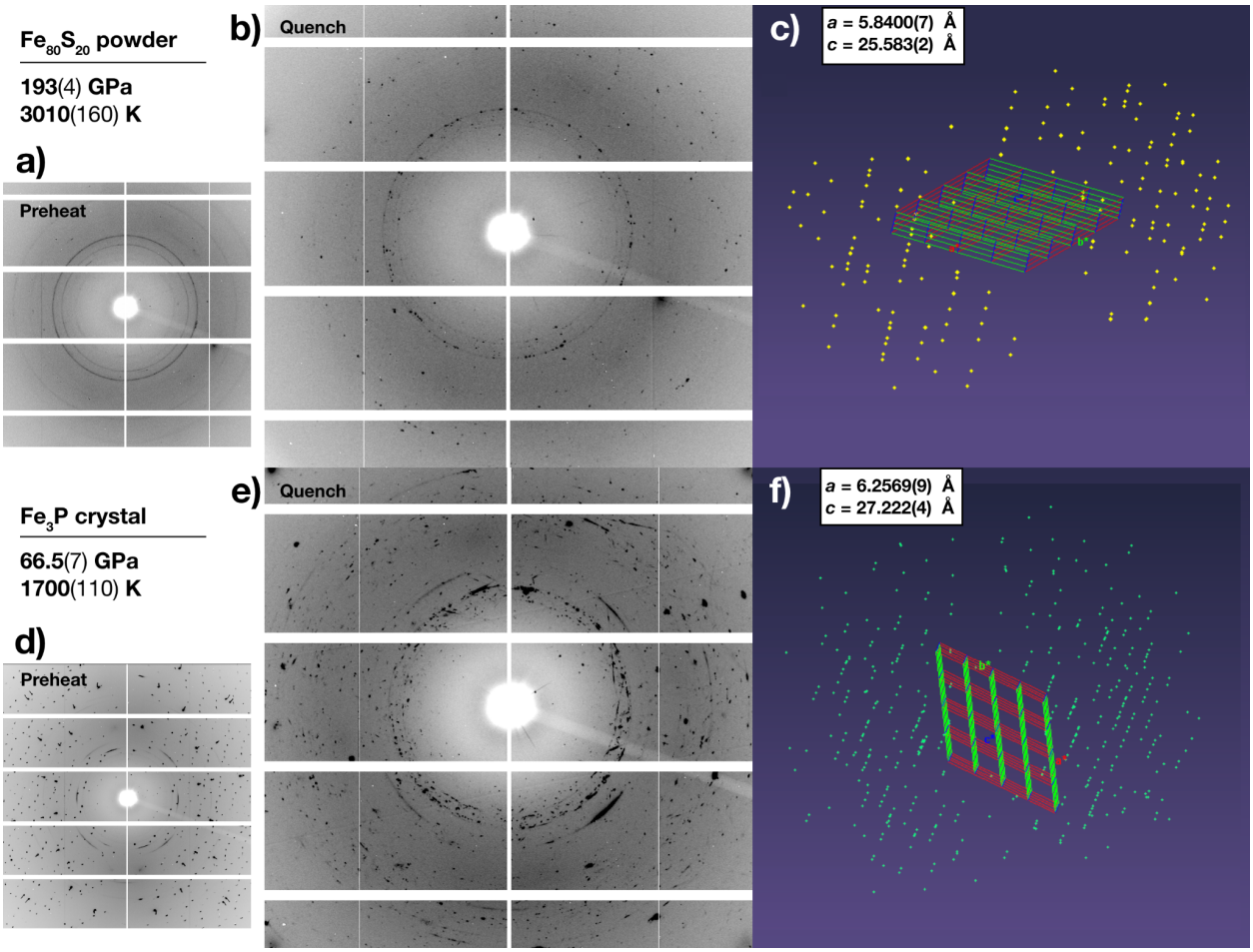

Figure 7.4. Quench products of a $Fe_{80}S_{20}$ powder in SiO_2 at 193(4) GPa from 3010(160) K and a Fe_3P crystal in Ne at 66.5(7) GPa from 1700(110) K. a) Room temperature diffraction image of the $Fe_{80}S_{20}$ starting powder in SiO_2 prior to heating at ~190 GPa. b) Diffraction image collected after quenching at 193(4) GPa and 3010(160) K showing the crystallization of the high temperature Fe-sulfide coexisting with iron. c) View into the reciprocal space of 189 isolated reflections of a lattice of the high temperature Fe-S phase at 193 GPa. Lattice indexing of the Fe-S yields a trigonal lattice with lattice parameters a = 5.8400(7) Å and c = 25.583(2) Å. d) Integrated diffraction images from a rotational scan of an Fe_3P crystal at room temperatures prior to heating at these conditions. e) Diffraction image collected after heating synthesis of the high temperature phase. f) Reciprocal mapping of the high temperature Fe-P lattice consisting of 303 reflections. The lattice was indexed to a trigonal unit cell with a = 6.3569(9) Å and c = 27.222(4) Å.

7.3.2. Phase relations in the Fe-P system to 67 GPa and to high temperatures

To test for an analogous trigonal Fe-P phase and assess the previously reported phase transitions in Fe_3P, powder and single crystal X-ray diffraction experiments were conducted on Fe_3P single crystals in Ne and Fe_3P foils in KCl to 67 GPa and high temperatures. With room temperature compression of a foil of Fe_3P in KCl to 36 GPa, crystallization of the new phase is observed even at room temperatures (Figure 7.1c), despite the broad, high intensity peaks of Fe_3P and hcp-Fe overwhelming the integrated diffraction patterns prior to heating (Figure 7.5). Observations of hcp-Fe in the starting unheated foil and at high temperatures indicates that the starting material, although labeled Fe_3P (Alfa Aesar, 99.5%), was composed of Fe_3P and Fe crystals. At moderate temperatures, the raw diffraction patterns become spotty as the Fe_3P peaks diminish in intensity, and this phase is stable coexisting with hcp-Fe to high temperatures (Figure 7.1c, Figure 7.5).

In determining the *I*-4 Fe_3P + Fe → high-temperature-phosphide + Fe transition between 36 and 67 GPa, the raw diffraction patterns reveal that a new phase is crystallizing even at room temperatures. These results suggest that the set of diffraction peaks that intensify at high temperatures in this pressure range (Figure 7.5), are associated with a phosphide phase that is stable at room temperatures in this pressure range, in agreement with the previous reports of a first order room temperature transition in Fe_3P above ~15 GPa (Scott et al. 2008). Tetragonal Fe_3P is likely metastable in the soft pressure KCl and Ne pressure media used in this study. The hydrostaticity of neon, in particular, induces little stress gradients on the sample, possibly hindering a room temperature transition. The Fe_3P single crystal experiments in neon did not show crystallization of the new phase with room temperature compression, but the phase did

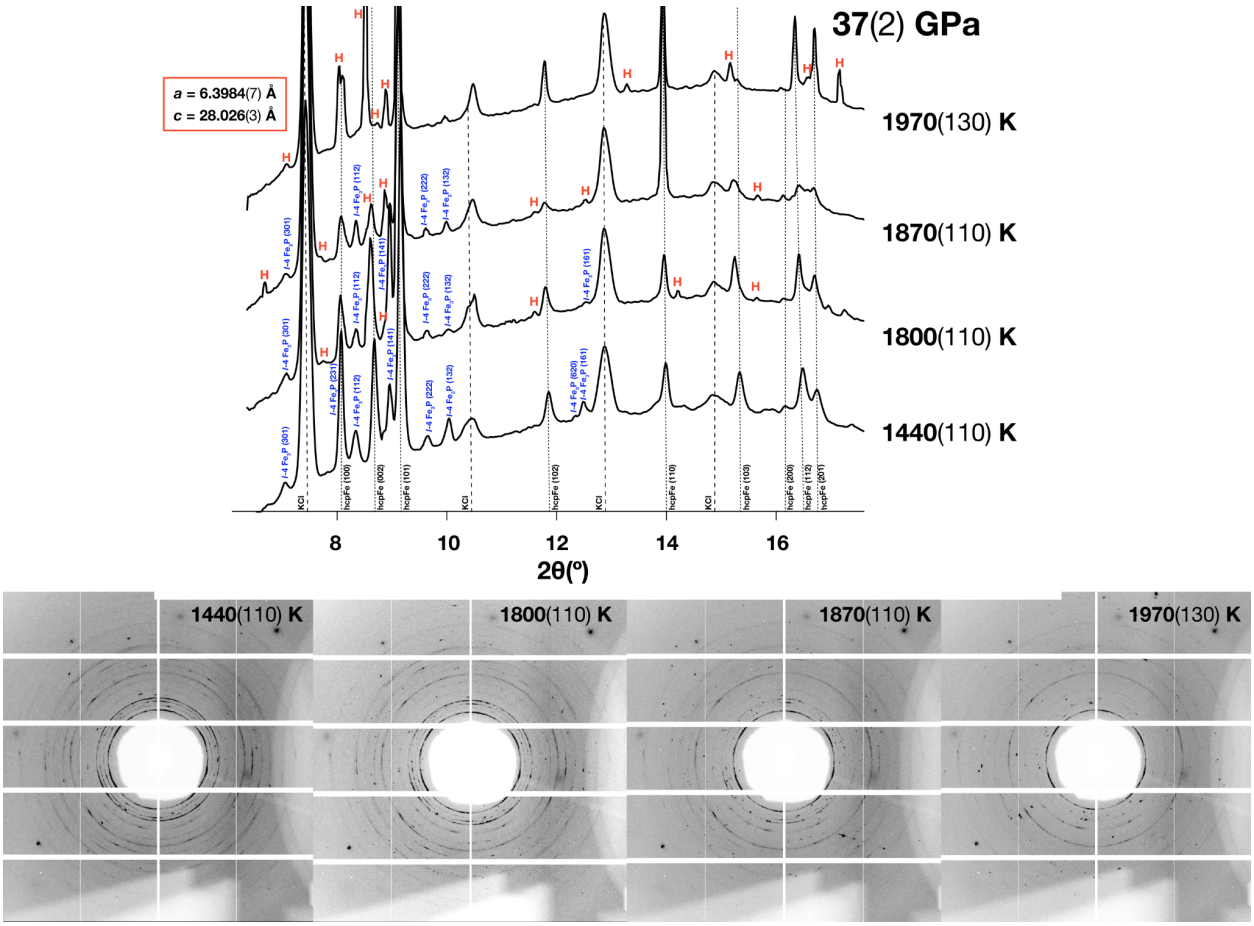

Figure 7.5. X-ray diffraction collected upon heating at 37(2) GPa on a foil of Fe_3P in KCl. The lowest temperature pattern evidences that the starting Fe_3P material had excess Fe in it. Tetragonal Fe_3P + hcp-Fe transitions to a high temperature phase (labeled "H") coexisting with iron. By 1970(130) K, the initial Fe_3P powder completely transformed while hcp-Fe remained stable. Upon quenching the sample and collecting rotational scans, crystallites of the high temperature phase were indexed in the reciprocal space to a trigonal unit cell with a = 6.3984(7) Å and c = 28.026(2) Å.

form immediately upon heating. The starting sample configurations are labeled for each heating cycle shown in Figure 7.1d, to demonstrate that the synthesis of this phase is repeatable with these differing sample configurations.

Similar to our observations of the Fe-S system, the peak intensities of the high temperature Fe-P phase vary in intensity with heating and form large spots, indicating multigrain

growth (Figure 7.1c, 7.5). Upon quenching from high temperatures at each pressure step, rotational scans across a ±30º range were collected on the Fe-P samples. Integration of the scans of the synthesized Fe-P phase reveal diffuse streaks and many reflections, a clear difference from the Fe_3P starting crystal (Figure 7.4d, e). Many grains of the high temperature phase were identified in the reciprocal space at each pressure step and up to 1136 reflections were identified for each lattice (Table 1, Figure 7.4f). Indexing of the high temperature Fe-P phase reveals that it adopts a trigonal lattice with unit cell parameters a = 6.2569(9) Å, c = 27.222(4) Å after synthesis at 66.5(7) GPa and 1700(11) K (Figure 7.4f). This elongated c axis is analogous to our observations of the Fe-S trigonal phase between 145 and 195 GPa. The c/a ratio of this Fe-P lattice at these pressures is ~4.35 and the c/a ratio of the Fe-S lattice indexed at 194 GPa is ~4.38 suggesting that they are isomorphic structures.

The lattice parameters measured in the reciprocal space for the Fe-P trigonal phase were then used to fit a room temperature equation of state (Table 1; Figure 7.6). Two samples with the synthesized trigonal phase in neon were decompressed from 67 GPa to ambient conditions (Table 1). At each pressure step, the trigonal phase unit cell was indexed in the reciprocal space and the volumes show a smoothly decreasing trend with pressure (Figure 7.6). A distinct loss of reflections of the trigonal phase is observed upon decompression below 16 GPa and a higher-than-expected volume is measured at 11 GPa (Table 1, Figure 7.6). Below 11 GPa, reflections from the trigonal phase are not observed. These observations suggest that the Fe-P trigonal phase becomes unstable below 16 GPa on decompression, in agreement with previous reports (Scott et al. 2007). The trigonal phase volumes measured between 16 and 67 GPa were then fit to a

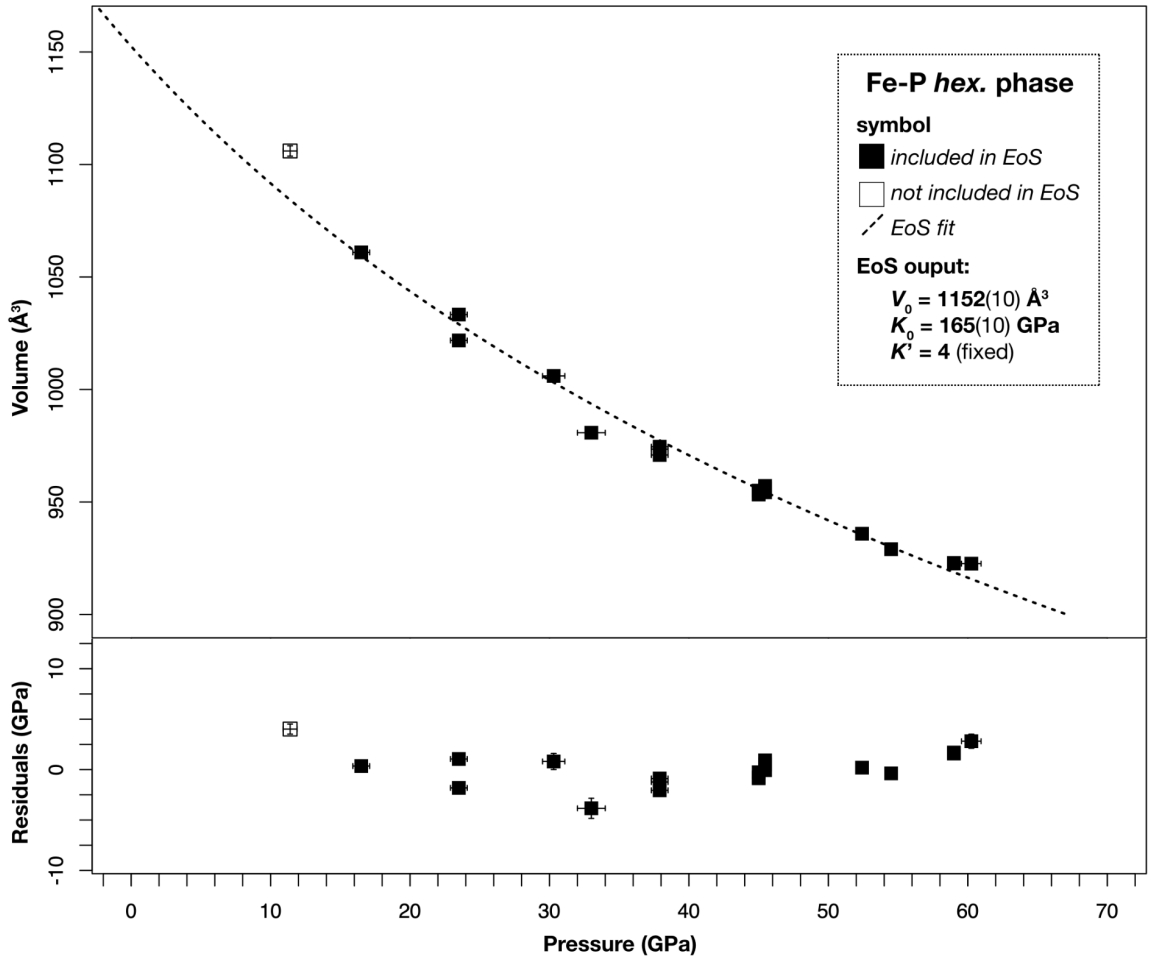

Figure 7.6. P-V relationship for the Fe-P trigonal phase measured on decompression in Ne from the high P-T synthesis conditions listed in Table 1. A room temperature equation of state (EoS) was fitted to the data above 16 GPa (filled squares) and the output is shown by the black dashed curve. Residuals to the fit are plotted in the lower panel. The datapoint at ~11 GPa (open square) is not included in the EoS fit, as it shows a higher-than-expected volume, and below these pressures, the trigonal phase is no longer observed. The higher-than-expected volume at 11 GPa likely represents the onset of phase instability on decompression. The calculated residuals of this low pressure datapoint compared to the EoS fit is given by the open square in the residuals plot. The root means square value of the residuals to the fit is 1.5 GPa.

second-order Birch-Murnaghan EoS (Birch, 1952) (Equation 7.1) with isothermal bulk modulus, K_0 and zero-pressure volume, V_0. The pressure derivative, *K,*' was fixed at 4.

$$P_{300}(V) = 3K_0 f(1 + 2f)^{2.5} * (1 + 1.5(K' - 4) f), f = 0.5 * ((V/V_0)^{(-2/3)} - 1) \quad 7.1$$

The equation of state fitting yields V_0 = 1152(11) Å^3 and K_0 = 165(10) GPa and the fit is plotted as the black dashed curve in Figure 4. The residuals to the fit show a root mean square value of 1.5 GPa (Figure 7.6).

7.3.3. Structural analysis of the hexagonal Fe-S and Fe-P isomorphs.

With the 34–60º access to the reciprocal space in the multigrain Fe-S and Fe-P experiments, the lattice parameters of the trigonal phase were accurately determined; however, attempts to solve the structure for the large unit cell proved more challenging. Constraints on the stoichiometry and the structure from examination of the reciprocal space and raw diffraction patterns were first discerned. For the samples conducted on the Fe_3P single crystals, no additional phases were identified in the diffraction patterns or in the reciprocal space after synthesis of the Fe-P trigonal phase. These results suggest the stoichiometry of the trigonal phase is close to 75% Fe. Mapping the (hk0) planes of a Fe-P trigonal phase lattice synthesized at 50.6(4) GPa and 1510(110) K reveals diffuse scattering between Bragg reflections along the *c* axis (Figure 7.7a). These features are likely related to positional disorder of the atomic sites along the *c* directions, attributing to the large *c/a* ratio for trigonal phase. The sharp Bragg reflections overlain on the diffuse signal are representative of an average atomic arrangement along the *c* axis (Figure 7.7a).

Diffuse scattering from positional disorder is difficult to analyze with single crystal X-ray diffraction techniques developed to model the structure factors for diffraction from regular repeating lattice sites. For each pressure step, the intensities of the Fe-P and Fe-S trigonal phase lattices were integrated and reduced. An analog search was then conducted, and the unit cell geometry of the trigonal phase appears similar to the Ni_8P_3 structure (Ilnitskaya et al. 1987), a doubling along the *c* axis of the $Fe_{12}As_5$ (Maaref et al. 1983), or a doubling along the *c* axis of the low temperature Ni_5P_2 structure (LT-Ni_5P_2) (Oryshchyn et al. 2004) (Figure 7.7b, Figure 7.9). The potential Ni_8P_3, $Fe_{12}As_5$, and LT-Ni_5P_2 analogs have Fe content ranging from 73–70 %, in agreement with the plausible chemistry of the trigonal phase. The Ni_8P_3 adopts the *R3c* space group with ambient lattice parameters *a* = 6.613 Å, *c* =37.914 Å (Ilnitskaya et al. 1987) (Figure 7.7c). The current Fe-P and Fe-S trigonal phase lattices exhibit a significantly smaller *c*/*a* ratio, and if the trigonal phase adopts the Ni_8P_3 structure, partial occupancies of the lattice sites as a result of disorder would be required to obtain a reasonable density for the trigonal phase. The $Fe_{12}As_5$ structure adopts the *R*32 space group with ambient parameters *a* = 6.7855 Å, *c* = 16.301 Å (Maaref et al. 1983). If the trigonal phase adopts the $Fe_{12}As_5$ structure, doubling of the *c* axis, and vacancies of some phosphorous sites as a result of positional disorder would be required to match the observed likely Fe-content and unit cell Fe-S and Fe-P trigonal phases. The $Fe_{12}As_5$ structure could represent an average structure with a superstructure resulting from the site disorder. The LT-Ni_5P_2 structure adopts the *P*-3*c*1 space group with ambient parameters *a* = 6.613 Å, *c* = 12.311 Å (Oryshchyn et al. 2004). Similar to the $Fe_{12}As_5$ structure type, a doubling of the *c* axis would be required to match the observed trigonal phase geometry.

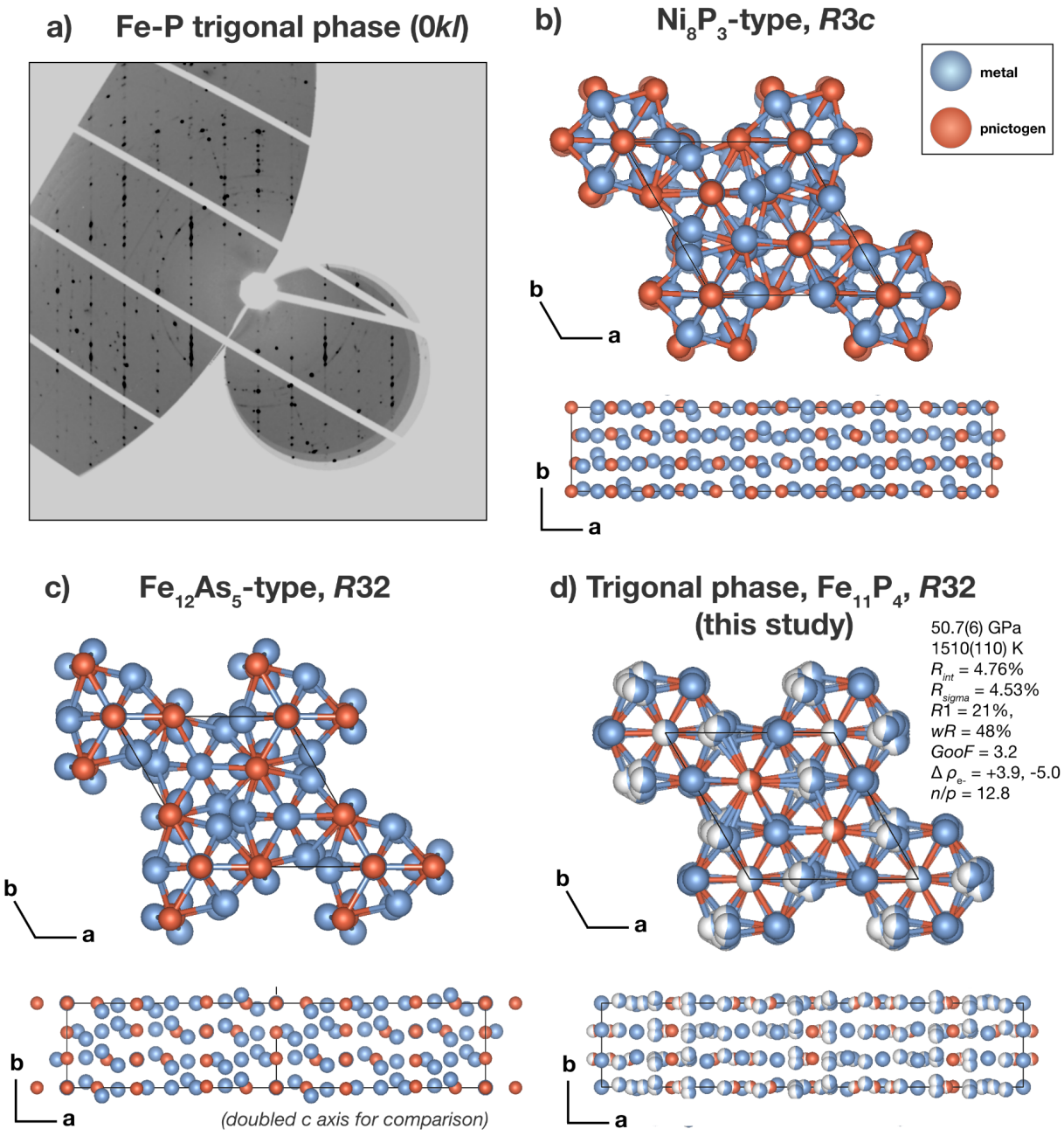

Figure 7.7. a) Unwarped diffraction mapping of the (0kl) layer of a trigonal Fe phosphide crystallite synthesized at 51(1) GPa and 1510(110) K, showing diffuse scattering as a result of positional disorder in the structure. b) The Ni_8P_3 structure with *R*3*c* space group (Ilnitskaya et al. 1987). c) The $Fe_{12}As_5$ structure in the *R*32 space group (Maaref et al. 1983). To produce reasonable Fe-S and Fe-P trigonal phase densities, an Ni_8P_3 structure model would have to be accompanied by partial vacancies. For an $Fe_{12}As_5$ structure model, a doubling of the unit cell along the *c* axis is required to match the trigonal phase *c/a* ratios. d) Attempt at a structure model

Figure 7.7. ***continued***
refinement for the Fe-P trigonal phase synthesized at 50(1) GPa and 1510 K. The structure solution resembled the atomic arrangement of the Ni_8P_3 and $Fe_{12}As_5$ structure types with disorder modeled by partial site occupancies. The refinement parameters are not adequate to consider this a resolved structural characterization but the disordered nature of the structures proposes significant challenges for modeling this structure using single crystal X-ray diffraction techniques. The *n,* and *p* characters denote the number of reflections (*n*) and number of parameters in the model (*p*).

Inputting the Ni_8P_3, $Fe_{12}As_5$ and LT-Ni_5P_2 structure types, Le Bail refinements of the powder diffraction patterns were conducted for the Fe-P and Fe-S synthesis products from 50.7(6 GPa) and 1510(110) K and 184(3) GPa and 3250(260) K, respectively (Figure 7.8, Figure 7.9). The Fe-P powder patterns consisted of neon, *I*-4 Fe_3P and the trigonal phase and the Fe-S powder patterns contained hcp-Fe + trigonal phase diffraction angles. Diffraction from the SiO_2 pressure medium was not observed above the background of the quenched patterns. The Ni_8P_3 and $Fe_{12}As_5$ structures both show a good match to the diffraction angles for both the Fe-P and Fe-S diffraction patterns (Figure 7.8), suggesting that they share a similar atomic arrangement. The LT-Ni_5P_2 diffraction angles do not account for all of the peaks and doubling of the *c* axis from site disorder would have to produce a high intensity diffraction angle at ~8.7º 2θ (Figure 7.9). It is possible that ordering of the sites along the doubled *c* axis in LT-Ni_5P_2-type structure could produce an additional high intensity peak, but the Ni_8P_3 of $Fe_{12}As_5$ structure types match the average diffraction angles of the trigonal phase without proposing further constraints (Figure 7.8).

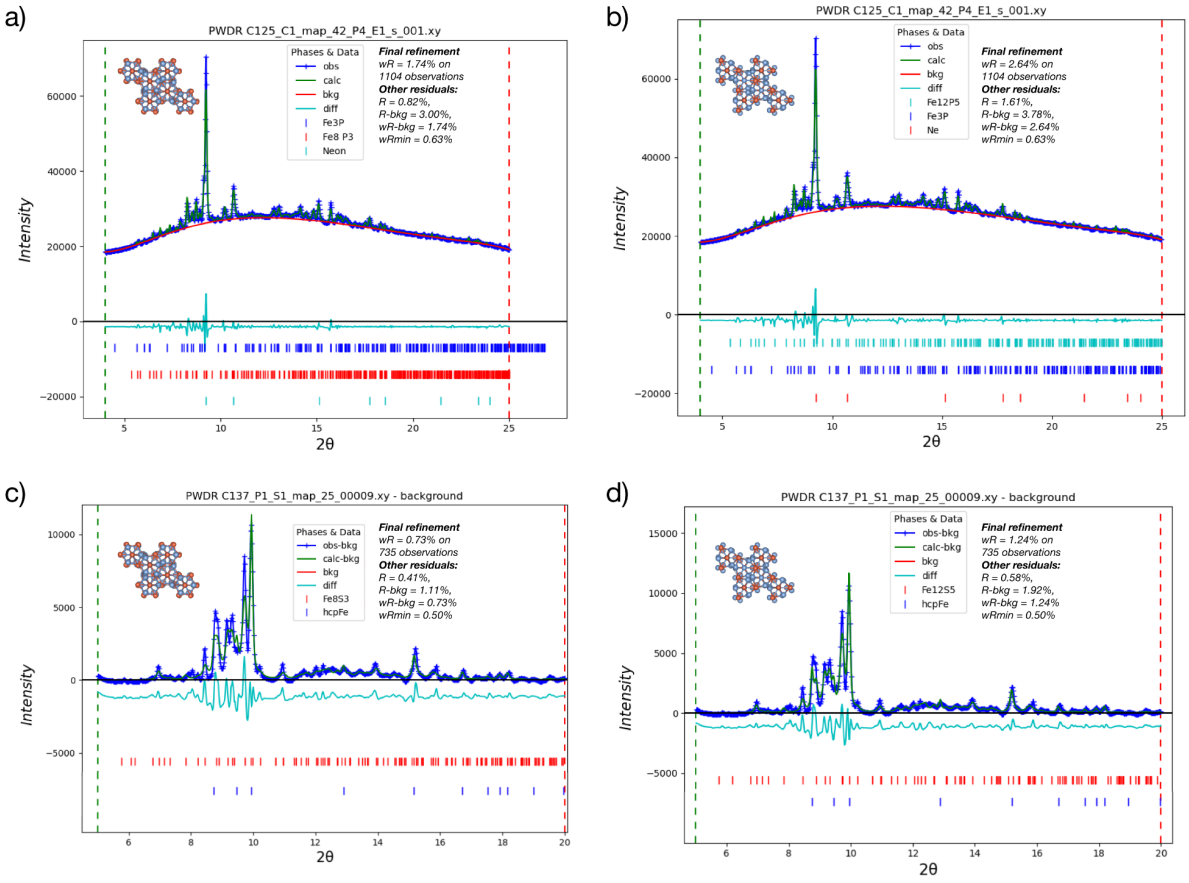

Figure 7.8. Le Bail refinements for a a) Ni_8P_3-type Fe-P trigonal phase, fcc-neon, and *I*-4 Fe_3P phase assemblage at 45.6(4) GPa and quenched from 50.7(6) GPa and 1510(110) K; b) $Fe_{12}As_5$-type Fe-P trigonal phase, fcc-neon, and *I*-4 Fe_3P phase assemblage at 45.6(4) GPa and quenched from 50.7(6) GPa and 1510(110) K; c) Ni_8P_3-type Fe-S trigonal phase, and hcp-Fe phase assemblage at 159(1) GPa and quenched from 184(3) GPa and 3250(260) K; and d) Ni_8P_3-type Fe-S trigonal phase, and hcp-Fe phase assemblage at 159(1) GPa and quenched from 184(3) GPa and 3250(260) K.

The Ni_8P_3 and doubled $Fe_{12}As_5$ structure solutions were then applied to the observed structure factors for the Fe-P trigonal phase after reduction of 791 trigonal phase reflections collected at 45.6(4) GPa. While the reported Ni_8P_3 and $Fe_{12}As_5$ structures did not immediately resolve the electron density distribution of the reduced trigonal phase, a structure model with *R*32 space group a similar atomic arrangement was calculated (Sheldrick 2015a). The atomic

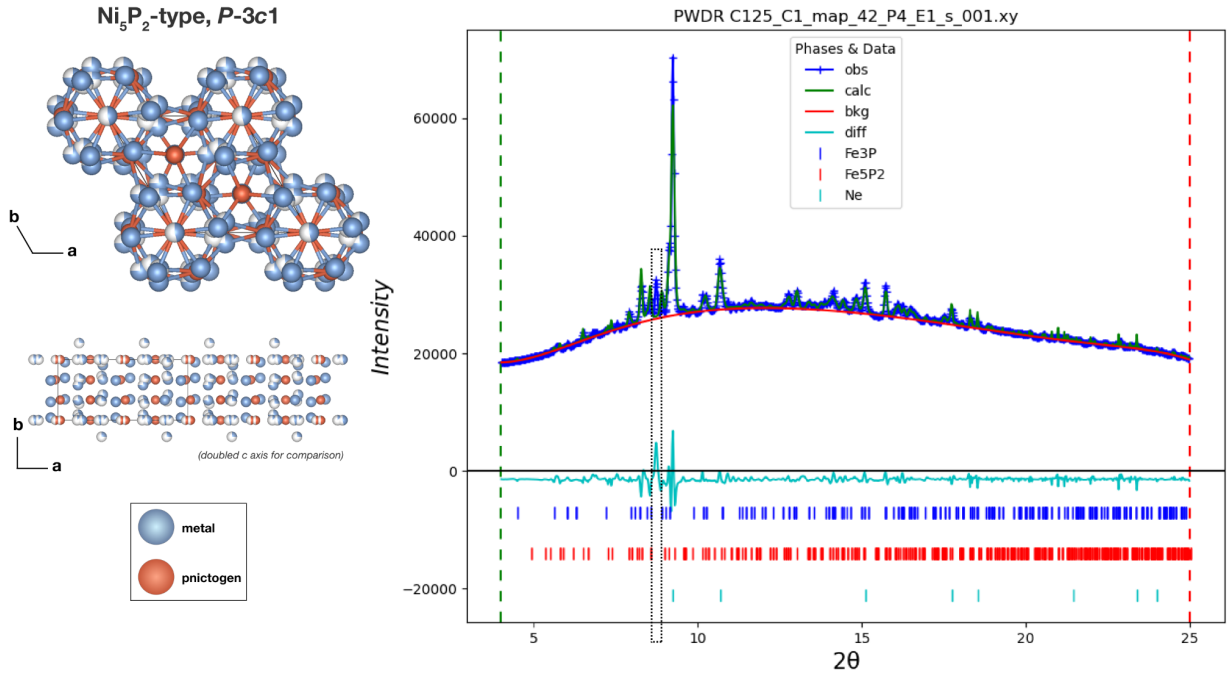

Figure 7.9. Le Bail refinement of a Fe-P powder pattern collected after synthesis at 50.7(6) GPa and 1510(110) K with neon, tetragonal Fe_3P, neon and the LT-Ni_5P_2-type structure (*P*-3*c*1) (Oryshchyn et al. 2004). The LT-Ni_5P_2 structure adopts the *P*-3*c*1 space group with ambient parameters a = 6.613 Å, c = 12.311 Å. The LT-Ni_5P_2-type structure of Fe_5P_2 does not account for all peaks not associated with *I*-4 Fe_3P or neon (dotted box). Doubling of the unit cell as a result of positional disorder would have to produce a high intensity peak ~8.7.º

coordinates and isotropic displacement parameters were initially refined. Then pairs of atomic sites with interatomic distances shorter than expected for *P-P* and *Fe-Fe* bonds were given split vacancies and atomic positions were added and refined where distinct Fourier peaks were found. The final model describes the disordered structure with final stoichiometry of $Fe_{11}P_4$, equating to 73% Fe, and an R_1 value of 21% and electron density residuals of < ± 5 (Figure 7.7d). These values are not optimal and do not indicate a resolved structure model, but additional experimental work addressing the diffuse scattering observed from this structure is necessary to better characterize the site occupancies and atomic arrangement. A CIF file of our effort to solve

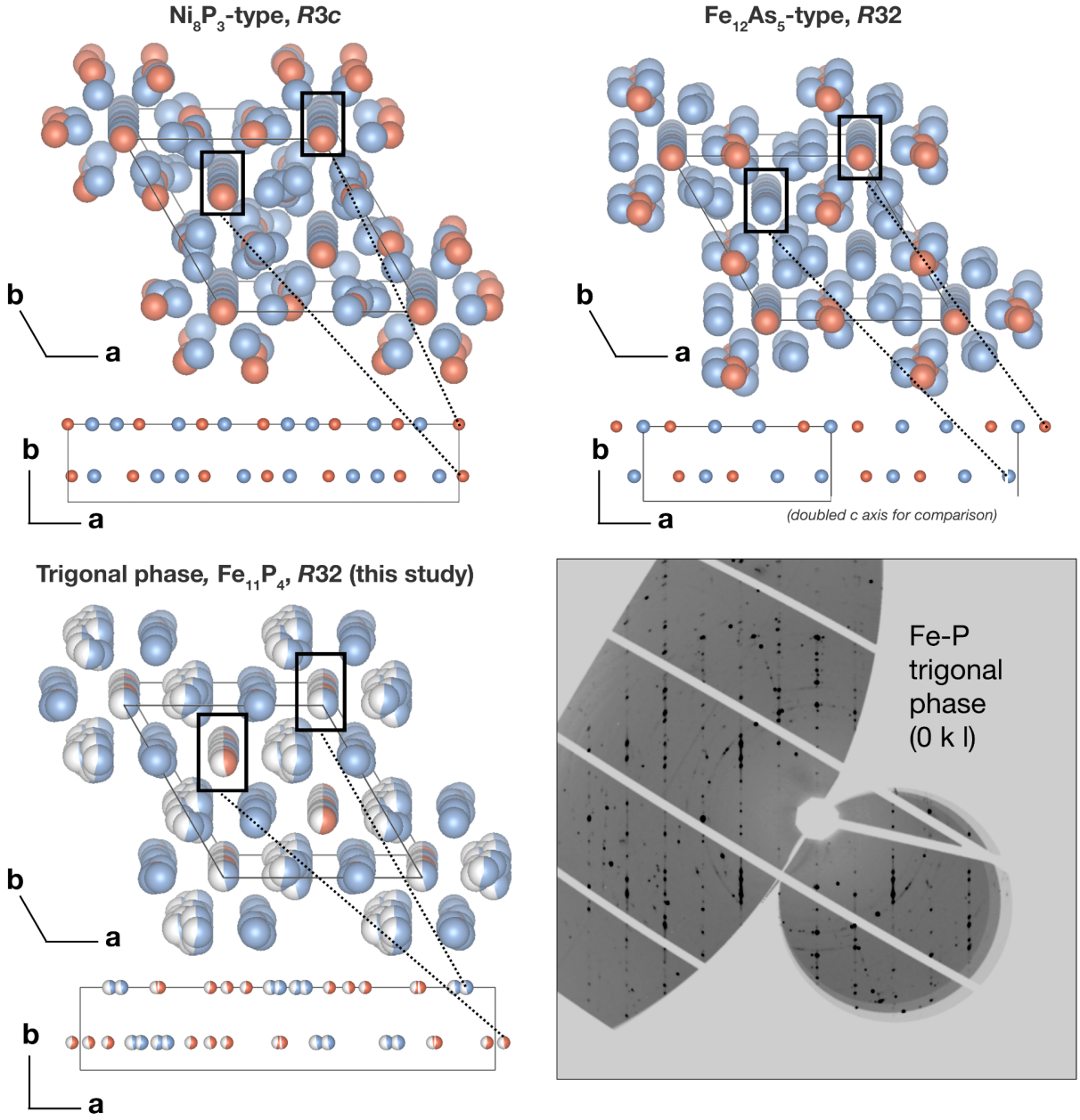

Figure 7.10. A view of the atomic arrangement of the Ni_8P_3, $Fe_{12}As_5$, and trigonal phase (this study), structures showing clustering of atomic sites around the 6-fold and 3-fold axes. The atomic arrangements along the 6-fold and 3-fold axes are isolated below each unit cell. These sites likely contribute to the sharp bragg peaks, as observed on the (0kl) diffraction mapping, while the diffuse streaks between the bragg peaks may be associated with the atomic clustering around these sites.

and refine the Fe-P trigonal phase structure is given in supplementary file SF7a. An improved characterization of the average and the disordered nature of the trigonal phase may greatly benefit from techniques such as 3-D difference pair distribution function (3D-ΔPDF) and computational random search methods developed or to analyze diffuse X-ray scattering from single crystals (Loa et al. 2012; Simonov et al. 2014).

Despite not being able to refine the structure of the trigonal phase against the Ni_8P_3 and $Fe_{12}As_5$ structure models, these structures equally describe the Fe-P and Fe-S trigonal phase diffraction angles, suggesting that they share an average structure. The structure models for Ni_8P_3, $Fe_{12}As_5$ and the trigonal phase, do exhibit similar atomic arrangements, with alignment of atomic sites along the 6-fold and 3-fold axes and the clustering of atoms around these sites (Figure 7.7, 7.10). The lattice sites along the 6-fold and 3-fold axes sites likely contribute to the sharp Bragg peaks, as observed on the (0kl) diffraction mapping (Figure 7.7a), while the diffuse streaks between the Bragg peaks may be associated with the atomic clustering around these sites (Figure 7.10).

7.4. Implications

Transitional metal binary compounds with metal:nonmetal ratios ranging from 2.33–2.66 predominantly adopt complex trigonal or hexagonal structures with considerable metal-metal bonding (Chen and Whitmire 2018). A previous study of the related $Fe_{12}As_5$ structure type reported that Fe_2As breaks down into $Fe_{12}As_5$ + FeAs at 1000ºC and 30 kbar, with $Fe_{12}As_5$ assuming a structure marked by atomic clustering and increased metal-metal interactions

(Maaref et al. 1983). As orthorhombic Fe_2S is observed at moderate temperatures between 25 and 306 GPa, the stabilization of the trigonal Fe-P phase between 145 and 195 GPa and to 3500 K likely marks a thermodynamic preference for increased metal-metal interactions at high temperatures in this pressure range. Observations of the tetragonal Fe_3P + Fe → trigonal phase + Fe transition between 16 and 67 GPa, also evidence that this structural configuration is favored over the Fe_3P structure at high *P-T* despite the Fe_3P-structure exhibiting a significant degree of Fe-Fe interaction. Further work grappling with the structural details of this complicated trigonal cell is required to construct the thermodynamic relationships between M_2X, $M_{12}X_5$, M_8X_3, $M_{11}X_4$, and M_3X compounds in Fe-rich systems.

After synthesis and equilibration of the Fe-P trigonal phase between 36 and 67 GPa, it is observed to become unstable on decompression in neon in the pressure range of 11–16 GPa. These results are supportive of the previously reported first-order transition in Fe_3P (Scott et al. 2007; 2008). In the room temperature compression study of Fe_3P (Scott et al. 2007), additional peaks were observed in the integrated diffraction patterns above 15 GPa but the nature of the transition was not discussed. A later study then reported that Fe_3P readily transitioned to this unknown phase upon heating Fe_3P at 20 GPa to 2100 K (Scott et al. 2008). These results are directly compatible with the current study; reflections from the trigonal phase are observed with room temperature compression and Fe_3P further transitions to the trigonal phase immediately upon heating between 36 and 67 GPa. Once the trigonal Fe-P phase is synthesized, it is observed on decompression to ~16 GPa. Combining observations from these previous studies, the trigonal phase is likely stable at room temperatures above ~15 GPa even though Fe_3P schreibersite may be metastable on room temperature compression (Scott et al. 2007; 2008).

These results differ from the experimental reports by Gu et al. 2014, where Fe_3P was observed in the tetragonal (*I*-4) structure to 64 GPa and moderate temperatures and observed to transition to a primitive tetragonal cell above ~1650 K at 64 GPa. These results also differ from previous reports of tetragonal Fe_3P stability at room temperature to 111 GPa (Lai et al. 2020). Several lines of reasoning may explain these discrepancies. The previous room temperature compression work was conducted in neon, a soft medium that imparts minimal stress gradients on the sample. The metastability of Fe_3P schreibersite on room temperature compression may be sustained in a neon pressure medium, as our single crystal experiments in neon also did not show a room temperature phase transition in Fe_3P. Furthermore, during the Fe_3P heating experiments, the crystallization of the trigonal phase was recognized by the first observable reflections in the raw diffraction patterns, as residual peaks associated with *I*-4 Fe_3P were observed to moderate temperatures, making it difficult to discern the growth of the trigonal phase in the integrated powder patterns (Figure 7.5). The peak intensities of the trigonal phase also fluctuate in the integrated powder patterns due to the synthesis of a multigrain sample at high *P*-*T*, and the cell could easily be misindexed. Without characterizing the trigonal phase cell in the reciprocal space, it would be difficult to assume such an elongated unit cell and complicated trigonal structure.

The Fe-P trigonal phase is observed to 2640 K at high pressures in the current study (Table 1). To the degree that phosphorus is present in Fe-rich planetary cores of Mercurian to Martian size, phosphorus may alloy with iron to adopt the trigonal phase on the liquidus. For the Fe-rich Mercurian core, the trigonal Fe-phosphide may contribute to the compositionally driven convection of the outer core, and for the light element-rich Martian core, the Fe-P trigonal phase

may crystallize with Fe_3S into a growing inner core. The stability of the Fe-P trigonal phase to pressures as low as 15 GPa and the decomposition of the structure with further decompression should also be taken into account when determining the thermodynamic history of Fe-P-rich meteorites.

Lattice indexing of the Fe-S trigonal phase in the reciprocal space and the Le Bail refinement of the multi-phase Fe-rich powder diffraction patterns, establish that tetragonal Fe_3S is not stable at these conditions, contrary to previous reports (Kamada et al. 2010; Kamada et al. 2012; Ozawa et al. 2013; Mori et al. 2017). Similar lines of reasoning can be applied to this discrepancy as was described above for the Fe-P system. Observations of Fe-S trigonal phase in the integrated powder diffraction patterns is difficult owing to the low intensity scattering from the disordered sites of the structure. The Fe-S trigonal phase also grows large crystallites (Figure 7.3), limiting the orientations of the phase such that identifying all of the diffraction angles of the trigonal phase in an integrated powder pattern is quite challenging. The implementation of single crystal X-ray diffraction techniques at high pressures was critical to accurately characterize the unit cell geometry of the trigonal Fe-sulfide in this study.

The trigonal phase was concluded as an $Fe_{11}X_4$ stoichiometry on the basis of our attempts to minimize electron density residuals in the Fe-P trigonal phase structural refinement, comparisons to the metal content of the analogous Ni_8P_3 and $Fe_{12}As_5$ structures, and the absence of additional phases observed after synthesizing the trigonal phase from an Fe_3P single crystal. Several studies have observed sulfide grains with ~75% Fe content using chemical analysis techniques of recovered high *P-T* samples (Mori et al. 2017; Yokoo et al. 2019; Ozawa et al. 2013). Differentiating between grains that are 73% iron and grains that are 75% iron using

chemical analyses techniques on nm-scale grains recovered from multi-megabar pressures is difficult. Observations of ~75% Fe chemistries in Fe-S and Fe-S-O sample recovery studies from these high pressures and temperatures therefore do not necessarily contradict the current results (Mori et al. 2017; Yokoo et al. 2019; Ozawa et al. 2013).

The stability of the Fe-S trigonal phase coexisting with hcp-Fe above 145 GPa and to 3500 K is directly relevant to the thermodynamics of Earth's outer core (136–330 GPa, ~3500–5500 K). Recent crystallographic analyses of tetragonal Fe_3S at 118 GPa and quenched from ~2400 K confirm that Fe_3S is stable in the Fe_3P structure (*I-4*, *Z* =8) to at least these conditions (Zurkowski et al. submitted, Chapter 4). The Fe_3S + Fe → Fe-S trigonal phase + Fe transition must occur at high temperatures between 120 and 145 GPa. As this pressure and temperature range overlaps with that of the core-mantle boundary, the volume change and elastic properties of these phases may play a role in the seismic properties and crystallization sequences of the outermost core. Recent work has also established a *C*23–*C*37 phase transition in Fe_2S coexisting with iron at moderate temperatures in the 120–150 GPa pressure range (Zurkowski et al. submitted, Chapter 4). This adds complexity to the thermodynamics at potentially core-mantle boundary pressures and the details of these phase boundaries must be addressed. The influence of the atomic configurations of the C23 and C37 Fe_2S structures on the high temperature formation of the Fe_3P-type versus Fe-S trigonal phase-type structures may also be the focus of future crystallographic studies. Although the Fe-S trigonal phase is observed in the current study to ~200 GPa and >3000 K, *C*37 Fe_2S is reported to become stable on the liquidus at 306 GPa in Fe-rich systems (Tateno et al. 2019). This suggests a positive phase boundary slope between the *C*37 Fe_2S + Fe and Fe-S trigonal phase + Fe phase fields, compatible with our observations to 200

GPa. The stability of Fe-S trigonal phase above 145 GPa also suggests a change in melting behavior in the Fe-rich Fe-S system. As the Fe-S trigonal phase was synthesized up to ~3250 K at 160 GPa, a kink in the Fe-sulfide solidus curve is proposed (Mori et al. 2017). Further changes in melting relations occur as *C*37 Fe_2S becomes stable on the liquidus above 306 GPa, and future experiments are required to investigate the shape of the liquidus curve and discuss its effects on the density structure of the lowermost core.

Comparisons of the observations to previous examinations of trigonal phase analogs indicate that the complexity of the trigonal phase structure is a likely result of increased metal-metal interactions, and the stability of this structure in the Fe-S system at Earth's outer core conditions may affect the electronic, conductive and convective properties of the liquid iron alloy. Thermal conductivity measurements of iron and iron alloys at Earth's core conditions are not succinct: some theoretical and shock experiment studies have reported low thermal conductivity values such that convection in the Earth's liquid core prior to inner core crystallization could have been thermally driven (Mattasov 1977; Stacey and Anderson 2001; Bi et al. 2002; Stacey and Loper 2007), while recent computational and laser-heated DAC experiments report higher conductivity values that would require chemically driven convection to drive an early dynamo (e.g., Pozzo et al. 2012; Gommi et al. 2013 ; Ohta et al.; 2016). The effects of pressure-temperature and short-range order of liquid iron alloys may influence these values and future work examining Fe-S alloy thermal conductivity should consider the electronic properties of Fe-S trigonal phase in the upper regions of the liquid outer core, as the increased metal-metal interactions in the Fe-S trigonal phase may contribute to higher thermal conductivity values.

7.5. Conclusions

The Fe-S and Fe-P systems were examined to high temperatures between 145–195 GPa and 36–67 GPa, respectively, using powder and single crystal X-ray diffraction techniques in a laser heated diamond anvil cell. At moderate temperatures between 145–195 GPa, *C*37 Fe_2S + Fe are observed to react to form a lattice that was indexed in the reciprocal space to a trigonal cell with an elongated *c* axis. This phase is observed to grow large crystallites coexisting with recrystallized iron to ~200 GPa and 3000 K. Analogously, in the Fe-P system, between 36 and 67 GPa, a trigonal phase forms with a compatible relative unit cell to that observed in the Fe-S system. The trigonal phase is marked by diffuse scattering, indicating positional disorder. LeBail refinements of the Fe-S and Fe-P powder diffraction patterns demonstrate the average structure of the Fe-P and Fe-S trigonal phase are well described by either the Ni_8P_3 or $Fe_{12}As_5$ structures. Solving and refining the electron density of the crystal structure using single crystal techniques was not attainable with high accuracy due to the disordered nature of the structure, but initial attempts support that the average structure is similar in structure to Ni_8P_3 and $Fe_{12}As_5$ with an $Fe_{11}X_4$ stoichiometry. The structural complexity of the Fe-S and Fe-P trigonal isomorphs is a likely result of increased metal-metal interactions, as has been observed in binary transition metal compounds with 70–73% metal content. The stability of Fe-P trigonal phase coexisting with iron in the pressure range of Mercury-to-Mars sized terrestrial planetary cores, may contribute to their chemistry and dynamics, and the stability field of Fe-P trigonal phase should be considered in interpretations of meteorite *P-T* histories. The stability of Fe-S trigonal phase coexisting with iron at outer core pressures and high temperatures adds new complexity to our understanding of the thermodynamics of Earth's liquid outer core. The increased metal-metal

interaction in the Fe-S trigonal structure may contribute to a high thermal conductivity in the outer core, and the tetragonal Fe_3S + Fe → Fe-S trigonal phase + Fe → *C*37 Fe_2S + Fe liquidus phase transitions occurring across outer core pressures may directly affect the crystallization sequences, melting behavior and density profile of the outer core.

8. Observations of a hexagonal $Fe_X(S, O)$ phase at Earth's outer core pressures and high temperatures.

Collaborators: Anne H. Davis[a], Stella Chariton[b], Eran Greenberg[b†], Vitali B. Prakapenka[b], and Andrew J. Campbell[a]

[a]University of Chicago, Department of the Geophysical Sciences, 5734 S Ellis Ave, Chicago, IL 60637, USA
[b]Center for Advanced Radiation Sources, 9700 South Cass Avenue, Building 434A, Argonne, IL 60439, USA
[†]Now at Applied Physics Department, Soreq Nuclear Research Center (NRC), Yavne 81800, Israel.

8.1. Introduction

In this ongoing project, we expanded the chemical complexity of our experiments from the binary Fe-S system to the ternary Fe-S-O system to begin comparing the structural properties and phase relations of the ternary system to the respective Fe-S and Fe-O binary studies. We explored the Fe-S-O phase relations to 180 GPa and 3700 K, using a combination of *in-situ* X-ray diffraction techniques and chemical analysis of recovered samples, and the next steps of this project include conducting multigrain diffraction experiments at these conditions. From our powder diffraction results, we observe *C*37 Fe_2S coexisting with *B*1 FeO and hcp-Fe at moderate temperatures in the 150–180 GPa pressure range, and with increasing temperature, *C*37 Fe_2S + hcp Fe react to form the trigonal phase, in agreement with the results from Chapter 7. At the highest temperatures in these Fe-S-O experiments, an additional set of peaks is observed to grow into the pattern as peaks associated with the trigonal phase and Fe decrease in intensity. The phase was indexed to a hexagonal structure related to the *B*8 (NiAs type) structure. Iron likely occupies the hexagonal closed packed lattice and Fe + (O, S) likely occupies the primitive

hexagonal sublattice. An experiment recovered from 172 GPa and 3300 K suggests that the *B*8-like phase is Fe-rich with contributions from both oxygen and sulfur. As this phase has not been observed in the Fe-FeO or Fe-FeS system alone, these results suggest the importance of S + O in stabilizing this phase and have important implications for the chemistry of multicomponent planetary cores such as that of Earth's. Further experiments aiming to constrain the S, O content using multigrain techniques and further chemical analysis is needed to expand on these implications.

8.2. Materials and methods

For the powder diffraction experiments conducted in this study, beveled Type I diamonds with culet diameters of 100 μm were used. Samples were prepared by mixing Fe (99.9+%, <10μm, Alfa Aesar), iron sulfide (FeS, 99.99%, Alfa Aesar) and iron oxide (FeO, 99.5%, Alfa Aesar) powders in a ball mill until a grain size of ≤1 μm was obtained. Scanning electron microscope (SEM) measurements indicate bulk sample compositions of Fe–6S–12O and Fe–13S–5O (dashed notation indicates wt%). Sample foils were loaded with KCl as a pressure medium and insulator. The sample loading techniques follow Section 2.2.2. Three samples and six experiments were included in this study.

Angle-dispersive X-ray diffraction and *in-situ* laser heating experiments were conducted at Argonne National Laboratory, sector 13 ID-D of the Advanced Photon Source, as described in Section 2.4.1. Powder X-ray diffraction patterns were integrated and examined using DIOPTAS (Prescher and Prakapenka, 2015) and peak positions were fit using Fityk (Wojdyr, 2010). The unit cell volumes of hcp-Fe were used to determine the pressure of the sample, using the

equation of state (EOS) of hcp-Fe (Dewaele et al. 2006). Powder diffraction patterns were calculated for differing site occupancies in the *B*8 structure using VESTA (Momma and Izumi 2011).

Chemical analysis of recovered samples took place at the University of Chicago using scanning electron microscopy. The methodology used for preparing and analyzing recovered samples can be found in Section 2.5.3.

8.3. Results and discussion

8.3.1. Fe-S-O high temperature phase relations between 150–180 GPa

An Fe–6S–12O composition was probed between 150–180 GPa and ~3500 K. In agreement with previous Fe-O and Fe-S studies in this pressure range (Ozawa et al. 2011; Fischer et al. 2011; Morard et al. 2017; This thesis, Chapter 7), hcp Fe is observed at low temperatures to coexist with *C*37 Fe_2S (Co_2Si-type, *Pnma, Z* = 4) + *B*8 FeO (NiAs -type, $P6_3/mmc$, *Z* = 2). At moderate temperatures, above around 2100 K at 177 GPa (Figure 8.1), *B*8 FeO transitions to *B*1 FeO (NaCl-type, *Fm*-3*m*, *Z* = 2) and *C*37 Fe_2S reacts with Fe to form the Trigonal phase (~$Fe_{11}P_4$, Chapter 7). Interestingly, above 2640 K at 170 GPa, a new set of peaks grow into the pattern as the peaks associated with the Trigonal phase, iron, as well as FeO decrease in intensity (Figure 8.1). Diffuse scattering from the onset of melting is observed simultaneously, suggesting that a reaction such as this may take place: Fe + FeO + trigonal phase → new phase + FeO + melt.

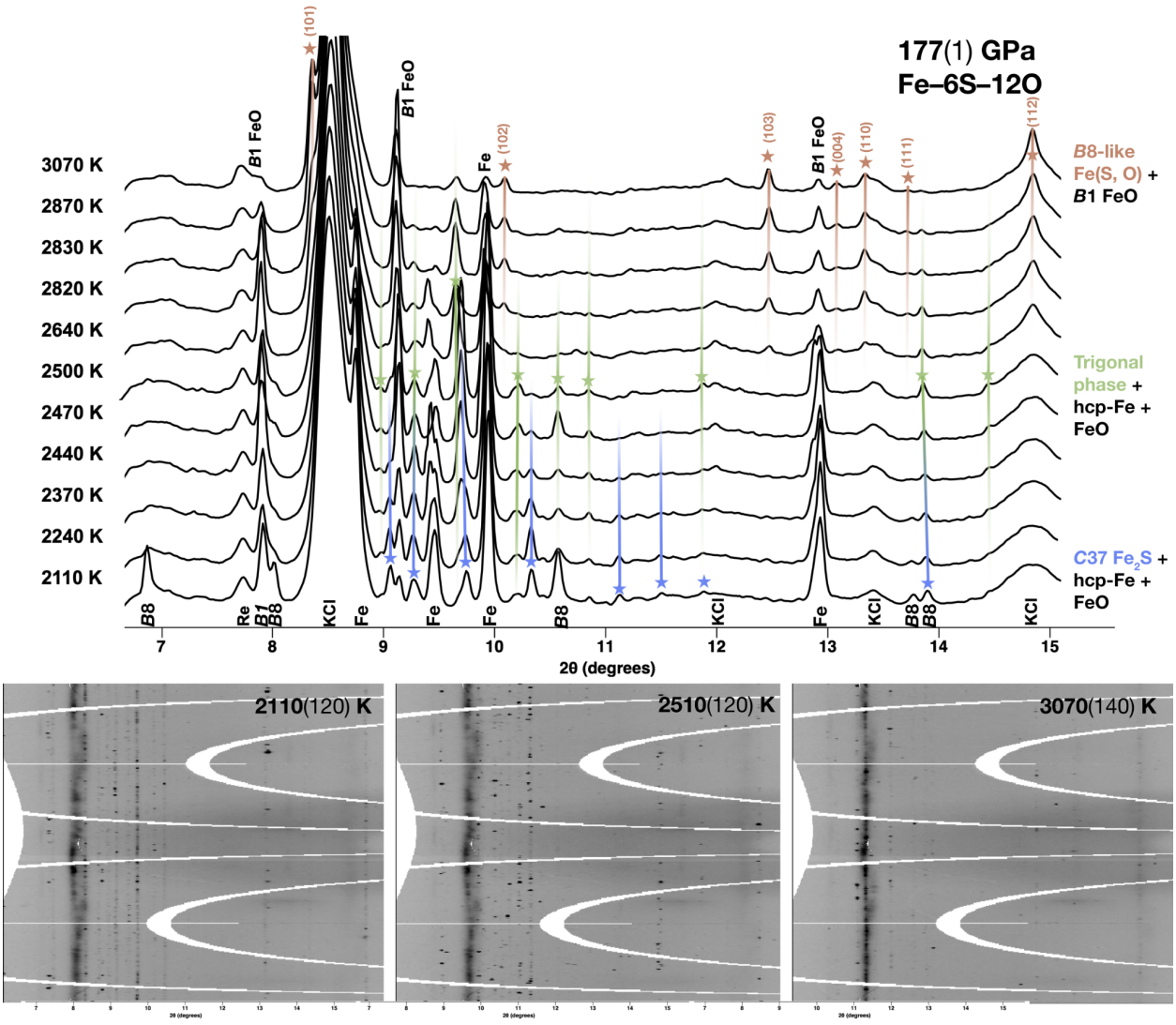

Figure 8.1. X-ray diffraction patterns with heating to 3070 K from an Fe–6S–12O sample at 177 GPa. At low temperatures, *C*37 Fe_2S (blue stars) + *B*8 FeO + hcp Fe is observed, and with continued heating, *C*37 Fe_2S reacts with iron to form the trigonal phase (green stars) and *B*8 FeO transitions to *B*1 FeO. The *B*8–*B*1 FeO transition is well constrained from previous studies (Fischer et al. 2011) and is not color coded here. The phase transition in the Fe-sulfides at moderate temperatures is novel based on this thesis work and is highlighted by the stars and color coded labels. Interestingly, above 2640 K, a new set of peaks is observed growing into the pattern (brown stars), as peaks associated with Fe and the trigonal phase decrease in intensity. The onset of melting is observed simultaneously as this phase grows in.

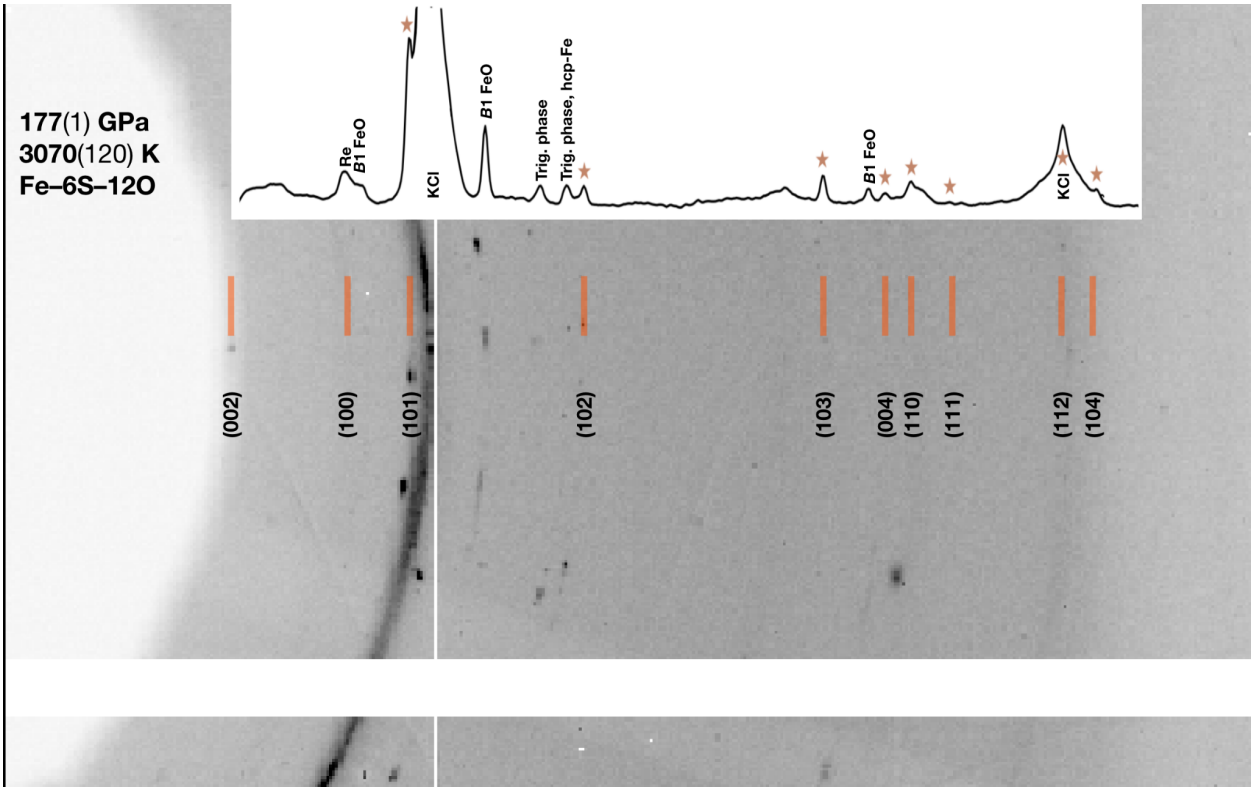

Figure 8.2. Raw diffraction pattern compared to the integrated diffraction pattern of the *B*8-like phase at 177(1) GPa and 3070(120) K with Miller indices labeled.

A compatible transformation is observed upon heating the Fe–6S–12O composition between 150–180 GPa above ~3000 K, with a plausible negative phase boundary slope (Figure 2), but additional experiments across a wider pressure range are needed to characterize these thermodynamics. Observations of this set of diffraction angles at high *P*-*T* differ from our previous Fe-S experiments in this pressure range (Figure 8.3); where the trigonal phase is observed coexisting with iron to high temperatures and no additional phases were synthesized (Figure 8.2, 8.3). These observations also differ from previous Fe-FeO studies at outer core pressures and high temperatures (Morard et al. 2017; Oka et al. 2019), where *B*1 FeO is reported coexisting with Fe on the liquidus. The high temperature phase may therefore stabilize in the

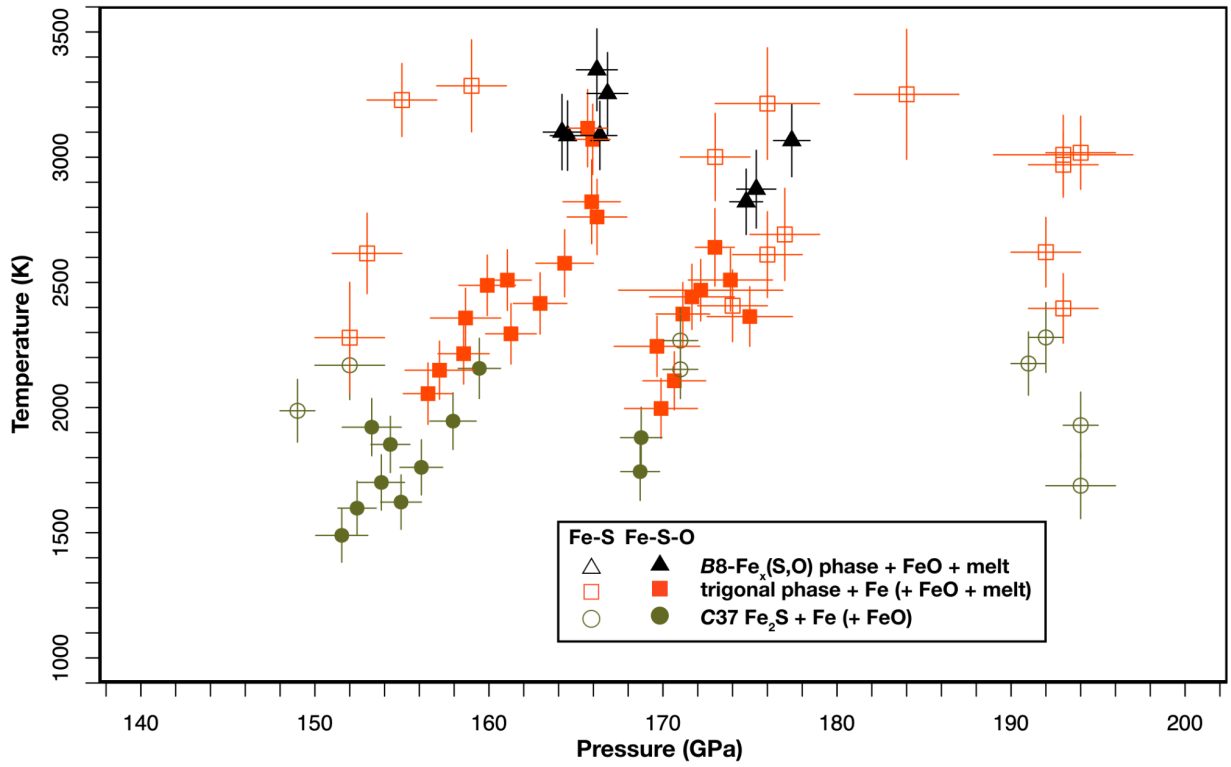

Figure 8.3. Phase relations observed in the Fe–6S–12O composition (filled symbols) between 150 and 180 GPa plotted with the phase relations observed in the Fe-S compositions measured in the previous study (Chapter 7). Notabl7, above ~2700 K between 150 and 180 GPa, the *B*8-like phase is observed to form in the O-rich experiments, where Fe + trigonal phase was observed at these conditions in Fe-rich Fe-S compositions.

presence of oxygen and sulfur, and the Fe-S-O ternary eutectic temperature is likely lower than the binary eutectic observed in the Fe-S system.

The reflections observed to grow in together at high *P-T* (Figure 8.1, 8.2) were indexed to a hexagonal unit cell volume of 29.08(3)A and unit cell dimensions a = 2.544(1) A, c = 5.188(4) A at 177(1) GPa and 3070(140) K. The diffraction angles of the hexagonal phase are compatible with a *B*8 structure, a common binary transition metal structure consisting of interpenetrating hexagonal closed packed and primitive hexagonal sublattices. A few characteristics of the high *P-T B*8-like diffraction pattern offers some information on the structures. We observe the (101)

Table 8.1. Indexing of the *B*8-like Fe_x(O, S) phase at 177(1) GPa and 3070(140) K.

d-spacing	dcalc	*h*	*k*	*l*
2.0282	2.0292	1	0	1
1.6804	1.6800	1	0	2
1.3603	1.3608	1	0	3
1.2961	1.2969	0	0	4
1.2723	1.2729	1	1	0
1.2332	1.2354	1	1	1
1.1434	1.1428	1	1	2
1.1178	1.1176	1	0	4

peak at 2θ = 8.35º to have the highest intensity rather than the (102) peak at 2θ = 11.45º (Figure 8.1, 8.2). This likely indicates a NiAs, rather than inverse NiAs structure, where the metal atoms occupy the hcp sublattice and light elements occupy the primitive hexagonal sublattice. We observe a low intensity peak at 2θ = 13.72º (Figure 8.1), associated with the (111) plane that is absent in the NiAs structure. Additional low intensity peaks may be a result of ordering within the structure. The *c/a* ratio of this high *P-T B*8-like phase is ~2.0 while the *c/a* ratio of an ideal *B*8 structure is ~1.4 and the ideal *c/a* ratio of hcp structures is ~1.63. Our observations of a structure with a significantly larger *c/a* ratio at high pressures compared to the ideal hexagonal structures distinguishes this phase from the *B*8 structure. The Miller indices indexed to the *B*8-*like* phase are shown in Figure 8.1, Figure 8.2, and Table 8.1.

8.3.2. Chemical analyses of recovered Fe-S-O samples

We aimed to constrain the stoichiometry of the *B*8 phase by chemically analyzing a sample recovered from 170(1) GPa and 3350(170) K. A backscattered image of the sample cross section is shown in Figure 8.4. The grains within the sample are <5 μm in size, such that signal from multiple grains was collected during point analyses. The EDS point analyses were then plotted onto a ternary diagram to assess the likely compositions of the endmember phases and resulting mixing between them due to grain overlap. The results are compatible with grains of FeO, as observed in the diffraction patterns (Figure 8.1), $Fe_{11}P_4$ (73% Fe, Trigonal phase), and a phase that is around 94 atm% Fe, with approximately equal parts oxygen and sulfur. The sample was recovered from temperatures where melting is expected, and the presence of a melt may indicate that conditions were near ternary eutectic temperatures. If the chemical analyses were instead interpreted as an FeO + trigonal phase + Fe_{94}(O, S) melt assemblage, the melt would be too iron rich to feasibly draw an FeO–trigonal phase cotectic with the given starting composition (Figure 8.4). These chemical analyses are challenging from such high *P-T* conditions, given the size of the recovered sample material, and further analyses using methods such as transmission electron microscopy may prove useful. The results do suggest, however, that the high *P-T* B8-*like* phase is Fe-rich.

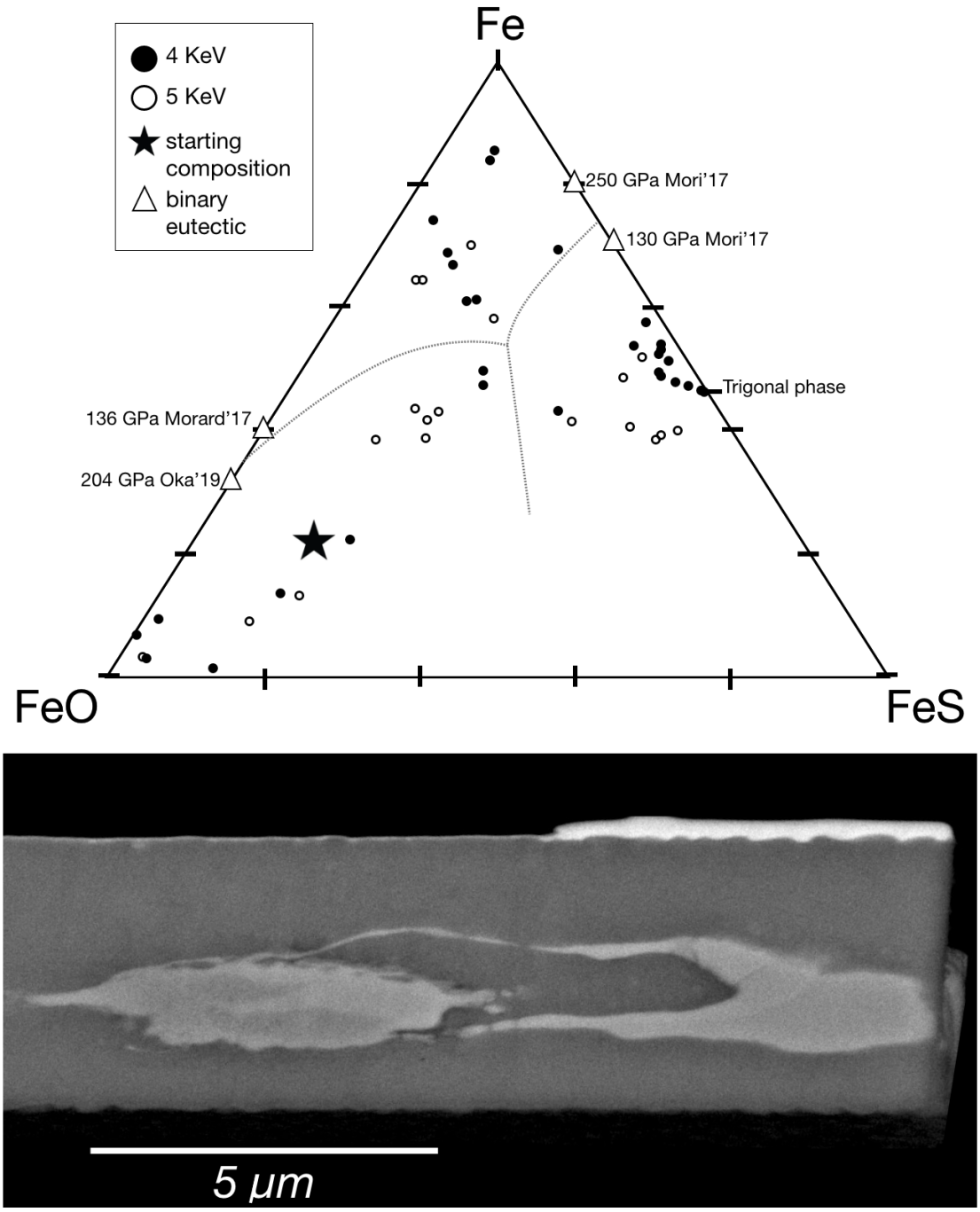

Figure 8.4. Sample recovery of an Fe–6S–12O compositions from 170(1) GPa and 3350(170) K with point analyses collected and plotted on a ternary diagram. The chemical compositions suggest overlapping grains of FeO, the trigonal phase, and an Fe-rich Fe-(O,S) (~94 atm% Fe) phase with peak *P-T* conditions near the ternary eutectic.

8.3.3. Details of the B8-like structure

The intensities of diffraction angles indicate that iron likely occupies the hexagonal close packed sublattice, but this plausible Fe-rich chemistry would require that iron also occupies the primitive hexagonal sublattice with O and S. Diffraction from the (111) plane of the NiAs structure is also achieved if ordering is present within the primitive hexagonal sublattice. A possible scenario depicting ordering of Fe and S, O in the *B*8-*like* phase is given in Figure 8.5 where iron occupies every other primitive hexagonal sublattice site. The resulting diffraction pattern matches the general trends observed in our high *P*-*T* experiments, but the presence of Fe in the primitive hexagonal sublattice does change the observed intensities of the calculated diffraction pattern so that it is less compatible with our raw data; namely the high intensity reflections at ~10º (Figure 8.5). With laser heated data, diffraction intensities cannot be directly related to the structure and the calculated and observed diffraction patterns must be compared with caution. For an >90% Fe composition; however, Fe would have to occupy > 4 out of every 5 primitive hexagonal sites, which may result in a weaker signal from the (111) plane or the formation of a superstructure to account for the ordering.

Placing iron in the hcp sublattice and Fe + (S, O) in the primitive hexagonal sublattice and inducing ordering of iron among the of the *B*8 structure may satisfy the diffraction angles and intensity trends observed, but these structural details do not resolve the difference in *c/a* ratio in the observed *B*8-like phase and the classic NiAs structure. In fact, a search for hexagonal structures with *c/a* ratio of ~2.0 returns limited results, as most hexagonally close packed structures do not form arrangements with *c/a* ratios far from $(8/3)^{0.5}$ (e.g., De Gelder and Janner 2005). One structure type that did produce similar diffraction intensities and angles with a *c/a*

ratio of 1.9 is the Ag_2F structure (*P*-3*m*1, *Z* = 1) (Ott and Seyfarth, 1928). This trigonal structure is very similar to the *B*8 structure; nonmetal sites are located at the corners of the trigonal unit cell and the metal sites are interior to the cell with coordinates Ag1 = (0.3333, 0.66667, 0.25), Ag2 = (0.66667, 0.33333, 0.75), as is observed in hcp structures. The Ag_2F structure can be thought of as the NiAs structure without the nonmetal sites located at $z = 0.5$. Simulated diffraction from this structure produces a high intensity peak at $2\theta = 8.35^{\circ}$ and a peak = 13.72º (42 keV) in agreement with our work. The Ag_2F structure type also shows an additional peak at ~9.8,º which is observed in our data, and was initially interpreted as residual iron. If the *B*8-like phase adopts this structure, then it could instead be interpreted that the crystallization observed at this diffraction angle is attributable to the Ag_2F-type $Fe_x(O, S)$ and not from the (101) plane of hcp-Fe.

To achieve an Fe-rich stoichiometry, Fe would have to dissolve into the primitive hexagonal sublattice, but ordering is not required, as the atomic configuration of this structure already produces diffraction from the (111) plane due to the absence of the lattice sites at $z = 0.5$. Interestingly, Ag_3O adopts the Ag_2F structure with O occupying only ⅔ of the nonmetal sites (Grzelak, 2008). This arrangement can be viewed as the anti-BiI_3-type structure (*P*-31*m*, *Z* = 2), and Fe_3O has been calculated to possibly adopt this structure with low enthalpies at Earth's core pressures while achieving close packing (Alfe et al. 1999). These results, however, are not consistent among iron oxide *ab-initio* studies (Weerasinghe et al. 2015; Huang et al 2018), and Alfe et al. 1999 suggests that better Fe-oxide atomic arrangements, that do not arrange oxygen sites as close together, may be more stable. The Ag_3O (anti-BiI_3 structure) diffraction pattern is also not compatible with our observations of the *B*8-like $Fe_x(S, O)$, as additional peaks are

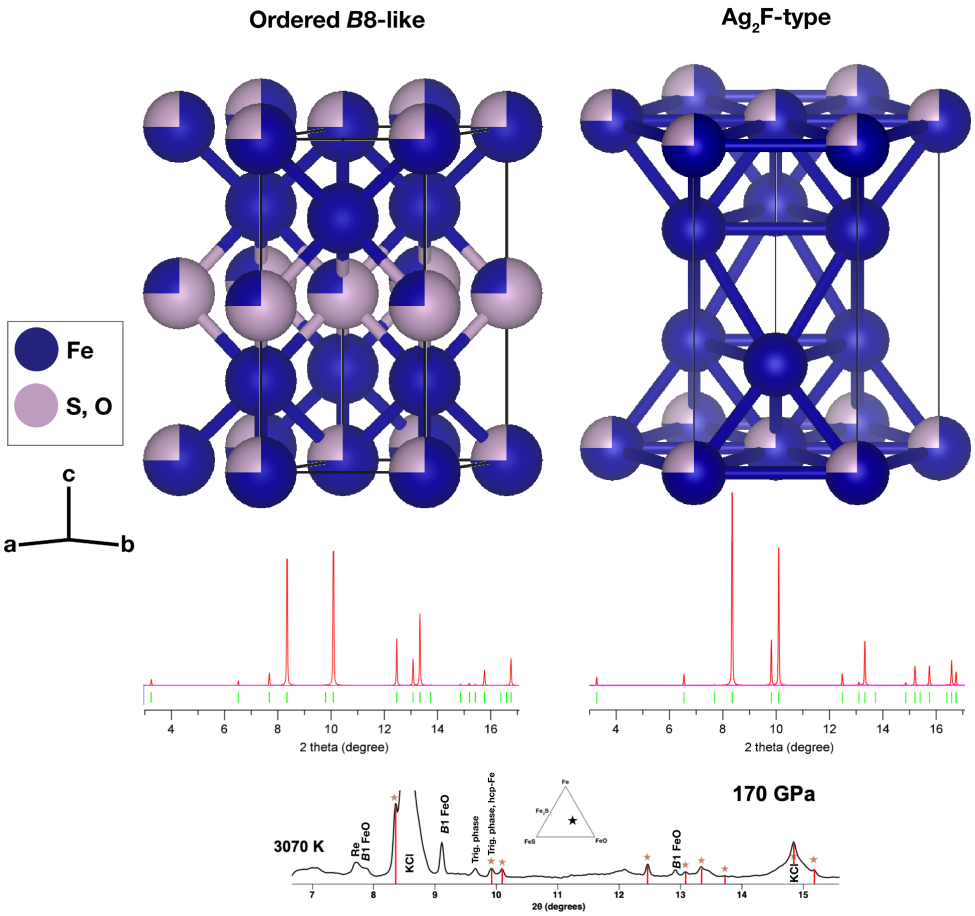

Figure 8.5. The possible ordered *B*8-like $Fe_x(O, S)$ ($P6_3/mmc$, $Z = 2$) structure and Ag_2F-type $Fe_x(O, S)$ (P-3m1, $Z = 1$) structures with Fe occupying the hexagonal closed packed sites and Fe + (O, S) occupying the primitive hexagonal sites. The Fe must be ordered in the *B*8-like structure to observe diffraction from the (111) plane (~13.72º two-theta at these conditions), but Fe can randomly occupy the primitive hexagonal sublattice of the Ag_2F structure, as diffraction from the (111) plane is present in this structure due to the absence of atomic positions at $z = 0.5$. The Ag_2F structure type also shows an additional peak at ~9.8,º which is observed in our data, and was initially interpreted as residual iron.

present from the ordering of Fe among the O sites, but it may be true that iron dissolving randomly into the primitive hexagonal sites of the Ag_2F structure achieves an iron rich stoichiometry, does not produce additional diffraction peaks, and is more energetically favorable to the Ag_3O structure.

Previous Fe-FeO melting studies at these conditions (Morard et al. 2017; Oka et al. 2019) did not observe the formation of a *B*8-like phase as is observed here. Further, our observations in the purely Fe-S system attempting to form this phase (Chapter 7) were not successful. These results highlight sulfur as a potentially critical component in the formation of this high *P-T* Fe-oxide phase. Our chemical analyses suggest a contribution from both oxygen and sulfur, and solid solution in transition metal compounds is common in metallurgy and can have a dramatic effect on the structural properties of a material (e.g., Heaney 2000 and references therein). These effects may be magnified at high pressures, as equation of state studies evidence that Fe, S, and O are more similar in size at such extreme conditions (e.g., Dewaele et al. 2006; Seagle et al. 2006; Zurkowski et al. submitted, Chapter 4; Fischer et al. 2011).

8.4. Further work

The possibility of a new Fe-rich (O,S) phase at Earth's outer core conditions is critical to investigate with further experiments. To date, we have conducted three experiments on this *B*8-like high *P-T* $Fe_x(O, S)$ phase: two powder diffraction experiments and one sample recovery experiment. Two experiments have also been conducted in O-free compositions and the *B*8 phase was not successfully synthesized. The next steps may include conducting powder diffraction experiments on S-free compositions to confirm whether the *B*8-like phase is O-rich and whether sulfur is required to stabilize the phase in Fe-rich compositions at high *P-T.* Additional sample recovery experiments, replicating our results is also critical, as these analyses are challenging upon recovery from such extreme conditions.

The *B*8-like phase also forms large grains and adopts a high symmetry structure (Figure 8.2), such that multigrain diffraction experiments, even over a limited angular range, may be sufficient to solve the structure. The general atomic arrangement is known: it is related to the NiAs structure and may adopt the Ag_2F structure. Therefore, the structural solution process should be fairly straightforward (unlike the challenges faced with the trigonal phase in Chapter 7) after data integration and reduction. Single crystal X-ray diffraction analyses will also be adequate for determining the likely chemistry and site occupancies of Fe, S and O. Future experiments will surely be conducted.

9. Summary

On the basis of powder diffraction and sample recovery, previous studies reported that tetragonal Fe_3S (I-4, Z = 8) is stable in Fe-rich systems across the pressures and temperature range probed in this thesis work (Figure 9.1a) (Fei et a. 2000; Seagle et al. 2006; Morard et al. 2008; Kamada et al. 2010; Kamada et al. 2012; Ozawa et al. 2013; Mori et al. 2017; Tateno et al. 2019; Thompson et al. 2020). With the addition of single crystal X-ray diffraction techniques on multigrain Fe-sulfide synthesis products, it is clear that the structural properties of Fe-rich sulfide system cannot be described by the tetragonal Fe_3S structure alone between 21 and 200 GPa and to high temperatures (Figure 9.1b). In agreement with previous studies that reported fitted lattice parameters for I-4 Fe_3S (<120 GPa) (Fei et al. 2000; Seagle et al. 2006; Morard et al. 2008; Thompson et al. 2020), we did observe and crystallographically characterize Fe_3S in the Fe_3P-type (I-4, Z = 8) structure (Zurkowski et al. Chapter 6) (Figure 9.1b) These results also support the previous Fe-Fe_3S melting studies (Morard et al. 2008; Kamada et al. 2012; Mori et al. 2017).

In the moderate temperature range between 25 and 200 GPa, however, Fe_2S, rather than Fe_3S, is observed coexisting with iron (Figure 9.1b). Crystallites of Fe_2S were synthesized at 89 GPa and 2400 K and determined to adopt the C23 structure, and compatible unit cells were observed to to 120 GPa at moderate temperatures (Zurkowski et al. 2021, Chapter 3; Zurkowski et al. submitted, Chapter 4) (Figure 9.1b). C23 Fe_2S exhibits a highly compressible a axis, as a likely result of bond angle distortion along this axial direction (Chapter 5), such that with increasing pressure, the C23 structure evolves towards the C37, Co_2Si structure (Zurkowski et al. submitted, Chapter 4). In the 120–150 GPa range, the Fe_2S unit cell geometry is transitional

between the *C*23 and *C*37 structures and above 150 GPa, a *C*37-like Fe_2S cell is observed, in agreement with previous studies (Tateno et al. 2019; Zurkowski et al. submitted, Chapter 4) (Figure 9.1b).

With heating above 145 GPa, *C*37 Fe_2S is observed to react with iron at high temperatures to form a Fe-rich sulfide with a complex trigonal lattice (Figure 9.1b). Indexing of this trigonal phase to 200 GPa and >3000 K with recrystallized iron unequivocally demonstrates that the tetragonal Fe_3S phase is not stable above 145 GPa on the liquidus in Fe-rich systems (Chapter 7). The stoichiometry of this trigonal Fe-sulfide is ~73 atomic % Fe. As this metal content is within a few atomic percent of an Fe_3S stoichiometry, previous observations of Fe-sulfide grains with ~75% Fe in sample recovery studies from >200 GPa do not contradict the stability of the Fe-S trigonal phase at these conditions.

The stability of the trigonal Fe-S phase above 145 GPa at high temperatures has several important implications in regards to Earth's outer core chemistry and dynamics. The *I*-4 Fe_3S + Fe → Fe-S trigonal phase + Fe transition must occur between ~120 –150 GPa at high temperatures (Figure 9.1b). As these conditions overlap that of the core-mantle boundary, the volume change and elastic properties of these phases may play a role in the seismic properties and crystallization sequences of the outermost core. The presence of Fe_8S_3 on the liquidus also requires a change in melting behavior above 145 GPa. Grains of the Fe-S trigonal phase were synthesized at temperatures higher than the previously reported Fe–Fe_3S solidus at these conditions, supporting that an increase in Fe-sulfide melting temperature is required to better characterize this system (Figure 9.1b). *C*37 Fe_2S is observed on the liquidus above ~300 GPa in Fe-rich systems (Tateno et a. 2019), suggesting a positive *C*37 Fe_2S + Fe → trigonal phase + Fe

phase boundary slope with pressure, as is observed in our work (Chapter 6) (Figure 9.1b). Finally, based on studies of analog transition metal binary compounds, the stability of the complex trigonal Fe-P phase is a likely result of increased metal-metal interactions at high pressures and temperatures. The stability of the Fe-S trigonal phase may influence the electronic properties of Earth's outer core, possibly attributing to the experimental observations of high thermal conductivity values for Earth's outer core (e.g., Pozzo et al. 2012; Gommi et al. 2013 ; Ohta et al.; 2016).

The complexity of the Fe-sulfide system at high pressures and temperatures was determined in the current thesis work with the implementation of single crystal X-ray diffraction techniques at high pressures. While powder X-ray diffraction remains critical for identifying the onset of a high *P-T* phase and melting transition *in-situ*, it was not suitable for readily identifying complex structures such as Fe-S trigonal phase or the structural mechanisms for the *C*23–*C*37 transition in Fe_2S. At high pressures and temperatures, our work also shows that Fe-sulfides readily form large grains, suitable for single crystal X-ray diffraction analysis. By conducting single crystal measurements on the quenched Fe-sulfide samples from our powder experiments, a wealth of knowledge was gained within one experiment. From my observations, other geoscience-relevant systems, including iron alloys and silicates, form multigrain samples at high pressures, such that the powder + single crystal methodology discussed over the course of this thesis may greatly benefit future research on these topics. The newly developed Fe-sulfide phase relations may directly influence future characterization and inspire future investigations of the many remaining unknown details of Earth's complex core.

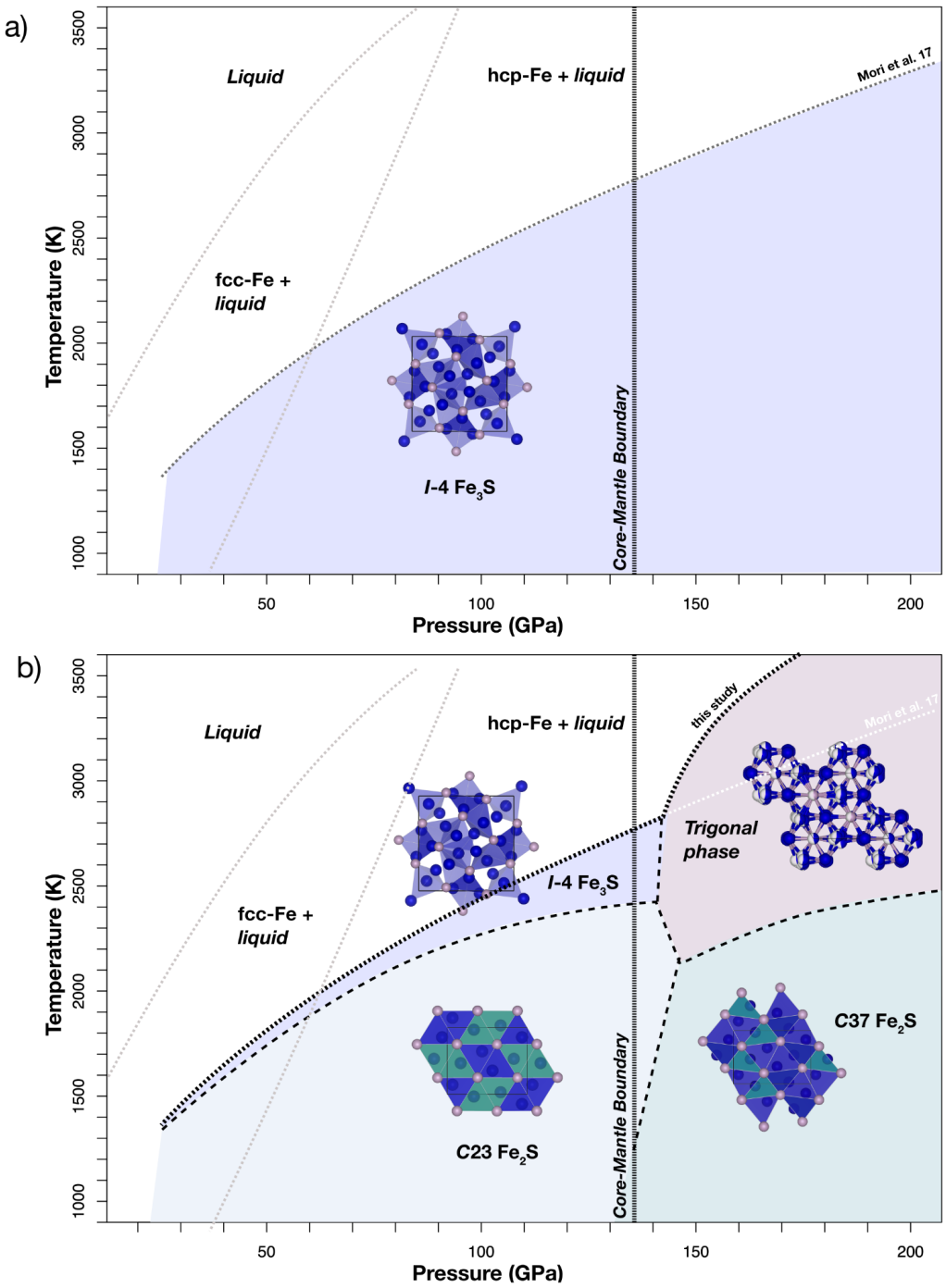

Figure 9.1. a) The previously reported Fe-saturated iron sulfide phase diagram between 21 and 200 GPa and to high temperatures. *I*-4 Fe_3S was reported as the stable phase across this pressure-temperature range. b) Fe-saturated Fe-S phase diagram incorporating the stability of the trigonal phase Fe-S trigonal phase based on the results from the current study. Data collected on the *C*37 + Fe (green circles) → Fe-S trigonal phase + Fe (red squares) phase relations are plotted based on this study. *C*23 and *C*37 Fe_2S are observed at low temperatures with a *C*23–*C*37 Fe_2S transition between 120 and 150 GPa (Zurkowski et al. submitted, Chapter 4). *I*-4 Fe_3S is

Figure 9.1 ***continued***
observed to at least 120 GPa (Fei et al. 2000; Seagle et al. 2006; Morard et al. 2008; Thompson et al. 2020). The *I*-4 Fe_3S + Fe → Fe-S trigonal phase + Fe transition must occur between 120 and 145 GPa, accompanied by a kink in the previously reported melting curves (Mori et al. 2017). As Fe-S trigonal phase was synthesized to 3250 K at 160 GPa, a plausible kink in the melting curve is drawn to account for these crystallite synthesis conditions. The phase relations of iron are also included in grey (Anzellini et al. 2013).

Bibliography

Abe, Y. (1993) Thermal evolution and chemical differentiation of the terrestrial magma ocean. Evolution of the Earth and planets(A 95-18465 03-91), Washington, DC/Brussels, Belgium, American Geophysical Union/International Union of Geodesy and Geophysics (Geophysical Monograph), 41–54.

Agnor, C.B., Canup, R.M. and Levison, H.F. (1999) On the character and consequences of large impacts in the late stage of terrestrial planet formation. Icarus, 142, 219–237.

Aitta, A., (2012) Venus' internal structure, temperature and core composition. Icarus, 218, 967–974.

Alfe, D., Price, G.D. and Gillan, M.J. (1999) Oxygen in the Earth's core: a first-principles study. Physics of the Earth and Planetary Interiors, 110, 191–210.

Anderson, D.L. (1972) Internal constitution of Mars. Journal of Geophysical Research, 77, 789–795.

Anderson, J.D., Colombo, G., Esposito, P.B., Lau, E.L. and Trager, G.B. (1987). The mass, gravity field, and ephemeris of Mercury. Icarus, 71, 337–349.

Anderson, O.L. (1998). The Grüneisen parameter for iron at outer core conditions and the resulting conductive heat and power in the core. Physics of the Earth and Planetary Interiors, 109, 179–197.

Angel, R. and Gonzalez-Platas, J. (2013) ABSORB-7 and ABSORB-GUI for single-crystal absorption corrections. Journal of Applied Crystallography, 46, 252–254.

Angel, R.J., Alvaro, M. and Gonzalez-Platas, J. (2014) EosFit7c and a Fortran module (library) for equation of state calculations. Zeitschrift für Kristallographie-Crystalline Materials, 229, 405–419.

Anzellini, S., Dewaele, A., Mezouar, M., Loubeyre, P. and Morard, G. (2013). Melting of iron at Earth's inner core boundary based on fast X-ray diffraction. Science, 340, 464–466.

Aronsson, B., (1955) The crystal structure of Ni_3P. (Fe_3P-Type) Acta Chemica Scandanavica, 9, 137–140.

Artigas, M., Bacmann, M., Fruchart, D. and Fruchart, R. (1996) La structure cristalline de Cr_2P: Distorsion orthorhombique de la structure hexagonale de type Fe_2P. Journal of Solid State Chemistry, 123, 306–312.

Baur, W.H. (1974) The geometry of polyhedral distortions. Predictive relationships for the phosphate group. Acta Crystallographica Section B: Structural Crystallography and Crystal Chemistry, 30, 1195–1215.

Bazhanova, Z.G., Roizen, V.V., and Oganov, A.R. (2017) High-pressure behavior of the Fe-S system and composition of the Earth's inner core. Uspekhi Fizicheskih Nauk, 187, 1105–1113.

Benedix, G.K., Haack, H. and McCoy, T.J. (2014) Iron and stony-iron meteorites. Meteorites and cosmochemical processes, 1, 267–285.

Benz W. and Cameron G. W. (1990) Terrestrial effects of the giant impact. In Origin of the Earth (ed. H. E. Newsom and J. H. Jones), 61–67. Oxford University Press.

Bi, Y., Tan, H. and Jing, F. (2002). Electrical conductivity of iron under shock compression up to 200 GPa. Journal of Physics: Condensed Matter, 14, 10849–10854.

Birch, F. (1952) Elasticity and constitution of the Earth's interior. Journal of Geophysical Research, 57, 227–286.

Blanchard, P.E., Grosvenor, A.P., Cavell, R.G. and Mar, A. (2008). X-ray Photoelectron and Absorption Spectroscopy of Metal-Rich Phosphides M_2P and M_3P (M= Cr − Ni). Chemistry of Materials, 20, 7081–7088.

Boehler, R. (1992). Melting of the FeFeO and the FeFeS systems at high pressure: constraints on core temperatures. Earth and Planetary Science Letters, 111, 217–227.

Boehler, R. and De Hantsetters, K. (2004) New anvil designs in diamond-cells. High Pressure Research, 24, 391–396.

Brandstätter, F., Koeberl, C. and Kurat, G. (1991) The discovery of iron barringerite in lunar meteorite Y-793274. Geochimica et Cosmochimica Acta, 55, 1173–1174.

Britvin, S. N., Rudashevsky, N. S., Krivovichev, S. V., Burns, P. C. and Polekhovsky, Y. S. (2002) Allabogdanite, $(Fe,Ni)_2P$, a new mineral from the Onello meteorite: The occurrence and crystal structure. American Mineralogist, 87, 1245–1249.

Britvin, S. N., Murashko, M. N., Vapnik, E., Polekhovsky, Y. S. and Krivovichev, S. V. (2017) Barringerite Fe_2P from pyrometamorphic rocks of the Hatrurim Formation, Israel. Geology of Ore Deposits, 59, 619–625.

Britvin, S.N., Shilovskikh, V.V., Pagano, R., Vlasenko, N.S., Zaitsev, A.N., Krzhizhanovskaya, M.G., Lozhkin, M.S., Zolotarev, A.A. and Gurzhiy, V.V. (2013) Allabogdanite, the high-pressure polymorph of $(Fe,Ni)_2P$, a stishovite-grade indicator of impact processes in the Fe–Ni–P system. Scientific Reports 9, #1047 (8 pp).

Brostigen, G. and Kjekshus, A. (1969) Redetermined crystal structure of FeS_2 (pyrite). Acta Chemica Scandinavica, 23, 2186–2188.

Buffett, B.A. (2000). Earth's core and the geodynamo. Science, 288, 2007–2012.

Burbine, T.H., McCoY, T.J., Nittler, L.R., Benedix, G.K., Cloutis, E.A. and Dickinson, T.L. (2002) Spectra of extremely reduced assemblages: Implications for Mercury. Meteoritics and Planetary Science, 37, 1233–1244.

Burkhardt, C., Kleine, T., Bourdon, B., Palme, H., Zipfel, J., Friedrich, J.M. and Ebel, D.S. (2008) Hf–W mineral isochron for Ca, Al-rich inclusions: age of the solar system and the timing of core formation in planetesimals. Geochimica et Cosmochimica Acta, 72, 6177–6197.

Burkhardt, C., Kleine, T., Dauphas, N. and Wieler, R. (2012) Nucleosynthetic tungsten isotope anomalies in acid leachates of the Murchison chondrite: Implications for hafnium-tungsten chronometry. The Astrophysical Journal Letters, 753, #L6 (6 pp).

Buseck, P.R., 1969. Phosphide from meteorites: barringerite, a new iron-nickel mineral. Science, 165, 169–171.

Bykova, E. (2015) Single-crystal X-ray diffraction at extreme conditions in mineral physics and material sciences (Doctoral dissertation, University of Bayreuth).

Campbell, A.J., Seagle, C.T., Heinz, D. L., Shen, G., and Prakapenka, V.B. (2007) Partial melting in the iron-sulfur system at high pressure: A synchrotron X-ray diffraction study. Physics of the Earth and Planetary Interiors, 162, 119–128.

Campbell, A.J., Danielson, L., Righter, K., Seagle, C.T., Wang, Y. and Prakapenka, V.B. (2009) High pressure effects on the iron–iron oxide and nickel–nickel oxide oxygen fugacity buffers. Earth and Planetary Science Letters, 286, 556–564.

Chambers, J.E. (2004). Planetary accretion in the inner Solar System. Earth and Planetary Science Letters, 223, 241–252.

Chambers, J.E. and Wetherill, G.W. (1998). Making the terrestrial planets: N-body integrations of planetary embryos in three dimensions. Icarus, 136, 304–327.

Chen, B., Li, J. and Hauck, S.A. (2008) Non−ideal liquidus curve in the Fe−S system and Mercury's snowing core. Geophysical Research Letters, 35, #07201 (5 pp).

Chen, J.H. and Whitmire, K.H. (2018) A structural survey of the binary transition metal phosphides and arsenides of the d-block elements. Coordination Chemistry Reviews, 355, 271–327.

Chenevier, B., Soubeyroux, J.L., Bacmann, M., Fruchart, D. and Fruchart, R. (1987) The high temperature orthorhombic ⇄ hexagonal phase transformation of FeMnP. Solid State Communications, 64, 57–61.

Chun, H.K. and Carpenter, G.B. (1979) Redetermination of the Crystal Structure of $Cr_{12}P_7$. Acta Crystallographica Section B: Structural Crystallography and Crystal Chemistry, 35, 30–33.

Connelly, J.N., Amelin, Y., Krot, A.N. and Bizzarro, M. (2008). Chronology of the solar system’s oldest solids. The Astrophysical Journal Letters, 675, L121–L124.

De Gelder, R. and Janner, A. (2005) Remarkable features in lattice-parameter ratios of crystals. I. Orthorhombic, tetragonal and hexagonal crystals. Acta Crystallographica Section B: Structural Science, 61, 287–295.

Dera, P., Lavina, B., Borkowski, L. A., Prakapenka, V. B., Sutton, S. R., Rivers, M. L., Downs, R. T., Boctor, N. Z., and Prewitt, C. T. (2008) High-pressure polymorphism of Fe_2P and its implications for meteorites and Earth's core. Geophysical Research Letters, 35, #L10301 (6 pp).

Dera, P., Zhuravlev, K., Prakapenka, V., Rivers, M.L., Finkelstein, G.J., Grubor-Urosevic, O., Tschauner, O., Clark, S.M. and Downs, R.T. (2013) High pressure single-crystal micro X-ray diffraction analysis with GSE_ADA/RSV software. High Pressure Research, 33, 466–484.

Dewaele, A., Loubeyre, P., Occelli, F., Mezouar, M., Dorogokupets, P.I. and Torrent, M. (2006) Quasihydrostatic equation of state of iron above 2 Mbar. Physical Review Letters, 97, #215504 (4 pp).

Dewaele, A., Belonoshko, A.B., Garbarino, G., Occelli, F., Bouvier, P., Hanfland, M. and Mezouar, M. (2012) High-pressure–high-temperature equation of state of KCl and KBr. Physical Review B, 85, #214105 (7 pp).

Dhahri, E. (1996). A study concerning problems of order and stability in the phases (rare earth-transition metal-non-metal). Journal of Physics: Condensed Matter, 8, 4351–4360.

Dreibus, G. and Wanke, H. (1985) Mars, a volatile-rich planet. Meteoritics, 20, 367–381.

Dziewonski, A.M. and Anderson, D.L. (1981) Preliminary reference Earth model. Physics of the Earth and Planetary Interiors, 25, 297–356.

Ellner, M. and Mittemeijer, E.J. (2001) The reconstructive phase transformation $\beta-Co_2P \rightarrow \alpha-Co_2P$ and the structure of the high−temperature phosphide $\beta-Co_2P$. Zeitschrift für anorganische und allgemeine Chemie, 627, 2257–2260.

Evans, H.T. (1970) Lunar troilite: crystallography. Science, 167, 621–623.

Ewald, P.P. (1979) A review of my papers on crystal optics 1912 to 1968. Acta Crystallographica Section A: Crystal Physics, Diffraction, Theoretical and General Crystallography, 35, 1–9.

Fei, Y., Prewitt, C.T., Mao, H.K. and Bertka, C.M (1995). Structure and density of FeS at high pressure and high temperature and the internal structure of Mars. Science, 268, 1892–1894.

Fei, Y., Bertka, C.M. and Finger, L.W. (1997) High-pressure iron-sulfur compound, Fe_3S_2, and melting relations in the Fe–FeS system. Science, 275, 1621–1623.

Fei, Y., Li, J., Bertka, C.M. and Prewitt, C.T. (2000) Structure type and bulk modulus of Fe_3S, a new iron-sulfur compound. American Mineralogist, 85, 1830–1833.

Fei, Y., Ricolleau, A., Frank, M., Mibe, K., Shen, G. and Prakapenka, V. (2007) Toward an internally consistent pressure scale. Proceedings of the National Academy of Sciences, 104, 9182–9186.

Fiquet, G., Auzende, A.L., Siebert, J., Corgne, A., Bureau, H., Ozawa, H. and Garbarino, G., (2010) Melting of peridotite to 140 gigapascals. Science, 329, 1516–1518.

Fischer, R.A., Campbell, A.J., Shofner, G.A., Lord, O.T., Dera, P. and Prakapenka, V.B. (2011) Equation of state and phase diagram of FeO. Earth and Planetary Science Letters, 304, 496–502.

Fischer, R.A., Campbell, A.J., Caracas, R., Reaman, D.M., Dera, P. and Prakapenka, V.B. (2012) Equation of state and phase diagram of Fe–16Si alloy as a candidate component of Earth's core. Earth and Planetary Science Letters, 357, 268–276.

Fischer, R.A., Campbell, A.J. and Ciesla, F.J. (2017) Sensitivities of Earth's core and mantle compositions to accretion and differentiation processes. Earth and Planetary Science Letters, 458, 252–262.

Fischer, R.A. and Nimmo, F. (2018) Effects of core formation on the Hf–W isotopic composition of the Earth and dating of the Moon-forming impact. Earth and Planetary Science Letters, 499, 257–265.

Fujii, S., Ishida, S. and Asano, S., 1988. Electronic structures and magnetic properties of Fe_2P, Co_2P and CoMnP. Journal of Physics F: Metal Physics, 18, 971–980.

Geller, S. and Wolontis, V.M. (1955) The crystal structure of Co_2Si. Acta Crystallographica, 8, 83–87.

Gomi, H., Ohta, K., Hirose, K., Labrosse, S., Caracas, R., Verstraete, M.J. and Hernlund, J.W., (2013) The high conductivity of iron and thermal evolution of the Earth's core. Physics of the Earth and Planetary Interiors, 224, 88–103.

Genova, A., Goossens, S., Mazarico, E., Lemoine, F.G., Neumann, G.A., Kuang, W., Sabaka, T.J., Hauck, S.A., Smith, D.E., Solomon, S.C. and Zuber, M.T. (2019) Geodetic evidence that Mercury has a solid inner core. Geophysical Research Letters, 46, 3625–3633.

Giacovazzo, G. (2011). Fundamentals of crystallography. Oxford University Press: Oxford, ISBN 9780199573660.

Girolami, G. (2015). X-Ray Crystallography. University Science Books: Mill Valley, California, ISBN 9781891389771.

Gonzalez-Platas, J., Alvaro, M., Nestola, F. and Angel, R. (2016). EosFit7-GUI: a new graphical user interface for equation of state calculations, analyses and teaching. Journal of Applied Crystallography, 49, 1377–1382.

Greenwood, R.C., Franchi, I.A., Jambon, A. and Buchanan, P.C. (2005) Widespread magma oceans on asteroidal bodies in the early solar system. Nature, 435, 916–91

Grzelak, A. (2018) Crystal structure and selected physical properties of AgO, AgF_2 and $AgCl_x$ phases under high pressure. (Doctoral dissertation, University of Warsaw).

Gu, T., Wu, X., Qin, S. and Dubrovinsky, L. (2011) In situ high-pressure study of FeP: Implications for planetary cores. Physics of the Earth and Planetary Interiors, 184, 154–159.

Gu, T., Fei, Y., Wu, X. and Qin, S. (2014) High-pressure behavior of Fe_3P and the role of phosphorus in planetary cores. Earth and Planetary Science Letters, 390, 296–303.

Gu, T., Fei, Y., Wu, X. and Qin, S. (2016) Phase stabilities and spin transitions of $Fe_3(S_{1-x}P_x)$ at high pressure and its implications in meteorites. American Mineralogist, 101, 205–210.

Haack, H. and McCoy, T. J. (2005) Iron and Stony-iron Meteorites. In Meteorites, Comets, and Planets (Ed. A. M. Davis) Vol 1 Treatise on Geochemistry (Exec. Eds. H. D. Holland and K. K. Turekian), 325–345.

Hamilton, W.C. (1965). Significance tests on the crystallographic R factor. Acta Crystallographica, 18, 502–510.

Hauck II, S.A., Dombard, A.J., Phillips, R.J. and Solomon, S.C. (2004) Internal and tectonic evolution of Mercury. Earth and Planetary Science Letters, 222, 713–728.

Hauck, S.A., Margot, J.L., Solomon, S.C., Phillips, R.J., Johnson, C.L., Lemoine, F.G., Mazarico, E., McCoy, T.J., Padovan, S., Peale, S.J. and Perry, M.E. (2013) The curious case of Mercury's internal structure. Journal of Geophysical Research: Planets, 118, 1204–1220.

Heaney, P.J. (2000) Phase transformations induced by solid solution. Reviews in Mineralogy and Geochemistry, 39, 135–174.

Heinz, D.L., and Jeanloz, R. (1987) Measurement of the melting curve of $Mg_{0.9}Fe_{0.1}SiO_3$ at lower mantle conditions and its geophysical implications. Journal of Geophysical Research, 92, 437–444.

Helffrich, G. (2017) Mars core structure—concise review and anticipated insights from InSight. Progress in Earth and Planetary Science, 4, 1–14.

Higgins, G. and Kennedy, G.C. (1971) The adiabatic gradient and the melting point gradient in the core of the Earth. Journal of Geophysical Research, 76, 1870–1878.

Hu, X., Fei, Y., Yang, J., Cai, Y., Ye, S., Qi, M., Liu, F. and Zhang, M. (2019) Phase stability and thermal equation of state of iron carbide Fe3C to 245 GPa. Geophysical Research Letters, 46, 11018–11024.

Huang, S., Wu, X. and Qin, S. (2018) Stability and anisotropy of $(Fe_xNi_{1-x})_2O$ under high pressure and implications in Earth's and super-Earths' core. Scientific Reports, 8, 1–8.

Hübschle, C.B., Sheldrick, G.M. and Dittrich, B. (2011) ShelXle: a Qt graphical user interface for SHELXL. Journal of Applied Crystallography, 44, 1281–1284.

Hyde, B.G., O'Keeffe, M., Lyttle, W.M. and Brese, N.E. (1992) Alternative descriptions of the *C*23 ($PbCl_2$), C37 (Co_2Si), $B8_b$ (Ni_2In) and related structure types. Acta Chemica Scandinavica, 46, 216–223.

Ilnitskaya O.N., Akselrud L.G., Mikhalenko S.I., Kuz'ma Y.B. (1987) Crystal structure of α-Ni_8P_3. Soviet Physics Crystallography (translated from Kristallografiya), 32, 26–28.

Irving, J.C., Cottaar, S. and Lekić, V. (2018) Seismically determined elastic parameters for Earth's outer core. Scientific Advances, 4, #eaar2538 (9 pp).

Jarosewich, E. (1990) Chemical analyses of meteorites: A compilation of stony and iron meteorite analyses. Meteoritics, 25, 323–337.

Jeitschko, W., Braun, D.J., Ashcraft, R.H. and Marchand, R., 1978. Phosphides with $Zr_2Fe_{12}P_7$-type structure. Journal of Solid State Chemistry, 25, 309–313.

Jeitschko, W. and Jaberg, B. (1980). New compounds with $Zr_2Fe_{12}P_7$ structure and refinement of the crystal structures of $Er_2Co_{12}P_7$ and $Er_2Ni_{12}P_7$. Zeitschrift für Anorganische und Allgemeine Chemie, 467, 95–104.

Jephcoat, A. and Olson, P., (1987) Is the inner core of the Earth pure iron? Nature, 325, 332–335.

Kamada, S., Terasaki, H., Ohtani, E., Sakai, T., Kikegawa, T., Ohishi, Y., Hirao, N., Sata, N. and Kondo, T. (2010) Phase relationships of the Fe–FeS system in conditions up to the Earth's outer core. Earth and Planetary Science Letters, 294, 94–100.

Kamada, S., Ohtani, E., Terasaki, H., Sakai, T., Miyahara, M., Ohishi, Y. and Hirao, N. (2012) Melting relationships in the Fe–Fe_3S system up to the outer core conditions. Earth and Planetary Science Letters, 359, 26–33.

Kantor, I., Prakapenka, V., Kantor, A., Dera, P., Kurnosov, A., Sinogeikin, S., Dubrovinskaia, N. and Dubrovinsky, L. (2012) BX90: A new diamond anvil cell design for X-ray diffraction and optical measurements. Review of Scientific Instruments, 83, #125102 (6 pp).

Koch-Müller, M., Fei, Y., Wirth, R. and Bertka, C.M. (2003) High-pressure iron-sulfur compounds and their implications for the mineralogy of the sulfur-bearing iron cores. EAEJA, abstract #3652.

King, H. and Prewitt, C.T. (1982) High-pressure and high-temperature polymorphism of iron sulfide (FeS). Acta Crystallographica Section B: Structural Crystallography and Crystal Chemistry, 38, 1877–1887.

Kokubo, E. and Ida, S. (2002) Formation of protoplanet systems and diversity of planetary systems. The Astrophysical Journal, 581, 666–680.

Kominami, J. and Ida, S. (2002) The effect of tidal interaction with a gas disk on formation of terrestrial planets. Icarus, 157, 43–56.

Kruijer, T.S., Touboul, M., Fischer-Gödde, M., Bermingham, K.R., Walker, R.J. and Kleine, T., (2014a) Protracted core formation and rapid accretion of protoplanets. Science, 344, 1150–1154.

Kruijer, T.S., Kleine, T., Fischer-Gödde, M., Burkhardt, C. and Wieler, R. (2014b) Nucleosynthetic W isotope anomalies and the Hf–W chronometry of Ca–Al-rich inclusions. Earth and Planetary Science Letters, 403, 317–327.

Kuwayama, Y., Morard, G., Nakajima, Y., Hirose, K., Baron, A.Q., Kawaguchi, S.I., Tsuchiya, T., Ishikawa, D., Hirao, N. and Ohishi, Y. (2020). Equation of state of liquid iron under extreme conditions. Physical Review Letters, 124, #165701 (6 pp).

Labrosse, S., Hernlund, J.W. and Coltice, N. (2007) A crystallizing dense magma ocean at the base of the Earth's mantle. Nature, 450, 866–869.

Ladd, M. and Palmer, R. (2003). Structure determination by X-Ray crystallography. Plenum Press: New York. ISBN 978-1-4614-3956-1.

Lai, X., Zhu, F., Liu, Y., Bi, W., Zhao, J., Alp, E.E., Hu, M.Y., Zhang, D., Tkachev, S., Manghnani, M.H. and Prakapenka, V.B. (2020). Elastic and magnetic properties of Fe_3P up to core pressures: Phosphorus in the Earth's core. Earth and Planetary Science Letters, 531, #115974, (10 pp).

Lavina, B., Dera, P., Kim, E., Meng, Y., Downs, R.T., Weck, P.F., Sutton, S.R. and Zhao, Y., (2011) Discovery of the recoverable high-pressure iron oxide Fe_4O_5. Proceedings of the National Academy of Sciences, 108, 17281–17285.

Lavina, B., Dera, P. and Downs, R.T. (2014) Modern X-ray diffraction methods in mineralogy and geosciences. Reviews in Mineralogy and Geochemistry, 78, 1–31.

Loa, I., Nelmes, R.J., Lundegaard, L.F. and McMahon, M.I. (2012). Extraordinarily complex crystal structure with mesoscopic patterning in barium at high pressure. Nature Materials, 11, 627–632.

Lomnitskaya, Y.F. (2001) Phase Relations in the Systems M–Mn–P (M= Cr, Mo, W, Re). Inorganic Materials, 37, 9–14.

Lennie, A.R., Redfern, S.A., Schofield, P.F. and Vaughan, D.J. (1995). Synthesis and Rietveld crystal structure refinement of mackinawite, tetragonal FeS. Mineralogical Magazine, 59, 677–683.

Litasov, K.D., Sharygin, I.S., Dorogokupets, P.I., Shatskiy, A., Gavryushkin, P.N., Sokolova, T.S., Ohtani, E., Li, J. and Funakoshi, K. (2013) Thermal equation of state and thermodynamic properties of iron carbide Fe3C to 31 GPa and 1473 K. Journal of Geophysical Research: Solid Earth, 118, 5274–5284.

Litasov, K. D., Ishikawa, A., Kopylova, A. G., Podgornykh, N. M. and Pokhilenko, N. P. (2019) Mineralogy, trace element composition, and classification of Onello high-Ni ataxite. Doklady. Earth Sciences. 485, 381–385.

Litasov, K.D., Bekker, T.B., Sagatov, N.E., Gavryushkin, P.N., Krinitsyn, P.G. and Kuper, K.E., (2020) $(Fe, Ni)_2P$ allabogdanite can be an ambient pressure phase in iron meteorites. Scientific Reports, 10, 1–11.

Loper, D.E. (1978) Some thermal consequences of a gravitationally powered dynamo. Journal of Geophysical Research: Solid Earth, 83, 5961–5970.

Lovering, J.F., Nichiporuk, W., Chodos, A. and Brown, H. (1957) The distribution of gallium, germanium, cobalt, chromium, and copper in iron and stony-iron meteorites in relation to nickel content and structure. Geochimica et Cosmochimica Acta, 11, 263–278.

Malavergne, V., Toplis, M.J., Berthet, S. and Jones, J. (2010) Highly reducing conditions during core formation on Mercury: Implications for internal structure and the origin of a magnetic field. Icarus, 206, 99–209.

Malvin, D.J., Wang, D. and Wasson, J.T. (1984) Chemical classification of iron meteorites—X. Multielement studies of 43 irons, resolution of group IIIE from IIIAB, and evaluation of Cu as a taxonomic parameter. Geochimica et Cosmochimica Acta, 48, 785–804.

Mao, H.K. and Bell, P.M. (1976) High-pressure physics: the 1-megabar mark on the ruby R1 static pressure scale. Science, 191, 851–852.

Maaref, S., Madar, R., Chaudouet, P., Senateur, J.P. and Fruchart, R. (1981) Crystal chemistry of $M_{12}P_7$ phases in relation with the M_2P phosphides. Journal of Solid State Chemistry, 40, 131–135.

Maaref, S., Madar, R., Chaudouet, P., Fruchart, R., Senateur, J.P., Averbuch-Pouchot, M.T., Bacmann, M., Durif, A. and Wolfers, P. (1983) Etude de la structure et des conditions de stabilite d'un nouvel arseniure de fer: $Fe_{12}As_5$. Materials Research Bulletin, 18, 473–480.

Masters, G. and Gubbins, D. (2003) On the resolution of density within the Earth. Physics of the Earth and Planetary Interiors, 140, 159–167.

Matassov, G. (1977) The electrical conductivity of iron-silicon alloys at high pressures and the Earth's core. (Doctoral Dissertation, University of California, Davis).

McDonough, W.F. and Sun, S.S. (1995) The composition of the Earth. Chemical geology, 120, 223–253.

McDonough, W.F., (2003) Compositional model for the Earth's core. In The Mantle and Core (Ed. R. W. Carlson), Vol. 2 Treatise on Geochemistry (Exec. Eds. H. D. Holland and K. K. Turekian), 547–568.

Momma, K. and Izumi, F. (2011). VESTA 3 for three-dimensional visualization of crystal, volumetric and morphology data. Journal of Applied Crystallography, 44, 1272–1276.

Morard, G., Andrault, D., Guignot, N., Sanloup, C., Mezouar, M., Petitgirard, S. and Fiquet, G. (2008). In situ determination of Fe–Fe_3S phase diagram and liquid structural properties up to 65 GPa. Earth and Planetary Science Letters, 620–626.

Morard, G., Andrault, D., Antonangeli, D., Nakajima, Y., Auzende, A.L., Boulard, E., Cervera, S., Clark, A., Lord, O.T., Siebert, J. and Svitlyk, V. (2017) Fe–FeO and Fe–Fe_3C melting relations at Earth's core–mantle boundary conditions: Implications for a volatile-rich or oxygen-rich core. Earth and Planetary Science Letters, 473, 94–103.

Mori, Y., Ozawa, H., Hirose, K., Sinmyo, R., Tateno, S., Morard, G. and Ohishi, Y. (2017) Melting experiments on Fe–Fe_3S system to 254 GPa. Earth and Planetary Science Letters, 464 135–141.

Murakami, M., Hirose, K., Kawamura, K., Sata, N. and Ohishi, Y. (2004) Post-perovskite phase transition in $MgSiO_3$. Science, 304, 855–858.

Murthy, V.R. and Hall, H.T. (1970) The chemical composition of the earth's core: Possibility of sulphur in the core. Physics of the Earth and Planetary Interiors, 2, 276–282.

Nagasawa, M., Thommes, E.W., Kenyon, S.J., Bromley, B.C. and Lin, D.N. (2007) The diverse origins of terrestrial-planet systems. In Protostars and Planets V (Eds. B. Reipurth, D. Jewitt, and K. Keil, University of Arizona Press, Tucson, 639–654.

Nakajima, Y., Araki, S., Kinoshita, D., Hirose, K., Tateno, S., Kawaguchi, S.I. and Hirao, N. (2020) New pressure-induced phase transition to Co_2Si-type Fe_2P. American Mineralogist, 105, 1752–1755.

Namur, O., Charlier, B., Holtz, F., Cartier, C. and McCammon, C. (2016) Sulfur solubility in reduced mafic silicate melts: Implications for the speciation and distribution of sulfur on Mercury. Earth and Planetary Science Letters, 448, 102–114.

Nimmo, F. (2002) Why does Venus lack a magnetic field? Geology, 30, 987–990.

Nimmo, F. (2015) Thermal and compositional evolution of the core. In Core Dynamics (Ed. Peter Olsen). Vol. 8 Treatise on Geophysics, (Exec. Eds. G. Schubert), 217–241.

Nittler, L.R., Starr, R.D., Weider, S.Z., McCoy, T.J., Boynton, W.V., Ebel, D.S., Ernst, C.M., Evans, L.G., Goldsten, J.O., Hamara, D.K. and Lawrence, D.J. (2011) The major-element composition of Mercury's surface from MESSENGER X-ray spectrometry. Science, 333, 1847–1850.

Ohta, K., Kuwayama, Y., Hirose, K., Shimizu, K. and Ohishi, Y. (2016) Experimental determination of the electrical resistivity of iron at Earth's core conditions. Nature, 534, 95–98.

Oka, K., Hirose, K., Tagawa, S., Kidokoro, Y., Nakajima, Y., Kuwayama, Y., Morard, G., Coudurier, N. and Fiquet, G. (2019) Melting in the Fe-FeO system to 204 GPa: Implications for oxygen in Earth's core. American Mineralogist: Journal of Earth and Planetary Materials, 104, 1603–1607.

Okamoto, H. and Massalski, T.B. (1990) Binary alloy phase diagrams. ASM International, Materials Park, OH, USA. ISBN: 9780871704030

Olofsson, O. and Ganglberger, E. (1970) Crystal structure of $V_{12}P_7$. Acta Chemica Scandanavica, 24, 2389–2396.

Olsen, E. and Fredriksson, K., 1966. Phosphates in iron and pallasite meteorites. Geochimica et Cosmochimica Acta, 30, 459–470.

Ono, S. and Kikegawa, T. (2006) High-pressure study of FeS, between 20 and 120 GPa, using synchrotron X-ray powder diffraction. American Mineralogist, 91, 1941–1944.

Ono, S., Oganov, A.R., Brodholt, J.P., Vočadlo, L., Wood, I.G., Lyakhov, A., Glass, C.W., Côté, A.S. and Price, G.D. (2008) High-pressure phase transformations of FeS: novel phases at conditions of planetary cores. Earth and Planetary Science Letters, 272, 481–487.

Oryshchyn, S., Babizhetskyy, V., Chykhriy, S., Aksel'rud, L., Stoyko, S., Bauer, J., Guérin, R. and Kuz'ma, Y. (2004) Crystal structure of Ni_5P_2. Inorganic materials, 40, 380–385.

Ott, H. and Seyfarth, H. (1928) XXVIII. Die Struktur des Silbersubfluorids Ag_2F. Zeitschrift für Kristallographie-Crystalline Materials, 67, .430–433.

Ozawa, H., Takahashi, F., Hirose, K., Ohishi, Y. and Hirao, N. (2011) Phase transition of FeO and stratification in Earth's outer core. Science, 334, 792–794.

Ozawa, H., Hirose, K., Suzuki, T., Ohishi, Y. and Hirao, N. (2013) Decomposition of Fe_3S above 250 GPa. Geophysical Research Letters, 40, 4845–4849.

Pozzo, M., Davies, C., Gubbins, D. and Alfe, D. (2012).Thermal and electrical conductivity of iron at Earth's core conditions. Nature, 485, 355–358.

Prakapenka, V.B., Kubo, A., Kuznetsov, A.Laskin, A., Shkurikhin, O., Dera, P., Rivers, M. L. and Sutton, S.R. (2008) Advanced flat top laser heating system for high pressure research at GSECARS: application to the melting behavior of germanium. High Pressure Research, 28, 225–235.

Pramanik, M., Tominaka, S., Wang, Z.L., Takei, T. and Yamauchi, Y., 2017. Mesoporous semi-metallic conductors: structural and electronic properties of cobalt phosphide systems. Angewandte Chemie, 129, 13693–13697.

Prescher, C., and Prakapenka, V.B. (2015) DIOPTAS: a program for reduction of two dimensional X-ray diffraction and data exploration. High Pressure Research, 35, 223– 230.

Prins, R. and Bussell, M.E. (2012). Metal phosphides: preparation, characterization and catalytic reactivity. Catalysis Letters, 142, 1413–1436.

Qian, Z., Xiang, W. and Shan, Q. (2011) In situ high-pressure X-ray diffraction experiments and *ab initio* calculations of Co_2P. Chinese Physics B, 20, #066101 (6 pp).

Raymond, S.N., O'Brien, D.P., Morbidelli, A. and Kaib, N.A. (2009) Building the terrestrial planets: Constrained accretion in the inner Solar System. Icarus, 203, 644–662.

Reehuis, M. and Jeitschko, W. (1989) Magnetic properties of lanthanoid iron and cobalt phosphides with $Zr_2Fe_{12}P_7$ type structure. Journal of Physics and Chemistry of Solids, 50, 563–569.

Ricard, Y., Šrámek, O. and Dubuffet, F. (2009) A multi-phase model of runaway segregation in planetary embryos. Earth and Planetary Science Letters, 284, 144–150.

Rigaku Oxford Diffraction (2018) CrysAlisPRO software system, ver. 1.171.39.44a Rigaku Corporation, Oxford, U.K.

Righter, K. and O'Brien, D.P. (2011) Terrestrial planet formation. Proceedings of the National Academy of Sciences, 108, 19165–19170.

Ringwood, A.E. (1966) The chemical composition and origin of the Earth. Advances in Earth Science, 65, 287–356.

Rivers, M., Prakapenka, V.B., Kubo, A., Pullins, C., Holl, C.M. and Jacobsen, S.D. (2008). The COMPRES/GSECARS gas-loading system for diamond anvil cells at the Advanced Photon Source. High Pressure Research, 28, 273–292.

Robinson, K., Gibbs, G.V. and Ribbe, P.H. (1971). Quadratic elongation: a quantitative measure of distortion in coordination polyhedra. Science, 172, 567–570.

Rubie, D.C., Melosh, H.J., Reid, J.E., Liebske, C. and Righter, K (2003) Mechanisms of metal–silicate equilibration in the terrestrial magma ocean. Earth and Planetary Science Letters, 205, 239–255.

Rubie, D.C., Frost, D.J., Mann, U., Asahara, Y., Nimmo, F., Tsuno, K., Kegler, P., Holzheid, A. and Palme, H. (2011) Heterogeneous accretion, composition and core–mantle differentiation of the Earth. Earth and Planetary Science Letters, 301, 31–42.

Rubie, D.C., Jacobson, S.A., Morbidelli, A., O'Brien, D.P., Young, E.D., de Vries, J., Nimmo, F., Palme, H. and Frost, D.J. (2015) Accretion and differentiation of the terrestrial planets with implications for the compositions of early-formed Solar System bodies and accretion of water. Icarus, 248, 89–108.

Rundqvist, S. (1960) The structures of Co_2P, Ru_2P and related phases. Acta Chemica Scandinavica, 14, 1961–1979.

Rundqvist, S. (1962) Phosphides of the B31 (MnP) structure type. Acta Chemica Scandinavica 16, 287–292.

Rundqvist, S. and Jellinek, F. (1959) The structures of Ni_6Si_2B, Fe_2P and some related phases. Acta Chemica Scandinavica, 13, 425–432.

Rundqvist, S., Andersson, Y. and Pramatus, S. (1979). Coordination and bonding in representatives of the Fe_3P-, Ti_3P-, α-V_3S-and β-V_3S-type structures. Journal of Solid State Chemistry, 28, 41–49.

Sakamaki, K., Takahashi, E., Nakajima, Y., Nishihara, Y., Funakoshi, K., Suzuki, T. and Fukai, Y. (2009) Melting phase relation of FeHx up to 20 GPa: Implication for the temperature of the Earth's core. Physics of the Earth and Planetary Interiors, 174, 192–201.

Schlesinger, M.E. (2002) The thermodynamic properties of phosphorus and solid binary phosphides. Chemical Reviews, 102, 4267–4302.

Scott, E.R. and Wasson, J.T. (1975) Classification and properties of iron meteorites. Reviews of Geophysics, 13, 527–546.

Scott, H.P., Huggins, S., Frank, M.R., Maglio, S.J., Martin, C.D., Meng, Y., Santillán, J. and Williams, Q. (2007) Equation of state and high−pressure stability of Fe_3P−schreibersite: Implications for phosphorus storage in planetary cores. Geophysical Research Letters, 34, #L06302 (5 pp).

Scott, H.P., Kiefer, B., Martin, C.D., Boateng, N., Frank, M.R. and Meng, Y. (2008) P–V equation of state for Fe2P and pressure-induced phase transition in Fe_3P. High Pressure Research, 28, 375–384.

Seagle, C.T., Campbell, A.J., Heinz, D.L., Shen, G. and Prakapenka, V.B. (2006) Thermal equation of state of Fe_3S and implications for sulfur in Earth's core. Journal of Geophysical Research: Solid Earth, 111, , #B06209, (7 pp).

Shannon, M.C. and Agee, C.B. (1996) High pressure constraints on percolative core formation. Geophysical Research Letters, 23, 2717–2720.

Sheldrick, G.M. (2015a) SHELXT–Integrated space-group and crystal-structure determination. Acta Crystallographica Section A: Foundations and Advances, 71, 3–8.

Sheldrick, G.M. (2015b) Crystal structure refinement with SHELXL. Acta Crystallographica Section C: Structural Chemistry, 71, 3–8.

Simonov, A., Weber, T. and Steurer, W. (2014) Yell: a computer program for diffuse scattering analysis via three-dimensional delta pair distribution function refinement. Journal of Applied Crystallography, 47, 1146–1152.

Smith, D.E., Zuber, M.T., Phillips, R.J., Solomon, S.C., Hauck, S.A., Lemoine, F.G., Mazarico, E., Neumann, G.A., Peale, S.J., Margot, J.L. and Johnson, C.L. (2012) Gravity field and internal structure of Mercury from MESSENGER. science, 336, 214–217.

Sohl F., Spogn T. (2011) SNC Meteorites. In: Gargaud M. et al. (eds) Encyclopedia of Astrobiology. Springer, Berlin, Heidelberg.

Solomon, S.C. (1976) Some aspects of core formation in Mercury. Icarus, 28, 509–521.

Stacey, F.D. and Anderson, O.L. (2001) Electrical and thermal conductivities of Fe–Ni–Si alloy under core conditions. Physics of the Earth and Planetary Interiors, 124, 153–162.

Stacey, F.D. and Loper, D.E. (2007) A revised estimate of the conductivity of iron alloy at high pressure and implications for the core energy balance. Physics of the Earth and Planetary Interiors, 161, 13–18.

Stevenson, D.J. (1988) Fluid dynamics of core formation. In Topical Conference Origin of the Earth, #681, 87 (2 pp).

Stevenson, D.J. (2003) Planetary magnetic fields. Earth and Planetary Science Letters, 208, 1-11.

Stout, G.H. Jensen, L.H (1989) X−Ray Structure Determination, A Practical Guide. John Wiley and Sons, New York, Chichester 1989. ISBN 0471607118

Stixrude, L., Wasserman, E. and Cohen, R.E. (1997) Composition and temperature of Earth's inner core. Journal of Geophysical Research: Solid Earth, 102, 24729–24739.

Suer, T.A., Siebert, J., Remusat, L., Menguy, N. and Fiquet, G. (2017) A sulfur-poor terrestrial core inferred from metal–silicate partitioning experiments. Earth and Planetary Science Letters, 469, 84–97.

Takahashi, S., Ohtani, E., Sakamaki, T., Kamada, S., Fukui, H., Tsutsui, S., Uchiyama, H., Ishikawa, D., Hirao, N., Ohishi, Y. and Baron, A.Q. (2019) Sound velocity of Fe_3C at high pressure and high temperature determined by inelastic X-ray scattering. Comptes Rendus Geoscience, 351, 190–196.

Tao, R. and Fei, Y. (2021) High-pressure experimental constraints of partitioning behavior of Si and S at the Mercury's inner core boundary. Earth and Planetary Science Letters, 562, #116849 (8 pp).

Tateno, S., Ozawa, H., Hirose, K., Suzuki, T., I-Kawaguchi, S., and Hirao, N. (2019) Fe_2S: the most Fe-rich iron sulfide at the Earth's inner core pressures. Geophysical Research Letters, 46, 11,944–11,949.

Taylor, G.J., (2013) The bulk composition of Mars. Geochemistry, 73, 401–420.

Taylor, S.R. and Norman, M.D. (1990) Accretion of differentiated planetesimals to the Earth. Origin of the Earth, 29–43.

Terasaki, H., Frost, D.J., Rubie, D.C. and Langenhorst, F. (2008) Percolative core formation in planetesimals. Earth and Planetary Science Letters, 273, 132–137.

Thompson, E.C., Chidester, B.A., Fischer, R.A., Myers, G.I., Heinz, D.L., Prakapenka, V.B. and Campbell, A.J. (2016) Equation of state of pyrite to 80 GPa and 2400 K. American Mineralogist, 101, 1046–1051.

Thompson, E.C., Davis, A.H., Bi, W., Zhao, J., Alp, E.E., Zhang, D., Greenberg, E., Prakapenka, V.B. and Campbell, A.J. (2018) High−pressure geophysical properties of FCC phase FeH_X. Geochemistry, Geophysics, Geosystems, 19, 305–314.

Thompson, S., Komabayashi, T., Breton, H., Suehiro, S., Glazyrin, K., Pakhomova, A. and Ohishi, Y. (2020) Compression experiments to 126 GPa and 2500 K and thermal equation of state of Fe_3S: Implications for sulphur in the Earth's core. Earth and Planetary Science Letters, 534, #116080 (10 pp).

Toby, B. H., and Von Dreele, R. B. (2013) GSAS-II: the genesis of a modern open-source all purpose crystallography software package. Journal of Applied Crystallography, 46, 544–549.

Treiman, A.H., Gleason, J.D. and Bogard, D.D. (2000) The SNC meteorites are from Mars. Planetary and Space Science, 48, 1213–1230.

Tremel, W., Hoffmann, R. and Silvestre, J. (1986) Transitions between NiAs and MnP-type phases: an electronically driven distortion of triangular (3^6) nets. Journal of the American Chemical Society, 108, 5174–5187.

Walter, M.J., Nakamura, E., Trønnes, R.G. and Frost, D.J. (2004) Experimental constraints on crystallization differentiation in a deep magma ocean. Geochimica et Cosmochimica Acta, 68, 4267–4284.

Wasson, J.T. (1967) The chemical classification of iron meteorites: I. A study of iron meteorites with low concentrations of gallium and germanium. Geochimica et Cosmochimica Acta, 31, 161–180.

Wasson, J.T., Ouyang, X., Wang, J. and Eric, J. (1989) Chemical classification of iron meteorites: XI. Multi-element studies of 38 new irons and the high abundance of ungrouped irons from Antarctica. Geochimica et Cosmochimica Acta, 53, 735–744.

Weerasinghe, G.L., Pickard, C.J. and Needs, R.J. (2015) Computational searches for iron oxides at high pressures. Journal of Physics: Condensed Matter, 27, #455501 (9 pp).

Weidenschilling, S.J., Spaute, D., Davis, D.R., Marzari, F. and Ohtsuki, K. (1997) Accretional evolution of a planetesimal swarm. Icarus, 128, 429–455.

Wetherill, G.W. (1985) Occurrence of giant impacts during the growth of the terrestrial planets. Science, 228, 877–879.

Wetherill, G.W. and Stewart, G.R. (1993) Formation of planetary embryos: Effects of fragmentation, low relative velocity, and independent variation of eccentricity and inclination. Icarus, 106, 190–209.

Williams, J.P. and Nimmo, F. (2004) Thermal evolution of the Martian core: Implications for an early dynamo. Geology, 32, 97–100.

Wojdyr, M. (2010). Fityk: a general−purpose peak fitting program. Journal of Applied Crystallography, 43, 1126–1128.

Yang, J., Goldstein, J.I. and Scott, E.R. (2010) Main-group pallasites: Thermal history, relationship to IIIAB irons, and origin. Geochimica et Cosmochimica Acta, 74, 4471–4492.

Yin, Q., Jacobsen, S.B., Yamashita, K., Blichert-Toft, J., Télouk, P. and Albarede, F. (2002) A short timescale for terrestrial planet formation from Hf–W chronometry of meteorites. Nature, 418, 949–952.

Yokoo, S., Hirose, K., Sinmyo, R. and Tagawa, S. (2019) Melting experiments on liquidus phase relations in the Fe−S−O ternary system under core pressures. Geophysical Research Letters, 46, 5137–5145.

Yoshino, T., Walter, M.J. and Katsura, T. (2003) Core formation in planetesimals triggered by permeable flow. Nature, 422, 154–157.

Yu, Z., Wu, W., Lu, P., Zhao, J., Cheng, J., Hu, Q., Yuan, Y., Li, X., Pei, C., Chen, F., Yan, Z., Yan, S., Yang, K., Sun, J., Luo, J., Wang, L. (2017) Structural evolution behavior of manganese monophosphide under high pressure: experimental and theoretical study. Journal of Physics: Condensed Matter, 29, #254002 (8 pp).

Zachariasen, W.H. (1949) Crystal chemical studies of the 5f-series of elements. IX. The crystal structure of Th_7S_{12}. Acta Crystallographica, 2, 288–291.

Zhao, Z., Liu, L., Zhang, S., Yu, T., Li, F. and Yang, G. (2017) Phase diagram, stability and electronic properties of an Fe-P system under high pressure: a first principles study. RSC Advances, 7(26), 15986–15991.

Zurkowski, C., Lavina, B., Chariton, S., Tkachev, S., Prakapenka, V. and Campbell, A. (2020). The novel high-pressure/high-temperature compound $Co_{12}P_7$ determined from synchrotron data. Acta Crystallographica Section E: Crystallographic Communications, 76, 1665–1668.

Zurkowski, C.C., Lavina, B., Chariton, S., Tkachev, S., Prakapenka V.B. and Campbell A.J., in press. The crystal structure of Fe_2S at 90 GPa based on single-crystal X-ray diffraction techniques. American Mineralogist, https://doi.org/10.2138/am-2022-7973

Appendices

Appendix 1. Reading a phase diagram

The Fe-FeS phase diagram from Fei et al. 1997 is provided and an example of the phase relations observed in a simple binary for an Fe-rich example composition is shown by the red star and dotted pathway. Upon cooling from an Fe-rich melt, the melt cools at fixed composition until it reaches a temperature where it begins to crystallize the first solid. This is called the liquidus temperature and in this example composition, the first solid to crystallize is Fe. As Fe continues to crystallize, the melt becomes increasingly FeS rich, and the composition of the melt propagates along the liquidus curve. Eventually, temperatures will cool enough for FeS to begin crystallizing. This *T-X* condition is called the eutectic. For the Fe-FeS system, the eutectic composition is around 30 atm% S (Fei et al. 1995). Below these temperatures, the system is *subsolidus* and both Fe and FeS crystallize. The same logic can be applied for a starting melt that is on the sulfur rich side of the eutectic in Figure (a) and for the remaining discussions as changes in Fe-S phase relations are observed. It should be kept in mind that the eutectic composition restricts melt compositions that will crystallize Fe first from a melt. This is an important constraint for planetary cores that are currently crystallizing an Fe-rich inner core (e.g., Earth, Mercury).

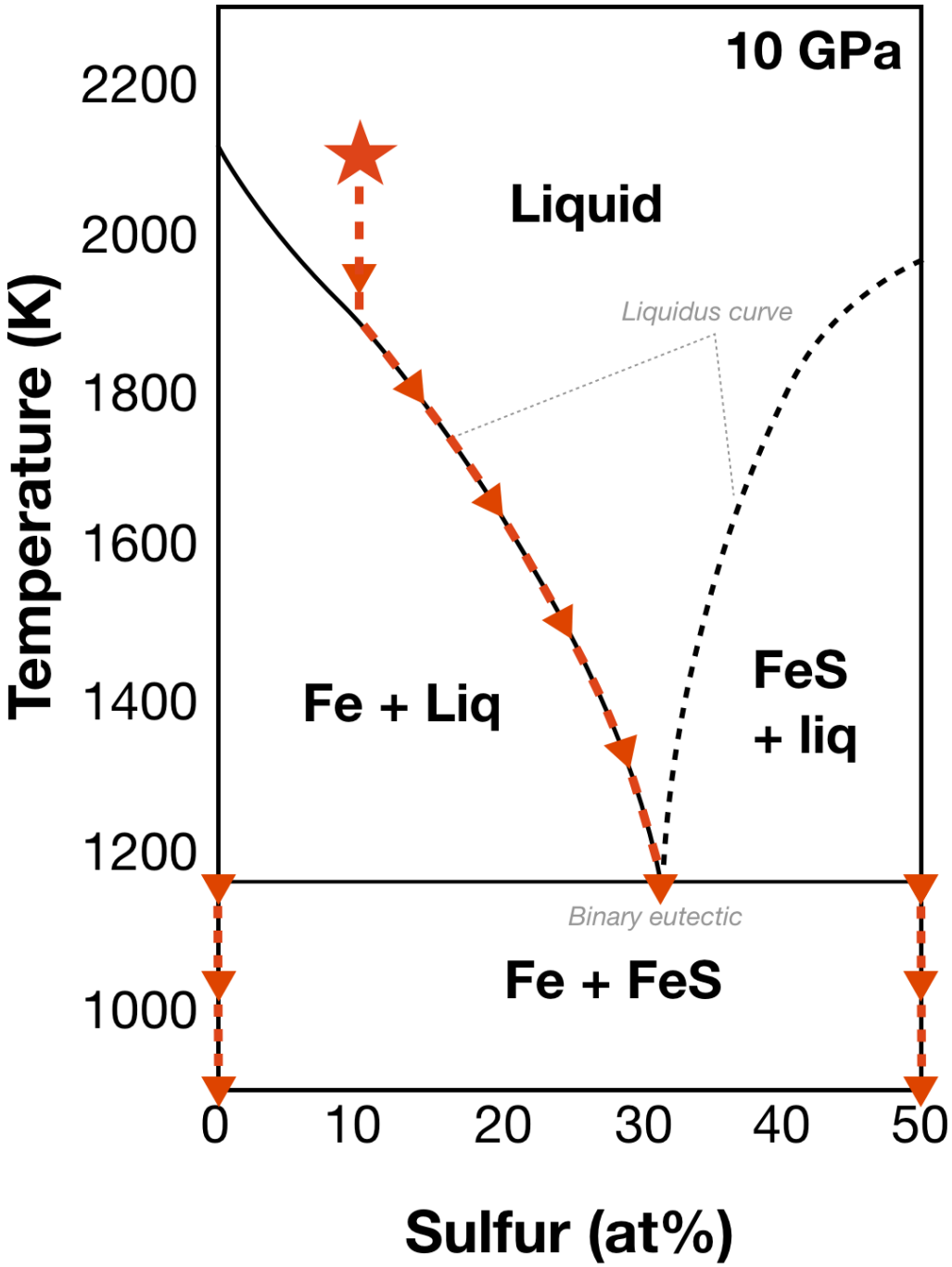

Figure A1. Fe–FeS phase diagram at 1 bar.

Appendix 2. Equations for calculating lattice parameters

Equations related the characteristic *d* spacing and lattice parameters associated with an *hkl* reflection for the differing lattice types.

Cubic: $d^{-2} = (h^2+k^2+l^2)*a^{-2}$

Tetragonal: $d^{-2} = (h^2+k^2)*a^{-2} + (l^2)*c^{-2}$

Orthorhombic: $d^{-2} = (h^2)*a^{-2} + (k^2)*b^{-2} + (l^2)*c^{-2}$

Hexagonal: $d^{-2} = (4/3)(h^2 + hk + k^2)*a^{-2} + (l^2)*c^{-2}$

Monoclinic: $d^{-2} = \sin^{-2}\beta * [(h^2)*a^{-2} + (k^2\sin^2\beta)*b^{-2} + (l^2)*c^{-2} - (2hl\cos\beta)*(ac)^{-1}$

Triclinic: $d^{-2} = V^{-2}(S_{11}h^2 + S_{22}k^2 + S_{33}l^2 + 2S_{12}hk + 2S_{23}kl + 2S_{13}hl)$

$S_{11} = b^2c^2\sin^2\alpha$

$S_{22} = a^2c^2\sin^2\beta$

$S_{33} = a^2b^2\sin^2\gamma$

$S_{12} = abc^2(\cos\alpha\cos\beta - \cos\gamma)$

$S_{23} = a^2bc(\cos\beta\cos\gamma - \cos\alpha)$

$S_{13} = ab^2c(\cos\gamma\cos\alpha - \cos\beta)$

Appendix 3. Interpreting space group diagrams

Instructions for reading and interpreting a space group from an International Tables diagram.

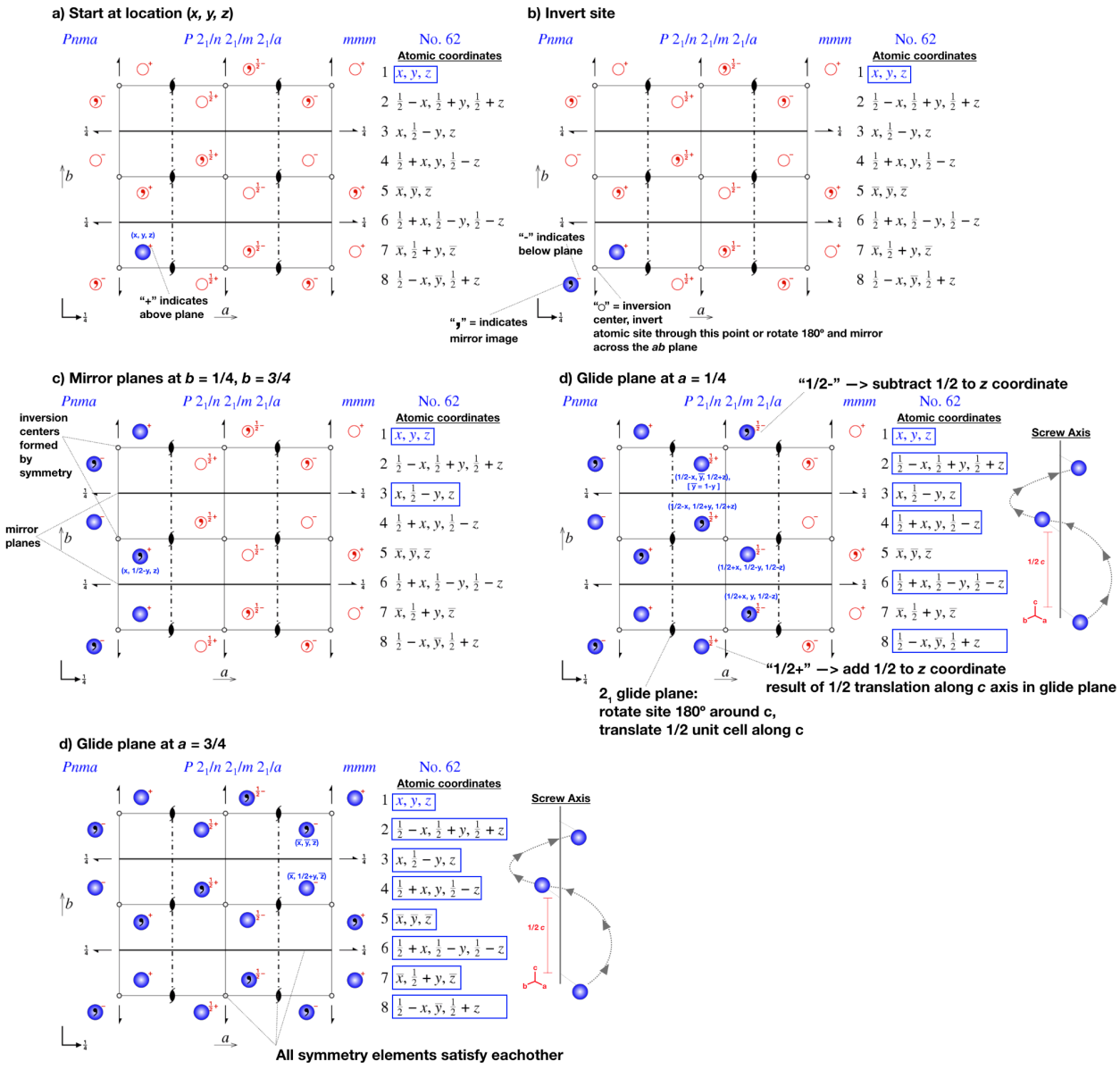

Appendix 4. Instructions for intensity integration and reduction, and structure solution and refinement based on analyses conducted in this work.

Data integration and reduction is conducted using CrysAlisPro. The *dc proffit* command will open a module that steps through the necessary specifications for the data integration and reduction process. In the first window, titled *Step 1: orientation matrix for data reduction,* the lattice constraint is applied (usually automatically) based on the lattice indexing from the previous step, and the presence of twinning or incommensurate structures can be specified (Figure A4.1a).

The second window, titled *Step 2: Experiment run list for data reduction,* prompts you to choose the range of diffraction images to incorporate into the integration and reduction (Figure A4.1b). As obtaining as many reflections as possible is important for crystallographic analysis, it is not recommended to exclude diffraction images initially, unless certain images at the beginning or end were not collected on the sample (e.g., diffraction from the DAC at the edge of the scan).

An integration box size must be defined along with a peak profile fitting model in the third window, titled *Step 3: Basic algorithm parameters* (Figure A4.2a). Choose: *Edit special parameters* (Figure A4.2b). The area within which a reflection's intensity is measured is selected by the *mask size.* The value options are scaled to the default value of *1,* and masks typically ranging from 0.75 for very small reflections to 1.75 for large reflections are available. The *3D peak profile fitting* should be checked, as reciprocal nodes intersect with the Ewald's sphere over a few collected frames, especially when the angular step size is small. Check that the angular opening of the DAC is specified (usually 30º or ½ of the angular scan range) (Figure

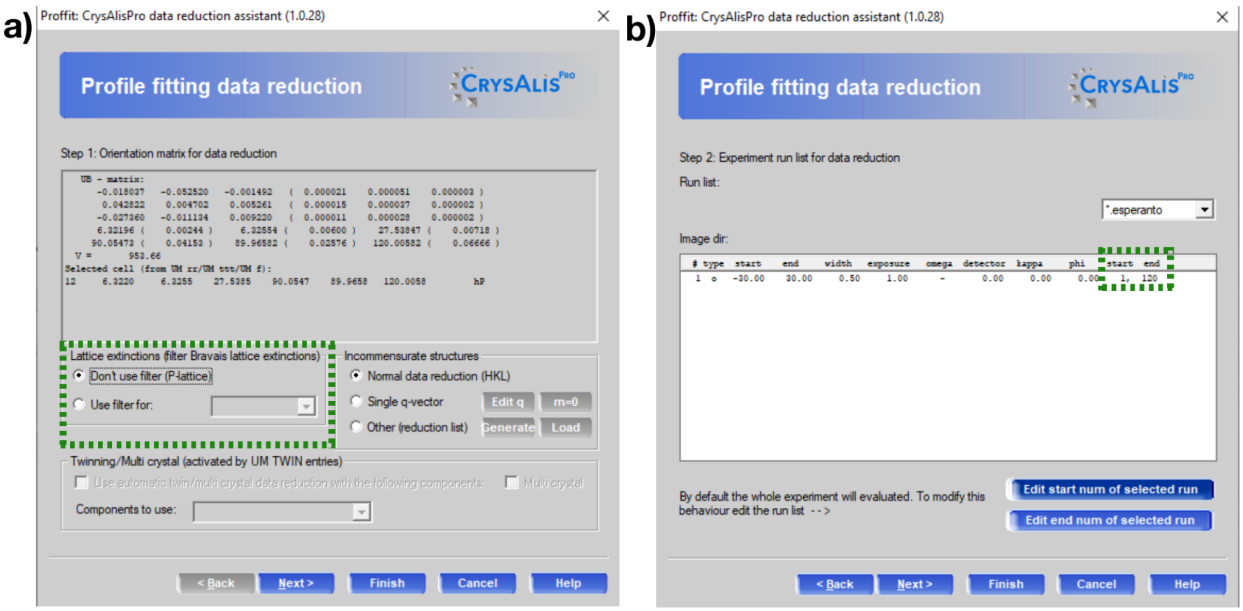

Figure A4.1. Steps 1 and 2 of the *Proffit* windows in *CrysAlisPro.* a) Step 1: check that the correct Bravais Lattice filter was applied based on the lattice indexing done in the previous step. b) Step 2: Choose the frame range for integration.

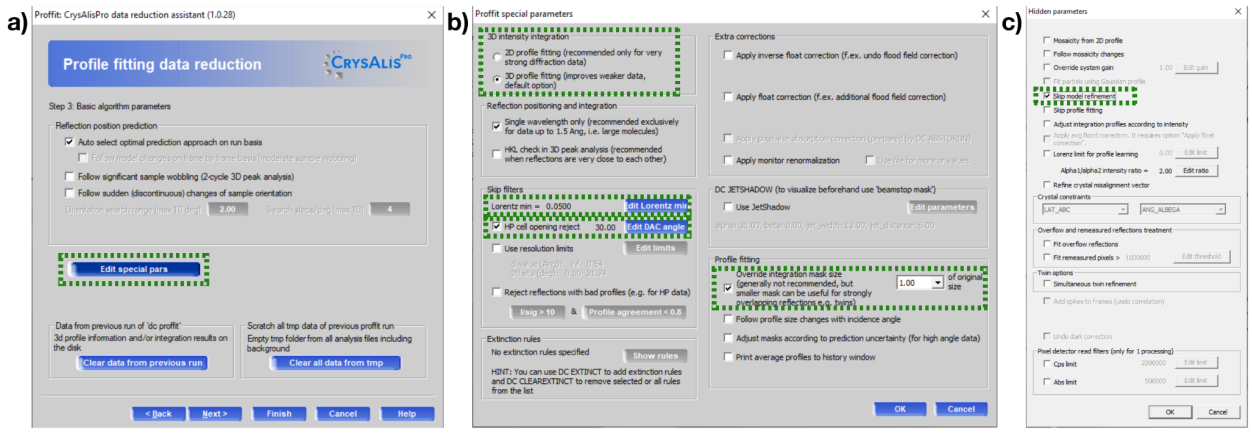

Figure A4.2. a) To begin *Step 3,* click *Edit special pars.* b) In the special parameters dialog box, choose between 2-D and 3-D peak profile fitting, check the Lorentz min, edit the *HP cell opening reject* to match the ½ the angular scan used in the experiment, and edit the mask size for the integration box. Hit *OK.* c) Hit *alt+e* to open the hidden parameters dialog box. Make sure the *skip model refinement* box is checked.

A4.2b), and use the command *alt+e* to check the box labeled, *skip profile fitting*, so that the calibration file will not be adjusted during the integration process (Figure A4.2c).

In *Step 4: Background evaluation,* the first prompt asks you to specify the *Re* (scan *range* for calculating the average background) and *Fr* (*frequency* or number of times this procedure is repeated) (Figure A4.3a). For Sector 13-ID-D, *Re* and *Fr* are set to 5 frames and for Sector 13-BM-D, these values are both set to 10 frames. In the second prompt, choose *Smart background* option (Figure A4.3a). For high *P-T* data, the background is high and will vary from frame to frame, and this feature calculates a background for each individual frame. Then choose the number of frames to incorporate into the background determination for each frame. You must choose an odd number ranging from 1-5: a value of 1 means that only the current image will be used, a value of 3 means that the current image plus the previous and next image will be included, and a value of 5 means that the current image plus the two previous and two following images will be included in the background calculation for each frame.

In *Step 5: Outlier rejection*, the lattice constraint is applied. Simply check here that the lattice is compatible with the unit cell indexed during the lattice finding step (Figure A4.3b). If it does not match, close out of the *Proffit* window and run the command *um ttt* once more to redo the indexing. Alternatively, you can run *um ttt solution* to check if there are other unit cells that match the data (i.e., a hexagonal cell initially indexed to an equivalent C-centered orthorhombic cell).

Back in the *Proffit* procedure, *Step 6: Output*, asks for the chemistry of the phase and density be specified (Figure A4.4a). Click *edit formula,* and input the chemical formula and formula units per cell for the phase (Figure A4.4b). This allows for the calculation of the

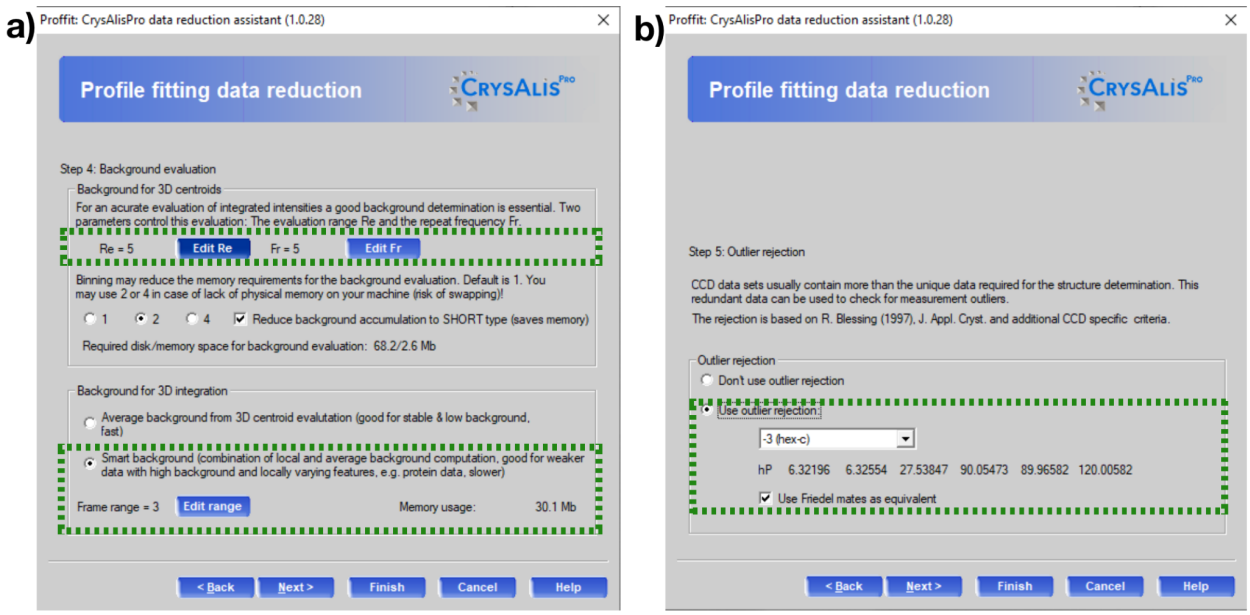

Figure A4.3. a) Step 4: Set background evaluation range (*Re)* and frequency (*Fr*) both to 5 (13-ID-D) or 10 (13 BM-D). Choose: *smart background*, and select a number of frames to be used for background determination: 1, 3, or 5. b) Step 5: Check that the lattice constraint is compatible with the auto indexing.

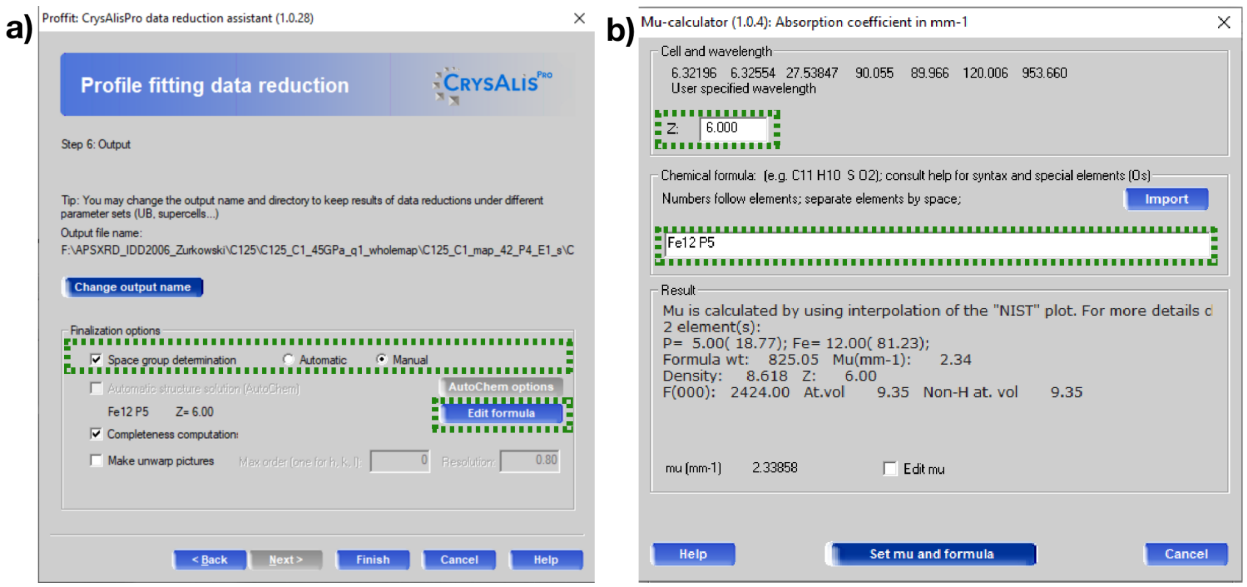

Figure A4.4. a) Choose *Manual* space group determination, then open the *Edit formula* dialog box. b) Edit the formula units per cell (*Z*) and the chemical formula here. An absorption coefficient and density will be calculated from this. Check that these values are reasonable.

absorption coefficient (μ). To monitor the integration and reduction process, manually choose the space group after reduction (Figure A4.4a).

The integration and reduction process will then run with these inputted parameters. After the program is done applying the intensity corrections, you will be prompted to choose the space group. Click through the windows monitoring that the recommended space groups seem reasonable for the indexed cell. The output of the integration and reduction is a table of R_{int} and R_{sigma} values per resolution ring for the dataset (Figure A4.5). It is common that the R_{int} and R_{sigma} values may be higher at low d-spacings, near the limits of the detector and where overall intensities are weaker. If you are not satisfied with the R_{int} and R_{sigma} values, inspect the data (Supplementary file SF2a) and redo the integration adjusting the mask size, smart background range, and finally the number of frames included.

Once the integration parameters have been optimized for the dataset, the structure factors must be finalized by applying the absorption and scaling corrections with the command *dc rrp* (Figure A4.6). The *automatic* empirical correction applied by CrysAlisPro uses the Scale3 Abspack program that approximates the scaling and absorption corrections using a multiscan method (Figure A4.6). If a CBN seat was used upstream; this must be accounted for here by manually choosing the *faces* numerical absorption options and following the prompts of the *high-pressure cell correction* program, Absorb (Figure A4.6) (Angel and Gonzalez-Platas 2013). During experiments using a cBN seat upstream, a rotational scan of the beam intensity through the cBN seat should be collected. A table of the normalized reflection intensities with rotational angle of the upstream and downstream sides of the sample can be input into the Absorb program to correct for the cBN absorption during rotation. An example Absorb *.exp* file is given

Statistics vs resolution (taking redundancy into account) - Laue group (anomalous pairs merged):

resolution(A)	# kept	# theory	# unique	% complete	average redundancy	mean F2	mean F2/sig(F2)	Rint	RsigmaB
inf-1.81	207	150	149	99.3	1.4	2705804.63	96.91	0.011	0.007
1.81-1.42	200	151	149	98.7	1.3	966787.49	36.01	0.015	0.018
1.42-1.23	383	149	149	100.0	2.6	621426.37	36.82	0.025	0.022
1.23-1.11	354	149	149	100.0	2.4	611508.35	33.12	0.024	0.026
1.11-1.03	244	152	149	98.0	1.6	381459.37	21.54	0.032	0.034
1.03-0.96	221	152	149	98.0	1.5	274842.61	17.99	0.032	0.037
0.96-0.92	215	152	149	98.0	1.4	149863.20	12.81	0.045	0.055
0.92-0.88	195	150	149	99.3	1.3	125577.26	11.69	0.034	0.059
0.88-0.84	192	153	149	97.4	1.3	94279.28	12.13	0.041	0.054
0.84-0.80	164	213	150	70.4	1.1	90566.45	11.97	0.051	0.049
inf-0.80	2375	1571	1491	94.9	1.6	611123.49	30.17	0.021	0.020

Figure A4.5. Output table from integration and reduction in CrysAlisPro. R_{int} and R_{sigma} values are listed per resolution ring and for the overall dataset. It is common that the R_{int} and R_{sigma} values may be higher at low resolution, near the limits of the detector. Ideally, R_{int} values of <5% (but no more than 10%) in the higher resolution rings and <10 % (but no more than 15%) at the lower resolution rings are optimal for successful structural solution and refinement. The overall R_{int} and R_{sigma} should also optimally be below 5%.

in the supplemental file SF2b. Also you may choose the *interactive* space group determination option to monitor and specify the symmetry operators written into the finalized files. After conducting the data finalization, an *.ins* file is prepared with the lattice geometry and symmetry operations, an *.hkl* file is prepared with the corrected squared structure factors, standard deviations and their respective Miller Indices, and a *.cif_od* file is also written with important information regarding the experimental set-up and reduction process.

Structure solution

With the .ins and .hkl files, a structural solution model may be determined using the iterative phase assignment and electron density calculations conducted by the ShelXT (Sheldrick 2015a) software. ShelXT can be run through your command prompt. By adding the shelxt.exe to your home path, you can navigate to the directory that includes your .ins and .hkl files, then

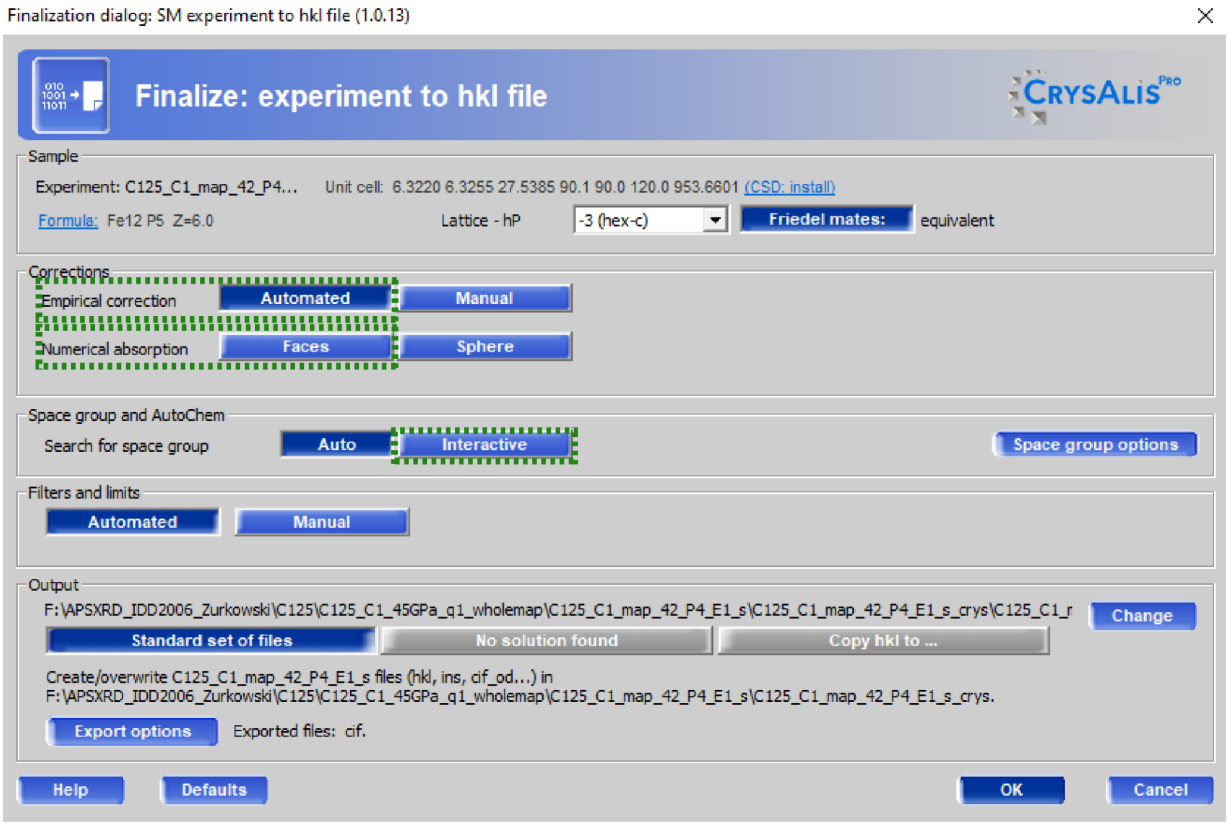

Figure A4.6. Data finalization window opened with the command: *dc rrp.* Here the automated multi-scan frame scaling and absorption correction is applied. If a CBN seat was used upstream; however, this must be accounted for manually by choosing *faces* and following the *high pressure cell correction* program, Absorb (Angel and Gonzalez-Platas 2013). Also choose the *interactive* space group search option.

execute the command *shelxt [file name]* (ex. *shelxt C124_45GPa_map23_rrp*). Be sure that the .ins and .hkl files have the same base name so that ShelXT knows which two files to use in the calculations.

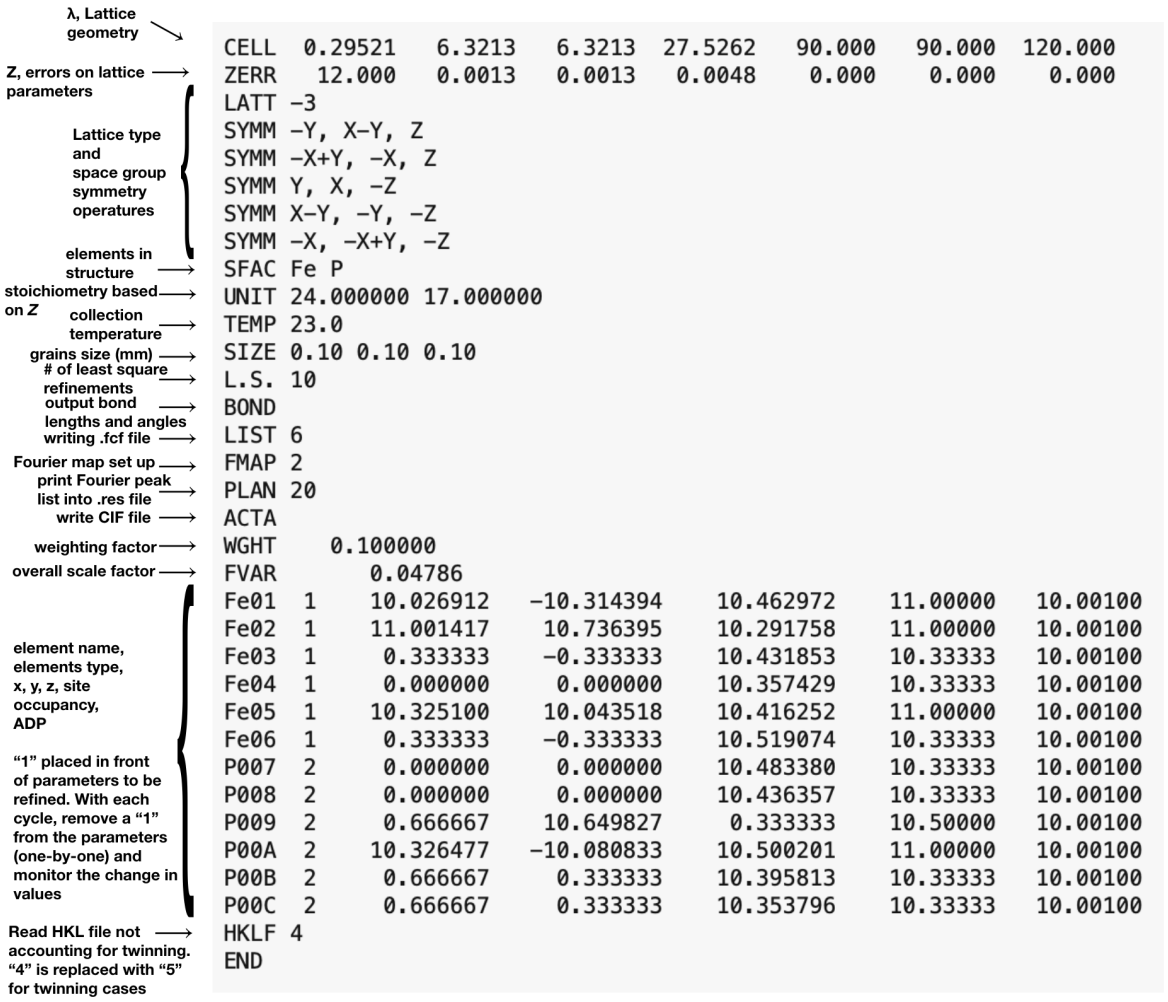

Figure A4.7. Example of an input .ins or .res file to run in ShelXL. The commands and syntax are explained on the left.

Structure refinement

After running ShelXT, an .res output file is written with a starting structure model, including atomic coordinates, site occupancies and displacement parameters, and a series of other commands (Figure A4.7). The file can be run through the terminal using ShelXL (Sheldrick 2015b), with command *shelxl [file name]* or it can be input into the ShelXLE GUI that runs ShelXL (Hübschle et al. 2011). ShelXL conducts a cycle of least-squares refinements adjusting

free parameters in the structure model to minimize the difference in observed and calculated reflection intensity (F^{2}_{hkl}) (Sheldrick 2015b). In this work, ShelXL was run repeatedly as one additional parameter was freed per refinement run. In the .ins or .res files (ShelXL will read either file type), put the number "1" in front of all refinable parameters (general atomic positions, site occupancies, ADPs) (Figure A4.7). Atomic sites that are located on special positions are fixed and will not be refined. The atomic coordinates should not move far if the structure model is reasonable and the residual electron densities should become smaller during this process.

After the atomic positions are refined, the atomic displacements are refined and should adopt a positive value. The vibration of an atomic site can be described as spherical via isotropic displacement parameters or as an ellipse via anisotropic displacement parameters. The starting values are always isotropic. If sufficient reflections are available, the structure may be refined with anisotropic displacement parameters (Figure A4.8). A ratio of 6 reflections per refined parameter is acceptable to consider the fitted parameter statistically meaningful for describing the experimental structure factors (Figure A4.8). Statistical tests can also help to determine whether anisotropic displacement parameters are meaningful to the refinement output (Hamilton, 1965).

During this process of adjusting the structural model, the quality of fit of the model to the experimental data may be assessed with the following output values:

$$\boldsymbol{R_1} = \Sigma||F_{obs}| - |F_{calc}||/ \Sigma|F_{obs}|$$

$$\boldsymbol{wR_2} = \{\Sigma [w(F^2_{obs} - F^2_{calc})^2] / \Sigma [w(F^2_{obs})^2] \}^{0.5}$$

$$\textbf{GooF} = \{ \Sigma [w(F^2_{obs} - F^2_{calc})^2] / (n-p) \}^{0.5}$$

The *w* variable represents the weighting scheme applied to minimize the difference between observed and calculated structure factors. *ShelXL* suggests a weight based on the refined model that may be applied on the final refinement run. The *n* parameter indicates the number of independent reflections and *p* represents the number of refined parameters in the model. (Figure A4.8). Typically R_1 values <0.1, wR_2 values <0.15 and GooF values ~ 1 demonstrate a well refined structure model for high pressure multigrain data (Figure A4.8).

Structure factors measured in microdiffraction in the LHDAC show some well-known limitations, such as limited resolution and redundancy, reflections overlapped by parasitic scattering, diamond diffraction (Loveday et al. 1990) and, more notably, variable volume of illuminated crystal during rotation. It is expected that during the refinement process, several outlier reflections will need to be omitted based on their anomalous calculated versus measured structure factors. This can be assessed by examining the table of *most disagreeable reflections in the* .lst file produced by *ShelXL*. For an outlier reflection, add the *OMIT* [*h k l*] *(*ex. OMIT 3 5 2) command to the .ins or .res file (Figure A4.9). If a significant percentage of reflections must be omitted to obtain R_1, R_{sigma}, and *GooF* values that are reasonable, then the quality of the data or compatibility of the structure model should be addressed.

In the .lst file, above the disagreeable reflection table, ShelXL writes a table with R_1 values broken down by resolution ring for the dataset Figure A4.10. Due to the limits of the detector, it is normal for the R_1 values to be higher at lower *d* spacings, but a desirable refinement may have R_1 values below 0.1 in all resolution rings. In the example of Figure A4.10, outlier reflections in the 0.65-0.68, and 0.71-0.74 ranges may be assessed, followed by those in the 0.68-0.71 and 0.74-0.79 ranges.

Once the outlier reflections are omitted and the R_1, *wR*, and *GooF* are optimized, the errors on site occupancies are assessed for each element type. Typically, the data quality of high *P-T* crystallites in a LHDAC is not sufficient to resolve statistically meaningful site occupancies, but observing that they do not change significantly when allowed to refine, suggests that the structure model and proposed stoichiometry are correct.

Finally, apply the suggested weighting scheme to complete the refinement procedure. Be sure that the *ACTA* command has been added to the input file before the final refinement. This instructs ShelXL to write a crystallographic information file (.CIF). Opening the .CIF file in Vesta during the refinement process may be helpful for monitoring changes to the structure model.

```
Final Structure Factor Calculation for  C125_P3_map_19_rrp_a.res in I-4

Total number of l.s. parameters =    17  Maximum vector length =  623   Memory required =     1649 /    28042

wR2 = 0.2170 before cycle  11 for     322 data and      2 /     17 parameters

GooF = S =     1.285;     Restrained GooF =      1.285 for       0 restraints

Weight = 1 / [ sigma^2(Fo^2) + ( 0.0599 * P )^2 +  82.93 * P ]   where  P = ( Max ( Fo^2, 0 ) + 2 * Fc^2 ) / 3

R1 =  0.0832 for     291 Fo > 4sig(Fo)  and  0.0977 for all     322 data
wR2 =  0.2170,  GooF = S =   1.285,  Restrained GooF =    1.285  for all data

Flack x =    0.344(708) by classical fit to all intensities
             0.532(201) from 85 selected quotients (Parsons' method)
```

Figure A4.8. Portion of the .lst file showing the R_1, wR_2, and GooF values along with the number of reflections, labeled *data*, and number of parameters, labeled *parameters.*

```
Most Disagreeable Reflections (* if suppressed or used for Rfree).
Error/esd is calculated as sqrt(wD^2/<wD^2>) where w is given by the weight
formula, D = Fo^2-Fc^2 and <> refers to the average over all reflections.

    h   k   l          Fo^2          Fc^2    Error/esd  Fc/Fc(max)  Resolution(A)

    3   5   2       3609.37        624.76       5.19       0.096       1.23
   -5   3   2       3831.05        666.37       4.91       0.099       1.23
   -2   8   0       3697.34        534.61       4.89       0.089       1.05
    6   2   2       2254.06        651.67       3.63       0.098       1.16
   -8   5   3       1100.02         69.82       3.60       0.032       0.78
    5   8   3       1575.20         57.75       3.40       0.029       0.78
    2   6   0       2811.28       1058.15       3.18       0.125       1.37
    6   5   1       6794.04       4080.48       2.91       0.246       1.08
```

Figure A4.9. Example of the table of *most disagreeable reflection* given in the .lst file. Use this table to determine outlier reflections that must be omitted from the refinement.

```
Analysis of variance for reflections employed in refinement      K = Mean[Fo^2] / Mean[Fc^2]  for group

Fc/Fc(max)       0.000    0.061    0.091    0.122    0.152    0.186    0.217    0.256    0.300    0.425    1.000

Number in group        34.      31.      32.      32.      32.      33.      32.      32.      32.      32.

          GooF      1.660    1.396    1.948    1.235    0.904    1.261    1.212    0.881    0.633    1.172

           K        3.714    6.117    1.441    1.187    1.055    1.156    1.036    0.989    0.975    0.956

Resolution(A)    0.65     0.68     0.71     0.74     0.79     0.85     0.92     1.02     1.19     1.49     inf

Number in group        36.      38.      24.      35.      31.      30.      35.      31.      30.      32.

          GooF      0.893    0.850    0.967    1.520    0.700    0.884    1.086    1.907    2.143    1.142

           K        1.863    1.038    0.926    1.089    1.035    1.003    1.021    1.018    1.028    0.969

           R1       0.230    0.100    0.157    0.118    0.059    0.078    0.081    0.085    0.090    0.056
```

Figure A4.10. Example of $R1$ values for each resolution ring of a dataset given in the .lst file.